Summer 2006

Oxygen Atom Transfer Chemistry of [Mo(VI)O2]2+ Cores and Geometric Rearrangement in [Mo(V)O]3+ Cores: Reactivity, Mechanisms and Electronic Structure of Functional Molybdoprotein Model Systems

Brian William Kail

Oxygen Atom Transfer Chemistry of $[Mo(VI)O_2]^{2+}$ Cores and Geometric Rearrangement in $[Mo(V)O]^{3+}$ Cores: Reactivity, Mechanisms and Electronic Structure of Functional Molybdoprotein Model Systems.

A dissertation presented to the Bayer School of Natural and Environmental Sciences, Duquesne University

In partial fulfillment of the requirements for the degree of Doctor of Philosophy

By:

Brian William Kail

August 2, 2006

Name: Brian W. Kail

Dissertation Title: Oxygen Atom Transfer Chemistry of $[Mo(VI)O_2]^{2+}$ Cores and Geometric Rearrangement in $[Mo(V)O]^{3+}$ Cores: Reactivity, Mechanisms and Electronic Structure of Functional Molybdoprotein Model Systems.

Degree: Doctor of Philosophy

Date: August, 02, 2006

Approved:

Partha Basu, Ph. D.
Dissertation Advisor
Associate Professor of Chemistry
Department of Chemistry and Biochemistry
Duquesne University

Approved:

Mitchell E. Johnson, Ph. D.
Associate Professor of Chemistry
Department of Chemistry and Biochemistry
Duquesne University

Approved:

A. Andy Pacheco, Ph. D.
Associate Professor of Chemistry
Department of Chemistry and Biochemistry
University of Wisconson - Milwaukee

Approved:

Jeffrey D. Madura, Ph. D.
Professor of Chemistry
Chairman
Department of Chemistry and Biochemistry
Duquesne University

Approved:

David W. Seybert, Ph. D.
Dean of the Bayer School of Natural and Environmental Sciences
Professor of Chemistry
Department of Chemistry and Biochemistry
Duquesne University

Abstract:

The oxygen atom transfer reactivity of a discrete dioxo-molybdenum(VI) complexes, $Tp^{iPr}MoO_2(OPh)$ (where Tp^{iPr}= hydrotris(3-isopropylpyrazol-1-yl)borate), $Tp^{Me2}MoO_2(OPh)$, $Tp^{Me2}MoO_2(SPh)$, $Tp^{Me2}MoO_2(Cl)$, (where Tp^{Me2}= hydrotris(3,5-dimethylpyrazol-1-yl)borate), with seven tertiary phosphines (PMe_3, PMe_2Ph, PEt_3, P(*n*-Bu)$_3$, PEt_2Ph, PPh_2Et and PPh_2Me) have been investigated. The first nucleophilic step follows a second-order rate with an associative transition state in all cases. The second step of the reaction, i.e., the exchange of the coordinated phosphine oxide with acetonitrile, follows a first-order process. The reaction follows a dissociative interchange (I_d) or associative interchange (I_a) type mechanism, as it is substrate and compound dependent.

It has been established that there are three main physico-chemical parameters that contribute to the reactivity of phosphorous (III) compounds, two of which are electronic and the third is of steric origin. It is commonly accepted that these reactions involve a σ-basicity component, a π-acidity component and a steric/size component. However, there has been little investigation into the reactivity of the analogue oxo-phosphorous (V) compounds which are typically generated during oxygen atom transfer reactions (OAT) when the parent phosphorous (III) compounds act as nucleophiles toward oxygen. Here, we explore the current concepts associated with reactivity, the origin of reaction parameters and the general applicability of phosphorous (III) parameters toward reactions that evolve phosphorous (V) products.

Lastly, the regeneration of a catalytically active enzyme, after formal OAT has occurred, is believed to involve two, one electron/ one proton transfer steps that result in a formal Mo(V) intermediate. However, no crystal structure exists for the enzyme in a transient 5+ state. To this end we have synthesized, and fully characterized a series of monooxo-Mo(V) complexes in attempt to model the transient Mo(V) state of the enzyme. Furthermore we show that these complexes can be isolated as two discrete isomers with respect to the position of a heteroatom donor relative to the oxo-group and have detailed the kinetics of isomerization and electronic structure of these complexes. Based upon our findings we have postulated a serine gated electron transfer hypothesis (SGET) to provide a possible explanation for the role of isomerism in the regeneration step of a catalytically active protein.

Acknowledgements:

I must first thank my wife Joanna and daughter Juliana. Joanna stood by me through the many highs and lows of both the daily life of a graduate student in addition to the long hours, late dinners, and financial woes that come with the package. Juliana proved to be a source of inspiration and my main reason for completing the program during the low points. I could not have completed the program without their emotional support and love.

Along these lines I must thank my mother, Marilyn, father and mother in-law, in-law Cecil and Kathy Courtney, for their understanding, love and willingness to help my family when we needed it during my adventure here.

I would like to thank my committee members, Drs. Mitchell Johnson, David Seybert, and Andy Pacheco. Dr. Seybert was always helpful, supportive and generous with the little spare time he had available as dean of the school. He was amazingly approachable, honest, open and willing to listen. Dr. Johnson was a constant source of encouragement in both my research and future aspirations, and was a strong guiding force in all that I have accomplished in this program. Dr. Pacheco offered his deep knowledge and experience in the field of bioinorganic chemistry with a selflessness that is unrivaled. I must also offer my thanks to Dr. Brett Larget, who was of great assistance by helping me; understand the workings of the Matlab software and participating in discussion on the singular value decomposition.

However, the experimental work that was performed in this dissertation could not have been accomplished without the dedicated, knowledgeable and highly experienced instrumentation shop. I find it impossible to imagine that the names of Dave Hardesty, Dan Bodner, Lance Crosby and Andrew Venanzio could not be mentioned in any experimental thesis or dissertation, as they have been the driving force behind the science in Mellon Hall.

Thanks to my friends that I have met during my years as a Duquesne Graduate Student. I can say that you all have offered encouragement, a much needed escape and some of the most memorable years I have had in the department. I hope that, as I do not mention specific names, you all realize that you are considered as part my extended family. I sincerely hope that our friendships will remain over the years to come.

Special thanks to Dr. Victor Nemykin, who was a post-doc in the Basu Lab for much of my time here. I certainly would not be writing these words now if it were not for his selfless encouragement and friendship. Thanks Victor.

Finally, I must thank my advisor Dr. Partha Basu. Dr. Basu has challenged me when I needed challenged, guided me when I was in need of guidance and created an environment in which I could excel and succeed. I owe the greater part of my success to you.

To my wife Joanna, my daughter Juliana, and mother Marilyn; you are my love, my support and my inspiration.

Comprehensive List of Figures:

Comprehensive List of Tables:

List of Compounds and Abbreviations

2-Pic-N-O = 2-picoline-N-oxide.

3-NS_2 = 2-[6-(2-Mercapto-2,2-diphenyl-ethyl)-pyridin-2-yl]-1,1-diphenyl-ethanethiol

4-MM-N-O = 4-methylmorpholine-N-oxide.

4-Pic-N-O = 4-picoline-N-oxide,

ANO = adenosine-N-oxide.

BPB = bromophenol blue.

$BV^{+\cdot}$ = reduced benzyl viologen.

Cyt. C = Cytochrome C

DMS = dimethylsulfide.

dmsABC = DMSO reductase

DMSO= dimethylsulfoxide,

DMSOR = dimethyl sulfoxide reductase.

DQH_2 = duroquinol

$L1O^-$ = hydrobis-pyrazol-1-yl methane (2-tertbutyl-phenolate)

$L3S^-$ = hydrobis-pyrazol-1-yl methane thiolate

LDAO= N,N-dimethyldodecylamine-N-oxide.

LNS_2 = 2,6-bis(2,2-diphenyl-2-thioethyl)pyridinate

LO^- = hydrobis-pyrazol-1-yl methane phenolate

$LPCH_2$ = Lapachol; (2-(3-methyl-but-2-enyl)-[1,4]napthoquinone

MetSO = methionine sulfoxide.

mnt = [*cis*-1,2-dicyano-1,2-ethylenedithiolate]$^{2-}$

$MV^{+\cdot}$ = reduced methyl viologen.

Nap = disimilatory nitrate reductase; periplasmic

Nar = respiratory nitrate reductase; membrane bound

Nas = assimilatory nitrate reductase.

NR = nitrate reductase.

OAT = Oxygen atom transfer

OPR_3 = Phosphine oxide

PBH_2 = Plumbagine (5-hydroxy-2-methyl- 1,4-Naphthoquinone)

PR_3 = Phosphine

PTA = phosphatriazaadamantane (1,3,5-triaza-7-phosphatricyclo[3.3.1.1]decane);

Py-N-O = pyridine-N-oxide

SO = sulfite oxidase.

S_2CNEt_2 = bis-dithiocarbamate

ssp= [2-(salicylindenamino)benzethiolate]$^{2-}$

*t*BuL-NS2 = {*tert*-butyl[2,6-bis(2,2-dipphenyl-2thioethyl)pyridinate]}$^{2-}$.

TMAO = trimethylamine-N-oxide.

TMAOR = trimethylamine N-oxide reductase.

TorA = trimethylamine N-oxide reductase

Tp*= Hydrotris(pyrazol-1yl)methane.

Tp= [Hydrotris(pyrazol-1yl)borate]$^{1-}$

Tp^{Me2} = Hydrotris(3',5'-dimethyl pyrazol-1-yl)borate

Tp^{iPr} = Hydrotris(3'-isopropyl pyrazol-1-yl)borate

Numerical Designations (3-dimensional diagrams of all compounds; ***Figure 2.1****):*

(1) = $Tp^{iPr}MoO_2(OPh)$; intermediate appended by phosphine letter (**1a-1g**)

(2) = $Tp^{Me2}MoO_2(Cl)$; intermediate appended by phosphine letter (**2a-2g**)

(3) = $Tp^{Me2}MoO_2(OPh)$; intermediate appended by phosphine letter (**3a-3g**)

(4) = $Tp^{Me2}MoO_2(SPh)$; intermediate appended by phosphine letter (**4a, 4g**)

(5) = $Tp^{iPr}MoO(OPh)(NCMe)$; acetonitrile solvated product of (**1**)

(6) = $Tp^{Me2}MoOCl(NCMe)$; acetonitrile solvated product of (**2**)

(7) = $Tp^{Me2}MoO(OPh)(NCMe)$; acetonitrile solvated product of (**3**)

(8) = $Tp^{Me2}MoO(SPh)(NCMe)$; acetonitrile solvated product of (**4**)

(9-12) = dimeric products of (**1**), (**2**), (**3**) and (**4**) respectively.

Letter designations:

a = $OPMe_3$; b = $OPMe_2Ph$; c = $OPEt_3$; d = $OP(n\text{-}Bu)_3$; e = $OPEt_2Ph$; f = $OPMePh_2$; g = $OPEtPh_2$

Chapter 1:

Oxygen Atom Transfer Reactivity of Metallo-Enzymes and Synthetic Metal Complexes

Chapter 1:

Oxygen Atom Transfer Reactivity of Metallo-Enzymes and Synthetic Metal Complexes

Abstract:

This work presents a general overview of oxygen atom transfer chemistry (OAT), and the synthetic and biological processes that follow this reaction path. The roles of metals in atom transfer chemistry are reviewed with special attention to ligand effects in the Mo and W-based synthetic and biological systems, which participate in primary-complete oxygen atom transfer reactions. For completeness, a few examples of secondary-complete oxygen atom transfer reactions have also been included. Special attention to charge effects, ligand derived acid-base effects and the effects of metal substitution are also addressed in both the biological and synthetic systems, in terms of primary-complete oxygen atom transfer chemistry.

Introduction:

Metal-Based Atom Transfer Chemistry.

Oxygen atom transfer reaction (OAT) is a subset of a broader class of reactions known as atom transfer reactions (ATR), which can involve Oxygen, Sulfur, Selenium, Hydrogen, Chlorine, and Nitrogen. In general, there are four different subclasses of OAT reactions that depend on the origin of the donor atom and the final degree of separation between the donor and acceptor and as such may be classified as: primary complete, primary incomplete, secondary complete and secondary incomplete. Primary OAT reactions designate that the atom donor and atom acceptor are separate molecules, while secondary OAT reactions designate the reaction designates that the donor and acceptor are located within the same molecule. On the other hand, the complete and incomplete designations represent a separation between the donor and acceptor and formation of a bridged species respectively. The most important subclass of atom transfer is the primary complete type OAT reactions, and will be the subject of further discussion while readers interested in the other three types are referred to the works of Holm[1], and Wu[2]

By formal definition, primary complete oxygen atom transfer reactions are centered about a competent oxo-donor molecule and a separate oxo-accepter molecule. The donor and acceptor generally participate in a 2-electron oxidation-reduction reaction coupled with the transfer of the oxygen atom from the donor to the acceptor, as defined in **Equation 1.1a** and **Equation 1.1b**.

$$OM^{n+2} + X^{m} \rightarrow M^{n} + OX^{m+2}$$ **Equation 1.1a**

$$OX^{m+2} + M^{n} \rightarrow X^{m} + OM^{n+2}$$ **Equation 1.1b**

Here M generally represents a high-valent metal center and X represents either another metal center, or more importantly, an organic molecule. Interestingly, one of the earliest mentions of atom transfer chemistry was presented in 1912 through the work of Hofmann which involved the oxidation of OsO_2 to OsO_4 with chlorate.[3] However in 1950, the work of Taube[4] has been attributed to be the advent of documented oxygen atom transfer through ^{18}O-labeling of the reaction between $^{18}OCl^-$ and NO_2^-, which resulted in the formation of Cl^- and $NO_2{}^{18}O^-$.

Over the past 5 decades, the list of metals (M) and their complexes have been expanded to range from, but are not limited to, iron, manganese, vanadium, osmium, chromium, rhenium, ruthenium, molybdenum, and tungsten, which may exist as discrete mononuclear and di-nuclear complexes or large multinuclear metal systems. Currently, the most studied metals are iron, molybdenum, and tungsten mainly because of their direct biological relevance, Mo and W will be the primary focus of this work; however, certain manganese and chromium complexes have been studied as models of iron proteins, rhenium has been applied to Mo and W oxo-transferase models, while vanadium and manganese have been employed in the study of bromoperoxidase enzymes. Here**,** only a subset of the ligand architectures used in atom transfer chemistry will be discussed in great detail

Iron is most commonly studied as either Fe(III), Fe(IV), or Fe(V) and is well represented by the Fe(III)/oxo-Fe(IV)/hydroxo-Fe(IV) porphyrins[5] and Fe(III)/oxo-Fe(V) salen[6] complexes. In addition, iron can perform secondary complete atom transfer as Fe(0), by activating its ligands (usually carbonyls, phosphines or arsines)[7] to participate as oxygen atom acceptors. Manganese has been shown to participate in

primary oxygen atom transfer chemistry, similar to iron and have been studied as Mn(III)/oxo-Mn(V) porphyrin[8] complexes and Mn(III)/oxo-Mn(V) salen[9] complexes. In addition, Mn(III) dipicolinate complexes also participate in OAT reactions[10]. Moreover, manganese carbonyl complexes have been shown to participate in secondary complete atom transfer. Along these same lines both Cr(III) and oxo-Cr(V) porphyrin and salen[9d]. complexes have been shown to participate in primary complete OAT chemistry as well as hydroperoxo complexes[11]. Vanadium has been studied as oxo-V(IV) and oxo-V(V) salen[12] complexes, and has been shown to react with oxophilic reagents to produce desoxo-V(II) and desoxo-V(III) salen complexes. Furthermore V(III) and V(IV) hydroxamates[13] and V(V) peroxo complexes[14] have been shown to be competent oxo-donors and acceptors as well.

The metals with the most diverse ligand architectures are the complexes of molybdenum and its isoelectronic metal tungsten. These are represented by six general ligand donor schemes that can be simplified as N_3, N_2O, N_2S, NS_2, NO_2, S_4, as exemplified in **Figure 1.1**. Thus examples of molybdenum can be represented as either dioxo-Mo(VI), monooxo-Mo(IV), in coordination complexes with any of the previously mentioned donor schemes. Examples include the mono-anionic, hydrotris-pyrazol-1yl borates[15] (Tp, Tp^{Me2}, Tp^{iPr}), and the neutral hydrotris-pyrazol-1yl methanes (Tp*), which provide N_3 ligand donor environments. The mono-anionic hydrobis-pyrazol-1-yl methane phenolate derivatives[16] (LO^- or $L1O^-$) and hydrobis-pyrazol-1-yl methane thiolate[17] ($L3S^-$); have been used to provide N_2O and N_2S ligand donor environments. NS_2 coordination sphere has also been provided in ligands such as: 2-(salicylindenamino)benzethiolate (ssp)[18], 2-[6-(2-Mercapto-2,2-diphenyl-ethyl)-pyridin-2-yl]-1,1-diphenyl-ethanethiol (3-

NS_2)[19], [2,6-bis(2,2-diphenyl-2-thioethyl)pyridinate], denoted as (LNS_2)[20], and its derivative *t*-Bu-LNS_2[21]. Lastly, bis-dithiocarbamate (S_2CNEt_2)[22] and bis-[*cis*-1,2-dicyano-1,2-ethylenedithiolate][23] (mnt; S_4) have been used to produce an S_4 donor scheme in primary-complete OAT chemistry.

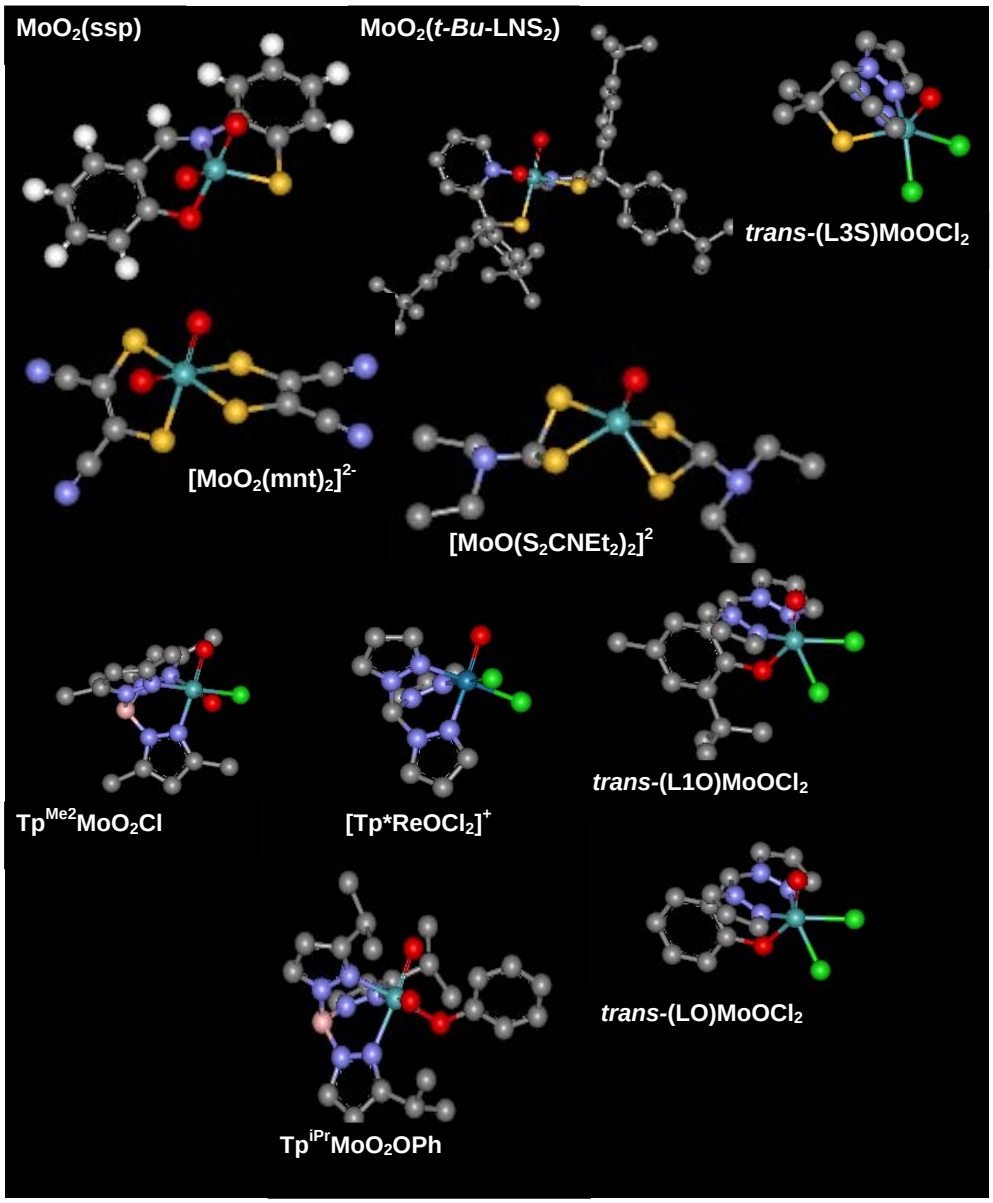

Figure 1.1: 3-dimensional representations of ligands used in OAT chemistry.

However, secondary-complete oxygen atom transfer from Mo(0) as carbonyl complexes[24] and carbonyl complex clusters has also been demonstrated. Tungsten

generally shares the same ligand architectures as molybdenum, but is generally studied with an S_4 ligand donor set as dioxo-W(IV) and monooxo-W(VI) or as W(0) in carbonyl complexes and carbonyl complex clusters.

In addition, the M in **Equation 1.1a**, may also represent an organic moiety such as a peroxide, epoxide, α,β-dicarbonyl, diol or alcohol. However, as this work is concerned only with the metal-based oxygen atom transfer reactions, the reaction of organic complexes will not be further discussed, unless there is a direct relation to a metal catalyzed reaction mechanism.

Substrates in Atom Transfer Chemistry

Of particular interest in the study of atom transfer chemistry are the possible substrates (X in **Equation 1.1a** and **Equation 1.1b**) that serve as oxygen donors and oxygen acceptors. These have been dominated by three major classes which can be defined by the element which actively accepts or donates oxygen. The first and most prominent of these are the organo-phosphorous compounds that contain either phosphorous (III) or an oxo-phosphorous (V) element. Typically the phosphorous (III) compounds are phosphines or phosphites, while the phosphorous (V) compounds are typically the corresponding oxide. In some cases, an isoelectronic As(V) complex, $OAsPh_3$ or As(III) complex, $AsPh_3$ has also been used.

The second major class of oxygen atom donors and acceptors comprises the sulfur containing compounds that contain sulfur (II), an oxo-sulfur (IV) or occasionally dioxo-sulfur (VI) motif. As such the sulfur acceptor compounds with sulfur (II) are well represented by organo-sulfur compounds in the form of thiols and thioethers. Sulfur has

been used as a donor in the form of organo sulfur (IV) and organo sulfur (VI) compounds which are well represented by the sulfoxides and the sulfones respectively. In addition, inorganic sulfur as sulfur (VI) can be in the form of sulfate as a donor or sulfur (IV) in the form of sulfite as the acceptor. Isoelectronic analogues to sulfur have also been employed as organo-Se(IV) or OSe(VI) complexes, while the most commonly encountered Se compounds are $OSePh_2$ and $SePh_2$.

The last of the main groups of are the nitrogenous donors and acceptors. Thus organo-nitrogen based oxygen donors and acceptors that either contains nitrogen (V) or nitrogen (III) have been employed in the form of N-oxides and their reduced N-alkyl and N-aryl amine counterparts. In addition to the organo-nitrogen compounds, inorganic nitrogen (V) as nitrate and nitrogen (III) as nitrite have also been used as the oxygen atom donor and acceptor respectively.

The last of the common donor and acceptor classes are the carbon-based donors and acceptors and are typified in the form of alcohols, diols, epoxides, alkenes or ketones as substrates for oxygen atom transfer chemistry. **Chapter 3** of this work presents the physico-chemical properties that are associated substrate reactivity of both organic and inorganic substrates through comparison with organo-phosphorous (III) compounds. Furthermore the implications of these physico-chemical parameters toward oxygen atom transfer chemistry are also provided.

The Role of Oxygen Atom Transfer in Chemistry and Biology

OAT chemistry plays key roles in a wide verity of biological and chemical applications and examples can be found in many fields of study such as biology, fuel

chemistry, food chemistry, manufacturing, environmental science, and inorganic, organic and organometallic synthesis. As previously mentioned, the majority of the oxygen atom transfer reactions involve high-valent metal centers, in which the complete transfer of the oxygen atom is coupled with the transfer of an electron pair. Although the exact nature of the reaction may vary, OAT reactions are thought to be involved in the mechanism of several metalloenzymes such as cytochrome P450[25], sulfite oxidase, nitrate reductase, DMSO reductase[26], and halo-peroxidases[27]. In fuel chemistry, OAT reactions have been investigated as stabilizers for the prevention of thermal oxidation of jet fuels as well as in the scrubbing of sulfite from flue gas emissions in the burning of coal. Food chemists have investigated the oxidation processes of wine, and protective films for food storage[28]. The oxidation of thiols, amines, alkanes, alkenes to yield sulfenic or sulfonic acids, nitrogen oxides, diols, and epoxides, respectively, are of great interest to the general synthetic community. Along these lines, such catalytic transfer of oxygen atoms is also important in industrial processes such as epoxide production[29].

Although OAT chemistry has a profound impact upon many fields of study, a large portion of the understanding of this chemistry has developed from the study of biological systems or discrete inorganic complexes designed as either structural mimics, functional mimics or structural and functional mimics of the biological system. As a result, this paper and the proceeding chapters will focus predominantly on the biologically inspired catalysts and the most well understood substrates in an attempt to establish a unified mechanistic understanding of OAT reactions. More specifically, **Chapter 2** this manuscript will focus on the mechanisms of OAT reactions involving $[MoO_2]^{2+}$ cores in an XN_3 coordination environment (where X = Cl, OPh and SPh) as an

oxo-donor to alkyl, aryl and mixed alky/aryl- phosphines. **Chapter 3**, as previously mentioned, will focus in the physico-chemical properties that are inherent in the reactivity phosphines and presumably all other inorganic and organic substrates that can be involved in OAT. Lastly, **Chapter 4** provides a look into the regeneration of the catalytically active state of DMSO reductase by modeling a transient Mo(V)O state with $[MoO]^{3+}$ cores.

The Reaction Mechanism of Oxygen Atom Transfer.

The common view of oxygen atom transfer chemistry was first proposed in the eloquent work of Taube, and could be described by a reaction coordinate that involved a single transition state, as presented in **Scheme 1.1** using molybdenum and phosphorous as examples**.**

Scheme 1.1

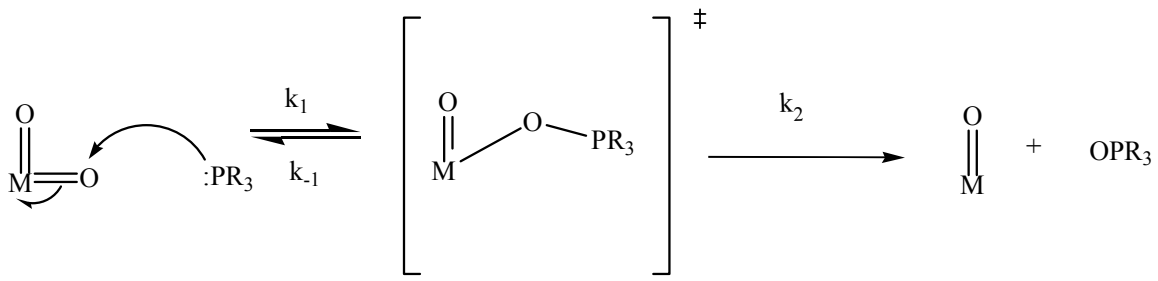

Under this view, the reaction was initiated by nucleophilic attack by the phosphorous (III) lone pair upon an oxo-group of the metal center. As a result a single transition state picture was developed for oxygen atom transfer that involved a concomitant two-electron transfer and oxygen atom transfer in a one-step process. However, this concept has been challenged through theoretical calculations[30] that have suggested, in most cases, the involvement of intermediate complexes along the reaction

coordinate to free phosphine oxide release. Experimentally, in 1984 Holm reported that reactions between $MoO_2(3\text{-}NS_2)$ 10mM and 1.88 equivalents of PPh_3 (in DMF) resulted in the formation of three distinct ^{31}P resonances at -4.7 ppm (PPh_3); 25 ppm ($OPPh_3$) and a resonance at 43.5 ppm, which was attributed to $MoO(3\text{-}NS_2)(OPPh_3)$, after 20 hours. No additional information could be found with respect to this complex except for a 1999 paper, written by Doonan et. al[31], which proved that the resonance attributed to $MoO(3\text{-}NS_2)(OPPh_3)$, was most likely $SPPh_3$. However, Holm was able to isolate the solvated product, $MoO(3\text{-}NS_2)(DMF)$[32], which could participate in reverse oxygen atom transfer with DMSO, as defined in **Scheme 1.2**.

Scheme 1.2:

$$MoO(3\text{-}NS_2)(DMF) + Me_2SO \underset{k_{-1}}{\overset{k_1}{\rightleftharpoons}} MoO(3\text{-}NS_2)(Me_2SO) + DMF \xrightarrow{k_2} MoO_2(3\text{-}NS_2) + Me_2S$$

Thus, this data suggested that the reverse OAT reaction proceeded through a rapid equilibrium process, followed by a 2 electron oxidation of the molybdenum center leading to DMS production. The presence of this equilibrium process suggests that there are at least two transition states in the reaction pathway leading to a formal oxygen atom transfer reaction.

However, a slightly different mechanistic behavior for the forward OAT reaction could be proposed by the combined efforts of two other research groups. In 2000, Brown and coworkers, published a paper on the reaction of $[Tp^*Re^VOCl_2]^+Cl$ with PPh_3 in methylene chloride that resulted in the formation of an intermediate complex $[Tp^*Re^VCl_2(OPPh_3)]^+Cl$ as identified by mass spectrometry and a ^{31}P NMR resonance at 170 ppm. That same year, the first experimentally isolated oxygen atom transfer intermediate, $Tp^{Me2}MoOCl(OPPh_3)$, was characterized[33] in non-coordinating solvent and

other intermediate complexes have been characterized since[34]. Taken together, the results suggest that the nucleophilic attack step results in a formally 2 electron reduced metal complex and seemingly incomplete atom transfer, while the second step involves solvation and complete atom transfer. Moreover, the a picture of OAT chemistry has evolved that allows for the existence of multiple transition states along the reaction coordinate.

The following chapters will expand upon the growing understanding of the primary complete OAT process, challenge the formality of the term completeness of the process and expand upon the known mechanistic behavior of the reactivity. More specifically the following chapters will show further evolution of the mechanistic understanding of OAT reactions, as shown in **Scheme 1.3.**

Scheme 1.3:

$$Tp^{R}MoO_2(X) + PR_3 \xrightarrow{k_1} Tp^{R}MoO(X)OPR_3 \xrightarrow{k_2} Tp^{R}MoO(X)(MeCN) + OPR_3$$

Of great interest to this study is the ability of, presumably all, but definitively DMSO reductase to function catalyically in single turnover experiments with PTA as the oxygen atom abstracting agent in DMSO reduction.[35] This places phosphines categorically in the role of model physiological OAT oxygen atom acceptors, as well as suitable reagents for OAT model complexes.

Biological Oxygen Atom Transfer.

As mentioned above, oxygen atom transfer chemistry has been suggested to be involved in the mechanism of several metalloenzymes such as cytochrome P450, sulfite oxidase, nitrate reductase, DMSO reductase, and halo-peroxidases. However, this chapter

will be limited to the reactions of Mo-centered enzymes and their W-centered analogues. Hille[36] has classified the molybdoproteins into classes based upon the structure about the active site, to produce the DMSO Reductase family, the Sulfite Oxidase family and the Xanthine Oxidase family. Over the years, there has been great efforts placed into defining the reaction mechanism of the molybdoproteins and has resulted in a greater understanding of the electron donors, and the substrates that are usable in catalysis. To this end, the OAT reactions of many enzymes have been investigated and a general compilation of the findings on isolated enzymes are presented in **Table 1.1a, Table 1.1b** and **Table 1.1c.**

It becomes immediately evident that there is a complex interdependence upon the electron donor, substrate, class of enzyme (nitrate reductase, sulfite oxidase, etc) and subclass of enzyme (Nap or Nar type nitrate reductases), in relation to catalytic efficiency. In many cases, the choice of electron donor strongly influences the observed catalytic competency of the enzyme, in terms of the k_{cat} and the K_m of the oxygen donor/acceptor, most likely through the intrinsic K_m of the electron source. In the sections to follow, some of these dependencies will be expanded upon, in terms of their overall efficiency as oxygen atom transfer biocatalysts.

Oxygen Atom Transfer Reactions in Nitrate Reductases

Nitrate reductase catalyzes the reduction of NO_3^{2-} to NO_2^{2-}, with transfer of nitrate-based oxygen to a molybdenum (IV) metal center with the concomitant transfer of two electrons from the metal to the nitrate nitrogen, followed by release of NO_2^{2-} from the enzyme, **Table 1.1a**. The ultimate biogeochemical fate of the nitrite produced in this

manner is in part determined by the sub-class of the nitrate reductase itself, and as such may eventually be assimilated into biomass, further transformed by additional enzymatic processes or released into the environment. A genetic analysis of the nitrate reductase sub-classes of enzymes was undertaken by Stolz and Basu[37], and clearly provides a molecular basis for the structural variations among nitrate reductase proteins.

In terms of OAT chemistry, it becomes immediately evident that nitrate reductases differ in reactivity as they differ in their biochemical role in cellular metabolism and respiration. For example the periplasmic Nap, isolated from denitrifying *Paracoccus sp*, shows a higher K_m for nitrate[45,47] (1150 ± 212 μM) than the membrane bound Nar, that is isolated from the nitrate respiring organisms such as *Rhobobacter sphaerodies*, *E. coli, Ps. auriginosa and Haloarcisa marismortui* (K_m for nitrate = 258.3 ± 141.8) when reduced methylviologen ($MV^{+\bullet}$) was used as the electron donor. However, using this same electron donor, the Nar proteins generally have a higher k_{cat} (340.7 ± 135.8 sec^{-1}) than the Nap proteins (245.0 ± 7 sec^{-1}), and maintain a significantly higher overall catalytic efficiency with a k_{cat}/K_m ratio of 1.33 ± 0.33 $(\mu M*sec)^{-1}$ when compared to that of the Nap proteins whose k_{cat}/K_m ratio is 0.22 ± 0.05 $(\mu M*sec)^{-1}$. In other words the Nar proteins of the nitrate respiring bacteria can produce approximately 6 times more nitrite per minute than the related Nap protein in the denitrifying bacteria. Interestingly, when the nitrate reducing activity of Nar is accessed using reduced benzylviologen ($BV^{+\bullet}$), the average k_{cat} and K_m value are statistically indifferent to those determined using ($MV^{+\bullet}$) as the electron donor, suggesting that the K_m of the two electron donors are equal, provided NarGHI is present. On the other hand, when more diverse electron donors are employed in the nitrate reduction assays, there is a significant variability in both the K_m for nitrate,

and the k_{cat} value of Nar such that the k_{cat}/K_m ratio may increase or decrease as a function of the donor. For example, lapachol functions similar to that of the viologen dyes with a k_{cat}/K_m value of 1.19 $(\mu M*sec)^{-1}$ while duroquinol and menediol decreases this ratio 60-fold to ~ 0.02 $(\mu M*sec)^{-1}$. Taken together, it remains uncertain whether the differences in reactivity that is observed between the Nap and Nar proteins are associated with their ability to react with nitrate, or are relics of different affinities for electron donors, that arise through different physiological roles in the organism. More importantly it is not obvious, due the limited available data on the Nap proteins, if the rate limiting step of oxygen atom transfer in these systems is associated with the electron donor binding, nitrate binding or nitrite release.

There is a significant difference in substrate affinity between other competent oxygen atom donor substrates, when the electron donor is constant. For example NarGHI with ($BV^{+\bullet}$) as the electron donor has its highest affinity for NO_3^-, followed by chlorate, while bromate has the highest K_m. However, when the k_{cat}/K_m values of nitrate and chlorate are compared, they are surprisingly close, with K_m NO_3^- of 1.00 $(\mu M*sec)^{-1}$ and K_m chlorate of 0.76 $(\mu M*sec)^{-1}$. Also of interest is that when the substrate specificity of Nap is examined, the affinity for nitrate is surprisingly similar to that of selenate with K_m values of 120 μM and 270 μM respectively.

Oxygen Atom Transfer Reactions in Sulfite Oxidases

Sulfite oxidase catalyzes the transfer of a labile oxygen atom from a Mo(VI) metal center to sulfite with the concomitant transfer of two electrons from sulfite to molybdenum, **Table 1.1b**. Unlike nitrate reductase, sulfite oxidase sequences have not

been subjected to the rigorous molecular sub-classing, and as such cannot be described with the detail used for NR. The existing data on sulfite oxidase, although limited, suggests that there is very little difference in the sulfite oxidizing reactivity when either cytochrome C or ferricyanide are used as electron donors when human SO and chicken SO are compared. On average, the k_{cat}/K_m ratio is ~ 5x larger than that of the nitrate reductases at 4.45 ± 1.4 $(\mu M*sec)^{-1}$. However, this apparent higher efficiency of NR over SO may simply be a function of electron donor K_m and as such should be considered with caution. On the other hand, chicken SO appears to show a strong substrate dependence on reactivity with the K_m of DMS being approximately 500 times higher than that of SO_3^{2-}, despite the similarity in k_{cat} values for these two substrates 53.9 ± 27.7 sec^{-1} and 89 sec^{-1} for SO_3^{2-} and DMS respectively. The reactivity of SO has particular importance in this work as the predominant experimental data that has been recorded in this lab is based upon functional SO models using Mo complexes of Tp ligand derivatives.

Oxygen Atom Transfer Reactions in DMSO Reductases

DMSO reductase catalyzes the OAT based reduction of DMSO, through the transfer of the oxo-group from the central S(IV) atom to the, presumably des-oxo, Mo(IV) metal center with a coupled 2 electron transfer from molybdenum to sulfur yielding a mono-oxo Mo(VI) center and a des-oxo S(II) center in the DMS product, **Table 1.1b**. Further detail into the structure and function of DMSO reductases can be found in **Chapter 4** of this work as well as the biogeochemical significance of this protein.

DMSOR isolated from *Rhodobacter capsulatus* or *Rhodobacter sphaeroides* is approximately 6 times more reactive towards DMSO than presumably their nitrate reductases (Nap or Nas) are towards nitrate with a k_{cat}/K_m ratio of 5.8 ± 1.9 $(\mu M*sec)^{-1}$. In addition, the high affinity (K_m for DMSO is 5.5 ± 1.9 μM) and comparably low k_{cat} of 31.0 ± 5 sec^{-1} (when $MV^{+\bullet}$ is used as the electron donor) make this enzyme one of the most reactive Mo proteins discussed. However, reactivity with other substrates is not as clearly defined as in the case of nitrate reductase. For example, the mean reactivity of DMSOR with TMAO results in near zero values: K_m for TMAO is 34 ± 48 mM, k_{cat} of 1.2 ± 1.5 sec^{-1} and k_{cat}/K_m ratio of 0.4 ± 0.5 $(\mu M*sec)^{-1}$, using $MV^{+\bullet}$. This inconsistency is difficult to resolve since the reactivity towards DMSO, as determined by both groups, was found to be virtually identical.

Oxygen Atom Transfer Reactions TMAO Reductases

TMAOR catalyzes the OAT reaction from nitrogen (V) as N-oxy amines to a molybdenum (IV) metal center yielding the two electron reduced, nitrogen (III), amines and an oxo-molybdenum (VI) protein, **Table 1.1c**. TMAOR represents the least well characterized protein of the molybdo-proteins discussed here, and only two electron donors have been studied to date. However, it appears that TMAOR has a much higher K_m for $BV^{+\bullet}$, than $MV^{+\bullet}$, due to the higher catalytic efficiency for TMAO as an oxo-donor. More explicitly, the k_{cat}/K_m ratio for TMAO is 3.10 times greater when $BV^{+\bullet}$ is used as the electron donor, which sharply contrasts DMSOR whose k_{cat}/K_m ratio for DMSO is 2.31 times greater with $MV^{+\bullet}$. The specificity for N-oxides over S-oxides is clearly evident when multiple substrates are tested, and is exemplified when the K_m for

TMAO or adensosine-N-oxide (194 μM and 260 μM respectively using $MV^{+\bullet}$) are compared to those of DMSO and methionine sulfoxide (6.0 mM and 7.1 mM respectively using $MV^{+\bullet}$). When compared to the specificity of DMSOR, TMAOR is apparently more substrate selective as DMSOR has shown a K_m for TMAO of 193 μM compared to 6 μM for DMSO, which presents a 20-fold increase in sulfoxide affinity in DMSOR and a 31-fold increase in N-oxide affinity in TMAOR, relative the contrasting oxide.

Table-1.1a- Reactivity of Nitrate reductases in Oxygen Atom Transfer Chemistry.

Enzyme	Organism	e^- Donor	e^- Acceptor	K_m (μM)	k_{cat} (s^{-1})	k_{cat}/K_m ($\mu M \cdot s)^{-1}$	Ref
EukNR	*Chlorella vulgaris*	NADH [a]	NO_3^-	80			38
Nap	*Ds. Desulfuricans*	$MV^{+\cdot}$ [f]	NO_3^-	80			39
Nap	*Ds. Desulfuricans*	$MV^{+\cdot}$ [k]	NO_3^-	32			40
Nap	*Ds. Desulfuricans*	$MV^{+\cdot}$ [k]	NO_3^-	12 [l]			
DNR(I)	*Bradyrhizobium japonicum*	$MV^{+\cdot}$ [a]	NO_3^-	300 [g]			41
DNR(II)	*Bradyrhizobium japonicum*	$MV^{+\cdot}$ [a]	NO_3^-	480 [g]			
DNR	*Bradyrhizobium lupinus*	NADH	NO_3^-	52			42
Nar	*Haloacula marismortui*	$MV^{+\cdot}$ [a]	NO_3^-	79 [e]	145	1.84	43
DNR	*Haloferax mediterranei*	$MV^{+\cdot}$[a]	NO_3^-	820			44
Nap	*Paracoccus pantotrophus*	$MV^{+\cdot}$ [a]	NO_3^-	240			45
Nap	*Paracoccus pantotrophus*	$MV^{+\cdot}$ [a]	NO_3^-	1000	250	0.25	
DNR	*Ps. Stutzeri*	$MV^{+\cdot}$ [a]	NO_3^-	3200			46
Nap	*Paracoccus dinitrificans*	$MV^{+\cdot}$ [a]	NO_3^-	1300	240	0.18	47
Nar	*Ps. auriginosa*	$BV^{+\cdot}$[a]	NO_3^-	300			48
DNR	*Micrococcus denitrificans*	$BV^{+\cdot}$ [a]	NO_3^-	960			49
NarGHI	*E. coli*	$MV^{+\cdot}$ [a]	ClO_3^-	1126.8 [h]	704	0.62	50
NarGHI	*E. coli*	$MV^{+\cdot}$ [a]	BrO_3^-	134615 [h]	76.9	$5.7x10^{-4}$	
NarGHI	*E. coli*	$MV^{+\cdot}$ [a]	NO_3^-	288.5 [h]	384.6	1.33	
NarGHI	*E. coli*	$MV^{+\cdot}$ [a]	NO_3^-	422.7 [h]	459	1.09	
NarGHI	*E. coli*	$BV^{+\cdot}$ [a]	NO_3^-	333.3 [h]	333.3	1.00	
NarGHI	*E. coli*	$BV^{+\cdot}$ [a]	ClO_3^-	1000 [h]	762.2	0.76	
NarGHI	*E. coli*	$BV^{+\cdot}$ [a]	BrO_3^-	10400 [h]	66.6	0.01	
NarGHI	*E. coli*	Menediol [i]	NO_3^-	916	31.9	0.03	51
NarGHI	*E. coli*	DQH_2 [i]	NO_3^-	746	12.3	0.02	
NarGHI	*E. coli*	PBH_2 [i]	NO_3^-	282	120	0.43	
NarGHI	*E. coli*	$LPCH_2$ [i]	NO_3^-	57	68	1.19	
EukNR	*N. cassa nit-3*	$MV^{+\cdot}$ [a]	NO_3^-	900			52
EukNR	*N. cassa nit-3*	$MV^{+\cdot}$ [a]	NO_3^-	200			
EukNR	*N. cassa* STA4	$FADH_2$ [a]	NO_3^-	300			
EukNR	*N. cassa* STA4	$FADH_2$ [a]	NO_3^-	400			
NasABC	*Rhodobacter Capsulatus*	NADH [a]	NO_3^-	96 [m]			53
NasABC	*Rhodobacter Capsulatus*	BPB [a]	NO_3^-	13000 [m]			
NasABC	*Rhodobacter Capsulatus*	$MV^{+\cdot}$ [a]	NO_3^-	130 [m]			
Nap	*Rhodobacter sphaeroides*	$BV^{+\cdot}$ [b]	NO_3^-	120			54
Nap	*Rhodobacter sphaeroides*	$BV^{+\cdot}$ [b]	TeO_3^{2-}	600			
Nap	*Rhodobacter sphaeroides*	$BV^{+\cdot}$ [b]	SeO_4^{2-}	270			
Nar	*E. coli* K12	$MV^{+\cdot}$ [a]	NO_3^-	420	455	1.08	50
Nar	*E. coli* K12	$BV^{+\cdot}$ [a]	NO_3^-	330	330	1.00	
NarGH	*E. coli*	$MV^{+\cdot}$ [j]	NO_3^-	243	260	1.07	55
NarGH	*E. coli*	$BV^{+\cdot}$ [j]	NO_3^-	571	118	0.21	
EukNR	*Aspergillus*	NADPH [c]	NO_3^-	199			56
NR	*Pyrobaculum aerophilum*	$BV^{+\cdot}$ [a]	NO_3^-	58 [d]			57
NR	*Pyrobaculum aerophilum*	$BV^{+\cdot}$ [a]	ClO_3^-	140 [d]			

a = saturating conditions assumed; b = 0.5 mM $BV^{+\cdot}$; c = 12.5 mM NADPH; d = 75 °C; e = 70 °C, pH 8, 3.6 M NaCl; f = 0.2 mM; $MV^{+\cdot}$, pH 7, 1 mM NaCl. g = 30 °C; h = 25 °C, pH 6.8.; i = 0.3 mM e- donor.; j excess e- donor, pH 6.5. k = 1.4mM $MV^{+\cdot}$; 37 °C, pH 8. l = 50 mM NaCl added. m = pH 8.

Table-1.1b- Reactivity of Sulfite Oxidases and DMSO reductases in Oxygen Atom Transfer Chemistry.

Enzyme	Organism	e^- Acceptor	e^- Donor	K_m (μM)	k_{cat} (s^{-1})	k_{cat}/K_m ($\mu M \cdot s)^{-1}$	Ref
SO	*Chicken liver*	Cyt. C [b]	SO_3^{2-}	28	79	2.82	58
SO	*Chicken liver*	Cyt. C [b]	DMS	6300	89	0.01	
SO	*Chicken liver*	Cyt. C [c]	SO_3^{2-}	19.1	92.6	4.84	59
SO	*Human*	$[FeCN_6]^{3-}$ [d]	SO_3^{2-}	6.12	25	4.10	60
SO	*D. radiodurans*	$[FeCN_6]^{3-}$ [a]	SO_3^{2-}	94.5			61
SO	*Arabidopsis thaliana*	$[FeCN_6]^{3-}$ [e]	SO_3^{2-}		190		62
SO	*Arabidopsis thaliana*	$[FeCN_6]^{3-}$ [a]	SO_3^{2-}	33.8 [g]			63
SO	*N. plumbaginifolia*	$[FeCN_6]^{3-}$ [a]	SO_3^{2-}	51.4 [g]			
SO	*Thiobacillus novellus*	Cyt. C [f]	SO_3^{2-}	27			64
Enzyme	**Organism**	**e^- Donor**	**e^- Acceptor**	**K_m (μM)**	**k_{cat} (s^{-1})**	**k_{cat}/K_m ($\mu M \cdot s)^{-1}$**	**Ref**
DmsABC	*Rb. capsulatus*	$MV^{+\cdot}$ [a]	DMSO	9.7	42.9	4.42	65
DmsABC	*Rb. capsulatus*	$MV^{+\cdot}$ [a]	TMAO	193.8	134.5	0.69	
DmsABC	*E. coli*	$LPCH_2$ [a]	DMSO	238	191	0.80	66
DmsABC	*E. coli*	$BV^{+\cdot}$ [a]	DMSO	32	61	1.91	67
DmsABC	*E. coli*	$BV^{+\cdot}$ [a]	Py-N-O	100	200	2.00	
DmsABC	*Rb. sphaeroides*	$MV^{+\cdot}$ [h]	DMSO	7	50	7.14	68
DmsABC	*Rb. sphaeroides*	$MV^{+\cdot}$ [h]	TMAO	68000	2300	0.03	
DmsABC	*Rb. sphaeroides*	$MV^{+\cdot}$ [h]	MetSO	330	58	0.18	
DmsABC	*Rb. sphaeroides*	$MV^{+\cdot}$ [h]	ANO	20	110	5.50	

a = assumed staturation; b = 21 μM Cyt C, pH 8.; c = 2.3mM Cyt. C, 25° C, pH 8..; d = 50 μM $[FeCN_6]^{3-}$, 25° C, pH 7; e= 400 μM $[FeCN_6]^{3-}$, pH 8.5; f= 0.05 mM, pH 8.; g= 1.5 mM $MV^{+\cdot}$. g = pH 8, 25° C. h = 0.5 mM $MV^{+\cdot}$, pH 7.5.

Table-1.1c- Reactivity of TMAOR reductase in Oxygen Atom Transfer Chemistry.							
Enzyme	**Organism**	**e^- Donor**	**e^- Acceptor**	**K_m (μM)**	**k_{cat} (s^{-1})**	**k_{cat}/K_m $(\mu M \cdot s)^{-1}$**	**Ref**
TorA	*E. coli*	$MV^{+\cdot}$ [b]	ANO	260	1400	5.38	68
TorA	*E. coli*	$MV^{+\cdot}$ [b]	MetSO	7100	40	0.01	
TorA	*E. coli*	$MV^{+\cdot}$ [b]	DMSO	6000	13	0.00	
TorA	*E. coli*	$MV^{+\cdot}$ [b]	TMAO	194	134	0.69	
TorA	*Shewanella massilia*	$BV^{+\cdot}$ [a]	4-MM-N-O	22	109.4	4.97	69
TorA	*Shewanella massilia*	$BV^{+\cdot}$ [a]	2-Pic-N-O	610	78	0.128	
TorA	*Shewanella massilia*	$BV^{+\cdot}$ [a]	LDAO	1000	151	0.151	
TorA	*Shewanella massilia*	$BV^{+\cdot}$ [a]	TMAO	17	119.8	7.05	
TorA	*Shewanella massilia*	$BV^{+\cdot}$ [a]	MetSO	**ND**	<4	**ND**	
TorA	*E. coli (wild-type)*	$BV^{+\cdot}$ [c]	TMAO	70	150	2.14	70
TorA	*E. coli (wild-type)*	$BV^{+\cdot}$ [c]	4-MM-N-O	20	96.5	4.83	
TorA	*E. coli (wild-type)*	$BV^{+\cdot}$ [c]	2-Pic-N-O	260	102.3	0.39	
TorA	*E. coli (wild-type)*	$BV^{+\cdot}$ [c]	4-Pic-N-O	320	49.55	0.15	
TorA	*E. coli (wild-type)*	$BV^{+\cdot}$ [c]	Py-N-O	1860	53.40	0.03	
TorA	*E. coli (wild-type)*	$BV^{+\cdot}$ [c]	DMSO	**ND**	**ND**	**ND**	
TorA	*E. coli (wild-type)*	$BV^{+\cdot}$ [c]	$(C_6H_5)_2SO$	**ND**	**ND**	**ND**	
TorA	*E. coli (wild-type)*	$BV^{+\cdot}$ [c]	$(CH_2)_4SO$	**ND**	**ND**	**ND**	
ND indicates that the value was not experimentally determined; a= assumed excess; b = 0.15 mM $MV^{+\cdot}$, pH 7.5.; c= 0.12 mM $BV^{+\cdot}$.							

Substitution of Mo with W in TMAOR

When Giordani and coworkers experimented with the trans-metallation of TMAOR (*wt*-TorA) with W (W-TorA) using the Mo reconstituted (Mo-TorA) TMAOR as a control, several unique features presented themselves in terms of the catalytic efficiency of the enzyme (**Table 1.2**). In general, after the Mo reconstitution or W replacement, the W-substituted analogue has a much greater reactivity toward substrates than either the wild-type enzyme or the reconstituted Mo protein. Secondly, upon W-substitution, the enzyme apparently loses a large degree of its substrate specificity, with an average K_m value for all N-oxides tested of 8.64 ± 1.21 μM (excluding Py-N-O) and an observable affinity towards sulfoxides that is lacking the native Mo-enzyme (**Table 1.1b**). Thus, the W-substituted enzyme expresses a much higher catalytic activity for the reverse OAT reaction than the Mo-protein, albeit with reduced substrate specificity. A similar effect has been reported for synthetic model systems, and is discussed in the sections to follow.

Table 1.2 Effects of W substitution on a Native Mo-enzyme								
Enzyme	**Organism**	**e^- Acceptor [a]**	**e^- Donor**	**K_m(μM)**	**$k_{cat}(s^{-1})$**	**k_{cat}/K_m $(\mu M \cdot s)^{-1}$ [b]**	**$(k_{Mo}/k_W)^{\blacklozenge}$**	**Ref**
wt-TorA	*E.coli*	$BV^{+\cdot}$	TMAO	70	150.5	2.15	0.60	70
Mo-TorA	*E.coli*	$BV^{+\cdot}$	TMAO	25.2	94.7	3.76		
W-TorA	*E.coli*	$BV^{+\cdot}$	TMAO	8.53	53.6	6.28		
wt-TorA	*E.coli*	$BV^{+\cdot}$	4-MM-N-O	20	96.5	4.83	0.24	
Mo-TorA	*E.coli*	$BV^{+\cdot}$	4-MM-N-O	42	71.4	1.70		
W-TorA	*E.coli*	$BV^{+\cdot}$	4-MM-N-O	7.5	52.2	6.96		
wt-TorA	*E.coli*	$BV^{+\cdot}$	2-Pic-N-O	260	102.3	0.39	0.02	
Mo-TorA	*E.coli*	$BV^{+\cdot}$	2-Pic-N-O	653	84.2	0.13		
W-TorA	*E.coli*	$BV^{+\cdot}$	2-Pic-N-O	9.91	54.7	5.52		
wt-TorA	*E.coli*	$BV^{+\cdot}$	Py-N-O	1860	53.40	0.03	0.75	
Mo-TorA	*E.coli*	$BV^{+\cdot}$	Py-N-O	2250	44.73	0.02		
W-TorA	*E.coli*	$BV^{+\cdot}$	Py-N-O	1080	42.22	0.04		
wt-TorA	*E.coli*	$BV^{+\cdot}$	DMSO	**ND**	**ND**	**ND**		
Mo-TorA	*E.coli*	$BV^{+\cdot}$	DMSO	**ND**	**ND**	**ND**		
W-TorA	*E.coli*	$BV^{+\cdot}$	DMSO	974	40.2	0.04		
♦ value expressed as $[k_{cat}/K_m]^{Mo}/[k_{cat}/K_m]^{W}$ a= 0.12 mM $BV^{+\cdot}$, 3.53 nM Mo-TorA, 1.64 nM W-TorA. b = Mo-Tor A temperature opt = 60 °C, W-TorA temperature opt > 80 °C.								

Brief Review of the OAT Reactivity of Structural and Functional Mo and W Model Complexes.

When the atom transfer chemistry of molybdenum and tungsten are considered as a whole, several key features emerge with regards to the effects of the ligand architecture complexed with the metal as well as the choice of substrate used. Historically, the complexes to follow and their reactions were developed as biomimics of the molydbo-proteins discussed in the previous section. The diversity in the synthetic complexes ligand architecture is a result of the ever evolving knowledge of the coordinating environments of these proteins. As previously mentioned, **Chapter 3** of this work is centered upon the effects of substrate upon atom transfer reactions; this chapter will predominately focus on the effects of ligand architecture and W/Mo substitution on the thermodynamics and rates of atom transfer to substrates. In general, Mo and W complexes have been most intensely investigated as oxygen atom acceptors, a role that will be classified here for clarity as "reverse atom transfer" while there is considerably less information regarding W and Mo as oxygen atom donors, classified here as "forward atom transfer". The choice of the terminology "forward" and "reverse" is implemented here due to the dual role metals may play in an atom transfer process and is only intended to provide a point of reference for the reader in the discussions to follow. To this end, **Chapter 2** and **Chapter 3** of this work provides full details into the role of molybdenum complexes as oxygen atom donors, "forward reaction" and as such will only be briefly discussed here for completeness of discussion.

The following table, **Table 1.3a,** provides kinetic data for atom transfer chemistry in which the metal functions as the oxo-donor, towards a variety of model substrates and highlights the variety of ligand architectures used as well as substrate. **Table 1.3b,** has been included to present a few examples of secondary-complete oxygen atom transfer in which the labile oxygen is generated from one of the coordinated carbonyl ligands.

Table 1.3a: Forward oxygen atom transfer reactions: metal as an oxo-donor in primary complete transfer

Metal complex Donor	**Substrate Acceptor**	**k_2 [a] x10^3 (M^{-1}·sec^{-1})**	**$\Delta H^{\ddagger}$ (kJ/mol)**	**$\Delta S^{\ddagger}$ (kJ/mol)**	**$\Delta G^{\ddagger}$ (kJ/mol)**	**Ref**
$[MoO_2(mnt_2)]^{2-}$	$P(OMe)_3$	2.5	48.14	-154.1	94.10	71
	$P(MeO)_2Ph$	450	39.48	-158.9	86.84	
	PEt_3	109	72.21	-62.6	90.87	
	PPh_3	55.9	52.96	-134.8	93.15	
	$P(OEt)_2Me$	1100	**NR**	**NR**	**NR**	
	$NaHSO_3$	8700 [c]	**NR**	**NR**	**NR**	72
$[MoO_2(S_2CNEt)_2]^{2-}$	PEt_3	530 [e]	**NR**	**NR**	**NR**	1,73
	$PPhEt_2$	430 [e]	**NR**	**NR**	**NR**	
	PPh_2Et	230 [e]	**NR**	**NR**	**NR**	
	PPh_3	71 [e]	35.12 [d]	-125.4	72.51	73,74
$[Tp^*Re^{V}OCl_2]^{+}Cl$	PPh_3	9.70 [g]	56.07	-79.50	79.75	75
$TpRe^{V}OCl_2$	PPh_3	0.0125 [g]	71.5	-82.4	96.20	
$[WO_2(mnt_2)]^{2-}$	PPh_3	0.45	**NR**	**NR**	**NR**	71
	$P(OMe)_3$	0.01	**NR**	**NR**	**NR**	
	$P(OMe)_2Ph$	0.45	**NR**	**NR**	**NR**	
	$P(OEt)_2Me$	3.40	**NR**	**NR**	**NR**	
$MoO_2(t$BuL-$NS_2)$	PEt_3	5.6	40.17	-154.81	86.30	81
MoO_2(L-NS_2)	PEt_3	**NR**	48.95	-118.83	84.36	76
MoO_2(L-NS_2)	PPh_3	70 [f]	**NR**	**NR**	**NR**	77
MoO_2(L-NS_2)	$P(p\text{-}FC_6H_4)_3$	97	48.91	-118.71	84.30	
MoO_2(ssp)(DMF)	PPh_2Et	0.102 [b]	65.2	-86.5	91.0	18
MoO_2(sse)(DMF)	PPh_2Et	0.0210 [b]	70.2	-82.4	94.8	
$Tp^{Me2}MoO_2SPh$	PPh_3	0.620	**NR**	**NR**	**NR**	78
$Tp^{Me2}MoO_2OPh$	PPh_3	0.002	**NR**	**NR**	**NR**	

NR indicates the value was not reported. a = Solvent taken to be DMF at 25 ° C unless otherwise noted b = 30° C, DMF; c (1:1 MeCN/H_2O) at 20 °C; MeCN at 25 ° C. d = MeCN at 25 ° C. e = 1,2-$C_2H_4Cl_2$ at 25 ° C. f = DMF at 23 ° C.; g = 1,2-$C_6H_4Cl_2$ at 38 °C.

Table 1.3a: Forward atom transfer reactions: secondary complete oxygen atom transfer						
Metal complex Donor	**Substrate Acceptor**	**k_2x10^3 $(M\cdot sec)^{-1}$**	**$\Delta H^{\ddagger}$ (kJ/mol)**	**$\Delta S^{\ddagger}$ (kJ/mol)**	**$\Delta G^{\ddagger}$ (kJ/mol)**	**Ref**
$Fe(CO)_3L_2$	$P(OPh)_3$/MeNO	**NR**	128.03	-32.22	137.63	7b
	$AsPh_3$/MeNO	**NR**	113.84	-16.74	118.79	
	PPh_3/MeNO	**NR**	117.99	-46.86	131.95	
$Fe_3(CO)_{12}$	PPh_3/MeNO	4180 [d]	52.23	-58.37	69.65	7a
	$P(OPh)_3$/MeNO	4080 [d]	51.63	-60.71	69.72	
	$AsPh_3$/MeNO	4620 [d]	57.91	-38.41	69.35	
$Ru_3(CO)_{12}$	PPh_3/MeNO	822 [d]	50.67	-76.99	73.61	
$Os_3(CO)_{12}$	PPh_3/MeNO	104 [d]	71.46	-24.77	78.84	
$Mo(CO)_5L$	$P(OMe)_3$/MeNO	0.15 [a]	97.73	-23.60	104.76	24
	PPh_3/MeNO	1.87 [a]	73.66	-79.00	97.20	
$Fe(CO)_5L$	PPh_3/MeNO	2.37 [b]	60.10	-68.90	81.17	79
$Ru(CO)_5L$	PPh_3/MeNO	7.41 [b]	57.68	-69.38	78.37	
$Os(CO)_5L$	PPh_3/MeNO	9.70 [b]	43.05	-118.29	78.32	
$Cr(CO)_6$	PPh_3/MeNO	13.4 [c]	51.00	-89.00	77.54	80
$Mo(CO)_6$	PPh_3/MeNO	16.2 [c]	54.34	-75.66	76.90	
$W(CO)_6$	PPh_3/MeNO	2.76 [c]	69.81	-18.81	75.41	
NR = not reported. a = (1:1 v/v MeCN:CH_2Cl_2), 34 º C; b = (1:2 v/v ethanol:hexane); 20.6 º C; c = dichloromethane; 23 º C; d = (2:1 v/v CHCl3:ethanol); 25.6º C.						

In general, the data in these tables are limited to those that provide either a variety of substrates or are reported with kinetic parameters, such as $\Delta H^{\ddagger}$ and $\Delta S^{\ddagger}$. When the bulk of the data is taken together, three distinct features present themselves in terms of the rate constants with respect to the metal, ligand and substrate. As this chapter deals only with the metal complexes and the effects of ligands, only short mention of substrate effects will be included for completeness. **Table 1.4a** and **Table 1.4b** provide examples of the ligand architecture used in the "reverse" atom transfer reactions in which the metal functions as the oxo-acceptor.

Table 1.4a: Reverse Atom Transfer Reactions: Metal as an Oxo-Acceptor.						
Metal complex Acceptor	**Substrate Donor**	**k [a] x10^3(M·sec)$^{-1}$**	**ΔH‡ (kJ/mol)**	**ΔS‡ (kJ/mol)**	**ΔG‡ (kJ/mol)**	**Ref**
Mo(OPh)($S_2C_2Me_2$)$^{1-}$	CH_3NO	2.00 x10^5	33.90	-87.9	60.10	81
	$(Bz)_3NO$	16000	39.75	-87.9	65.94	
	$(CH_2)_4SO$	0.150	42.26	-163.2	90.91	
	$(CH_3)_2SO$	0.013	61.92	-150.6	106.83	
	H_2O	1.2	41.84	-142.3	84.30	
	Ph_3AsO	2.8	30.54	-175.7	82.94	
	Ph_3AsS	26.0	20.10	-184.1	74.97	
	SeO_4^{2-}	0.72	50.2	-142.3	92.6	82
W(OPh)($S_2C_2Me_2$)$^{1-}$	$(CH_2)_4SO$	0.900	48.53	-138.07	89.70	83
	$(CH_3)_2SO$	0.039	60.25	-125.52	97.67	
	Ph_3AsO	3200	39.33	-100.42	69.30	
	Py-N-O	340	41.42	-112.97	75.10	
	SeO_4^{2-}	3.3	53.55	-117.15	88.47	82
MoO(L-NS_2)DMF	*m*-F-Py-N-O	**NR**	97.91	30.12	88.93	84,85
	p-F(C_6H_4)$_2$SO	1.40	92.47	10.88	89.22	
	NO_3^-	1.49	99.16	33.47	89.19	
	Me_2SO	1.50	**NR**	**NR**	**NR**	
MoO($^{t\text{-Bu}}$L-NS)$_2$	Me_2SO	0.101	56.90	-129.70	95.80	21
	Ph_2SO	0.314	59.41	-112.97	93.09	
	$(CH_2)_4SO$	1.44	48.12	-138.07	89.28	
	Ph_3AsO	56.0	44.35	-121.34	80.53	
	m-F-Py-N-O	65.0	41.42	-129.70	80.09	
	Ph_2SeO	2160	44.35	-87.86	70.55	
$[(bpy)_2Ru(IV)O(py)]^{2+}$	Me_2SO	134	28.45	-163.18	77.07	86
$[Tp^{Me2}MoO\{S_2P(OEt)_2\}]$	Me_2SO	0.015 [b]	63.95	-121.22	100.10	87
	Me_2SO	0.043 [c]	**NR**	**NR**	**NR**	
NR indicates the value was not reported in the literature; a = Solvent taken to be DMF at 25 º C unless otherwise noted ; b = tolune, 25 º C. c = MeCN, 25 º C.						

Table 1.4b: Reverse Atom Transfer Reactions: Metal as an Oxo-Acceptor.				
Metal complex Acceptor	**Substrate Donor**	**Rate (K) [a] Rate x10^{-3} (M·sec)$^{-1}$**	**Rate (k_2) Rate x10^3 (M·sec)$^{-1}$**	**Reference**
MoO(L-NS_2)DMF	Me_2SO	4.2	1.50	77
	Ph_2SO	11.0	1.40	
	d-Biotin-SO	16.0	1.36	
	d- or *l*- Methionine-SO	5.3	1.68	
a = Solvent taken to be DMF at 25 º C unless otherwise noted				

A Comparison of Mo and W in Forward OAT.

When equivalent ligand systems are coordinated to either a central Mo (VI) or W (VI) metal, the rate of oxygen atom transfer is significantly slower to phosphine acceptors (forward OAT reaction) in the W-containing systems, as shown in **Table 1.5**.

Table 1.5: A Comparison of Mo and W in Forward OAT. (data from ref 71)	
Oxygen Acceptor	**(k_2^{Mo}/k_2^{W}) as $[MO_2(mnt)_2]^{2-}$**
PPh_3	124
$P(OMe)_3$	250
$P(MeO)_2Ph$	1000
$P(OEt)_2Ph$	324

A Comparison of Mo and W in Reverse OAT.

In contrast to the reactivity expressed in the forward direction, the W containing systems are more reactive than the Mo containing systems when the metal is in the role of an oxygen atom acceptor. One important feature of this model system is that the reactivity ratio, in terms of (k_2^{Mo}/k_2^{W}) with DMSO, reproduces a rather large increase in reactivity that has been observed in previously discussed the W and Mo-Tor systems, when either TMAO, Py-N-O, or 4-MM-N-O were used as substrates.

Table 1.6: A Comparison of Mo and W Reactivity in Reverse OAT (taken from references 81, 82, and 83).	
Oxygen Donor	**(k_2^{Mo}/k_2^{W}) as $[M(OPh)(S_2C_2Me_2)]^{2-}$**
$(CH_2)_4SO$	0.167
$(CH_3)_2SO$	0.333
Ph_3AsO	0.001
$SeO4^{2-}$	0.218

Thus there is also a clear dependence upon the metal when its role in the OAT reaction is switched. This is best exemplified when the reactivities of $Mo(OPh)(S_2C_2Me_2)^{2-}$ and $W(OPh)(S_2C_2Me_2)^{2-}$ towards reverse atom transfer chemistry are compared, as shown in **Table 1.6**. In this case both the net charge and steric environment offered by the ligand are identical, but the reactivity of the W-complex

ranges from 10 to 1000 times faster than the corresponding Mo, complex. Unfortunately, phosphines have not been employed in the study of the reverse reaction, but a general comparison may be gleaned from the reactivity when the isoelectronic Ph_3AsO. In this light it is not a surprise that the k_2^{Mo}/K_2^{W} of reduction of the As compound is opposite the trend for the oxidation of the phosphorous analogue, PPh_3. More specifically rate for the "forward" (substrate oxidation reaction) is 1.2 x 10^5 faster than the "reverse" reaction (substrate reduction) when the ($k_{Mo/W}^{forward}/ k_{Mo/W}^{reverse}$) ratio is considered.

Effects of Ligand Architecture in Forward OAT Reactions.

In terms of ligand effects, it has been noted by Holm, that there is a significant ligand-donor atom effect upon the rates of oxygen atom transfer such that $S_4 > S_2N_2 > N_2O_2$, however, the effect of the net charge on the complex was not fully addressed. Brown clearly showed that there is a distinct effect of the charge on the complex, which will be referred to as a "macroscopic" charge effect through this manuscript. We define a "macroscopic" charge as a physically observable charge that exists on the complex, usually evidenced by the presence of cationic or anionic counter ions. The macroscopic charge effect clearly has a strong influence upon the rate of the forward atom transfer reaction as displayed in **Table 1.7** by the approximate 900 fold increase in the reaction rate when the neutral $TpRe^{V}OCl_2$ complex and the mono cationic $[Tp^*Re^{V}OCl_2]^+$ complex are compared in reactions with identical substrates.

Table 1.7. Subset of atom transfer data with thermodynamic parameters included. (taken from references 1, 18, 75, and 81)					
Compound Donor	**Reactant**	**k^a x10^5(M·sec)$^{-1}$**	**$\Delta H^{\ddagger}$ (kJ•mol^{-1})**	**$\Delta S^{\ddagger}$ (J•mol^{-1}•K^{-1})**	**$\Delta G^{\ddagger}$ (kJ•mol^{-1})**
$Mo^{VI}O_2$(ssp)(DMF)	PPh_2Et	7.1	65.2	-86.5	91.0
$[Tp^*Re^{V}OCl_2]^{+}$	PPh_3	970	56 ± 2	-79.4 ± 8.4	78.8
$TpRe^{V}OCl_2$	PPh_3	1.25	71.5 ± 2	-82.4 ± 1.7	-82.4 ± 1.7
$[Mo^{VI}O_2(mnt)_2]^{2-}$	PPh_3	934	62.7	95.3	62.7
$[Mo^{VI}O_2(mnt)_2]^{2-}$	PEt_3	417	78.9	-54.3	46
$Mo^{VI}O_2$(*t*BuL-NS_2)	PEt_3	49	80.9	-117.4	40.1
a = Solvent taken to be DMF at 25 º C unless otherwise noted					

Furthermore there is an approximate 10-fold increase in the rate when the reactivity of the neutral $Mo^{VI}O_2$(*t*BuL-NS_2) complex is compared with the reactivity of the di-anionic $[Mo^{VI}O_2(mnt)_2]^{2-}$ species towards identical substrates. However, the latter comparison need not be entirely charge influenced, as there is no strict guarantee that the ligand systems involved (provided they could result in complexes of equivalent charge) would present an isosteric or isoelectronic ligand field environment for the metal. This topic as well as variable substrate reactivity within the same complex is discussed in greater detail in **Chapter 3**.

Summary:

Mechanistically, the understanding of oxygen atom transfer has progressed dramatically over the years. This rich history shows a progression in understanding from a single transition state that involved concomitant transfer of two electrons with the labile oxygen atom to one of formal electron transfer followed by complete separation of the donor and acceptor pair. Thus, this new perspective on the mechanism of oxygen atom transfer challenges the definition of the complete and incomplete formalism of the

reaction by blurring the limits of "completeness". More specifically, the data presented in **Chapter 2**, along with the analysis in **Chapter 3**, shows that there are two steps in the atom transfer process: The first nucleophilic attack step involves formal oxidation/reduction while the second solvation step results in complete separation of the donor/acceptor pair.

Atom transfer chemistry of both biological and synthetic metal centers presents a complex problem in that the intrinsic rates of reaction are dependent upon several key factors. In the biological systems, the reaction rates are not only dependent upon the substrate, but show a strong reliance upon the electron donor. This was exemplified by the near 60-fold decrease in the catalytic nitrate reduction efficiency of NarGHI when the lapachol and menediol k_{cat}/K_m values are compared. This may reflect variability in the individual proteins to regenerate a catalytically active metal center after formal OAT. **Chapter 4** discusses the regeneration of the catalytically competent metal center via model complexes of the putative transient $[MoO]^{3+}$ state, though to be involved in this process. The comparison of reactivity is further complicated by variable affinities for the same substrates between enzymes that perform similar catalytic function in different physiological roles. This is demonstrated by the comparison of the Nap and Nar-type NR enzymes which provide a 6-fold difference in nitrate reduction with $MV^{+\cdot}$ as the electron donor. Lastly substitution of the native metal with an isoelectronic analogue, i.e. Mo exchanged for W in TorA, not only results in a protein with higher catalytic efficiency, but also dramatically reduces substrate specificity, as evidenced by a 2 to 65 fold increase in K_m^{Mo}/K_m^{W} ratio for various N-oxides.

In the synthetic systems, three clear factors influence the rate of atom transfer reactions. The first major factor is associated with the ligand environment that is coordinated to the metal center and manifests as either a charge effect or as a donor atom acid-base effect. The ligand effect is demonstrated by the approximate 5-fold increase in rate of PEt_3 oxidation when the di-anionic $[MoO_2(mnt_2)]^{2-}$ and $[MoO_2(S_2CNEt)_2]^{2-}$ complexes are compared . The oxygen atom transfer reactions from $[MoO_2]^{2+}$ cores to phosphines are further explored in **Chapter 2**. Moreover, the content of the discussion will focus on reactivity as a function of both the metals ligand environment as well as the phosphine substrate. The second influence upon the reaction rate is associated with the metal chosen such that W participates in the "reverse" atom transfer chemistry much more rapidly than Mo, while the opposite situation is true for the "forward" reaction. Lastly, a third pronounced effect upon atom transfer rates is associated with the donor/acceptor substrate, a phenomenon that is explored in **Chapter 3**.

However, two distinct commonalities exist between the enzymes and their model systems. First, it has also been shown that phosphines, the OAT substrate of choice in synthetic systems, can participate as artificial, biological oxygen atom abstracting agents in catalytic oxygen atom transfer experiments with DMSOR. Secondly, the substitution of W, for Mo, generally results in a complex or enzyme that has a higher catalytic OAT efficiency than the Mo-based analogue in terms of the reverse OAT reaction. Lastly, the differences in reactivity that are observed between substrates in the model systems, suggests that the local geometry of the protein active site may also impact substrate specificity and overall catalytic efficiency.

References

[1] a) Holm, R.H. *Chem. Rev*. **1987**, 87, 1401-1449. b) Holm, R.H. *Chem. Rev*. **2004**, 104, 1175-1200.

[2] Woo, K.L. *Chem. Rev*. **1993**, 93, 1125-1136

[3] Hofmann, K. A. *Chem. Ber.* **1912,**45, 3329.

[4] **a)** Halperin, J.; Taube, H. J. *Am. Chem. Soc.* 1950, 72, 3319**; b)** Halperin, J.; Taube, H. J. *Am. Chem. Soc***. 1952.** 74. 375**. c**) RuGnberg, A. C.; Halperin, J.; Taube, H. ***J. Am.*** *Chem. soc***. 1961,** 73, 4487. **d)** Anbar, M.; Taube, H. *J. Am. Chem. Soc***. 1968,** *80,* 1073.

[5] **a**) O'Shea, S. K.; Wang, W.; Wade, R. S.; Castro, C. E. **1996,** *J. Org.Chem.* 61(18), 6388. **b**) Bernadou, J.; Meunier, B. **1998***, Chem. Comm.* (Cambridge) (20), 2167-2173. **c**) Bruice, T.C.; Dicken, C. M.; Balasubramanian, P. N.; Woon, T. C.; Lu, F. L.. **1987,** *J. Am. Chem. Soc.* 109(11), 3436. **d)** Woon, S.; Yon Ok, R.; ; Song, R.; Nam, W. **2005,** *J. Biol. Inorg.Chem.*, 10(3), 294-304. **e)** Baciocchi, E.; Gerini, M. F.; Lanzalunga, O.; Lapi, A.; Lo P., Maria G. **2003,** *Org. Biomol. Chem.*, 1(2), 422-426.

[6] Kurahashi, T.; Kobayashi, Y.; Nagatomo, S.; Tosha, T.; Kitagawa, T.; Fujii, H. **2005***, Inorganic Chemistry,* 44(22), 8156. **b)** Sivasubramanian, V. K.; Ganesan, M.; Rajagopal, S.; Ramaraj, R.**2002**, *J. Org. Chem.*, 67(5), 1506.

[7] **a)** Shen, J., Shi,Y. Gao, Y. Shi, Q. and Basolo, F. *J. Am. Chem. Soc.;* **1988**; *110*(8); 2414-2418. **b)** Modi, S.P., and Atwood, J.D. *Inorg. Chem.;* **1983**; *22*(1); 26-28.

[8] **a**) Sorokin, A.; Robert, A.; Meunier, B. **1993***, J. Am. Chem. Soc.* 115(16), 7293. **b**) Park, S.-E.; Song, W. J.; Ryu, Y. O.; Lim, M. H.; Song, R.; Kim, K. M.; Nam, W.. **2005,** *J. Biol. Inorg.Chem.*, 99(2), 424-431

[9] **a**) Shitama, H.; Katsuki, T. **2006,** *Tetrahedron Lett.* 47(19), 3203. **b**) Zhang, H.; Zhang, Y.; Li, **2006,** *Can. J. Catal.* 238(2), 369. **c)** Chellamani, A.; Kulanthaipandi, P.; Rajagopal, S. *J. Org. Chem.;* **1999**; *64*(7); 2232-2239. **d)** McGarrigle, E.M.; and Gilheany, D. G. **2005,** *Chemical Rev.,* 105(5), 1563

[10] Yao, Wenbin; Kavallieratos, Konstantinos; De Gala, Susan; Crabtree, Robert H. **2000,** *Inorg. Chim. Acta*, 311(1-2), 45-49.

[11] Pestovsky, Oleg; Bakac, Andreja. **2003,** *J. Am. Chem.* Soc. 125(48), 14714-14715.

[12] Yamamoto, K.; Oyaizu, K.; Tsuchida, E. **1996**, *J. Am.Chem. Soc.*,118(50), 12665

[13] Brown, D. A.; Bogge, H.; Coogan, R.; Doocey, D.; Kemp, T. J.; Muller, A.; Neumann, B. **1996,** *Inorg. Chem.*; *35*(6); 1674-1679.

[14] Arlene F. Ghiron, Richard C. Thompson *Inorg. Chem.;* **1990**; *29*(22); 4457-4461.

[15] **a)** Cleland, W.E.; Barnhart, K. M.; Yamanouchi, K.; Collison, D.; Mabbs, F.E.; Ortega, R.B.; Enemark, J.H. *Inorg. Chem.* **1987**, 26, 1017-1025. b) Roberts, S.A.; Young, C.G.; Kipke, C. A.; Cleland, W.E.; Yamanouchi, K.; Carducci, M.D.; Enemark, J.H. *Inorg. Chem.* **1990**, 29, 3650. c) Dhawan, I.K.; Pacheco, A.; Enemark, J.H. *J. Am. Chem. Soc.* **1994**, 116, 7911.

[16] a) Hammes, B. S.; Chohan, B. S.; Hoffman, J. T.; Einwachter, S.; Carrano, C. J. *Inorg. Chem.;* **2004**; *43*(24); 7800-7806. Kail, B.; Nemykin, V. N.; Davie, S. R.; Carrano, C. J.; Hammes, B.; Basu, P. *Inorg. Chem.;* **2002**; *41*(5); 1281-1291.

[17] **a)** Peariso, K.; Chohan, B. S.; Carrano, C. J.; Kirk, M. L. *Inorg. Chem.;* **2003**; *42*(20); 6194-6203. **b)** Carrano, C. J.; Chohan, B. S.; Hammes, B. S.; Kail, B. W.; Nemykin, V. N.; Basu, P. *Inorg. Chem.;* **2003**; *42*(19); 5999-6007.

[18] Topich, J. and Lyon, J.T. III., **1984,** *Inorg. Chem.* 23(20), 3202-6.

[19] Berg, J.M.; and Holm, R. H. *J. Am. Chem. Soc.* **1984**, 106(10), 3035-6.

[20] Edgar W. Harlan, Jeremy M. Berg, R. H. Holm *J. Am. Chem. Soc.;* **1986**; *108*(22); 6992-7000.

[21] Schultz, B. E.and Holm, R. H., **1993**, *Inorg. Chem.,* 32(20), 4244-8.

[22] Grace J. J. Chen, John W. McDonald, W. E. Newton *Inorg. Chem.;* **1976**; *15*(11); 2612-2615.

[23] Kenneth M. Nicholas, Masood A. Khan *Inorg. Chem.;* **1987**; *26*(10); 1633-1636.

[24] Gao, Y., Shi, Q., Kershner, D. L., and Basolo, F. *Inorg. Chem.;* **1988**; *27*(1); 188-191.

[25] **a)** Meunier, B., de Visser, S.P., and Shaik, S. Chem. Rev., 104, 3947-3980. **b)** Higgins, L.; Bennett, G. A.; Shimoji, M.; Jones, J. P. **1998,** *Biochemistry*, 37(19), 7039.

[26] **a)** Hille, R. *Trends in Biochemical Sciences.*; **2002,** 7, 360 – 367. **b)** McNamara, J. P.; Hillier, I. H.; Bhachu, T. S.; Garner, C. D**. 2005***, JCS*., *Dalton Trans.* (21), 3572

[27] Carter-Franklin, J.N.; Butler, A. **2004,** *J. Am. Chem. Soc.* 126(46), 15060.

[28] Yamada, S.; Sakuma, I.; Himeshima, Y.; Aoki, T.; Uemura, T.; Shirakura, A. *Oxygen scavenger films for packaging materials.* Eur. Pat. Appl. (1992), 17 pp

[29] Kodadek, T.; Raybuck, S. A.; Collman, J. P.; Brauman, J. I.; Papazian, L. M. **1985,** *J. Am. Chem.Soc.* 107(14), 4343.

[30] **a)** Thapper, A.; Deeth, R. J.; Nordlander, E. *Inorg. Chem.* **2002**; *41*(25); 6695-6702. **b)** Thapper, A.; Deeth, R. J.; Nordlander, E. *Inorg. Chem.* **1999**; *38*(5); 1015-1018. **c)** Thomson, L. M.; Hall, M. B. *J. Am. Chem. Soc.* **2001**; *123*(17); 3995-4002. **d)** Pietsch, M. A.; Hall, M. B. *Inorg. Chem.***; 1996**; *35*(5); 1273-1278.

[31] Doonan, C. J.; Slizys, D. A.; Young, C. G. *J. Am. Chem. Soc.;* **1999**; *121*(27); 6430-6436.

[32] Jeremy M. Berg, R. H. Holm.**,** *J. Am. Chem. Soc.*; **1985,** *107*(4); 925-932.

[33] Smith, P. D.; Millar, A. J.; Young, C. G.; Ghosh, A.; Basu, P. *J. Am. Chem. Soc.* **2000**; *122*(38); 9298-9299.

[34] **a)** Nemykin, V. N.; Basu, P. *Inorg. Chem.* **2005**; *44*(21); 7494-7502. **b)** Nemykin, V. N.; Laskin, J.; Basu, P. *J. Am. Chem. Soc.* **2004**; *126*(28); 8604-8605. **c)** Millar, Andrew J.; Doonan, Christian J.; Smith, Paul D.; Nemykin, Victor N.; Basu, Partha; Young, Charles G. *Chem. Eur. J.* **2005**, 11(11), 3255-3267.

[35] Cobb, N., Conrads, T., and Hille, R. *J. Biol Chem* **2005,** 280,(12), 1007–11017.

[36] Hille, R. *Chem. Rev.* **1996**, 96(7), 2757-2816.

[37] Stolz, J .F., and Basu, P. **2002**, *Chem. BioChem*. 3, 198-206.

[38] **a)** Kay, C. J., Barber, M.J., *Biochemistry* **1989**, 28(14), 5750-8. **b)** Kay, C.J.; Barber, M. J. *J. Biol. Chem.* **1986**, 261(30), 14125-9.

[39] **a)** Carneiro, C., Almendra, M.J., Bursakov, S., Liu, M-Y., Payne, W.J., LeGall, J., Moura, J.J.G., and Moura, I. **1995.** *J. Inorg. Biochem., 59, 73.* ***b)*** Bursakov, S., Liu, M-Y., Payne, W. J., LeGall, J., Moura, I., and Moura, J.J.G. **1995***, Anaerobe,* 55-60

[40] Bursakov, S.A.; Carneiro, C., Almendra, M.J., Duarte, R. O.; Caldeira, J.; Moura, I.; and Moura, J. J. C. *Biochem. Biophys. Res. Comm.* **1997**, 230, 816-822.

[41] Fernández-López, M., Olivares, J., and Bedmar, E.J. **1996***, FEBS Lett.,* 392, 1-5

[42] Chamber-Pérez, M.A., Camacho, M., Burgos R. C. A., Mercedes-Lucas, M., Fernandez-Pascual, M., Manclús, J.J., and Rosario de Felipe, M.. *J. Plant Phys.,* **2002***,* 159, 525-533

[43] Yoshimatsu, K.; Sakurai, T.; Fujiwara, T. **2000,** *FEBS Letters,* 470(2), 216-220.

[44] B. Lledó, R. M. Martínez-Espinosa, F. C. Marhuenda-Egea and M. J. Bonete. *Biochimica et Biophysica Acta* **2004**,*1674, (1), , 50-59*

[45] Gates, A.J.; Hughes, R.O.; Sharp, S.R.; Millington, P.D.; Nilavongse, A.; Cole, J.A.; Leach, E-R.; Jepson, B; Richardson, D.J.; and Butler, C.S. ***2003,*** *FEMS Microbiol. Lett.* 220, *(2), 261-269.*

[46] Hettmann, T.; Anemüller, S.; Borcherding, H.; Mathé, L.; Steinrücke, P.; and Diekmann, S. **2003** *FEBS Lett,* 534,(1-3), 143-150.

[47] Sears, H. J.; Ferguson, S.J.; Richardson, D.J.; and Spiro, S. **1993.** *FEMS Microbiol.* Lett., 113,(1), 107-111.

[48] Fewson, C. A. and Nicholas, D. J. D. **1961,** *Biochim et Biophys. Acta, 49,(2), 335-349.*

[49] Lam, Y. and Nicholas, D. J. D. **1969,** *Biochim. et Biophys. Acta - Enzymology, 178, (2),* 225-234.

[50] Morpeth, F. F.and Boxer, D. H., *Biochemistry,* **1985**, 24(1), 40-6.

[51] Giordani, R.; Buc, J.; Cornish-Bowden, A.; Cardenas, M.L. **1997**, *European Journal of Biochemistry*, 250(2), 567-577.

[52] Antoine, A. D. **1974**, *Biochemistry,* 13(11), 2289-94.

[53] Blasco, R.; Castillo, F.; Martinez-Luque, M. **1997***, FEBS Letters*, 414(1), 45-49.

[54] Applied Environ. Microbiol. 2001, 5122-5126.

[55] Buc, J.; Santini, C-L.; Blasco, F.; Giordani, R.; Cardenas, M. L.; Chippaux, M.; Cornish-Bowden, A.; Giordano, G. **1995***, European Journal of Biochemistry*, 234(3), 766-72.

[56] Gilliam M. B., Sherman M. P., Griscavage J. M. and Ignarro L. J. **1993,** *Analytical Biochemistry,* 212, (2), 359-365.

[57] Afshar, S.; Johnson, E.; de Vries, S. and Schröder, I. **2001.,** *J. Bacteriol.* (183) 5491-5495.

[58] Brody, M.S. and Hille, R. **1995,** *Biochimica et Biophysica Acta – Prot. Struct. and Mol. Enz.,* 1253,(2), 133-135

[59] Brody, M.S.; Hille, R. **1999**, *Biochemistry,* 38(20), 6668-6677.

[60] Wilson, H. L.; Rajagopalan, K. V. **2004,** *J. Biol. Chem.* 279(15), 15105-15113.

[61] D'Errico, G.; Di Salle, A.; La Cara, F.; Rossi, M.; Cannio, R.. **2006,** *J. Bac.* 188(2), 694-701.

[62] Hemann, C.; Hood, B. L.; Fulton, M.; Haensch, R.; Schwarz, G.; Mendel, R. R.; Kirk, M. L.; Hille, R, **2005,** *J. Am. Chem. Soc.* 127(47), 16567-16577.

[63] Eilers, T.; Schwarz, G.; Brinkmann, H.; Witt, C.; Richter, T.; Nieder, J.; Koch, B.; Hille, R.; Hansch, R.; Mendel, R. R. **2001***, J.Biol. Chem.* 276(50), 46989-46994.

[64] Kappler, U.; Bennett, B.; Rethmeier, J.; Schwarz, G.; Deutzmann, R.; McEwan, A. G.; Dahl, C. **2000,** *J. Biol. Chem.* 275(18), 13202-13212.

[65] Ridge, J.P.; Aguey-Zinsou, K-F., Bernhardt, P.V. Hanson, G.R. and McEwan, A.G. **2004**, FEBS Lett., 563, (1-3), 197-202.

[66] Rothery, R. A.; Chatterjee, I.; Kiema, G.; McDermott, M. T.; Weiner, J. H. **1998,** *Biochem. J.*, 332(1), 35-41.

[67] Simala-Grant J L; Weiner J. H., **1998,** *Eur. J. Biochem.* 251(1-2), 510-5.

[68] Johnson K E; Rajagopalan K V., **2001***, J. Biol. Chem.* 276(16), 13178-85.

[69] Dos Santos, J-P., Lobbi-Nivol, C., Couillault, C., Giordano, G., and Mejean, V. **1998***, J. Mol. Biol.* 284, 421-433.

[70] Buc, J.; Santini, C-L.; Giordani, R.; Czjzek, M.; Wu, L-F.; Giordano, G. **1999,** *Mol. Microbiol.* 32(1), 159-168.

[71] **a)** Tucci, G. C.; Donahue, J. P.; Holm, R. H., **1998,** *Inorg. Chem.* 37(7), 1602-1608. **b)** Lorber, C.; Plutino, M. R.; Elding, L. I.; Nordlander, E. *J. Chem.* Soc., Dalton Trans. **1997**, 3997.

[72] Samar K. Das, Pradeep K. Chaudhury, Dulali Biswas, Sabyasachi Sarkar. *J. Am. Chem. Soc.;* **1994**; *116*(20); 9061-9070.

[73] Martha S. Reynolds, Jeremy M. Berg, Richard H. Holm *Inorg. Chem*.; **1984**; 23(20); 3057-3062.

[74] Durant, R. *Dalton Trans*.; **1977**, 955

[75] Seymore, S. B.and Brown, S. N. *Inorg. Chem.;* **2000**; *39*(2); 325-332.

[76] **a)** Craig, J. A.; Holm, R. H., **1989,** *J. Am. Chem. Soc*., 111(6), 2111-15. **b)** Caradonna, J. P.; Reddy, P. R.; Holm, R. H., **1988**, *J. Am. Chem. Soc*., 110(7), 2139-44.

[77] Berg, J.M. and Holm, R. H. **1985,** *J. Am. Chem. Soc*. 107(4), 925-32.

[78] Sue A. Roberts, Charles G. Young, Cary A. Kipke, W. E. Cleland, , Jr. Katsumoto Yamanouchi, Michael D. Carducci, John H. Enemark *Inorg. Chem*.; **1990**; 29(19); 3650-3656.

[79] Jiankun Shen, Yici Gao, Qizhen Shi, Fred Basolo. *Organometallics;* **1989**; 8(9); 2144-2147.

[80] Yan Lung Shi, Yi Ci Gao, Qi Zhen Shi, David L. Kershner, Fred Basolo. *Organometallics;* **1987**; 6(7); 1528-1531.

[81] a) Lim, B. S. and Holm, R. H., **2001,** *J. Am. Chem. Soc.*,123(9), 1920-1930. b) Lim, B. S.; Sung, K.-M.; Holm, R. H. **2000,** *J. Am. Chem. Soc.*, 122(30), 7410-7411.

[82] Wang, J.-J.; Tessier, C.; Holm, R. H. **2006,** *Inorg. Chem.*, 45(7), 2979-2988.

[83] Sung, K.-M.; Holm, R. H. **2002***, J. Am. Chem. Soc*, 124(16), 4312-4320.

[84] John P. Caradonna, P. Rabindra Reddy, R. H. Holm *J. Am. Chem. Soc*.; **1988**; 110(7); 2139-2144.

[85] Julia A. Craig, R. H. Holm *J. Am. Chem. Soc*.; **1989**; 111(6); 2111-2115.

[86] Roecker, L., Dobson, J.C., Vining, W.J., Meyer, T.J., *Inorg. Chem.;* **1987**; *26*(5); 779-781.

[87] Sue A. Roberts, Charles G. Young, W. E. Cleland, , Jr. Richard B. Ortega, John H. Enemark. *Inorg. Chem*.; **1988**; 27(17); 3044-3051.

Thesis Chapter 2

Mechanistic Investigation of the Oxygen Atom Transfer Reactivity of Dioxo-Molybdenum(VI) Complexes[‡].

Brian W. Kail

Thesis Chapter 2

Mechanistic Investigation of the Oxygen Atom Transfer Reactivity of Dioxo-Molybdenum(VI) Complexes

Abstract.

The oxygen atom transfer reactivity of a discrete dioxo-molybdenum(VI) complexes, $Tp^{iPr}MoO_2(OPh)$ (where Tp^{iPr}= hydrotris(3-isopropylpyrazol-1-yl)borate), $Tp^{Me2}MoO_2(OPh)$, $Tp^{Me2}MoO_2(SPh)$, $Tp^{Me2}MoO_2(Cl)$, (where Tp^{Me2}= hydrotris(3,5-dimethylpyrazol-1-yl)borate), with seven tertiary phosphines (PMe_3, PMe_2Ph, PEt_3, $P(n\text{-}Bu)_3$, PEt_2Ph, PPh_2Et and PPh_2Me) have been investigated. The first nucleophilic step ($Tp^{R'}MoO_2(X) + PR_3 \rightarrow Tp^{R'}MoO(X)(OPR_3)$ (R_3 = Me_3, Me_2Ph, Et_3, $(n\text{-}Bu)_3$, Et_2Ph, Ph_2Et or Ph_2Me; R' = *i*-Pr or Me_2; X= OPh or SPh) follows a second-order rate with an associative transition state in all cases: For example: $Tp^{iPr}MoO_2(OPh)$ + PMe_3, $\Delta H^{\ddagger}$ = 74.6 kJ mol^{-1}, $\Delta S^{\ddagger}$ = -53.1 $mol^{-1}.K^{-1}$, $\Delta G^{\ddagger}$ = 90.42 kJ mol^{-1}; $Tp^{Me2}MoO_2(OPh)$ + PMe_3, $\Delta H^{\ddagger}$ = 65.5 mol^{-1}, $\Delta S^{\ddagger}$ = -101.5 J $mol^{-1}.K^{-1}$, $\Delta G^{\ddagger}$ = 94.8 kJ mol^{-1}; $Tp^{Me2}MoO_2(SPh)$ + PMe_3, $\Delta H^{\ddagger}$ = 39.64 mol^{-1}, $\Delta S^{\ddagger}$ = -118.3 J $mol^{-1}.K^{-1}$, $\Delta G^{\ddagger}$ = 74.9 kJ mol^{-1}). With PMe_3 as a model substrate, the geometry and the free energy of the transition state for the formation of the phosphine oxide coordinated intermediate has been calculated ($\Delta G^{\ddagger}$ of 95 kJ mol^{-1}), which is in good agreement with the experimental value. The second step of the reaction, i.e., the exchange of the coordinated phosphine oxide with acetonitrile, $Tp^{R'}MoO(X)(OPR_3)$ + MeCN $\rightarrow$ $Tp^{R'}MoO(X)(MeCN) + OPR_3$) follows a first-order process, (where X= OPh, Cl or SPh and R' are as previously stated). The reaction follows a dissociative interchange (I_d) or associative interchange (I_a) type mechanism, as it is substrate and compound dependent. For example, the activation

---

‡ A portion of these results have been published in *Chem. Eur. J.* **2006**, in press

parameters for $Tp^{iPr}MoO(OPMe_3)(OPh)$ of $\Delta H^{\ddagger}$ = 56.3 kJ mol^{-1}; $\Delta S^{\ddagger}$ = -134.3 J $mol^{-1}.K^{-1}$; $\Delta G^{\ddagger}$ = 93.9 kJ mol^{-1} are similar to those of $Tp^{Me2}MoO(OPMe_3)(Cl)$ $\Delta H^{\ddagger}$ = 87.5 kJ mol^{-1}; $\Delta S^{\ddagger}$ = -30.5 J $mol^{-1}.K^{-1}$; $\Delta G^{\ddagger}$ = 96.6 kJ mol^{-1} and $Tp^{Me2}MoO(OPMe_3)(SPh)$ $\Delta H^{\ddagger}$ = 67.8 kJ mol^{-1}; $\Delta S^{\ddagger}$ = -82.5 J $mol^{-1}.K^{-1}$; $\Delta G^{\ddagger}$ = 92.3 kJ mol^{-1}, while being quite dissimilar from $Tp^{iPr}MoO(OPEt_3)(OPh)$ with $\Delta H^{\ddagger}$ = 93.5 kJ mol^{-1}; $\Delta S^{\ddagger}$ = 18.2 J $mol^{-1}.K^{-1}$; $\Delta G^{\ddagger}$ = 88.1 kJ mol^{-1}. However, the activation parameters for $Tp^{Me2}MoO(OPEt_3)(Cl)$ of $\Delta H^{\ddagger}$ = 81.1 kJ mol^{-1}; $\Delta S^{\ddagger}$ = -44.9 J $mol^{-1}.K^{-1}$; $\Delta G^{\ddagger}$ = 94.5 kJ mol^{-1} reflect a mechanism similar to that observed for both $Tp^{iPr}MoO(OPMe_3)(OPh)$ and $Tp^{Me2}MoO(OPMe_3)(Cl)$. Although gas-phase calculations indicate that the Mo-$OPMe_3$ bond is stronger than the Mo-NCMe bond in the model $Tp^{iPr}MoO(OPMe_3)(OPh)$ complex, solvation provides the driving force for the release of the phosphine oxide and formation of $Tp^{iPr}MoO(OPh)(MeCN)$. The latter complex serves as the precursor to a dinuclear complex via a dissociative pathway.

Introduction.

The transfer of a labile atom (e.g., oxygen, nitrogen or sulfur) between competent centers is a fundamental reaction in chemistry and biology, and during the past decades these reactions have been extensively studied.[1,2,3,4,5] Often the donor-acceptor pair is a metal complex, and a Lewis base. The most commonly reported atom transfer reaction involves the transfer of an oxygen atom. In the case of complete atom transfer, the oxygenated product no longer remains bonded to the donor. The majority of the complete oxygen atom transfer (OAT) reactions involve high-valent metal centers, and the transfer of an oxygen atom is coupled with the transfer of an electron pair (**Equation 2.1** and **Equation 2.2**). Furthermore a vast majority of well characterized reactions involve P, N, or S compounds as the donor/acceptor, but C, As and Se have also been used, as discussed in detail in **Chapter 3**. While the exact nature of the reaction may vary, OAT reactions are thought to be involved in the mechanism of several metalloenzymes such as cytochrome P450, sulfite oxidase, nitrate reductase, and DMSO reductase. In addition, such catalytic transfer of oxygen atoms is also important in industrial processes as well as bench-top synthesis in reactions as diverse as the epoxidation of olefins[6,7] or catalysis of epoxide ring opening reactions analogous to the Witting reaction.[8]

$$[MO]^{n+} + X \longrightarrow [M]^{(n-2)+} + XO \qquad \textbf{Equation 2.1}$$

$$XO + [M]^{(n-2)} \longrightarrow [MO]^{n+} + X \qquad \textbf{Equation 2.2}$$

Among the many metal complexes that exhibit OAT reactivity, those involving high-valent oxo-molybdenum complexes have been investigated in great detail.[9,10,11,12] Generally, such investigations are directed at improving catalytic epoxidation reactions or to understand the OAT

reactivity of mononuclear molybdenum enzymes. Although the transfer of an oxygen atom during catalysis has not been universally established in all molybdenum enzymes, it has been unequivocally demonstrated in native and tungsten substituted DMSO reductase.[13,14] Thus, there is substantial interest in understanding the details of catalytic reactions carried out by mononuclear molybdenum enzymes. To this end, many synthetic systems have been developed to probe specific aspects of the reaction. Among the prominent analog systems that exhibit OAT reactivity are the oxo-molybdenum complexes stabilized by dithiocarbamate,[15] ene-dithiolate[16,17,18] and hydrotris(pyrazolyl)borate[19,20] ligands. In a large number of cases, the metal center acts as a source of the oxygen atom and is generally reduced by two electrons; however, the reverse role of the metal is also common place. Thus, both $Mo^{VI}O_2/Mo^{IV}O$ and $Mo^{VI}O/Mo^{IV}$ couples have been reported to involve substrate oxidation and reduction. For many years a variety of biological and organic substrates have been used in model systems, but tertiary phosphines have become the reagent of choice, due to their higher solubility in organic solvents and the ability to tune their reactivity through the substitution at phosphorous. For example, the basicity of these phosphorous compounds increases with an increasing degree of alkylation at the phosphorus center, such that the basicity is as follows: $PMe_3 \sim PEt_3 > PPh_2Me > PPh_2Et > PPh_3$. A more detailed discussion of the reactivity of phosphorous compounds is presented in **Chapter 3** of this dissertation.

A long standing mechanistic description of OAT from dioxo-Mo(VI) centers to tertiary phosphines involves a nucleophilic attack of the phosphine lone pair on an empty Mo=O π^* orbital. In these reactions, the existence of a single transition state has been supported by experimental data. A computational investigation, however, indicated that such a reaction proceeds via the formation of a phosphine oxide coordinated intermediate.[21] The other oxo-group participates in the reaction, but is not transferred. This so-called "spectator" oxo acts to stabilize the intermediate by

strengthening its Mo=O bond as the phosphine weakens the other Mo=O by its attack via an associative mechanism.[22] It has also been suggested that the initial nucleophilic attack proceeds rapidly, and is followed by a slow process involving the loss of coordinated phosphine oxide from the intermediate. Experimental confirmation of the proposed intermediate has been provided through the *in situ* detection of intermediate molecules of the general formula $Tp^{Me2}MoO(OPPh_3)X$ where Tp^{Me2} = hydrotris(3,5-dimethyl pyrazol-1-yl) borate; X^- = SPh^-, OPh^-, Br^-, and Cl^-.[23] Additional confirmation came through isolation and structural characterization of intermediates of the type, $Tp^{iPr}MoO(OPR_3)X$ (where Tp^{iPr}= hydrotris(3-isopropylpyrazol-1-yl)borate; X=Cl, substituted phenol or alkyl thiol)[23,24] and $Tp^{Me2}MoO(OPMe_3)Cl$.[25] This reported system models the reactivity of oxidation of DMS by DMSO reductase and the oxidation of sulfite by sulfite oxidase where a catalytically labile oxygen atom is passed from the enzyme to the substrate with the concomitant transfer of two electrons.[26] Recent calculations have predicted similar intermediates in a variety of systems, including models for DMSO reductase.[27] Here, we describe a detailed kinetic investigation of the formation and the solvation of $Tp^{R'}Mo(OPR_3)(X)$ (R_3 = Me_3, Me_2Ph, Et_3, (n-Bu)$_3$, Et_2Ph, Ph_2Et or Ph_2Me; R' = i-Pr or Me_2; X= Cl, OPh or SPh), and provide an experimental analysis of the rate-limiting step for these two substrates. These experimental results are supported by theoretical calculations of the intermediates involved in these reactions, the transition states connecting them, and their geometries.

Experimental

Synthesis of Complexes:

The $Tp^{Me2}MoO_2OPh$ (**3**), $Tp^{Me2}MoO_2SPh$ (**4**) and $Tp^{Me2}MoO_2Cl$ (**2**) compounds**, Figure 2.1a-2.1d**, were prepared as previously reported while $Tp^{iPr}MoO_2OPh$ (**1**) was received through collaborative efforts from Dr. Charles Young, and all compounds were stored in vials until used. The $Tp^{iPr}MoOOPh(OPEt_3)$ (**1b**) and $Tp^{iPr}MoOOPh(OPMePh_2)$ (**1f**) complexes were prepared as reported,[23,24] or obtained through collaboration with Dr. Charles Young and stored in a dry-box, under a nitrogen atmosphere until used. All of the $Tp^{Me2}MoOOPh(OPR_3)$ complexes (**3a** to **3f**), remaining $Tp^{iPr}MoOOPh(OPR_3)$ (**1a**, **1c-1d, 1g**) complexes (R_3 = Me_3, Me_2Ph, Et_2Ph, *n*-Bu_3 and $EtPh_2$) as well as $Tp^{Me2}MoOSPh(OPEtPh_2)$ (**4f**) were characterized *in situ* in either dry benzene or dry acetonitrile. Furthermore, all of the $Tp^{Me2}MoOCl(OPR_3)$ complexes (**2a-2f**) were synthesized using modifications of previously reported procedures. Here, the phosphine oxide complexes are designated by both a number which relates to the parent dioxo complex, followed by a letter to designate the phosphine oxide in the complex. Thus (**a**) = $OPMe_3$; (**b**) = $OPMe_2Ph$; (**c**) = $OPEt_3$; (**d**) = $OPEt_2Ph$; (**e**) = OP(*n*-$Bu)_3$; (**f**)= $OPMePh_2$ and (**g**) = $OPEtPh_2$, respectively. The final atom transfer reaction products, $Tp^{iPr}MoOOPh(NCMe)$ (**5**), $Tp^{Me2}MoOCl(NCMe)$ (**6**) and $Tp^{Me2}MoOSPh(NCMe)$ (**7**) were characterized *in situ,* and were produced by solvolysis of **1a-1f**, **2a-2f** and **4a** or **4f** through standing in acetonitrile solution.

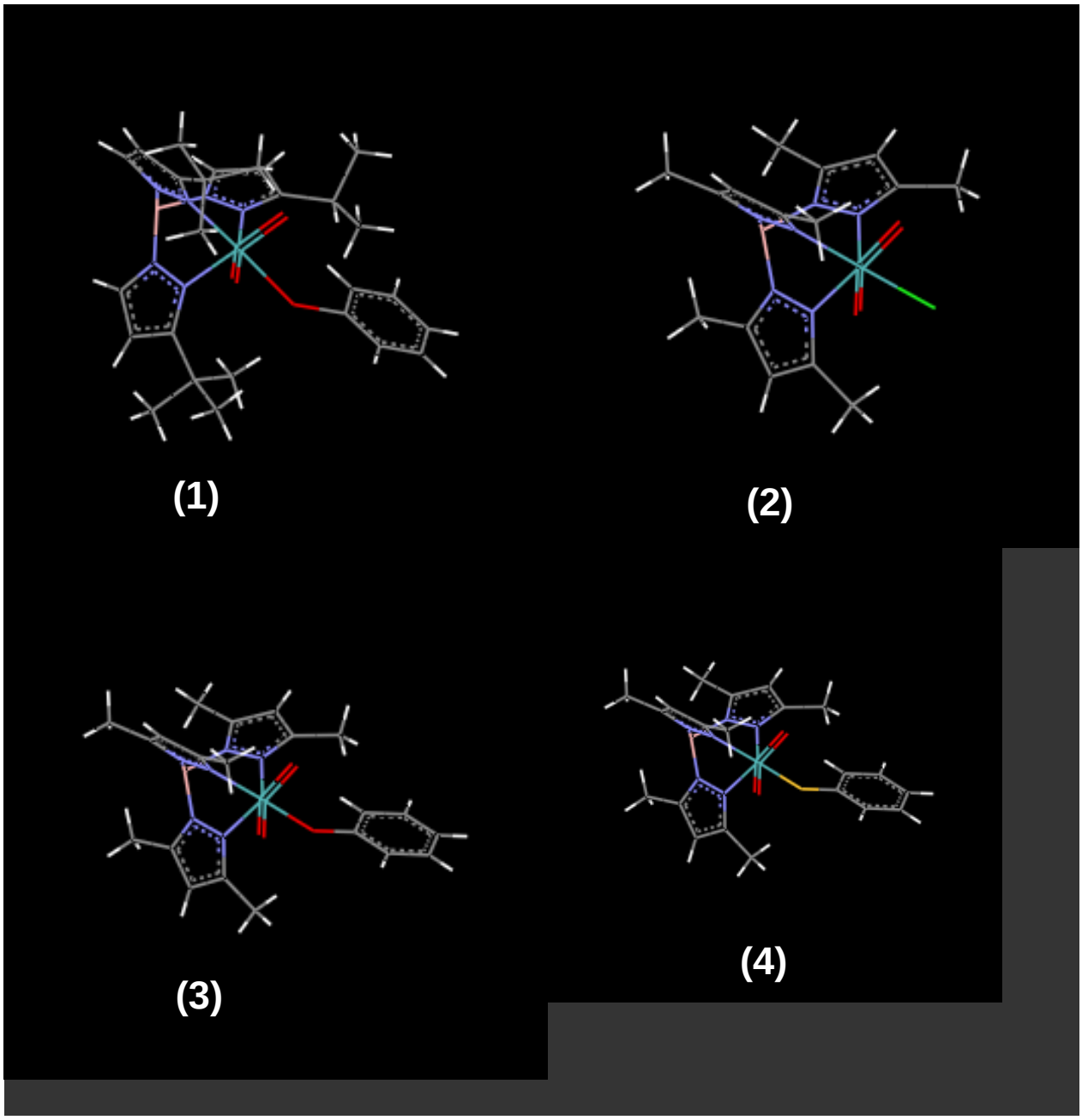

Figure 2.1a: 3-dimensional representation of complexes (**1**), (**2**), (**3**) and (**4**)

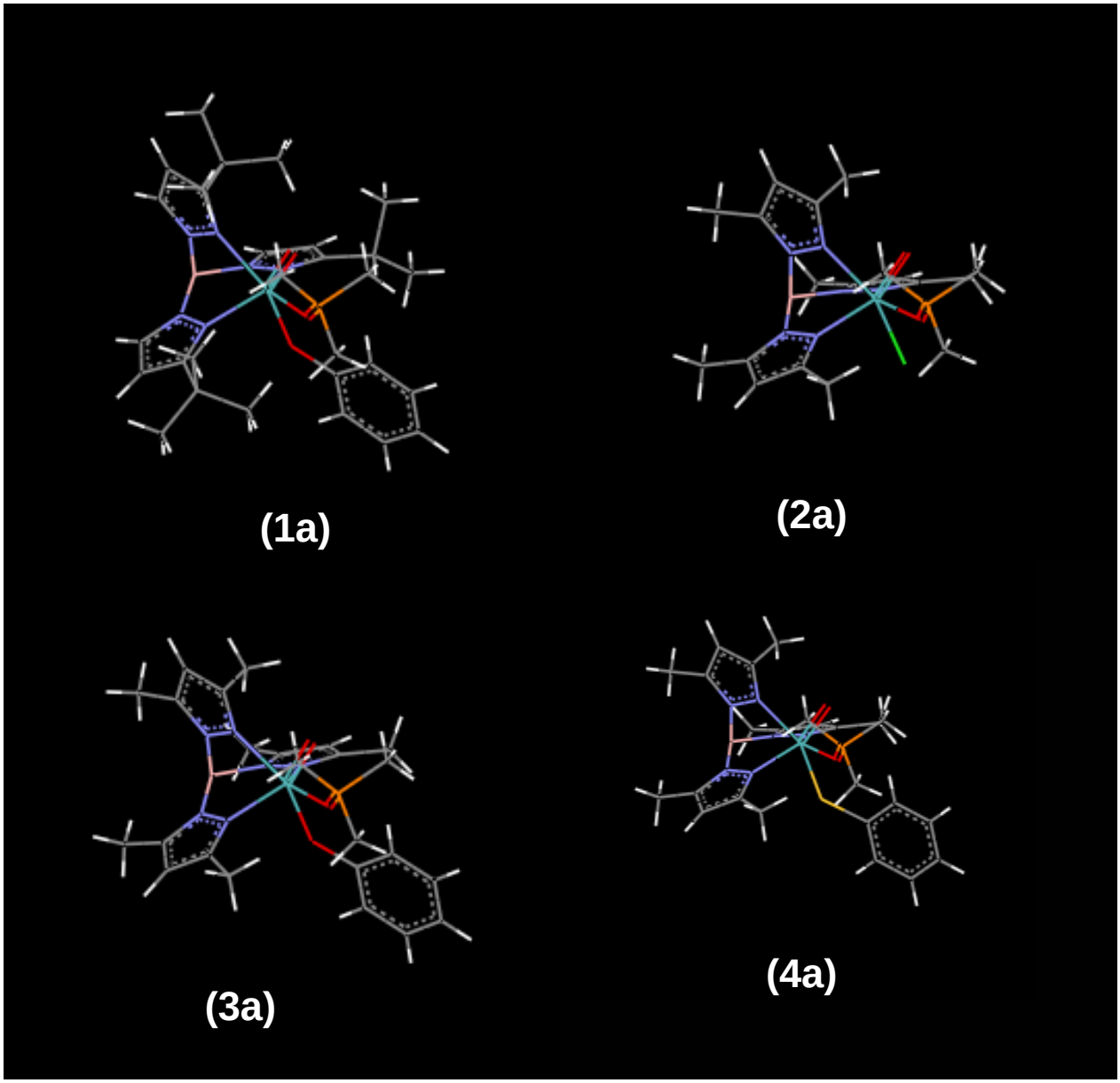

Figure 2.1b: 3-dimensional representation of the intermediate complexes represented by the respective $OPMe_3$ complex (**1a**), (**2a**), (**3a**) and (**4a**)

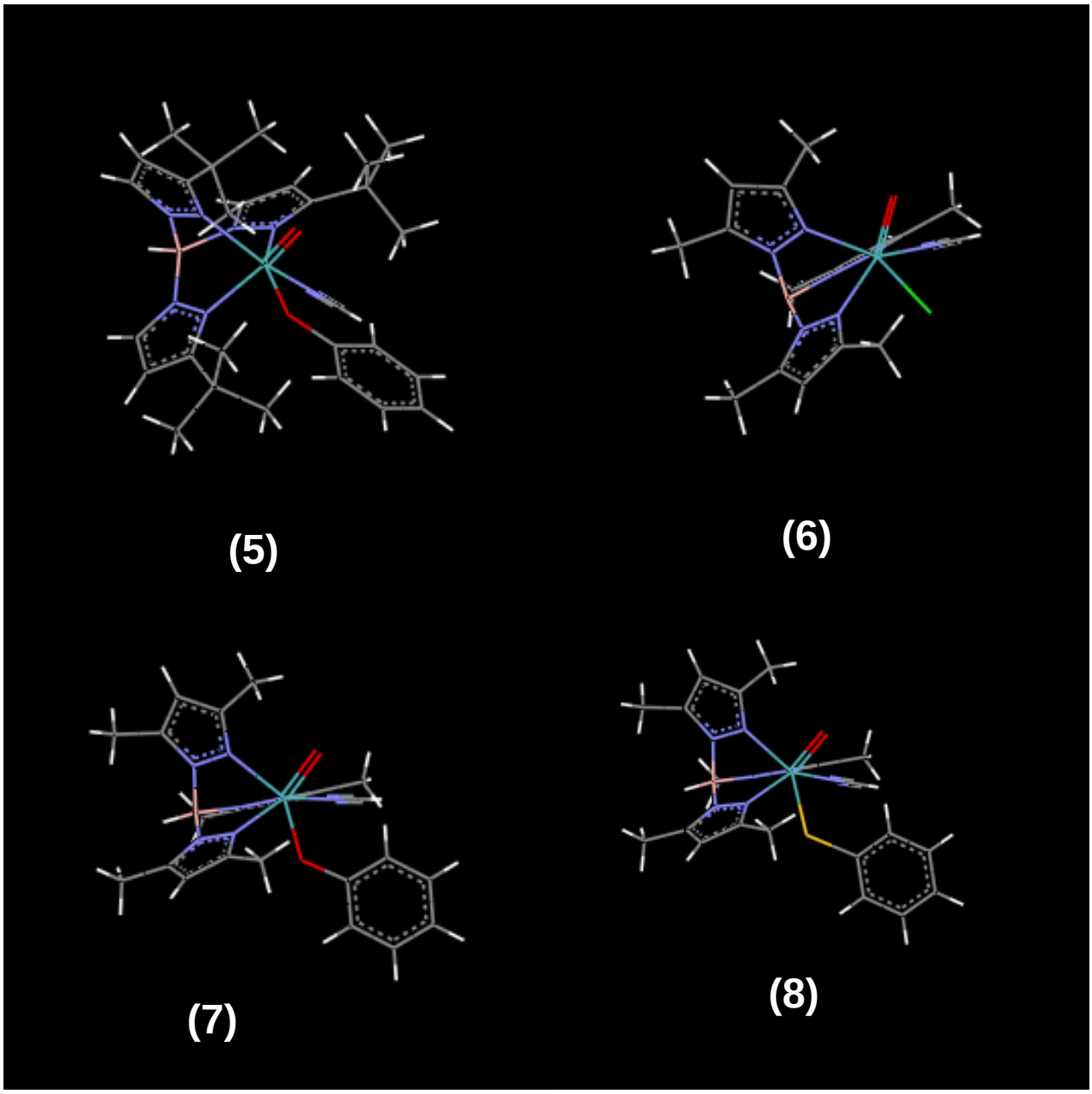

Figure 2.1c: 3-dimensional representation of the solvated products of (**1**), (**2**), (**3**) and (**4**); designated as (**5**), (**6**) (**7**) and (**8**) respectively.

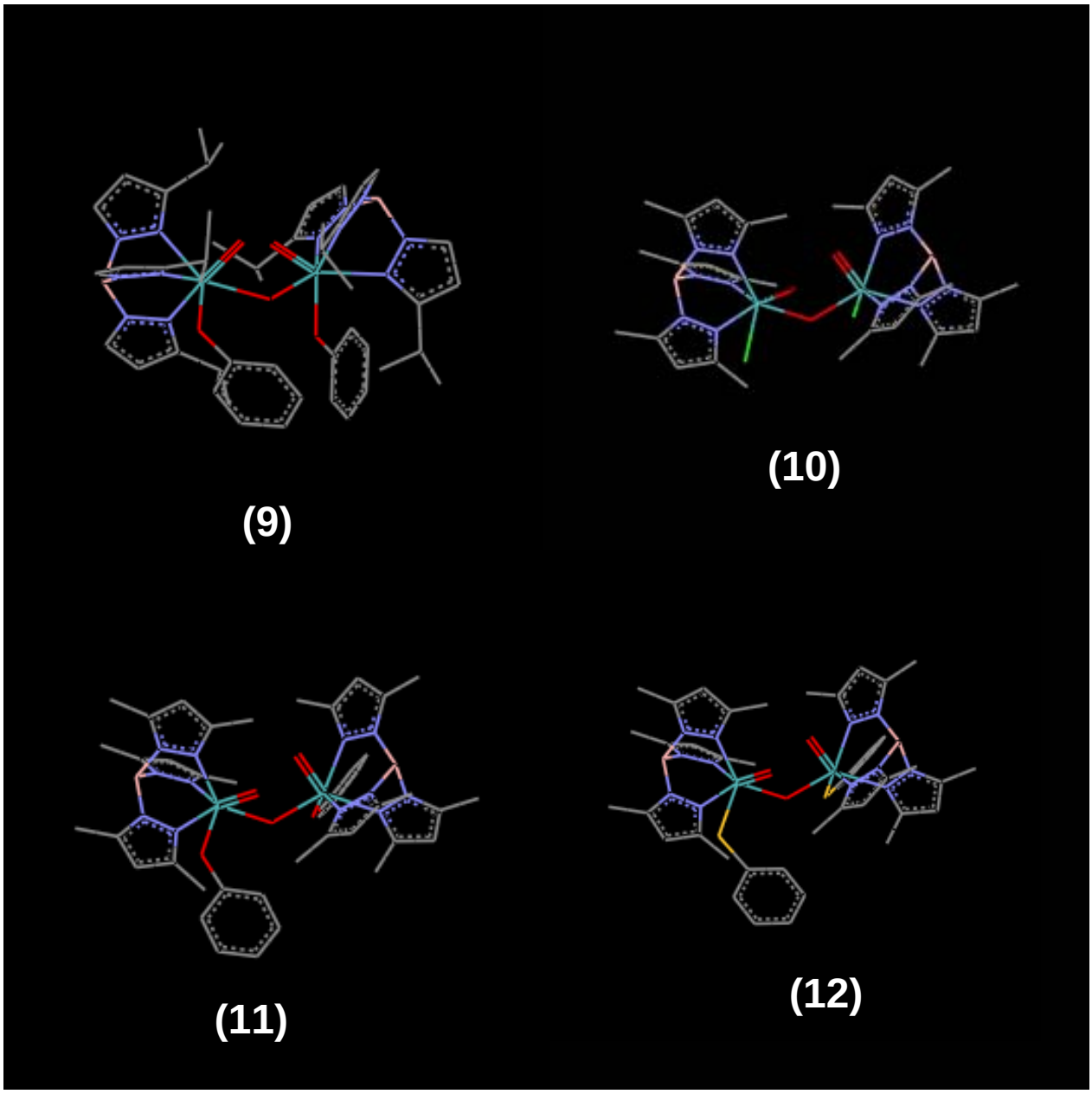

Figure 2.1d: 3-dimensional representation of the dimeric products of (**1**), (**2**), (**3**) and (**4**); designated as (**9**), (**10**) (**11**) and (**12**) respectively.

However, the $Tp^{Me2}MoO(NCMe)OPh$ complex (**8**) could not be characterized due to the production of a dimeric complexes (**11**), presumably of the general formula $[Tp^{Me2}MoO(L)OPh]_2O$, (where L= NCMe, OPR_3) as determined by allowing the analogue complex **2**, stand in benzene solutions, which yields (**10**). In an analogous manner (**9**) is perceived as the final product from either the isolated intermediate (**1a-1g**) or via *in situ* reaction between (**1**) and phosphines, over long observation periods or at elevated temperatures.

Characterization

Electronic spectra were recorded on a Cary 14 spectrophotometer with an OLIS 14 version 2.6.99 operating system connected to a constant-temperature circulator. Electrochemical measurements were carried out in a Bioanalytical Systems (BAS) model CV-50W cyclic voltammeter. Voltammograms were recorded with a standard three-electrode system consisting of a Pt-disk working electrode, a Ag/Ag^+ reference electrode, a Pt-wire auxiliary electrode, and tetrabutylammonium perchlorate (TBAP) as the charge carrier. All voltammograms were internally referenced with ferrocene, and the potentials are reported with respect to the Fc^+/Fc couple without junction correction. In addition, all electrochemical work was performed inside a dry-box, under a nitrogen atmosphere, at room temperature, while the free energy of formation ($\Delta G°$) was computed using **Equation 2.3**.

$$\Delta G^\circ = -nF\Delta E^\circ_{1/2} \qquad \textbf{Equation 2.3}$$

Where $\Delta E^\circ_{½}$ was taken as the Mo(VI)/Mo(V) oxidation/reduction couple with respect to the Fc^+/Fc couple, n was taken to be 1 and F, Faradays constant, was taken to be 96485.3 $C{\cdot}mol^{-1}$. In

this way, a typical cyclic voltammogram was recorded by placing $1x10^{-5}$ to $2x10^{-5}$ mol of the metal complex, and 200 mg of TBAP into 5ml of dry oxygen-free acetonitrile with ~$2x10^{-4}$ mol of ferrocene added upon completion.

Infrared spectra were recorded by attenuated total reflectance (ATR) on a Thermo-Nicolet 380 FT-IR equipped with a smart orbit module containing a 30,000cm^{-1} to 200 cm^{-1} diamond. The powdered Mo(VI) complexes (~2mg) were handled under ambient conditions, while the same quantity of the Mo(IV) complexes were transferred to the ATR stage in vials under nitrogen atomosphere and immediate recorded upon opening.

NMR spectra of the dioxo-molybdenum complexes were recorded on a Bruker 300 MHz NMR spectrometer in either CD_3CN or C_6D_6, and referenced to TMS. NMR spectra for the characterization of the intermediates were recorded on a Varian 500 MHz spectrophotometer, with ^{31}P spectra referenced to PPh_3, in a sealed NMR tube, under nitrogen atmosphere, in C_6D_6 solution. Typically 10mg of the intermediate complexes ($Tp^{Me2}MoO(OPR_3)Cl$ only) were dissolved in cold CD_3CN or C_6D_6, and referenced to TMS (^1H) or -4.7 ppm of PPh_3 (^{31}P). The other intermediates were characterized *in situ*, with typically $1.8x10^{-5}$ to $2x10^{-5}$ mol of the parent Mo(VI) complex and a five fold molar excess of the phosphine.

All solvents, except the NMR solvents and acetonitrile, were distilled from sodium, deoxygenated using the freeze-pump-thaw technique, and stored inside a dry-box until needed. The acetonitrile used in this study was triple-distilled from $KMnO_4$, CaH_2 and P_4O_{10}, and was stored anaerobically. All NMR solvents that were used in the intermediate characterization were dried by flushing them through an activated alumina micro-column inside a dry-box, while the solvents for the spectra of the Mo(VI) complexes were used as received. In addition, all solutions were prepared under an argon atmosphere using standard Schlenk techniques and gas-tight syringes. All mass

spectra were collected using a Micromass ZMD quadrupole spectrometer with acetonitrile as the mobile phase.

Kinetics Investigations:

The predominance of the kinetic investigations were conducted by recording the electronic spectra on a Cary 14 spectrophotometer with an OLIS 14 version 2.6.99 operating system connected to a constant-temperature circulator. However, some of the single-wavelength and repeat scan measurements were conducted on a Cary 3E diode array spectrophotometer with a Varian operating system or a Hewlet-Packard 8452A diode array spectrophotometer at room temperature. All ultraviolet-visible kinetic measurements were conducted using an anaerobic cuvette that was oven-dried and cooled under argon flow.

Additional kinetics experiments were performed on a Bruker 300 MHz NMR spectrometer fitted with a liquid-nitrogen cooled temperature control module. The thermocouple for low temperature NMR work was calibrated using MeOH as previously reported using **Equation 2.4,**[28] while an example calibration-cooling curve may be found in **Table 2.1** and **Figure 2.2**.

$$T(K) = 435.5 - 1.193 \cdot \left|\frac{\Delta\nu}{5}\right| - 29.3 \cdot \left|\frac{\Delta\nu \cdot 10^{-2}}{5}\right|^2 \qquad \textbf{Equation 2.4}$$

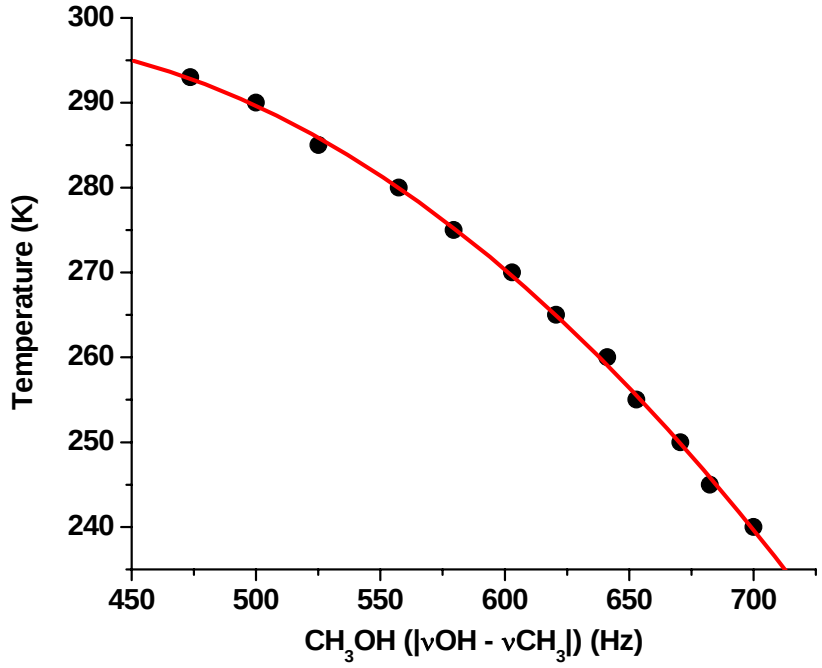

Figure 2.2: Representative Cooling Curve for the Calibration of the Thermocouple used in Low Temperature NMR Experiments.

For the kinetics experiments, NMR spectra were collected using sealed NMR tubes in dry CD_3CN with PPh_3 as the ^{31}P reference.

Table 2.1: Representative Data for the Calibration of the Thermocouple During Low Temperature NMR Experiments on a Bruker 300 MHz NMR Spectrometer				
Set Temp. (K)	**υOH (Hz)**	**υCH_3 (Hz)**	**$\Delta\upsilon$ $\lvert\upsilon OH - \upsilon CH_3\rvert$ (Hz)**	**Actual Temp (K)[a]**
293	6014.81	5541.24	473.57	296.21
290	6042.75	5542.71	500.04	286.89
285	6067.76	5542.71	525.05	277.91
280	6100.11	5542.71	557.40	266.09
275	6122.17	5542.71	579.46	257.89
270	6145.71	5542.71	603.00	249.01
265	6163.35	5542.71	620.64	242.27
260	6183.94	5542.71	641.23	234.31
255	6195.71	5542.71	653.00	229.72
250	6213.36	5542.71	670.65	222.77
245	6225.12	5542.71	682.41	218.10
240	6241.30	5541.24	700.06	211.03
a) calculated by **Equation 2.4** in the text				

Reaction Kinetics of $LMoO_2(X)$ + PR_3: (L=Tp^{iPr}, Tp^{Me2} and X = OPh or SPh)

The reaction of $Tp^{iPr}MoO_2(OPh)$ (**1**) with PEt_3 or PPh_2Me, was monitored by single wavelength assays at 910 nm over the temperature range of 4 °C to 38 °C to yield (**1c**) and (**1f**) respectively. The reaction was investigated in MeCN as well as in benzene to probe the influence of solvent on the rate of the reaction. All solutions were prepared using the previously discussed techniques with two notable differences. First, fresh stock solutions of $Tp^{iPr}MoO_2(OPh)$ were prepared using standard Schlenk techniques, at a concentration of ~2.5 mg/mL (4.5 mM) in an attempt to keep the complex concentration as uniform as possible throughout the study. Second, stock PR_3 solutions of ~ 1-2 M were prepared and stored in a dry-box, but were otherwise handled using Schlenk techniques during the measurement. A typical assay was performed in the following manner: 750 μL of the $Tp^{iPr}MoO_2(OPh)$ stock solution was added to the anaerobic cuvette under argon containing the requisite amount of solvent so that, after the desired volume of phosphine was added, the final volume would be 1 mL (~3.4 mM in $Tp^{iPr}MoO_2(OPh)$). The reaction mixtures were prepared using a 4.5 mM stock solution of $Tp^{iPr}Mo^{VI}O_2(OPh)$ and 1-2 M stock solutions of the

respective phosphine in appropriate solvents. The ratios of concentrations of PEt_3 to $Tp^{iPr}Mo^{VI}O_2(OPh)$ were 7.8, 15, 29.8, and 59.7 to maintain pseudo first-order conditions, while those of PPh_2Me to $Tp^{iPr}Mo^{VI}O_2(OPh)$ were: 10, 20, 40 and 90. The cuvette was then allowed to equilibrate to the desired temperature in the sample chamber of the spectrophotometer while the stock PR_3 solution was equilibrated separately. Once equilibrated, the reaction was initiated by the addition of the desired volume of PR_3 solution via a gas-tight Hamilton syringe, shaken for 5-10 s and assayed at the desired wavelength. Each assay was monitored for 5-8 times the predicted half-life ($t_{½}$) of formation, with a typical resolution of 1 data point per 10 s, and a total of 1024 data points collected. Once complete, all single-wavelength assays were fit to determine the rate constants, these rate constants were used to calculate the activation parameters from the Arrhenius and Eyring Equations, **Equation 2.5** and **Equation 2.6**.

$$\ln k = \ln(A)\cdot e^{\left(\frac{-E_a}{R\cdot T}\right)} \qquad \textbf{Equation 2.5}$$

$$\ln\left(\frac{k\cdot h}{k_b\cdot T}\right) = -\frac{\Delta H^*}{RT} + \frac{\Delta S^*}{R} \qquad \textbf{Equation 2.6}$$

Reactions of $Tp^{Me2}MoO_2(OPh)$, $Tp^{Me2}MoO_2(SPh)$ and the remaining reactions of $Tp^{iPr}MoO_2(OPh)$ were conducted in a similar manner with the exception that solvent effects were not included in the analysis. Unfortunately, the reactions of $Tp^{Me2}MoO_2(Cl)$ were not amenable to kinetic analysis due to the inherent low solubility of the dioxo-metal complex. However a suspension of this compound, in benzene, toluene or acetonitrile, does react with phosphines to yield $Tp^{Me2}MoO(Cl)(OPR_3)$. In addition the reactions of $Tp^{iPr}MoO_2OPh$ and $Tp^{Me2}MoO_2SPh$ were performed with PMe_3 at 1:1 ratios and followed spectophotometrically as detailed above, with

further investigation of the 1:1 reaction conducted electrochemically and via ^{1}H NMR. The ^{1}H NMR was performed on a Bruker 300 MHz spectrometer in dry CD_3CN at room temperature, with data collection every 30 seconds upon addition of 1 eq. of PMe_3.

For the 1:1 (actual ratio was1:1.3) reaction of $Tp^{Me2}MoO_2SPh$ ($1.46x10^{-5}$ mol) with PMe_3 ($1.93x10^{-5}$ mol), electrochemical experiments involving repeat scanning cyclic voltammograms were typically collected over a sweep width spanning from +500 mV to –1400 mV, with a scan rate of 100mV/sec at 10μA/V sensitivity in acetonitrile with TBAP as the supporting electrolyte and the previously mentioned electrode system. Similarly, the 1:1 (actual ratio was 1:1.5) reaction of $Tp^{iPr}MoO_2OPh$ ($2.19x10^{-5}$ mol) with PMe_3 ($3.29x10^{-5}$ mol), electrochemical experiments involving repeat scanning cyclic voltammograms were typically collected over a sweep width spanning from -300 mV to –1400 mV, with a scan rate of 100mV/sec at 10μA/V resolution in acetonitrile with TBAP. However, experiments with both compounds were conducted at room temperature in a dry box under nitrogen atmosphere.

Kinetics of LMoO(X)(OPR$_3$) Decomposition: (L=Tp^{iPr}, Tp^{Me2} and X = OPh, SPh or Cl)

The kinetics of the decomposition of the reaction intermediate, (**1c**) $Tp^{iPr}MoO(OPh)(OPEt_3)$, were investigated using three complementary methods. First, time-dependent, multi-wavelength scans were collected in two major regions: 1200 nm to 500 nm, denoted the low energy region, and 600 nm to 230 nm, denoted as the high-energy region. For a typical low energy experiment, a pre-weighted finely ground 3-5 mg ($4.8x10^{-6}$ – $8.0x10^{-6}$ mol) of $Tp^{iPr}MoO(OPh)(OPEt_3)$ was dissolved in 750 μL to 1mL of the dry-degassed solvent, to a final concentration of 4.8—10.6 mM. A typical dead time for this set up was ~ 1.5 minutes. Data were recorded with a resolution of 1 - 2 nm/data point and at a rate of 2.5 - 5 minutes per scan, over 200 - 500 minutes. A typical high-energy

experiment was also conducted similarly but to a final concentration of ~375 μM, and scanning from 600-230 nm. Each dataset was deconvoluted into three component species using the Singular Value Decomposition (SVD) technique[29] (**Appendix 1;** page 105) using Matlab 6.0 and Mathcad 2000I. Appropriate spectral and temporal eigenvectors, derived from SVD, were selected and the temporal vectors were fitted using the Origin 6.1 software package.[30] Once fits to the temporal vectors had been obtained, the pure component spectra were reconstructed as a function of the pre-exponential multiplier obtained from the fits, the SVD determined spectral eigenvectors and the corresponding eigenvalues, using Microsoft Excel. After the spectra of the component species were determined, an extinction profile was calculated and used in conjunction with the predicted decay times to construct a linear combination of the pure component species contributions to the observed spectrum. This linear combination was then used to provide a simulation as well as a global fit to the observed, time dependent absorption spectra.

Figure 2.3 shows the observed, calculated and the difference between the observed and the calculated spectra at different time intervals. Once the individual data sets (high or low-energy) were processed, they were spliced together and processed as one entity. Appropriate wavelengths for single wavelength kinetics assays were selected based on the spectra of the pure components. **Figure 2.4** shows the calculated spectrum for the three individual components.

In the case of $Tp^{iPr}MoOOPh(OPEt_3)$, single-wavelength assays were conducted at 301 nm, 680 nm and 910 nm, using the previously mentioned sample preparation and handling methodology over a temperature range of 4 – 37 °C.

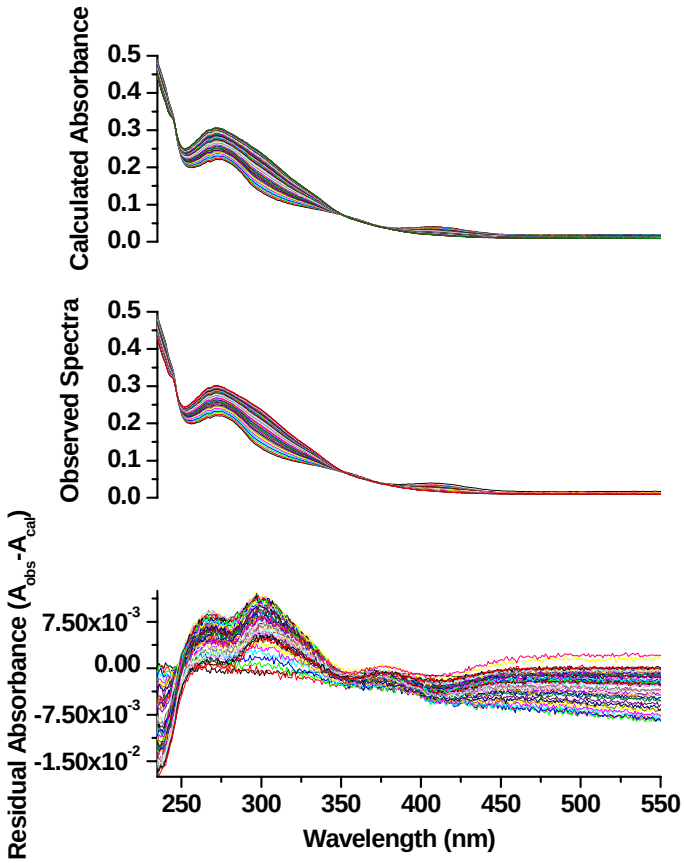

Figure 2.3: Representative SVD results for the decomposition of (**1c**) in acetonitrile at 11º C. **Top:** Calculated Time Dependent Spectra. **Middle:** Observed Time Dependent Spectra and **Bottom:** Calculated Residual as Observed Spectra – Calculated Spectra.

A typical single wavelength experiment consisted of pre-incubation of the solvent, cuvette and sample cell to thermal equilibrium at the desired temperature, choosing an appropriate number of data points (generally between 400 and 1000), and total assay time (~5.5 – 6 times the SVD predicted $t_{½}$ of the exponential decay).

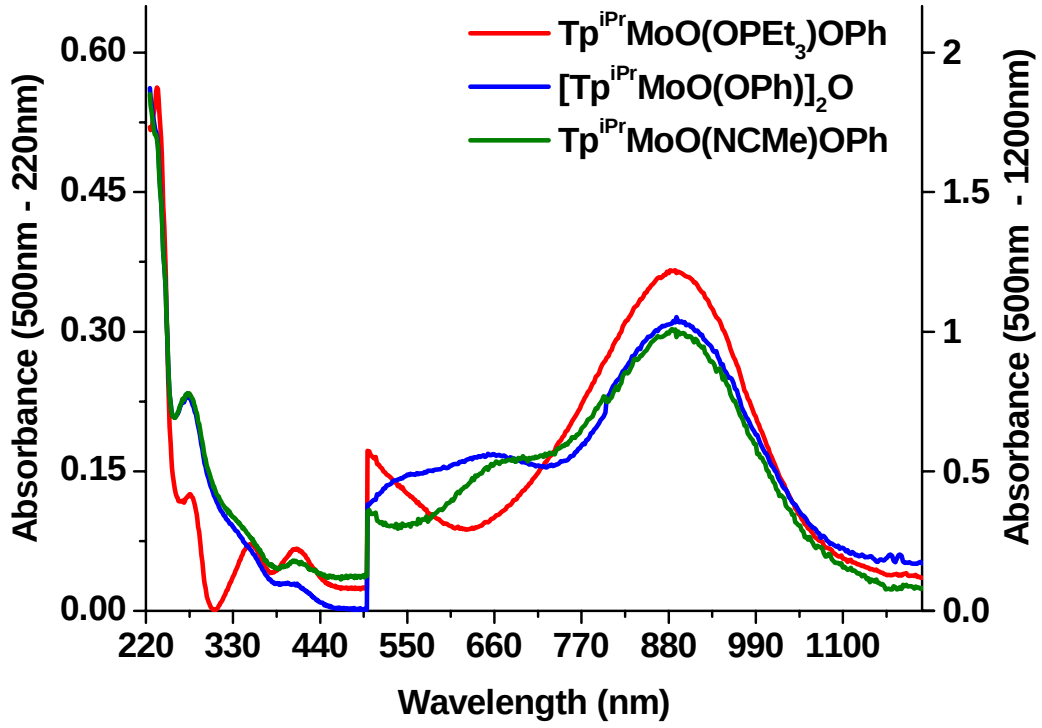

Figure 2.4: Calculated spectra of the pure components, as determined from SVD analysis. Note: Right side of the spectra was recorded at ten times the concentration of the starting (**1c**) complex, relative to the left side of the spectra.

The decomposition was then initiated by the addition of the solvent, followed by dilution, if required, and mixing. The rate constants were determined by fitting the absorption data as either a single (910 nm and 301 nm) or double exponential (680 nm). The activation parameters for the first and second step in the decomposition of $Tp^{iPr}MoO(OPh)(OPEt_3)$ were determined from the Eyring and Arrhenius equations.

Lastly, the dissociation of the phosphine oxide was probed by both low temperature and room temperature ^{1}H and ^{31}P NMR spectroscopy. The solvents (C_6D_6 and CD_3CN) for the NMR experiments were purchased from commercial sources and dried inside a dry-box by passing the

contents of a 1 mL ampoule through alumina. Following this step, the MeCN was cooled to 4 ºC along with an anaerobic NMR tube for 30 minutes in the dry-box refrigerator, while the benzene was stored anaerobically at room temperature. A typical sample was prepared by dissolving 10 mg ($1.6x10^{-5}$ mol), of $Tp^{iPr}MoO(OPh)(OPEt_3)$ in 700 μL of the dry-solvent (cold and dry in the case of MeCN) in the dry-box and immediately analyzed. The typical delay between the sample preparation step and the recording of the first spectrum was two minutes. Spectra of $Tp^{iPr}MoO(OPh)(OPEt_3)$ and $Tp^{iPr}MoO_2(OPh)$ were collected at room temperature, in dry C_6D_6, and used for comparison with time dependent NMR experiments. Once the initial spectrum was recorded, the sample was immediately incubated in a water-bath at 11 ºC for 5 minutes before returning to record the subsequent spectrum. Spectra were continually recorded in this manner until no changes were observable in the spectrum for at least one-hour, while the terminal time point was collected after 24 h. The integrated areas of ^{31}P resonances were used for single exponential fits to determine the rate of phosphine oxide release.

Single-wavelength spectrophotometric measurements were conducted in MeCN, benzene, tetrahydrofuran (THF) and deoxygenated MeCN-water mixtures to test the effects of solvent. Repetition of the assays at 680 nm with THF and MeCN with added water (10 and 100 fold excess with respect to the molybdenum complex) tested the effects of solvent dryness. These experiments were conducted to test the possibility of a water-assisted process, followed by bulk solvent exchange to the final product. In this phase of the experiment, water was deoxygenated and added to dry-deoxygenated MeCN using Schlenk techniques, to a stock concentration of 1 M, under an argon atmosphere.

The decomposition kinetics of $Tp^{iPr}MoO(OPh)(OPPh_2Me)$ (**1f**) were carried out in the fashion described for $Tp^{iPr}MoO(OPh)(OPEt_3)$. Like in the previous case, the SVD analysis showed

three components, and the rates of transformation of these components agreed well with those determined from the single-wavelength measurements. Furthermore, there were no significant variations in the principal spectra of the species, aside from a ~10 nm blue-shift of the 910 nm band to approximately 900 nm; otherwise the wavelengths chosen for the single-wavelength measurements were the same as those used for $Tp^{iPr}MoO(OPh)(OPEt_3)$.

The decomposition of the $Tp^{Me2}MoOCl(OPR_3)$ series (**2a-2g**), was conducted in a similar fashion as $Tp^{iPr}MoO(OPh)(OPPh_2Me)$, although SVD analysis was not performed. However, the decay of the $Tp^{Me2}MoOCl(OPMe_3)$ complex was additionally followed in mixed acetonitrile:benzene solutions with compositions ranging from 0.19M to 19M acetonitrile, to assist in the determination of the mechanism of decay in these complexes.

The remaining decomposition reactions of $Tp^{iPr}MoO(OPh)(OPR_3)$, $Tp^{Me2}MoO(OPh)(OPR_3)$ and $Tp^{Me2}MoO(SPh)(OPR_3)$ complexes were performed *in situ* and as such the methods employed were similar those used in probing the reaction kinetics of $Tp^{iPr}MoO_2(X) + PR_3$, with the exception that the PR_3 concentrations were ~ 1000X the concentration of the starting molybdenum complex in order to saturate the rate of formation of the intermediate species. Furthermore since these solvation reactions were monitored *in situ,* SVD analysis was not performed. Interestingly, it has been demonstrated that complexes of the type $Tp^{Me2}MoO$ (*p*-X-C_6H_4S)($OPMe_3$) (where X= H, OMe, COOH) form unusually stable $Tp^{Me2}MoO$ (*p*-X-C_6H_4S) (NCMe) complexes,[31] which can be crystallographically characterized. In striking contrast to this are the solvation reactions of $Tp^{Me2}MoOOPh(OPR_3)$, which favors either the direct formation of the previously mentioned dimeric product or simultaneous formation of the solvated product and the dimeric product at room temperature and higher, thus obscuring the solvation reaction. Furthermore, this dinucleation

reaction has hindered attempts of crystallization of the $Tp^{Me2}MoOOPh(OPR_3)$ series, which generally results in a brown dimeric solution.

Theoretical details:

The theoretical model system for the reaction of $Tp^{iPr}MoO_2(OPh)$ with PMe_3 was performed through collaboration with professor Michael Hall and consisted of the full $Tp^{iPr}MoO_2(OPh)$ reactant and PMe_3 as a model substrate. The geometries of all structures for the theoretical model system were fully optimized by the B3LYP[32] DFT[33] method as implemented in Gaussian 98 or Gaussian 03.[34] Analytical harmonic frequencies have been calculated for all stationary points to confirm the nature of these points, for the zero point energies, and for the thermodynamic properties. Solvation corrections in MeCN were performed by the Polarizable Continuum Model (PCM) method[35] as implemented in Gaussian 03. The results reported in this work have been obtained with a standard valence double-ζ quality basis set (D95V)[36] for B, C, N, O, and H. A small core ECP[37] was used for Mo (1s2s2p3s3d) with a double-ζ quality basis set that includes the outer 5p function developed by Couty and Hall.[38] An ECP (1s2s2p) with a double-ζ quality basis set (LANL2DZ)[39] was used for P, and to properly describe the hypervalent character of P, a polarization function with an exponent of 0.340 was added.[40]

The geometries of all phosphines and phosphine oxide structures for the theoretical charges, energies and volumes were fully optimized by the B3LYP[41] DFT[42] method as implemented in Gaussian 98 or Gaussian 03.[43] Analytical harmonic frequencies have been calculated for all stationary points to confirm the nature of these points, for the zero point energies, for the thermodynamic properties. The results reported here, and discussed in greater detail in **Chapter 3**, were obtained using the 6-311G(d,p) basis set for all phosphine atoms, and the 6-311G(d) basis set

for all phosphine oxides, with charges calculated with the Mulliken,[44] natural bond order[45] and electrostatic potentials, and electrostatic potential-derived charges using the Merz-Kollman-Singh[46] methods. All volume calculations were performed as described by the Onsager[47] Method as contained in the Gaussian 98 or Gaussian 03 [48] software packages.

Results

*Electronic Absorption of Complexes (**1a-1g**).*

Because the intermediate complexes (**1a-1g**) decompose in solution, a direct measurement of the extinction coefficient for $Tp^{iPr}MoO(OPh)(OPR_3)$ was first conducted at low temperatures, typically in the range of 4º - 8º C, in acetonitrile solution. In addition the extinction coefficients of (**1c**) and (**1g**) were computed through singular value decomposition, as described in the following sections, at 11º C, then compared to the direct measurements. In the decomposition process, the green (**1c**) $Tp^{iPr}Mo^{IV}O(OPh)(OPEt_3)$, whose principal absorption was determined by SVD at 910 nm (10,989 cm^{-1}; ε 120 $M^{-1}cm^{-1}$) arises from a $d_{xy} \rightarrow d_{xz}/d_{yz}$ transition rapidly converts to either a blue complex exhibiting two $d_{xy} \rightarrow d_{xz}/d_{yz}$ transitions at 680 nm (14,706 cm^{-1}; ε = 90 $M^{-1}cm^{-1}$) and 910 nm (ε = 100 $M^{-1}cm^{-1}$) or a brown complex that exhibited characteristic absorption at ~ 500 nm (20,000 cm^{-1}; ε = 1600 $M^{-1}cm^{-1}$). However, at lower temperature, the conversion of the blue complex is followed by the slow, yet readily observable transformation to a brown complex. **Table 2.2** provides a comprehensive list of the d-d bands characteristic of complexes (**1a-1g**) as determined by direct measurements, while the same transitions in the blue complex are discussed in later sections. Similar SVD treatment of greenish-yellow (**1f**) resulted in a shifted $d_{xy} \rightarrow d_{xz}/d_{yz}$ transition at 900 nm (11,111 cm^{-1}; ε 100 $M^{-1}cm^{-1}$), while absorptions of the blue complex and brown complex were identical to those observed in the analysis of (**1c**). When the SVD determined

absorptions are compared to the directly determined absorptions for (**1c**) and (**1f**), there is an approximate 300 cm^{-1} blue-shift of the $d_{xy} \rightarrow d_{xz}/d_{yz}$ transition in each complex (300cm^{-1} in (**1c**) and 258 cm^{-1} in (**1f**)).

Table 2.2: Visible spectra of complexes with the general formula $Tp^{iPr}MoO(OPR_3)OPh$		
Compound	**$d_{xy} \rightarrow d_{xz}$ / d_{yz} (cm^{-1})**	**$d_{xy} \rightarrow d_{x2-y2}$ (cm^{-1})**
1a	**11230**	**23260**
1b	**11210**	**23225**
1c	**11290**	**23360**
1d	**11420**	**23300**
1e	**11338**	**23260**
1f	**11370**	**23220**
1g	**11742**	**22243**

*NMR Characterization of **(1a-1g)***

NMR was performed on the intermediate complexes (**1a-1g**) as defined in the materials and method section of this paper on intermediate complexes form via an *in situ* reaction between (**1**) and ~1 to 1.5 fold excess of the appropriate phosphine. **Table 2.3** shows relevant chemical shift data that were observed in the ^{31}P spectra, while **Table 2.4** provides important details acquired from the ^{1}H spectra.

Table 2.3: Phosphorous chemical shift data for complexes (**1a-1f**), the free phosphine and free phosphine oxide*.					
Phosphine (Complex)	**δ^{31P} OPR_3^F (ppm)**	**δ^{31P} PR_3^F (ppm)**	**δ^{31P} Mo-OPR_3^C (ppm)**	**$\Delta\delta^{31P}$ F-C (ppm)**	**$\Delta\delta^{O31P}$ F-C (ppm)**
PMe_3 **(1a)**	35.6	-62.0	64.0	-126	-28.4
PMe_2Ph **(1b)**	28.9	-46.9	58.4	-105.3	-29.5
PEt_3 **(1c)**	48.3	-20.4	74.9	-95.3	-26.6
$P(n\text{-}Bu_3)$ **(1d)**	45.5	-32.2	74.4	-106.6	-28.9
PEt_2Ph **(1e)**	42.1	-15.1	64.8	-79.9	-22.7
$PMePh_2$ **(1f)**	32.4	-10.8	72.8	-83.6	-40.4
$PEtPh_2$ **(1g)**	31.9	-12.0	43.2	-55.2	-11.3
* F and ^{F} indicate free phosphine or free phosphine oxide and C and ^{C} indicate coordinated phosphine or phosphine oxide.					

Table 2.4: ^{1}H NMR Data for the *i*-Pr-Pyrazol, *i*-Pr-Methine Protons in Complexes (**1a-1g**)						
Complex	**δ^{1}H CH (*i*-Pr-PZ_1)**	**δ^{1}H CH (*i*-Pr-PZ_2)**	**δ^{1}H CH (*i*-Pr-PZ_3)**	**δ^{1}H CH (PZ_1)**	**δ^{1}H CH (PZ_2)**	**δ^{1}H CH (PZ_3)**
(**1a**)	2.73	4.09	4.41	5.84	5.99	6.30
(**1b**)	3.46	4.02	4.79	6.44	6.70	6.70
(**1c**)	3.11	3.69	4.29	6.06	6.27	6.43
(**1d**)	2.61	4.23	4.45	5.87	5.96	6.01
(**1e**)	2.72	4.17	4.34	5.87	5.98	6.02
(**1f**)	3.46	4.02	4.60	5.89	6.21	6.23
(**1g**)	3.46	4.02	4.60	6.46	6.70	6.78

One interesting feature of this system is the nearly constant change in the chemical shift of the free phosphine oxide relative to that of the coordinated phosphine oxide, calculated as ($\Delta\delta^{O31P}$ F-C) at -26.8 ± 8.7 ppm (**Table 2.3**). This change upon coordination is similar to the variation in the chemical shifts of the free phosphine oxides (δ^{31P} OPR_3^{F}) at 37.8 ± 7.5 ppm, but is quite different than the variation observed in the coordinated phosphine oxides: δ^{31P} Mo-OPR_3^{C} at 64.6 ± 11.3 ppm.

*Electrochemical Measurements on **1, 1a-1g** and **5**:*

Cyclic voltammograms (CV) of **1**, **1a-1g** and **5** were recorded using the electrochemical methods described in the materials and methods section. All CV of the intermediate complexes, **1a-1g**, were recorded *in situ*, as produced from the reaction of **1** with ~2 to 5 fold excess of the desired phosphine, at room temperature, in a dry-box (**Table 2.5** and **Table 2.6**).

Table 2.5:
Results of CV experiments in the characterization of (**1**), (**1a-1g**), and (**5**)

Compound	**Average $E_{1/2}$ (mV)**	**Average ΔG^o (kJ/mol)**
$Tp^{iPr}MoO_2OPh$ ***(1)***	-1183.0 ± 8.0	114.2 ± 0.7
$Tp^{iPr}MoOOPh(OPR_3)$ ***(1a-g)***	-686.6 ± 13.1	66.3 ± 1.3
$Tp^{iPr}MoOOPh(NCMe)$ ***(5)***	-316.2 ± 2.7	30.5 ± 0.3

When recorded in this way, the accuracy of the measurement can be internally calibrated before phosphine addition (**1**) and after phosphine addition (**1a-1g**) and (**5**) with the mean $E_{1/2}$ and $\Delta G°$ expressed through seven independent measurements. As expected for the Mo(IV) complex (**5**), there was a small error associated with the measurements, -316.2 ± 2.7 mV and 30.5 ± 0.3 kJ/mol, while that for the remaining Mo(IV) complexes (**1a-1g**) show an approximate 3 fold greater deviation in the measurements, -686.6 ± 13.1 mV and 66.3 ± 1.3 kJ/mol, suggesting that there is a small but significant electronic effect that modulates the stability in these complexes.

Table 2.6: CV measurements of the intermediate complexes (**1a-1g**)			
Intermediate	**$E_{1/2}$ (mV)**	**ΔG^o (kJ/mol)**	**T (^{o}C)**
$Tp^{iPr}MoO(OPh)(OPMe_3)$ **(1a)**	-664.1	64.1	22
$Tp^{iPr}MoO(OPh)(OPMe_2Ph)$ **(1b)**	-687.5	66.3	22
$Tp^{iPr}MoO(OPh)(OPEt_3)$ **(1c)**	-684.7	66.1	21.5
$Tp^{iPr}MoO(OPh)(OP(n\text{-}Bu_3))$ **(1d)**	-699.5	67.9	21.5
$Tp^{iPr}MoO(OPh)(OPEt_2Ph)$ **(1e)**	-685	66.1	22
$Tp^{iPr}MoO(OPh)(OPMePh_2)$ **(1f)**	-704.4	68.0	22
$Tp^{iPr}MoO(OPh)(OPEtPh_2)$ **(1g)**	-681	65.8	21.5

Taken together, these results allow for the approximation of the reaction coordinate for the first step of the reaction between the starting Mo(VI) complex (**1**) and a phosphine, to yield the Mo(IV) intermediate complexes (**1a-1g**), (**Table 2.7** and **Figure 2.5**), while the solvation of complexes (**1a-1g**) to the final Mo(IV) product (**5**) are described in the sections to follow.

Table 2.7: Approximate Reaction Coordinate for the First Step in the Reaction: Reduction of (**1**) with Phosphines to Yield Compounds (**1a-1g**)

Compound	**ΔG^o (kJ/mol)[a]**	**$\Delta G^{\ddagger}$ (kJ/mol)[b]**	**$\Delta G'^o$ (kJ/mol)[c]**	**$\Delta G'^{\ddagger}$ (kJ/mol)[d]**
$Tp^{iPr}MoO_2OPh$ **(1)**	114.2 ± 0.7	NA	0	NA
$Tp^{iPr}MoO(OPh)(OPMe_3)$ **(1a)**	64.1	90.42	-50.1	90.42
$Tp^{iPr}MoO(OPh)(OPMe_2Ph)$ **(1b)**	66.3	89.84	-47.9	89.84
$Tp^{iPr}MoO(OPh)(OPEt_3)$ **(1c)**	66.1	92.88	-48.1	92.88
$Tp^{iPr}MoO(OPh)(OP(n\text{-}Bu_3))$ **(1d)**	67.9	93.98	-46.3	93.98
$Tp^{iPr}MoO(OPh)(OPEt_2Ph)$ **(1e)**	66.1	93.23	-48.1	93.23
$Tp^{iPr}MoO(OPh)(OPMePh_2)$ **(1f)**	68.0	94.83	-46.2	94.83
$Tp^{iPr}MoO(OPh)(OPEtPh_2)$ **(1g)**	65.8	97.46	-48.4	97.46

a) ΔG^o approximated from CV measurements at 298 K; b) $\Delta G^{\ddagger}$ taken from kinetics measurements at 298 K;
c) $\Delta G'^o$ represents the relative energy expressed as [ΔG^o(**1-1g**)- ΔG^o(**1**)];
d) $\Delta G'^{\ddagger}$ relative energy expressed as [$\Delta G^{\ddagger}$ (**1a-1g**) + $\Delta G'^o$(**1**)].

Details of the kinetics for the formation of the intermediate complexes (**1a-1g**) and their subsequent solvation in acetonitrile to compound (**5**) can be found in the sections to follow.

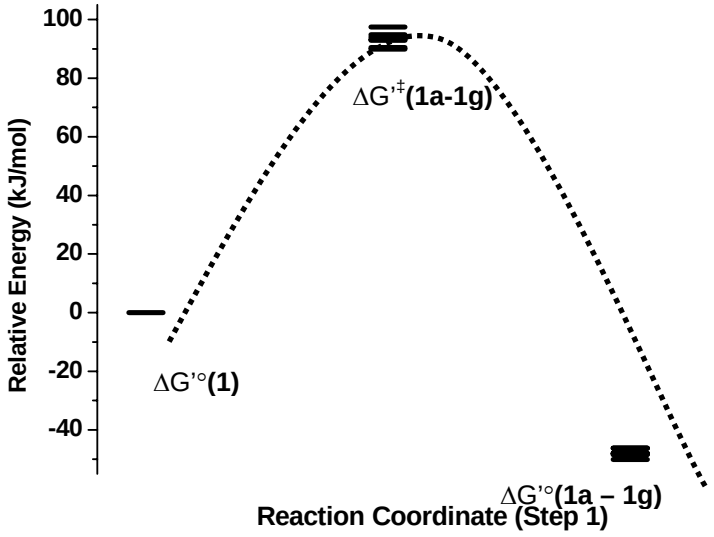

Figure 2.5: Reaction Coordinate for the formation of (**1a-1g**) from the reaction of (**1**) with phosphines. $\Delta G'^{o}$(**1**) , $\Delta G'^{o}$(**1a-1g**) and $^{o}\Delta G'^{\ddagger}$(**1a-1g**) are defined in the text.

Synthesis and Characterization of of $Tp^{Me2}MoO_2Cl$ ***(2)***, $Tp^{Me2}MoOCl(OPR_3)$ ***(2a-g)*** *and* $Tp^{Me2}MoOCl(MeCN)$ *complexes* ***(6)*****.**

*<u>$Tp^{Me2}MoOCl(OPMe_3)$: **(2a)**</u>* ~230 mg of $Tp^{Me2}MoO_2Cl$ was placed in a 50 ml round bottom flask, with a stir bar and heated in a drying oven for 1 hour to remove excess water from the glassware. Next, the flask was transferred to a dry box. Approximately 10 ml of dry, oxygen free benzene was added with rapid stirring to produce a pale yellow suspension. Once suspended, a 2x molar excess of PMe_3 was added, the reaction was capped and rapid stirring was maintained until an intense light green color was produced (approximately 5-10 minutes). This green mixture was then vacuum filtered, leaving the yellow unreacted $Tp^{Me2}MoO_2Cl$ in the filter and the green $Tp^{Me2}MoOCl(OPMe_3)$ as the filtrate. Once filtered, the volume of the $Tp^{Me2}MoOCl(OPMe_3)$

solution was reduced to approximately 1/3 of its original volume and was then immediately cooled in a 4 ^{o}C refrigerator in the dry box for approximately 20 minutes. After cooling, 3 volumes of ice cold hexane were added, followed by further cooling for an additional 20 minutes, which resulted in the formation of a bright green precipitate that was filtered and washed 6 times with ice cold hexane to yield pure $Tp^{Me2}MoOCl(OPMe_3)$. δ^{1H} (ppm) HC(Pz) (s) 1H each 5.749, 5.662, 5.456; H_3C(Pz) (s) 3H each 2.969, 2.744, 2.595, 2.233, 2.190, 2.058; H_3C ($OPMe_3$) (d) 12H 1.264, J= 13.067 Hz; δ^{31P} (ppm) 64.1. $\nu_{Mo=O}$ 953 cm^{-1}. $\nu_{P=O}$ 1100 cm^{-1}. λ_{max} (dd) 12300 cm^{-1} (ε=74 $mol^{-1}\bullet cm^{-1}$); 23657 cm^{-1} (ε=152 $mol^{-1}\bullet cm^{-1}$).

<u>$Tp^{Me2}MoOCl(OPEt_3)$: (2b)</u> This complex was synthesized following the procedure developed for $Tp^{Me2}MoOCl(OPMe_3)$, with the exception that the $Tp^{Me2}MoO_2Cl$ was allowed to react for approximately 3-5 minutes, and produced a darker olive green color upon reaction with a 2x molar excess of PEt_3. In addition, $Tp^{Me2}MoOCl(OPEt_3)$ precipitated as a dark, olive green powder. δ^{1H} (ppm) HC(Pz) (s) 1H each: 5.776, 5.657, 5.465, H_3C(Pz) (s) 3H each: 2.964, 2.822, 2.653, 2.232, 2.192, 2.054, H_2C ($OPEt_3$) d of p J=7.395 Hz: 2.036, 2.022, 2.006, H_3C ($OPEt_3$) (dt) J=16 Hz: 1.630, 1.623, 1.615, 1.608, 1.598, 1.592, 1.133, 1.125, 0.863, 0.847, 0.831, 0.815, 0.803, 0.787, 0.770, 0.753, 0.738. δ^{31P} (ppm) 77.348. $\nu_{Mo=O}$ 949 cm^{-1}. $\nu_{P=O}$ 1090 cm^{-1}. λ_{max} (dd) 12185 cm^{-1} (ε=56 $mol^{-1}\bullet cm^{-1}$); 23421cm^{-1} (ε=110 $mol^{-1}\bullet cm^{-1}$).

<u>$Tp^{Me2}MoO(OPMe_2Ph)Cl$: (2c)</u> This complex was synthesized following the procedure developed for $Tp^{Me2}MoOCl(OPMe_3)$, with the exception that the $Tp^{Me2}MoO_2Cl$ was allowed to react for approximately 2 minutes, and produced a yellow green color upon reaction with a 2x molar excess of PMe_2Ph. In addition, $Tp^{Me2}MoOCl(OPMe_2Ph)$ precipitated as a dark, olive green powder. $\nu_{Mo=O}$ 947 cm^{-1}. $\nu_{P=O}$ 1110 cm^{-1}. δ^{1H} (ppm) *o*-HC PMe_2Ph (dd) 7.278, 7.255: *m*-HC PMe_2Ph (dt) 6.903, 6.882: *p*-HC PMe_2Ph (t) 7.000: HC(Pz) (s) 1H each: 5.744, 5.691, 5.493, H_3C(Pz) (s) 3H each:

3.034, 2.642, 2.619, 2.258, 2.203, 2.080: H_3C PMe_2Ph (d) 1.949, 1.885 J_{HP}= 63.7 Hz. δ^{31P} (ppm) 53.392. λ_{max} (dd) 12100 cm^{-1} (ε=41 $mol^{-1}\bullet cm^{-1}$); 22700cm^{-1} (ε=92 $mol^{-1}\bullet cm^{-1}$).

Tp^{Me2}MoOCl(OP(n-Bu$_3$)): (2d) This complex was synthesized following the procedure developed for $Tp^{Me2}MoOCl(OPEt_2Ph)$, with the exception that the $Tp^{Me2}MoO_2Cl$ was allowed to react for approximately 1.5 minutes, and produced a dark green color upon reaction with a 2x molar excess of ice cold P(*n*-Bu)$_3$. In addition, $Tp^{Me2}MoOCl(OP(n\text{-}Bu)_3)$ dried as a dark, olive green powder. δ^{1H} (ppm) HC(Pz) (s) 1H each: 5.795, 5.667, 5.478: H_3C(Pz) (s) 3H each: 2.956, 2.921, 2.728, 2.239, 2.184, 2.054: H_3C OP(*n*-Bu)$_3$ 9H (t) 0.792: H_2C OP(*n*-Bu)$_3$ (m) 2H 1.867, (m) 2H 1.536, (m) 2H 1.446, (m) 6H 1.349, (m) 6H 1.211. δ^{31P} (ppm) 73.274. $\nu_{Mo=O}$ 953 cm^{-1}. $\nu_{P=O}$ 1110 cm^{-1}. λ_{max} (dd) 12321 cm^{-1} (ε=43 $mol^{-1}\bullet cm^{-1}$); 22547cm^{-1} (ε=147 $mol^{-1}\bullet cm^{-1}$).

Tp^{Me2}MoOCl(OPEt$_2$Ph): (2e) This complex was synthesized following the general procedure for $Tp^{Me2}MoOCl(OPMe_3)$, $Tp^{Me2}MoOCl(OPEt_3)$, and $Tp^{Me2}MoOCl(OPMe_2Ph)$. Once the round bottom flask containing $Tp^{Me2}MoO_2Cl$ and a stir bar was placed in the dry box, approximately 15-20ml of benzene was added and the flask was capped and cooled 1 hour to overnight. Once cooled, the flask was returned to the stir plate and a 2x molar excess of ice cold Et_2Ph was added and allowed to react for approximately 2 minutes, resulting in a yellowish-green solution. The reaction mixture was filtered, and the unreacted $Tp^{Me2}MoO_2Cl$ was washed with 3 volumes of hexane. The yellowish-green filtrate was immediately evaporated to dryness and washed with 6 volumes of ice cold hexane, resulting in the greenish-yellow $Tp^{Me2}MoOCl(OPEt_2Ph)$. $\nu_{Mo=O}$ 947 cm^{-1}. $\nu_{P=O}$ 1090 cm^{-1}. δ^{1H} (ppm) *o*-HC $OPEt_2Ph$ (dd) 7.397 : *m*-HC $OPEt_2Ph$ (dt) 7.005: *p*-HC $OPEt_2Ph$ (dt) 6.916: HC(Pz) (s) 1H each: 5.756, 5.675, 5.503, H_3C(Pz) (s) 3H each: 3.022, 2.668, 2.653, 2.247, 2.199,

2.076: H_2C $OPEt_2Ph$ (m) 2H each 2.740, 2.480, 1.495, 1.159: H_3C $OPEt_2Ph$ (dt) 0.938, 0.744. δ^{31P} (ppm) 67.403. λ_{max} (dd) 12316 cm^{-1} (ε=51 $mol^{-1}\bullet cm^{-1}$); 22673cm^{-1} (ε=112 $mol^{-1}\bullet cm^{-1}$).

$Tp^{Me2}MoOCl(OPMePh_2)$: (2f) This complex was synthesized following the procedure developed for $Tp^{Me2}MoO(OPEt_2Ph)Cl$, with the exception that the $Tp^{Me2}MoO_2Cl$ was allowed to react for approximately 0.5- 1 minutes, and produced a yellow-gold color upon reaction with a 2x molar excess of ice cold $PMePh_2$. In addition, $Tp^{Me2}MoOCl(OPMePh_2)$ dried as a yellow-gold powder. $\nu_{Mo=O}$ 953 cm^{-1}. $\nu_{P=O}$ 1090 cm^{-1}. δ^{1H} (ppm) *o*-HC $PMePh_2$ (m) 7.590: *m*-HC $PMePh_2$ (m) 6.855: *p*-HC $PMePh_2$ (m) 6.996: HC(Pz) (s) 1H each: 5.726, 5.652, 5.437, H_3C(Pz) (s) 3H each: 3.036, 2.470, 2.438, 2.221, 2.172, 2.042: H_3C $PMePh_2$ (d) 2.420, 2.402 J_{HP}= 53.399 Hz. δ^{31P} (ppm) 53.392. λ_{max} (dd) 12350 cm^{-1} (ε=42 $mol^{-1}\bullet cm^{-1}$); 22091cm^{-1} (ε=128 $mol^{-1}\bullet cm^{-1}$).

$Tp^{Me2}MoO(OPEtPh_2)Cl$: (2g) This complex was synthesized following the procedure developed for $Tp^{Me2}MoOCl(OPEt_2Ph)$, with the exception that the $Tp^{Me2}MoO_2Cl$ was allowed to react for approximately 0.5- 1 minutes, and produced a golden brown color upon reaction with a 2x molar excess of ice cold $PEtPh_2$. In addition, $Tp^{Me2}MoOCl(OPMePh_2)$ dried as a yellow-gold powder. $\nu_{Mo=O}$ 947 cm^{-1}. $\nu_{P=O}$ 1090 cm^{-1}. δ^{1H} (ppm) *o*-HC $OPEtPh_2$ (dd) 7.724, 7.654 : *m*-HC $OPEtPh_2$ (m) 6.985, 6.906: *p*-HC $OPEtPh_2$ (m) 7.029: HC(Pz) (s) 1H each: 5.738, 5.662, 5.444, H_3C(Pz) (s) 3H each: 3.039, 2.522, 2.423, 2.233, 2.192, 2.054: H_2C $OPEtPh_2$ (m) 1.826: H_3C $OPEtPh_2$ (dt) 1.144. δ^{31P} (ppm) 57.538. λ_{max} (dd) 12366 cm^{-1} (ε=64 $mol^{-1}\bullet cm^{-1}$); 22030cm^{-1} (ε=124 $mol^{-1}\bullet cm^{-1}$).

*NMR Characterization of (**2a-2g**)*

NMR was performed on the intermediate complexes (**2a-2g**) as defined in the materials and methods section of this paper on the isolated complex. **Table 2.8** shows relevant chemical shift data

that was observed in the ^{31}P spectra, while **Table 2.9** provides important details acquired from the ^{1}H spectra.

Table 2.8: Phosphorous chemical shift data for complexes (**2a-2f**), the free phosphine and free phosphine oxide*.

Phosphine (Complex)	**δ^{31P} OPR_3^F (ppm)**	**δ^{31P} PR_3^F (ppm)**	**δ^{31P} Mo-OPR_3^C (ppm)**	**$\Delta\delta^{31P}$ F-C (ppm)**	**$\Delta\delta^{O31P}$ F-C (ppm)**
PMe_3 **(2a)**	35.6	-62.0	64.1	-126.1	-28.5
PMe_2Ph **(2b)**	28.9	-46.9	58.0	-104.9	-29.1
PEt_3 **(2c)**	48.3	-20.4	77.4	-97.8	-29.1
$P(n\text{-}Bu)_3$ **(2d)**	45.5	-32.2	73.3	-105.5	-27.8
PEt_2Ph **(2e)**	42.1	-15.1	67.4	-82.5	-25.3
$PMePh_2$ **(2f)**	32.4	-10.8	53.7	-64.5	-21.3
$PEtPh_2$ **(2g)**	31.9	-12.0	57.5	-69.5	-25.6

* F and ^{F} indicate free phosphine or phosphine oxide and C and ^{C} indicate coordinated phosphine or phosphine oxide.

Interestingly the changes change in the chemical shift of the free phosphine oxide relative to that of the coordinated phosphine oxide mirrors the trends that were observed in (**1a-1g**), when calculated as ($\Delta\delta^{O31P}$ F-C) at -26.8 ± 2.8 ppm (**Table 2.8**) Again, this change upon coordination is similar to the variation in the chemical shifts of the free phosphine oxides (δ^{31P} OPR_3^F) at 37.8 ± 7.4 ppm, and the free phosphines (δ^{31P} PR_3^F) at -28.5 ± 19.6 ppm, but is quite different than the variation observed in the coordinated phosphine oxides: δ^{31P} Mo-OPR_3^C at 64.5 ± 8.8 ppm. Taken together, these characterization results suggest that ^{31}P NMR would be a useful tool for understanding the decay kinetics of these complexes through an approximate average shift in the phosphine oxide resonance upon coordination of 30 ppm. **Table 2.9** and **Table 2.10** highlights the changes in the chemical shifts of the pyrazole methine protons as a function of phosphine oxide ligand.

Table 2.10: Comparison of the phosphorous chemical shift data for complexes **(3a-3g)**, (**2a-2g**) and (**1a-1g**) with respect to the coordinated and free phosphine oxide*.

Phosphine (Complex)	**δ^{31P} OPR_3^F (ppm)**	**δ^{31P} Mo-OPR_3^C (ppm)**	**$\Delta\delta^{O31P}$ F-C (ppm)**
PMe_3 **(1a)**	35.6	64.0	-28.4
PMe_3 **(2a)**		64.1	-28.5
PMe_3 **(3a)**		65.0	-29.4
PMe_2Ph **(1b)**	28.9	58.4	-29.5
PMe_2Ph **(2b)**		58.0	-29.1
PMe_2Ph **(3b)**		162.1	ND
PEt_3 **(1c)**	48.3	74.9	-26.6
PEt_3 **(2c)**		77.4	-29.1
PEt_3 **(3c)**		77.9	-29.6
PEt_2Ph **(1d)**	45.5	64.8	-19.3
PEt_2Ph **(2d)**		67.4	-21.9
PEt_2Ph **(3d)**		69.2	-27.1
P(*n*-Bu)$_3$ **(1e)**	42.1	74.4	-32.3
P(*n*-Bu)$_3$ **(2e)**		73.3	-31.2
P(*n*-Bu)$_3$ **(3e)**		74.6	-29.1
$PMePh_2$ **(1f)**	32.4	72.8	-40.4
$PMePh_2$ **(2f)**		53.7	-21.3
$PMePh_2$ **(3f)**		116.2	ND
$PEtPh_2$ **(1g)**	31.9	43.2	-11.3
$PEtPh_2$ **(2g)**		57.5	-25.6
$PEtPh_2$ **(3g)**		58.5	-26.6

* F and ^{F} indicate free phosphine or phosphine oxide and C and ^{C} indicate coordinated phosphine or phosphine oxide.

Table 2.9: ^{1}H NMR Data for the Pyrazole Methine Protons in Complexes (**2a-2g**)

Complex	**δ^1H CH PZ_1**	**δ^1H CH PZ_2**	**δ^1H CH PZ_3**
(**2a**)	5.75	5.66	5.46
(**2b**)	5.78	5.66	5.47
(**2c**)	5.74	5.69	5.49
(**2d**)	5.80	5.67	5.48
(**2e**)	5.76	5.68	5.50
(**2f**)	5.73	5.65	5.44
(**2g**)	5.74	5.66	5.44

Furthermore **Figure 2.6 and 2.7** shows the dependence of the chemical shift of these resonances upon the chemical shift of the coordinated phosphine oxide, as well as tolmans electronic parameter[49] and suggests that the pyrazole ring PZ_1 is situated trans to the terminal-oxo ligand as it has the strongest correlation $R^2 = 0.7845$ with respect to the phosphine oxide, while Pz_2 and Pz_3 show little ($R^2 = 0.3400$) to no ($R^2 = -.01522$) correlations respectively. Even more interesting is the correlation of these pyrazol chemical shifts to the chemical shift of the phosphine-oxide coordinated complex, such that Pz_1: $R^2 = 0.91437$; Pz_3: $R^2 = 0.38301$ and Pz_2: $R^2 = -.09218$. Based upon these results, the chemical shift of Pz_1 is clearly strongly correlated to the nature of the phosphine ligand, while Pz_2 and Pz_3 are not affected. However, when the results are plotted against Tolmans electronic parameter for the parent phosphine, Pz_1 has no correlation ($R^2 = -0.27608$) while Pz_2 and Pz_3 are strongly negatively correlated with $R^2 = -0.89691$ and 0-.90621 respectively. Furthermore, neither the chemical shift of the phosphine oxide nor the chemical shift of the coordinated phosphine oxide correlate with Tolmans electronic parameter with $R^2 = -0.13779$ and 0.01542 respectively. Collectively, this suggests that there are two separate electronic effects generated by the coordinated phosphine oxide.

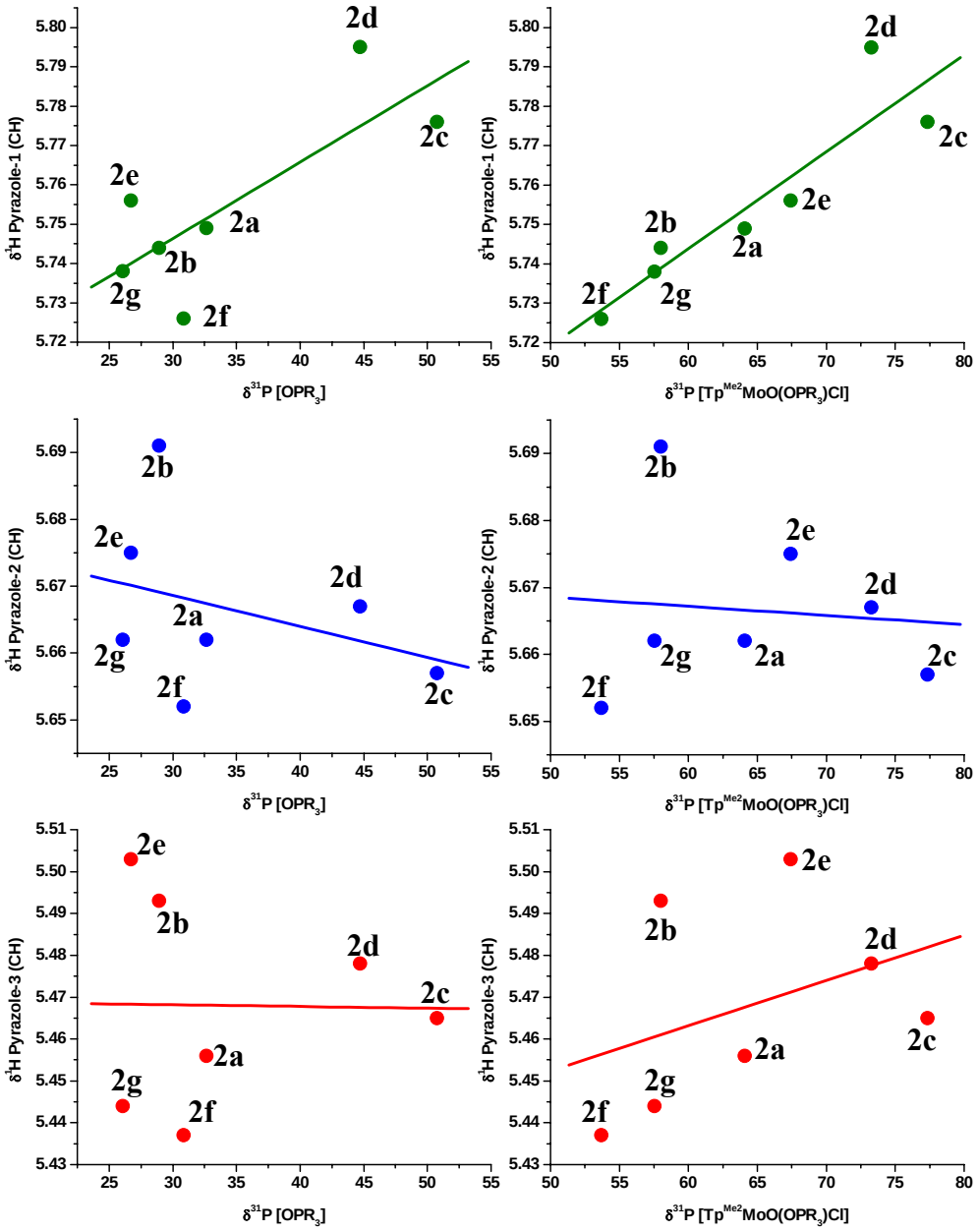

Figure 2.6: δ ^{1}H of the pyrazole methine protons of (**2a-2g**) verses Left: δ ^{31}P of the free phosphine oxide and Right: $^{\delta}$ 31P of the coordinated phosphine oxide.

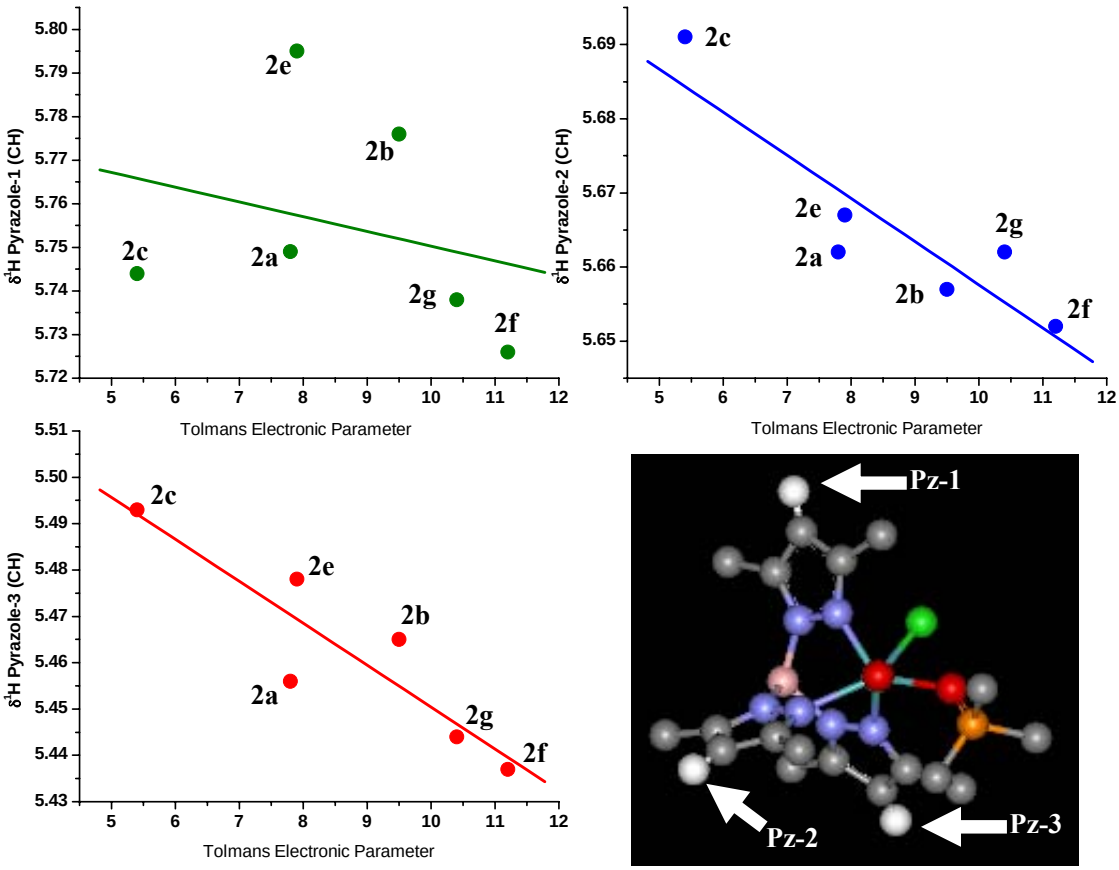

Figure 2.7: δ ^{1}H of the pyrazol methine protons of (**2a-2g**) verses Tolman's Electronic Parameter for the phosphine; Bottom Right: 3 dimensional representation of the structure of (**2a**) with all protons other than the methine protons removed for clarity.

First, the correlations between the ligand chemical shifts and Tolmans electronic parameters indicate that Pz_2 and Pz_3 are under the influence of a trans effect from the equatorial phosphine oxide through their joint interactions with the Mo d_{x2-y2} orbital. Secondly, Pz_1 is affected by the phosphine oxide, most likely through tetragonal compression arising from an increase in the partial triple bond character of the terminal oxo-bond, via π backdonation into low-lying unoccupied phosphorous d orbitals. This in turn creates a situation in which the length of the axial pyrazole nitrogen to molybdenum bond varies as a function of the Mo=O bond strength, as shown in **Table 2.10.**

Infra-red and UV/Vis Spectrophotometry:

Infrared spectra were collected as reported in the materials and methods section of this document, and were performed on the isolated product (**Table 2.10**). Ultraviolet-visible spectra were collected on the isolated intermediate in acetonitrile at room temperature due to the higher stability of these complexes relative to those derived from (**1**).

Table 2.10: Infra-red and near Infra red/visible spectra of complexes with the general formula $Tp^{Me2}MoO(OPR_3)Cl$

Compound	$\nu_{Mo=O}$ **(cm^{-1})**	$\nu_{P=O}$ **(cm^{-1})**	$d_{xy} \rightarrow d_{xz} / d_{yz}$ **(cm^{-1})**	$d_{xy} \rightarrow d_{x2-y2}$ **(cm^{-1})**
2a	953	1100	12300	23657
2b	949	1090	12185	23421
2c	947	1110	12100	22700
2d	953	1110	12321	22547
2e	947	1090	12316	22673
2f	947	1090	12350	22091
2g	947	1090	12366	22030

*Electrochemistry of **(2a-2g)***

Cyclic voltammograms (CV) of **2**, **2a-2g** and **6** were recorded using the electrochemical methods described in the materials and methods section. All CV of the intermediate complexes, **2a-2g**, were recorded on the isolated product as outlined in the materials and methods section, with the results tabulated in **Table 2.11** and **Table 2.12**.

Table 2.11: CV for the characterization of complexes **(2a-2g)**

Intermediate	**$E_{1/2}$ (mV)**	**ΔG^o kJ/mol**	**T (^{o}C)**
$Tp^{Me2}MoOCl(OPMe_3)$ **(2a)**	-484.7	46.8	22
$Tp^{Me2}MoOCl(OPMe_2Ph)$ **(2b)**	-472.4	45.6	22
$Tp^{Me2}MoOCl(OPEt_3)$ **(2c)**	-487.7	47.1	21.5
$Tp^{Me2}MoOCl(OP(n\text{-}Bu)_3)$ **(2d)**	-498.5	48.1	21.5
$Tp^{Me2}MoOCl(OPEt_2Ph)$ **(2e)**	-483.2	46.6	22
$Tp^{Me2}MoOCl(OPMePh_2)$ **(2f)**	-472.4	45.6	22
$Tp^{Me2}MoOCl(OPEtPh_2)$ **(2g)**	-467.8	45.1	21.5

The accuracy of the measurement can be internally calibrated similar to the CV data obtained from (**1**) with the mean $E_{1/2}$ and $\Delta G°$ expressed through seven independent measurements. **Figure 2.8** shows representative CV for the $Tp^{Me2}MoOCl(OPR_3)$ complexes. As expected there was a small error associated with the measurements for the Mo(IV) complex (**6**), of -71.6 ± 1.4 mV and 6.9 ± 0.1 kJ/mol, while that for the remaining Mo(IV) complexes (**2a-2g**) show an approximate 10 fold greater deviation in the measurements, -480.9 ± 10.1 mV and 46.4 ± 1.0 kJ/mol, which further supports the findings observed in the reactions of (**1**).

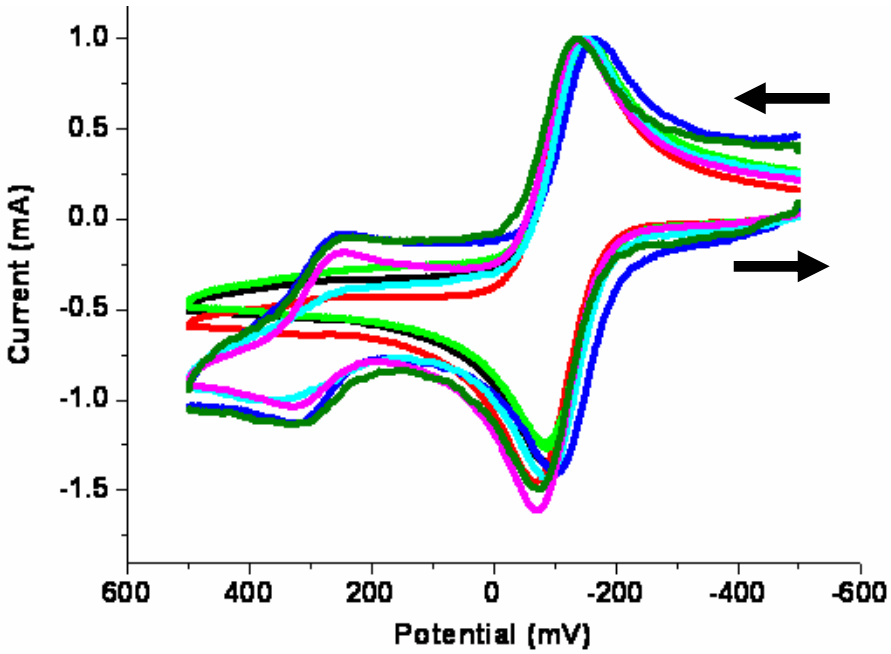

Figure 2.8: Representative CV, recorded during the solvation of (**2a-2g**) in acetonitrile **Step 2** of the reaction coordinate. Scans shown here are prior to Fc/Fc^{+} correction. Black = **2a**, light green = **2b**, Red = **2c** Light Blue, = **2d**, Pink = **2e**, Dark Green = **2f,** Dark Blue = **2g**. Couples ca. 275 mv are diagnostic of the formation of (**6**).

Table 2.12: CV for the characterization of complexes (**2**), (**2a-2g**) and (**6**)

Compound	**Average $E_{1/2}$ (mV)**	**Average ΔG^{o} (kJ/mol)**
$Tp^{Me2}MoO_2Cl$ **(2)**	-1155.0 ± 1.1	110.5 ± 0.1
$Tp^{Me2}MoOCl(OPR_3)$ **(2a-2f)**	-480.9 ± 10.1	46.4 ± 1.0
$Tp^{Me2}MoOCl(NCMe)$ **(6)**	-71.6 ± 1.4	6.9 ± 0.1

More specifically, these results suggest that there is a small but significant electronic effect that modulates the stability in all of the phosphine oxide complexes. However unlike (**1**), the low solubility of (**2**) allows only for the approximation of the reaction coordinate for the second step of the reaction that begins with the intermediate Mo(IV) complexes (**2a-2g**), to yield the Mo(IV)

solvated complex (**6**) and is discussed in detail in the sections to follow. (**Table 2.14** and **Figure 2.17**). Details of the kinetics experiments for the solvation reaction of (**2a-2f**), resulting in the formation of complex (**6**) can be found in the sections to follow.

*NMR Characterization of (**3a-3g**)*

NMR was performed on the intermediate complexes (**3a-3g**) as defined in the materials and method section of this paper on intermediate complexes derived via *in situ* reactions. **Table 2.13** shows relevant chemical shift data that was observed in the ^{31}P spectra, while **Table 2.14** provides important details acquired from the ^{1}H spectra.

Table 2.13: Phosphorous chemical shift data for complexes (**3a-3f**), the free phosphine and free phosphine oxide*.

Phosphine (Complex)	**δ^{31P} OPR_3^F (ppm)**	**δ^{31P} PR_3^F (ppm)**	**δ^{31P} Mo-OPR_3^C (ppm)**	**$\Delta\delta^{31P}$ F-C (ppm)**	**$\Delta\delta^{O31P}$ F-C (ppm)**
PMe_3 **(3a)**	35.6	-62.0	65.0	-127	-29.4
PMe_2Ph **(3b)**	28.9	-46.9	**162.1**[a]	**-129.74**	**-172.94**
PEt_3 **(3c)**	48.3	-20.4	77.9	-98.3	-29.6
$P(n\text{-}Bu)_3$ **(3d)**	45.5	-32.2	74.6	-106.8	-29.1
PEt_2Ph **(3e)**	42.1	-15.1	69.2	-84.3	-27.1
$PMePh_2$ **(3f)**	32.4	-10.8	**116.2**[a]	**-87.3**	**-163.1**
$PEtPh_2$ **(3g)**	31.9	-12.0	58.5	-70.5	-26.6

a = identity of this complex is not yet known. * F and ^{F} indicate free phosphine or phosphine oxide and C and ^{C} indicate coordinated phosphine or phosphine oxide.

As mentioned earlier, the changes in the chemical shift of the free phosphine oxide relative to that of the coordinated phosphine oxide mirrors the trends that were observed in (**1a-1g**), and (**2a-2g**) when calculated as ($\Delta\delta^{O31P}$ F-C), while not including (**3b**) and (**3f**), at -28.4 ± 1.4 ppm (**Table 2.8** and **Table 2.10**). However there were two exceptions, namely (**3b**) and (**3f**), which produced ^{31}P chemical shifts that are not clearly understood when a 1:1 phosphine: (**3**) ratio were used. However, by excluding the data from (**3b**) and (**3f**), the ^{31}P chemical shifts of the intermediate complexes are quite similar to those previously noted at 69.0 ± 7.7 ppm

Table 2.14: ^{1}H NMR Data for the Pyrazol Methine Protons in Complexes (**3a-3g**)			
Complex	**δ^1H CH PZ_1**	**δ^1H CH PZ_2**	**δ^1H CH PZ_3**
(**3a**)	6.000	5.985	5.623
(**3b**)	**ND**	**ND**	**ND**
(**3c**)	6.018	6.006	5.635
(**3d**)	6.018	6.002	5.639
(**3e**)	6.027	5.953	5.633
(**3f**)	**5.992**	**5.945**	**5.584**
(**3g**)	6.031	5.934	5.444

As noted previously, the pyrazol methine protons clearly express different chemical shifts as a function of the coordinated phosphine. However, as the ^{31}P resonances of (**3b**) and (**3f**) cannot be confidently assigned, the ^{1}H resonances of these species provide a similar view with slightly lower Pz_1 and Pz_3 chemical shifts.

Electrochemistry of $Tp^{Me2}MoO_2OPh$ ***(3)****, $Tp^{Me2}MoO(OPh)(OPR_3)$* ***(3a-3g)*** *and $Tp^{Me2}MoO(OPh)(MeCN)$ complexes* ***(7)*****.**

Cyclic voltammograms of **3**, **3a-3c** and **7** were recorded using the electrochemical methods described in the materials and methods section. All CV of the intermediate complexes, **3a-3g**, were recorded *in situ* as outlined in the materials and methods section, with the results tabulated in **Table 2.15** and **Table 2.16**. Unlike the series of intermediates (**1a-1g**) or (**2a-2g**), intermediates derived from (**3**) were found to be quite unstable. This instability is quantitatively evidenced both by their ~10 kJ/mol and ~30 kJ/mol increased destabilization relative to the average (**1a-1g**), (**2a-2g**), (**5**) and (**6**) energy. More specifically, the entire reaction coordinate for the (**3**)→(**7**) conversion is ~10 kJ/mol higher than that of the (**1**) → (**5**) and ~30 kJ/mol higher than the (**2**) → (**6**) conversions, which results in a significantly more reactive solvated product (**7**). Furthermore, attempts to record CV's of (**3d-3g**) were unsuccessful due to low levels of the accumulated intermediate under the

reaction conditions possibly due to an increased rate of dimerization relative to the rate of solvation. Lastly, these results find increased support in the following sections which focus on the reaction kinetics of (**3**).

Table 2.15: CV for the characterization of complexes (**3**), **(3a**,**3b** and **3c**) and (**7**)		
Compound	**Average $E_{1/2}$ (mV)**	**Average ΔG^o (kJ/mol)**
$Tp^{Me2}MoO_2OPh$ **(3)**	-1459.2 ± 6.7	123.0 ± 1.5
$Tp^{Me2}MoOOPh(OPR_3)$ **(3a-3c)**	-785.5 ± 40.1	77.2 ± 2.0
$Tp^{Me2}MoOOPh(NCMe)$ **(7)**	-459 ± 0.5	44.4 ± 0.1

Table 2.16: CV for the characterization of complexes **(3a-3c**)			
Intermediate	**$E_{1/2}$ (mV)**	**ΔG^o kJ/mol**	**T (^{o}C)**
$Tp^{Me2}MoOOPh(OPMe_3)$ **(3a)**	-788.4	76.1	23
$Tp^{Me2}MoOOPh(OPMe_2Ph)$ **(2b)**	-744.1	71.8	22
$Tp^{Me2}MoOOPh(OPEt_3)$ **(2c)**	-824	79.5	22.5

*Electrochemistry of $Tp^{Me2}MoO_2SPh$ **(4)**, $Tp^{Me2}MoO(SPh)(OPR_3)$ **(4a)** and $Tp^{Me2}MoO(SPh)(MeCN)$ complexes **(8)**.*

Cyclic voltammograms of **4**, **4a** and **8** were recorded for comparison to the previously discussed intermediate complexes, using the electrochemical methods described in the materials and methods section. The CV of the intermediate complex, **4a**, was recorded *in situ* as outlined in the materials and methods section, with the results tabulated in **Table 2.17**. In the case of these complexes, the values in **Table 2.17**, represent a single measurement and as such are a departure from the previously discussed intermediate complexes of (**1**), (**2**) and (**3**) which are average values of at least 3 measurements.

Table 2.17: CV for the characterization of complexes (**4**), (**4a**), (**4f**) and (**8**)		
Compound	**$E_{1/2}$ (mV)**	**ΔG^o (kJ/mol)**
$Tp^{Me2}MoO_2SPh$ **(4)**	-1166 ± 8.4	112.5 ± 0.8
$Tp^{Me2}MoOSPh(OPMe_3)$ **(4a)**	-527.8	50.9
$Tp^{Me2}MoOSPh(OPEt_2Ph)$ **(4g)**	-522.4	50.4
$Tp^{Me2}MoO(NCMe)SPh$ **(8)**	-149 ± 4.8	14.4 ± 0.5

Reaction kinetics of $Tp^RMoO_2(X)+PR_3$:

Solutions of yellow-orange $Tp^{iPr}Mo^{IV}O_2(OPh)$ (**1**), $Tp^{Me2}MoO_2(OPh)$ (**3**), brown $Tp^{Me2}MoO_2(SPh)$ (**4**), and suspensions of $Tp^{Me2}MoO_2Cl$ (**2**) react with the phosphines: PMe_3, PEt_3, PMe_2Ph, PEt_2Ph, P(*n*-Bu)$_3$, PPh_2Et and PPh_2Me to produce green to gold solutions containing the isolable oxo-Mo(IV)(phosphoryl) complexes $Tp^{iPr}Mo^{IV}O(OPh)(OPR_3)$ (**1a-g**), $Tp^{Me2}Mo^{IV}O(Cl)(OPR_3)$ (**2a-g**) and $Tp^{Me2}Mo^{IV}O(SPh)(OPR_3)$ (**4a**) and (**4d**) while $Tp^{Me2}Mo^{IV}O(OPh)(OPR_3)$ (**3a-g**) were not isolatable due their low stability; (a = $OPMe_3$, b = $OPEt_3$, c = $OPMe_2Ph$, d = $OPEt_2Ph$, e = OP(*n*-Bu)$_3$, f = $OPPh_2Et$ and g = $OPPh_2Me$).[23,24] The reactions of (**1**), (**3**) and (**4**) follow a second order rate law, dependent on both the complex and phosphine (**Figure 2.9**, step 1). All complexes exhibit two low energy d-d transitions, presumably $d_{xy} \rightarrow d_{xz}/d_{yz}$, that are absent in the starting Mo(VI) species. The lowest energy transition in is observed around 910 nm (ε 110 $M^{-1}cm^{-1}$) in the case of $Tp^{iPr}Mo^{IV}O(OPh)(OPEt_3)$ (**1b**) and $Tp^{Me2}Mo^{IV}O(OPh)(OPEt_3)$ (**3b**); and at 900 nm (ε 92 M^{-1} cm^{-1}) in $Tp^{iPr}Mo^{IV}O(OPh)(OPPh_2Me)$ (**1g**) and $Tp^{Me2}Mo^{IV}O(OPh)(OPPh_2Me)$ (**3g**). In complexes (**2a-g**) these transitions are shifted to ~ 800 to 820 nm (ε 60-90 M^{-1} cm^{-1}) with the second band appearing as a shoulder or buried beneath the first. In the case of (**4a**) and (**4b**), these bands are further shifted to ~762 ~780 nm respectively. However, the reaction kinetics of (**2**) → (**2a-2g**) were not possible under the reaction conditions

established for (**1**), (**3**) and (**4**) due to the extremely low solubility (solubility < 0.1mg/ml) of (**2**) in acetonitrile and as such were not performed.

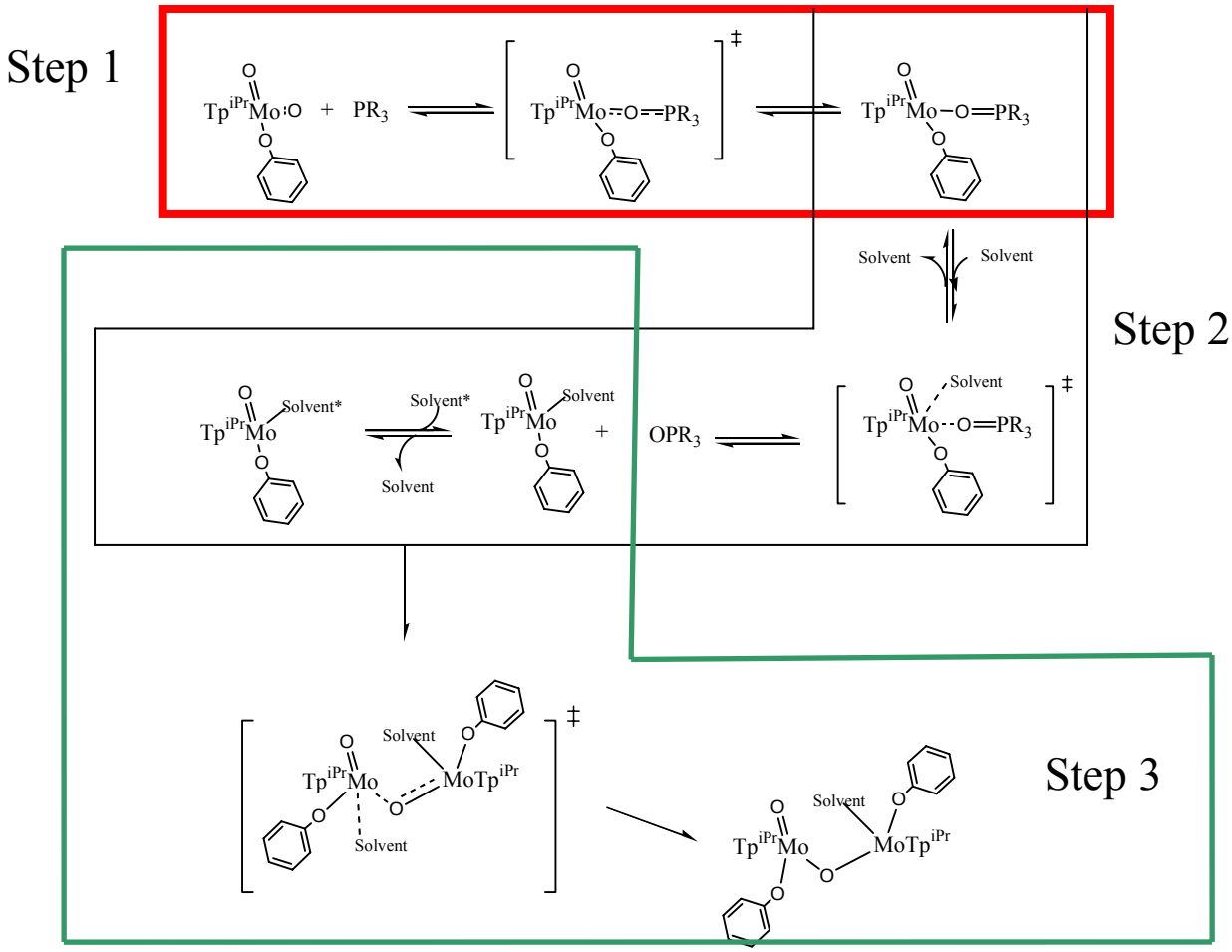

Figure 2.9: Full reaction scheme, presented for the reaction of (**1**) with phosphines to form (**1a-1g**) – **Step1**; followed by subsequent solvation to (**5**)- **Step 2**; and dimerization to (**9**) **Step 3**.

*Reaction kinetics of (**1**) to form (**1a-1f**):*

Reactions conducted under pseudo-first order conditions, at complex to substrate mole ratios higher than 59.7 and 90 for PEt_3 and PPh_2Me, respectively, proved to be too rapid for detection in the upper temperature ranges and as such were used as an upper limit. These boundary concentrations were further extended to the concentration ratios for the reactions of the remaining alkyl (PMe_3 and P(*n*-Bu_3)) and mixed alkyl-aryl (PMe_2Ph, PEt_2Ph and $PEtPh_2$) phosphines with (**1**). **Figure 2.10** shows the pseudo first-order rate constants as a function of the concentration of phosphine, resulting in the formation of (**1a-1g**), while the experimental data are tabulated in **Table 2.18a – Table 2.18g**.

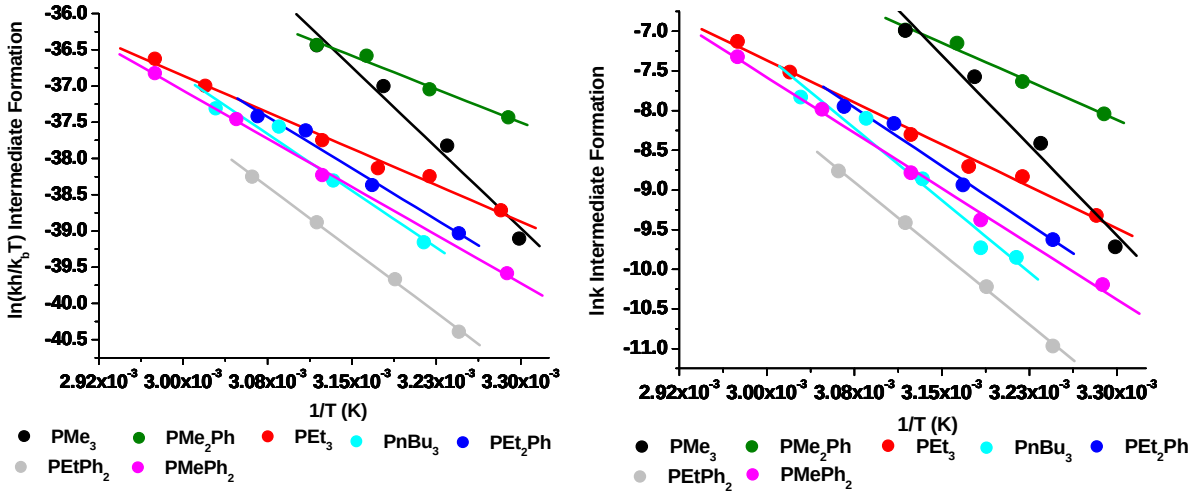

Figure 2.10: Reaction kinetics for the formation of (**1a-1g**) from the reaction of (**1**) with phosphines. **Left:** Eyring Plot and **Right**: Arrhenious Plot.

Table 2.18a. The rate constants for reaction of $Tp^{iPr}MoO_2(OPh)$ with substrate measured in MeCN.

$Tp^{iPr}MoO_2OPh + PMe_3$

temp C	temp K	temp 1/K	k $(M*sec)^{-1}$	kx$10^5$$(sec)^{-1}$	lnk	ln(kh/k_bT)
5	278.15	0.003595	0.0165	6.02	-9.72	-39.11
11	284.15	0.003519	0.0609	22.2	-8.41	-37.82
16.5	289.65	0.003452	0.141	51.4	-7.57	-37.00
22.5	295.65	0.003382	0.252	92.0	-6.99	-36.44
38	311.15	0.003214	0.651	237.1	-6.04	-35.54

lnA	Ea kJ/mol	$\Delta H^{\ddagger}$ kJ/mol	$\Delta S^{\ddagger}$ $(J*mol^{-1}*K^{-1})$	$\Delta G^{\ddagger}_{298}$ kJ/mol
24.07	77.05	74.60	-53.05	90.42

Table 2.18b. The rate constants for reaction of $Tp^{iPr}MoO_2(OPh)$ with substrate measured in MeCN.

$Tp^{iPr}MoO_2OPh + PPhMe_2$

temp C	temp K	temp 1/K	k $(M*sec)^{-1}$	kx$10^5$$(sec)^{-1}$	lnk	ln(kh/k_bT)
5.9	279.05	0.003584	0.0896	32.2	-8.04	-37.43
11.5	284.65	0.003513	0.197	70.7	-7.25	-36.67
12.5	285.65	0.003501	0.135	48.4	-7.63	-37.05
18	291.15	0.003435	0.218	78.5	-7.15	-36.58
22.5	295.65	0.003382	0.258	92.6	-6.99	-36.43

lnA	Ea kJ/mol	$\Delta H^{\ddagger}$ kJ/mol	$\Delta S^{\ddagger}$ $(J*mol^{-1}*K^{-1})$	$\Delta G^{\ddagger}_{298}$ kJ/mol
11.7	43.12	43.12	-156.72	89.84

Table 2.18c. The rate constants for reaction of $Tp^{iPr}MoO_2(OPh)$ with substrate measured in MeCN.

$Tp^{iPr}MoO_2OPh + PEt_3$

T (ºC)	T (K)	T (1/K)	k $(M*sec)^{-1}$	kx$10^5$$(sec)^{-1}$	lnk	ln(kh/k_bT)
6.5	279.65	0.003576	0.0254	8.64	-9.36	-38.75
12.5	285.65	0.003501	0.0415	13.7	-8.90	-38.31
17	290.15	0.003446	0.0472	19.8	-8.53	-37.96
22	295.15	0.003388	0.0704	23.9	-8.34	-37.80
33	306.15	0.003266	0.155	55.7	-7.49	-36.98
38	311.15	0.003214	0.229	82.2	-7.10	-36.60

lnA	Ea kJ/mol	$\Delta H^{\ddagger}$ kJ/mol	$\Delta S^{\ddagger}$ $(J*mol^{-1}*K^{-1})$	$\Delta G^{\ddagger}_{298}$ kJ/mol
12.5	50.85	48.39	-149.22	92.88

Table 2.18d. The rate constants for reaction of $Tp^{iPr}MoO_2(OPh)$ with substrate measured in MeCN.

$Tp^{iPr}MoO_2OPh$ + $PPhEt_2$

T (ºC)	T (K)	T (1/K)	k $(M*sec)^{-1}$	kx10^5 $(sec)^{-1}$	lnk	ln(kh/k_bT)
10	283.15	0.003532	0.0183	6.59	-9.63	-39.03
17.5	290.65	0.003441	0.0367	13.2	-8.94	-38.37
23.5	296.65	0.003371	0.0793	28.5	-8.16	-37.62
28	301.15	0.003321	0.0983	35.3	-7.95	-37.42

lnA	Ea kJ/mol	$\Delta H^{\ddagger}$ kJ/mol	$\Delta S^{\ddagger}$ $(J*mol^{-1}*K^{-1})$	$\Delta G^{\ddagger}_{298}$ kJ/mol
19.7	69.18	66.75	-88.8	93.23

Table 2.18e. The rate constants for reaction of $Tp^{iPr}MoO_2(OPh)$ with substrate measured in MeCN.

$Tp^{iPr}MoO_2OPh$ + $P(n\text{-}Bu)_3$

T (ºC)	T (K)	T (1/K)	k $(M*sec)^{-1}$	kx10^5 $(sec)^{-1}$	lnk	ln(kh/k_bT)
13	286.15	0.003495	0.0148	5.27	-9.85	-39.27
16	289.15	0.003458	0.0166	5.94	-9.73	-39.18
21	294.15	0.0034	0.0397	14.2	-8.86	-38.30
26	299.15	0.003343	0.0850	30.4	-8.10	-37.56
32	305.15	0.003277	0.1114	39.8	-7.83	-37.31

lnA	Ea kJ/mol	$\Delta H^{\ddagger}$ kJ/mol	$\Delta S^{\ddagger}$ $(J*mol^{-1}*K^{-1})$	$\Delta G^{\ddagger}_{298}$ kJ/mol
26.09	85.64	83.19	-36.2	93.98

Table 2.18f. The rate constants for reaction of $Tp^{iPr}MoO_2(OPh)$ with substrate measured in MeCN.

$Tp^{iPr}MoO_2OPh$ + $PMePh_2$

T (ºC)	T (K)	T (1/K)	k $(M*sec)^{-1}$	kx10^5 $(sec)^{-1}$	lnk	ln(kh/k_bT)
12	285.15	0.003507	0.0116	3.97	-10.13	-39.55
16	289.15	0.003458	0.0171	5.83	-9.75	-39.18
21	294.15	0.0034	0.0257	8.76	-9.34	-38.79
27	300.15	0.003332	0.0575	19.59	-8.54	-38.00
38	311.15	0.003214	0.156	54.89	-7.51	-37.01

lnA	Ea kJ/mol	$\Delta H^{\ddagger}$ kJ/mol	$\Delta S^{\ddagger}$ $(J*mol^{-1}*K^{-1})$	$\Delta G^{\ddagger}_{298}$ kJ/mol
21.78	75.79	73.31	-72.17	94.83

Table 2.18g. The rate constants for reaction of $Tp^{iPr}MoO_2(OPh)$ with substrate measured in MeCN.						
$Tp^{iPr}MoO_2OPh + PEtPh_2$						
T (ºC)	T (K)	T (1/K)	k $(M*sec)^{-1}$	$kx10^5(sec)^{-1}$	lnk	$ln(kh/k_bT)$
15.5	288.65	0.003464	0.0048	1.73	-10.97	-40.39
22.5	295.65	0.003382	0.0102	3.65	-10.22	-39.67
28.5	301.65	0.003315	0.0219	8.18	-9.41	-38.88
35	308.15	0.003245	0.0420	15.66	-8.76	-38.25
lnA	Ea kJ/mol	$\Delta H^{\ddagger}$ kJ/mol	$\Delta S^{\ddagger}$ $(J*mol^{-1}*K^{-1})$	$\Delta G^{\ddagger}_{298}$ kJ/mol		
24.41	84.96	82.48	-50.26	97.46		

*Reactions of kinetics (**3**) to form (**3a-3f**):*

The reactions of (**3**) with various phosphines were performed similarly to the reactions of (**1**), with one notable exception. In general, the reaction of (**3**) was complicated by the formation of dimeric products (formation reaction of **3b-3g**) at temperatures greater than 30°C, while the formation of (**3a**) which was facile below 40°C. These observations are supported by the previously discussed electrochemical measurements, which suggest that intermediates can be arranged in order of increasing stability as follows: (**3a-3g**) < (**1a-1g**) < (**4a-4g**) < (**2a-2g**).Thus the temperature range for the reactions of (**3**) with phosphines was generally limited to 27°C to 30°C at the maximum. However, in all cases, the phosphine concentrations for the reactions of (**3**) were similar to those of (**1**), with the upper limit of the alkyl phosphines represented by PMe_3 (~52x excess) and the upper limit of the mixed alky-aryl phosphines represented by $PMePh_2$ (~84x excess). The data for these reactions are tabulated in **Table 2.19a- Table 2.19g** and graphically presented in **Figure 2.11.**

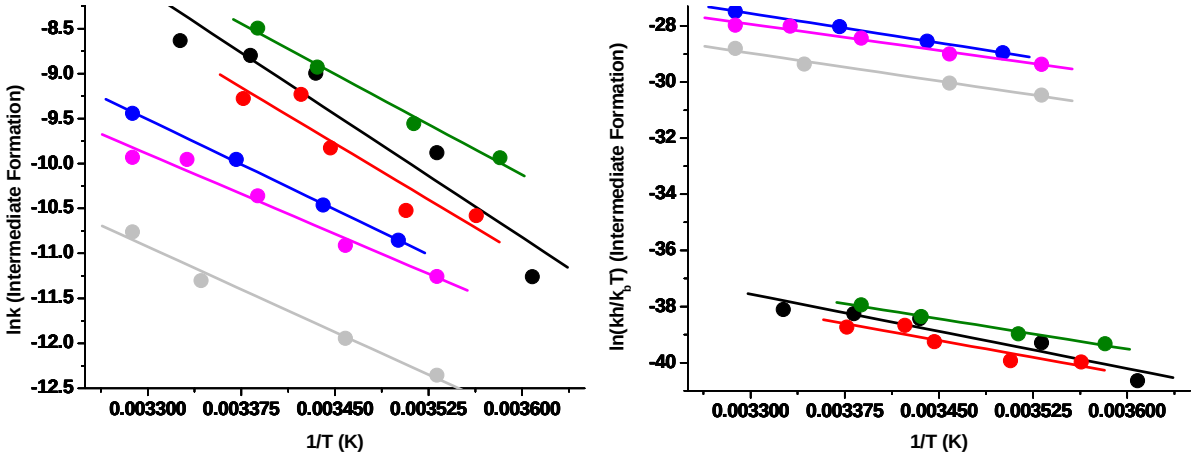

Figure 2.11: Reaction kinetics for the formation of (**3a-3g**) from the reaction of (**3**) with phosphines. **Left:** Arrhenious Plot; and **Right**: Eyring Plot.

Table 2.19a: $Tp^{Me2}MoO_2OPh + PMe_3$

temp (ºC)	temp (K)	temp (1/K)	k $(M*sec)^{-1}$	k x $10^5(sec)^{-1}$	lnk	$ln(kh/k_bT)$
4	277.15	0.003608	0.0039	1.3	-11.26	-40.64
10	283.15	0.003532	0.0151	5.1	-9.88	-39.29
18	291.15	0.003435	0.0342	12.4	-9.00	-38.43
22.5	295.65	0.003382	0.0418	15.1	-8.80	-38.25
27.5	300.65	0.003326	0.0386	17.8	-8.63	-38.10

lnA	Ea kJ/mol	$\Delta H^{‡}$ kJ/mol	$\Delta S^{‡}$ $(J*mol^{-1}*K^{-1})$	$\Delta G^{‡}_{298}$ kJ/mol
22.23	76.37	73.97	-68.13	94.27

Table 2.19b: $Tp^{Me2}MoO_2OPh + PEt_3$

temp (ºC)	temp (K)	temp (1/K)	k $(M*sec)^{-1}$	k x $10^5(sec)^{-1}$	lnk	$ln(kh/k_bT)$
7.5	280.65	0.003563	0.00747	2.5	-10.58	-39.98
12	285.15	0.003507	0.00793	2.7	-10.52	-39.93
17	290.15	0.003446	0.01588	5.4	-9.83	-39.26
19	292.15	0.003423	0.02879	9.8	-9.23	-38.67
23	296.15	0.003377	0.02746	9.3	-9.28	-38.73

lnA	Ea kJ/mol	$\Delta H^{‡}$ kJ/mol	$\Delta S^{‡}$ $(J*mol^{-1}*K^{-1})$	$\Delta G^{‡}_{298}$ kJ/mol
18.9	69.15	66.75	-95.69	95.28

Table 2.19c: $Tp^{Me2}MoO_2OPh + PPhEt_2$

temp (ºC)	temp (K)	temp (1/K)	k $(M*sec)^{-1}$	k x $10^5(sec)^{-1}$	lnk	ln(kh/k_bT)
12.5	285.65	0.003501	0.00583	1.9	-10.85	-28.96
17.5	290.65	0.003441	0.00863	2.9	-10.46	-28.55
23.5	296.65	0.003371	0.01517	4.8	-9.95	-28.02
31	304.15	0.003288	0.030501	7.9	-9.44	-27.48

lnA	Ea kJ/mol	$\Delta H^{\ddagger}$ kJ/mol	$\Delta S^{\ddagger}$ $(J*mol^{-1}*K^{-1})$	$\Delta G^{\ddagger}_{298}$ kJ/mol
12.6	55.60	58.05	-37.51	69.23

Table 2.19d: $Tp^{Me2}MoO_2OPh + PPhMe_2$

temp (ºC)	temp (K)	temp (1/K)	k $(M*sec)^{-1}$	k x $10^5(sec)^{-1}$	lnk	ln(kh/k_bT)
6	279.15	0.003582	0.01448	4.8	-9.94	-39.33
11.5	284.65	0.003513	0.02120	7.1	-9.56	-38.97
17.9	291.05	0.003436	0.03969	13.3	-8.93	-38.36
22	295.15	0.003388	0.06524	20.5	-8.49	-37.94

lnA	Ea kJ/mol	$\Delta H^{\ddagger}$ kJ/mol	$\Delta S^{\ddagger}$ $(J*mol^{-1}*K^{-1})$	$\Delta G^{\ddagger}_{298}$ kJ/mol
16.75	62.08	59.69	-113.61	93.57

Table 2.19e: $Tp^{Me2}MoO_2OPh + PMePh_2$

temp (ºC)	temp (K)	temp (1/K)	k $(M*sec)^{-1}$	k x $10^5(sec)^{-1}$	lnk	ln(kh/k_bT)
10	283.15	0.003532	0.0039	1.29	-11.26	-29.37
16	289.15	0.003458	0.0055	1.82	-10.91	-29.01
22	295.15	0.003388	0.0101	3.17	-10.36	-28.43
27	300.15	0.003332	0.0143	4.75	-9.96	-28.01
31	304.15	0.003288	0.0147	4.86	-9.93	-27.97

lnA	Ea kJ/mol	$\Delta H^{\ddagger}$ kJ/mol	$\Delta S^{\ddagger}$ $(J*mol^{-1}*K^{-1})$	$\Delta G^{\ddagger}_{298}$ kJ/mol
9.67	49.30	51.74	-61.54	70.09

Table 2.19f: $Tp^{Me2}MoO_2OPh + PEtPh_2$						
temp (ºC)	temp (K)	temp (1/K)	k $(M*sec)^{-1}$	k x $10^5(sec)^{-1}$	lnk	ln(kh/k_bT)
10	283.15	0.003532	0.0013	0.43	-12.35	-30.47
16	289.15	0.003458	0.00193	0.65	-11.94	-30.04
26	299.15	0.003343	0.00364	1.24	-11.30	-29.36
31	304.15	0.003288	0.0064	2.12	-10.76	-28.80
lnA	Ea kJ/mol	$\Delta H^{\ddagger}$ kJ/mol	$\Delta S^{\ddagger}$ $(J*mol^{-1}*K^{-1})$	$\Delta G^{\ddagger}_{298}$ kJ/mol		
9.95	52.59	55.04	-59.23	72.69		

When the kinetic measurements are combined with the results from the CV of (**3**), a reaction coordinate may be approximated, similar to the case of (**1**) and (**2**), as shown in **Table 2.20**. Here, the barrier to intermediate formation is generally quite high (~15 kJ/mol) when compared to the same reactions of (**1**), and may result from slight changes in the electronic structure of molybdenum that arise from different electron donor properties of methyl groups verses a single isopropyl group.

Table 2.20: Approximate Reaction Coordinate for the First Step in the Reaction: Reduction of (**3**) with Phosphines to Yield Compounds (**3a, 3b** and **3c**)

Compound	**ΔG^o (kJ/mol)[a]**	**$\Delta G^{\ddagger}$ (kJ/mol)[b]**	**$\Delta G'^o$ (kJ/mol)[c]**	**$\Delta G'^{\ddagger}$ (kJ/mol)[d]**
$Tp^{Me2}MoO_2OPh$ **(3)**	123.0 ± 1.5	NA	0	NA
$Tp^{Me2}MoO(OPh)(OPMe_3)$ **(3a)**	76.1	94.3	-46.9	94.3
$Tp^{Me2}MoO(OPh)(OPMe_2Ph)$ **(3b)**	71.8	93.6	-51.2	93.6
$Tp^{Me2}MoO(OPh)(OPEt_3)$ **(3c)**	79.5	94.7	-43.5	94.7

a) ΔG^o approximated from CV measurements at 298 K; b) $\Delta G^{\ddagger}$ taken from kinetics measurements at 298 K;
c) $\Delta G'^o$ represents the relative energy expressed as [ΔG^o(**3-3c**)- ΔG^o(**3**)];
d) $\Delta G'^{\ddagger}$ relative energy expressed as [$\Delta G^{\ddagger}$ (**3a-3c**) + $\Delta G'^o$(**3**)].

*Reactions kinetics of (**4**) to form (**4a** and **4f**):*

The reactions of (**4**) with PMe_3 to yield (**4a)** and $PEtPh_2$ to yield (**4g)** were conducted similar to the reactions of (**1**) and (**3**) in attempt to access the effects of substituting a sulfur ligand for and

oxygen containing ligand upon rates of OAT. However, the greater stability of **4a** and **4g** relative to the corresponding complexes of (**1**) and (**3**) allowed for facile experiments to approximately 40° C for PMe_3 and 32° C for $PEtPh_2$ at 762nm and 778nm respectively (**Table 2.21a**, **Table 2.21b,** and **Table 2.21c**) and **(Figure 2.12).**

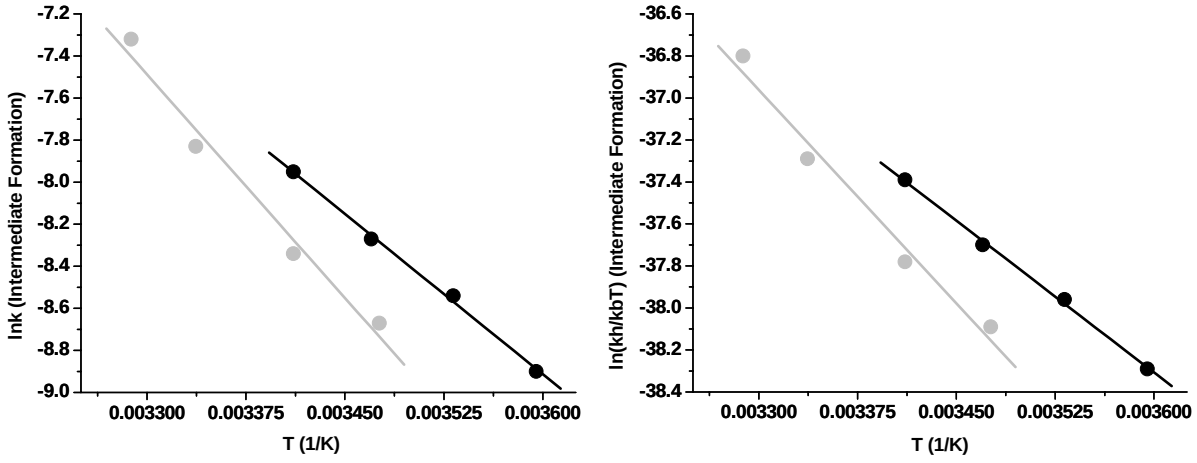

Figure 2.12: Reaction kinetics for the formation of (**4a** and **4g**) from the reaction of (**4**) with phosphines. **Left:** Arrhenious Plot and **Right:** Eyring Plot.

Table 2.21a: ($Tp^{Me2}MoO_2SPh + PMe_3$)[a]						
temp C	temp K	temp 1/K	k $(M*sec)^{-1}$	$kx10^5(sec)^{-1}$	lnk	$ln(kh/k_bT)$
10.5	283.65	0.003525	0.0744	23.5	-8.36	-37.76
20	293.15	0.003411	0.3855	122.0	-6.71	-36.15
40	313.15	0.003193	0.4824	152.0	-6.49	-35.99
lnA	Ea kJ/mol	$\Delta H^{\ddagger}$ kJ/mol	$\Delta S^{\ddagger}$ $(J*mol^{-1}*K^{-1})$	$\Delta G^{\ddagger}_{298}$ kJ/mol		
9.8	41.72	39.25	-173.0	90.55		
a) This work, recorded at 726nm in acetonitrile						

Table 2.21b: ($Tp^{Me2}MoO_2SPh + PMe_3$)[a]						
temp C	temp K	temp 1/K	k $(M*sec)^{-1}$	$kx10^5(sec)^{-1}$	lnk	$ln(kh/k_bT)$
5	278.15	0.003595	0.713	13.6	-8.90	-38.29
10	283.15	0.003532	1.0182	19.5	-8.54	-37.96
15	288.15	0.00347	1.3339	25.6	-8.27	-37.70
20	293.15	0.003411	1.8299	35.1	-7.95	-37.39
lnA	Ea kJ/mol	$\Delta H^{\ddagger}$ kJ/mol	$\Delta S^{\ddagger}$ $(J*mol^{-1}*K^{-1})$	$\Delta G^{\ddagger}_{298}$ kJ/mol		
9.4	42.25	40.1	-174.2	92.02		
a) taken from reference 50, recorded at 393 nm in acetonitrile						

Table 2.21c: $Tp^{Me2}MoO_2SPh + PEtPh_2$						
temp C	temp K	temp 1/K	k $(M*sec)^{-1}$	$kx10^5(sec)^{-1}$	lnk	$ln(kh/k_bT)$
14.5	287.65	0.003476	0.0545	17.2	-8.67	-38.09
20	293.15	0.003411	0.0752	23.8	-8.34	-37.78
26.5	299.65	0.003337	0.126	39.9	-7.83	-37.29
31	304.15	0.003288	0.210	66.3	-7.32	-36.80
lnA	Ea kJ/mol	$\Delta H^{\ddagger}$ kJ/mol	$\Delta S^{\ddagger}$ $(J*mol^{-1}*K^{-1})$	$\Delta G^{\ddagger}_{298}$ kJ/mol		
15.9	58.93	56.31	-121.76	92.53		

phosphines; the second-order rate constants at different temperatures are listed in **Table 2.21a, Table 2.21b** and **Table 2.21c** along with the activation parameters. When this data is added to the data obtained from the CV, a reaction coordinate for the formation of the intermediates (**4a**) and (**4f**) can be approximated as shown in **Table 2.22**, **Figure 2.13** and (**step 1**) of **Figure 2.9**.

Loss of OPR_3 from $Tp^{iPr}MoO(OPh)(OPR_3)$, $Tp^{Me2}MoO(Cl)(OPR_3)$, $Tp^{Me2}MoO(OPh)(OPR_3)$ and $Tp^{Me2}MoO(SPh)(OPR_3)$:

When solutions of (**1a-1g**), (**2a-2g**), (**3a-3f**) or (**4a** or **4f**) are prepared in acetonitrile from the isolated compound or via *in situ* reaction, the green to gold colored intermediate changes to either a pale blue or a brown, depending upon the starting complex and conditions. For example the

decay of complexes of the type $Tp^{Me2}MoOOPh(OPR_3)$ could not be cleanly observed as they generally proceed from green to brown without observation of the blue species.

Table 2.22: Approximate Reaction Coordinate for the First Step in the Reaction: Reduction of (**4**) with Phosphines to Yield Compounds (**4a** and **4g**)

Compound	**ΔG^o (kJ/mol)[a]**	**$\Delta G^{\ddagger}$ (kJ/mol)[b]**	**$\Delta G'^o$ (kJ/mol)[c]**	**$\Delta G'^{\ddagger}$ (kJ/mol)[d]**
$Tp^{Me2}MoO_2SPh$ **(4)**	112.5 ± 0.8	NA	0	NA
$Tp^{Me2}MoO(SPh)(OPMe_3)$ **(4a)**	50.9	92.0	-61.6	92.0
$Tp^{Me2}MoO(SPh)(OPEtPh_2)$ **(4g)**	50.4	92.7	-62.1	92.7

a) ΔG^o approximated from CV measurements at 298 K; b) $\Delta G^{\ddagger}$ taken from kinetics measurements at 298 K;
c) $\Delta G'^o$ represents the relative energy expressed as [ΔG^o(**4**-**4g**)- ΔG^o(**4**)];
d) $\Delta G'^{\ddagger}$ relative energy expressed as [$\Delta G^{\ddagger}$ (**4a**-**4g**) + $\Delta G'^o$(**4**)].

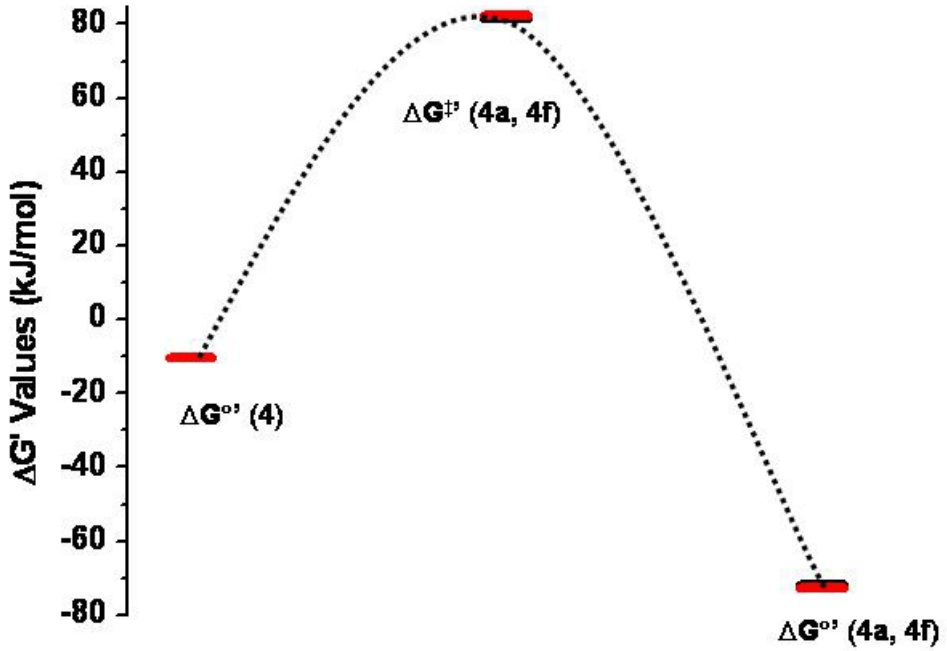

Figure 2.13: Reaction Coordinate for the formation of (**4a** and **4g**) from the reaction of (**4**) with phosphines.

This is highlighted by the reaction of PMe_3 with (**3**) which results in the visual observation of the persistence of the green intermediate (**3a**) for greater than 1000 minutes at room temperature in acetonitrile, but transforms to the brown complex without the formation of a detectable blue species. However, the decay of (**3a-3f**) and (**4a** and **4f**) follow the progression from green to blue in acetonitrile without the observation of the brown complex.

Moreover, when single wavelength assays, centered upon the principle d→d band of the intermediate complex (**1c**) were conducted, the resultant curve could be fit with either one or two exponential functions. Furthermore this behavior was mirrored in the LMCT region of the intermediate complex spectra. To this end, the following sections provide a detailed look into the processes and species present in the decay reactions of these atom transfer intermediates as well as the reaction kinetics of all observable steps involved.

Identification of the Observable Species:

In attempt to identify the predominant species that are present in the intermediate decay, SVD analysis was first employed on the isolated intermediate complex (**1c**) at relatively low temperature to slow the process. Thus the SVD analyses of the multiwavelength scans for the decomposition of isolated $Tp^{iPr}Mo^{IV}O(OPh)(OPR_3)$ (**1c**), collected in the high and low energy region of the spectrum, were conducted in three phases. First, the difference spectral (absorption) matrix in the low-energy region was constructed and deconvoluted as $A_t—A_0$ where A_t represents the absorption at a time t and A_0 is the initial absorbance. The data collected at higher energy were processed similarly in the second phase while the third phase was comprised of a combined high and low difference spectral matrix, following the same methodology. To this end, the decomposition of $Tp^{iPr}Mo^{IV}O(OPh)(OPEt_3)$ in acetonitrile at 11°C, **Figure 2.9** step 2 and step 3,

indicates that the reaction involves three observable species (**A**, **B** and **C**), with an initial, comparatively rapid, increase in **B** followed by a slower decay to **C**. Visually, this reaction proceeds from emerald green (**A**) to pale blue (**B**) and then to brown (**C**). Here, species (**A**) was could be immediately identified as the starting intermediate complex (**1c**), while the identity of species (**B**) and species (**C**) were in question. From the SVD analysis of the data matrix, the temporal eigenvectors were first fit to a sum of three exponentials with $-d[\mathbf{1c}]/dt = 0.0204\ min^{-1}$, $d[\mathbf{B}]/dt = 0.015\ min^{-1}$, $d[\mathbf{C}]/dt = 0.00327\ min^{-1}$, and clearly indicated the presence of two processes.

The decomposition of $Tp^{iPr}Mo^{IV}O(OPh)(OPEt_3)$ was further probed by NMR spectroscopy in benzene and in acetonitrile. ^{31}P NMR spectroscopy was found to be informative as coordinated and free phosphine oxides resonate at different positions: ~78 ppm for coordinated $OPEt_3$ and 48 ppm for free $OPEt_3$. The ^{31}P NMR spectra in C_6D_6 show complete release of the coordinated phosphine oxide within 144 h. As previously noted, the decomposition follows a color change that proceeds directly from green to brown with no observation of the blue colored species. In analogy with the hydrotris(3,5-dimethylpyrazol-1-yl)borate ligand system, this brown compound has been assigned as a dinuclear species, ($Tp^{iPr}MoO(OPh)OMo(OPh)(MeCN)Tp^{iPr}$), where one of the molybdenum centers remained coordinated by a phosphine oxide.[51]

In attempt to identify the blue species, temperature dependent NMR spectra were acquired at –40° C in CD_3CN. Interestingly, spectra become increasingly complex during the initial stage of the reaction, and then simplify. Furthermore, the initial spectrum, which has been reported previously, is substantially different from the subsequent spectra. For example the methylene protons (δ 1.69) and the methyl protons (δ 0.78) of the bound $OPEt_3$ decrease in intensity with time while the same resonances for free $OPEt_3$ increase in intensity at δ 1.06 and 0.42, respectively. In addition, the coordinated acetonitrile resonance at δ 2.99 grows as a function of time, while that of free

acetonitrile (δ 1.96) eventually broadens. This time-dependent broadening suggests that, acetonitrile coordinates to the Mo center; but exchanges rapidly with the bulk solvent. This was further tested by spiking the blue CD_3CN solution with CH_3CN, which resulted in a significant increase in the intensity of the signal at δ 2.99. Lastly, the isopropyl methyl protons of Tp^{iPr} that are positioned *trans* to the equatorial OPR_3 group, are a sensitive indicator to changes in the metal coordination (similar to the pyrazol- methine protons of (**2a-2g)** shown in **Figure 2.6**). The methyl resonance at ca -0.5 decrease in intensity with time as the nitrile complex form (product resonances obscured). When considered together with the kinetic parameters, the data indicate that the phosphine oxide dissociation is the first step of the decomposition, as depicted in **Figure 2.9**, step 2. The rate of the phosphine oxide dissociation was calculated from the integrated intensity of both the free and the coordinated $OPEt_3$ resonances (**Figure 2.14**).

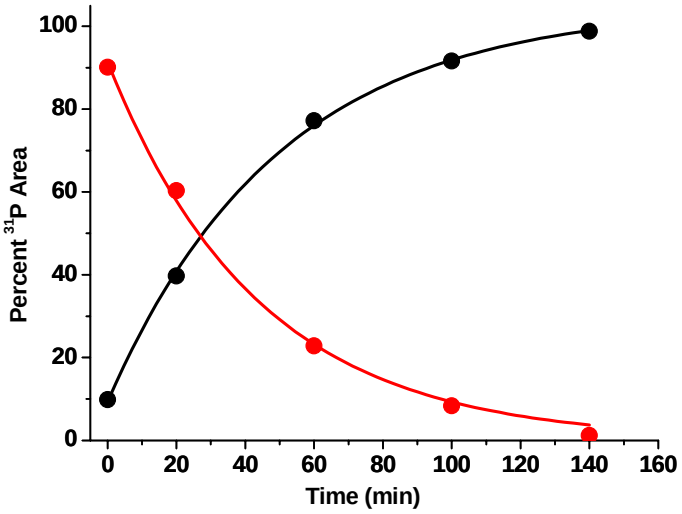

Figure 2.14: ^{31}P NMR Data for the solvation of (**1c**) to (**5**), collected at low temperature after incubation at 11° C . **Red Circles**: Percent peak area of (**1c**). **Black Circles:** Percent peak area of $OPEt_3$

At 11°C, the increase in free $OPEt_3$ follows a single exponential process with a half-life of ~50 minutes in MeCN, which is in good agreement with the SVD predicted temporal changes associated with the (**1c)** to (**5)** conversion, as well as the single-wavelength measurements presented in detail in the following section. Thus, ^{31}P NMR spectra provide direct evidence for the loss of phosphine oxide during the first step in the decomposition of $Tp^{iPr}Mo^{IV}O(OPh)(OPEt_3)$, while the ^{1}H spectra provide evidence for MeCN coordination and its exchange with the bulk solvent. Considering all the evidence, the NMR spectra strongly indicate that the second blue species is $Tp^{iPr}Mo^{IV}O(OPh)(MeCN)$. Furthermore, when the decay of $Tp^{Me2}MoOCl(OPMe_3)$ was observed by ^{1}H NMR in CD_3CN, a concerted growth of a coordinated acetonitrile peak ~3ppm and a growth of a peak attributed to free phosphine-oxide ~32 ppm was observed and further confirmed the identity of the blue species as $Tp^{R'}MoO(X)(MeCN)$.

In CH_3CN, the third and final brown component does not exhibit any ^{1}H NMR resonance attributable to the coordinated $OPEt_3$, however, resonances due to the Tp^{iPr} ligand, the phenolate group and free phosphine oxide could be observed. At low cone voltages (5-20 V) the electrospray ionization mass spectra (ESIMS) of this brown solution, showed several weak peaks attributable to dinuclear complexes and at higher cone voltage the weak peaks do not persist. Such voltage dependent ESIMS provides a vehicle for understanding the decomposition reaction under mass spectrometric conditions.[52] The strong peaks in the mass spectra could be assigned to monomeric complexes originated from the loss of phenolate group. This pattern suggests that the dinuclear complexes are unstable under mass spectrometric condition and the coordinated phenolate group is lost. Interestingly, no such behavior was observed for the monomeric (**1c)** or (**5)** under similar mass spectrometric conditions. Although the brown dinuclear compound has not yet been crystallized, a related compound from the hydrotris(3,5-dimethylpyrazol-1-yl)borate ligand has been structurally

characterized. We conclude that the brown complex, resultant from reactions involving the Tp^{iPr} ligand, is a dinuclear complex.

Thus, the absorbance changes at 301 nm and 910 nm were assigned to the solvation of (**1c)** to (**5),** based upon the spectral shape of the reconstructed species that fit well to a single exponential. The $d_{xy} \rightarrow d_{xz/yz}$ transitions at 910 nm mirror the changes that occur in the pπ to dπ charge transfer transitions at 301 nm, and as such validate the SVD based assignment for the species (**1c)** to (**5)** conversion in both regions of the spectrum. On the other hand, the absorbance changes at 680 nm were fit to a two exponential function, as expected from the SVD analysis. The first of the two processes corresponds to the conversion of (**1c)** to (**5)** and the second one was assigned to the conversion of **(5)** to (**9)**. Because the concentrations used in the single wavelength measurements at 301, 680 and 910 nm differ nearly by an order of magnitude, there appears to be no concentration dependence on this reaction rate. Although the observed trends at 680 nm were found to be in good agreement with the SVD, the d[**C**]/dt value did not match exactly with the single-wavelength measurements due to a shorter collection time in the case of SVD. More specifically a $t_{1/2}$ of ~ 212 minutes was observed in the single wavelength measurements, conducted over a 1000-1400 min collection time, while the SVD data were collected for 200 minutes. Thus the SVD decay data was monitored for approximately one to two half-lives and as such provided a poor estimation of the true temporal eigenvector for the later stage of the reaction. Although this truncation leads to a larger error in the temporal eigenvectors associated with the conversion of **(5)** to (**C)**, there was little impact on the temporal vectors for the (**1b)** to **(5)** conversion.

Taken together, the rates of the **(1b)** to **(5)** and **(5)** to (**C)** conversions and the known concentrations of the starting material were used to establish a concentration profile. Once a concentration profile was established, the data were used to reconstruct the observed spectrum with

the residuals calculated by subtracting $A_{obs}(t) - A_{calc}(t)$. **Figure 2.3** demonstrates the goodness of fit obtained when using an irreversible [**1b**]→[**5**]→[**C**] reaction model. Inclusion of one or more reversible steps did not improve the fit appreciably and therefore only the minimal scheme was used. A detailed mechanistic investigation into these processes can be found in the following sections.

Mechanistic Considerations in the Loss of Phosphine Oxide:

Based upon the SVD analysis and the NMR experiments conducted on (**1c**), the first step is the loss of the phosphine oxide coupled to solvation, when conducted in coordinating solvents, and the second step is the formation of a dinuclear compound. Not surprisingly, the loss of phosphine oxide occurs concurrently with the dinucleation reaction when observed in non-coordinating solvents. However, the mechanistic details with regard to how and why the intermediate complex decays remained unclear as two possible limiting pathways are viable. The first pathway is via a dissociative mechanism (d-type mechanism) which is analogous to an organic SN_1-type mechanism involving a transition state or intermediate whose coordination number (C.N.) is formally reduced by one. Thus in the decay of (**1c**), this would be indicated by the detection of either a penta-coordinated intermediate or a transition state that expresses a large positive entropy of activation. In contrast, the second possible pathway is an associative mechanism (a-type mechanism) which is analogous to an organic SN_2-type mechanism involving a transition state or intermediate whose coordination number (C.N.) is formally increased by one. Here the decay of (**1c**) would show evidence of either a detectable hepta-coordinted intermediate or a transition state defined by a large negative entropy of activation. As eluded in the previous discussion the d and a-type mechanistic distinction represents the two extreme cases of reactivity, however, intermediate type reaction

mechanisms (Ia and Id-type mechanisms) are quite common. Thus in the Ia and Id-type mechanisms, true identification of the nature of the transition state becomes more complex as both mechanisms involve the simultaneous varying degrees of bond making and bond breaking. In attempt to address the mechanism of the loss of phosphine oxide, the complexes of (**1**), (**2**) and (**4**) were examined under variable temperature. In addition, the decay of (**1c**) and (**1g**), as well as (**2a**) were examined in different solvents in attempt to fully assess the mechanism of reaction.

Kinetics of Loss of OPR_3 from $Tp^{iPr}MoO(OPh)(OPR_3)$:

The solvation reaction of (**1a – 1b)** was performed as outlined in the materials and methods section of this paper. Complexes (**1c** and **1g**) were first examined by starting with the isolated complex, and later initiated from the *in situ* reaction of (**1**) with the appropriate phosphine. Furthermore, reactions with these complexes were acquired at the appropriate SVD determined wavelengths and included monitoring the reaction in the LMCT region (~301nm) as well as the d-d region (~910nm and 680nm). All other complexes (**1a-1b** and **1d-1f**) were investigated through the *in situ* reaction of (**1**) with the appropriate phosphine, and monitored at the 900nm d-d band.

Table 2.23 contains the principle d-d transitions assigned to complex (**5**) and a representative absorption spectrum.

Table 2.23: visible spectra of complex (**5**) $Tp^{iPr}MoO(OPh)(NCMe)$		
$d_{xy} \rightarrow d_{xz} / d_{yz}$ (cm^{-1})	**$d_{xy} \rightarrow d_{xz} / d_{yz}$ (cm^{-1})**	**$d_{xy} \rightarrow d_{x2-y2}$ (cm^{-1})**
11092	14749	26596

Tables 2.24a through **Table 2.24g** and **Figure 2.15** provides a comprehensive list of all of the observed rate constants for $Tp^{iPr}Mo^{IV}O(OPh)(OPEt_3)$ and $Tp^{iPr}Mo^{IV}O(OPh)(OPPh_2Me)$, including NMR and SVD data, as well as the optical data for the remaining

$Tp^{iPr}Mo^{IV}O(OPh)(OPR_3)$ complexes. **Table 2.25** lists the rate constants for $Tp^{iPr}Mo^{IV}O(OPh)(OPEt_3)$ and $Tp^{iPr}Mo^{IV}O(OPh)(OPPh_2Me)$ systems.

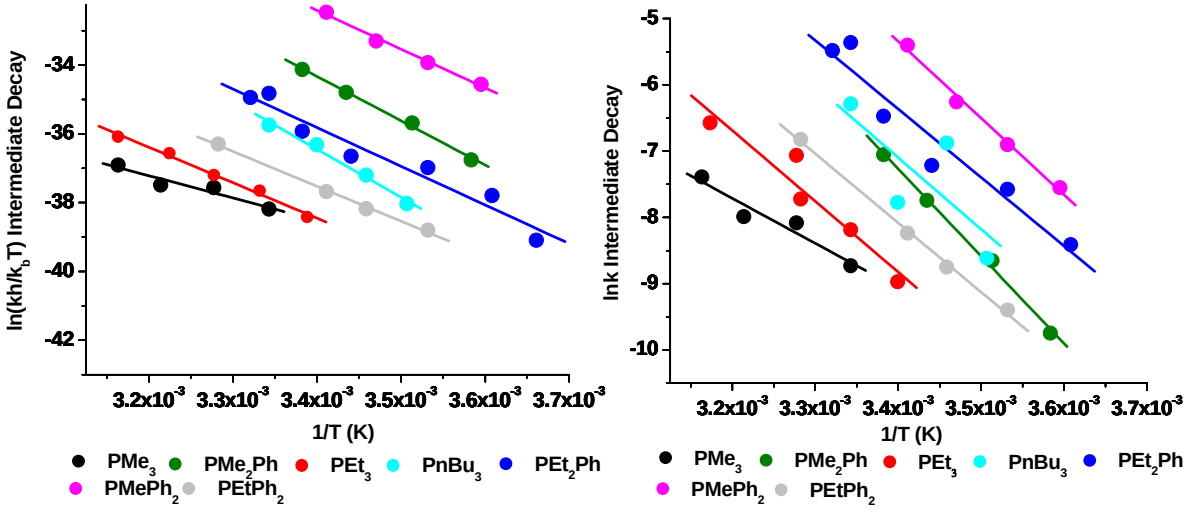

Figure 2.15: Reaction kinetics for the solvation of (**1a-1g**) to form (**5**). **Left:** Eyring Plot and **Right**: Arrhenious Plot.

Table 2.25. Rate constants for the loss of phosphines oxide to form the solvated complex.			
Compound		**Temp, °C**	**Rate constants (min^{-1})**
$Tp^{iPr}MoO(OPh)(OPEt_3)$	Measured at 301 nm	5	6.07×10^{-3} [c]
		11	$1.45 (\pm 0.01) \times 10^{-2}$
		16	$2.39 (\pm 0.08) \times 10^{-2}$
		22	$6.47 (\pm 0.18) \times 10^{-2}$
	Measured at 910 nm	11	$1.38 (\pm 0.01) \times 10^{-2}$
		16	$2.39 (\pm 0.08) \times 10^{-2}$
		22	$6.30 (\pm 0.18) \times 10^{-2}$
		22	6.30×10^{-2}, [a,c]
	Measured at 680 nm	22	$7.07 (\pm 0.18) \times 10^{-2}$
		27	14.14×10^{-2}
		32	22.35×10^{-2}
		37	43.31×10^{-2}
		42	77.00×10^{-2}
		26	9.80×10^{-2}, [b]
	^{31}P NMR	11	1.40×10^{-2}
	SVD	11	1.50×10^{-2}
$Tp^{iPr}MoO(OPh)(OPPh_2Me)$	Measured at 900 nm	5	$4.500 (\pm 0.002) \times 10^{-2}$
		10	$8.700 (\pm 0.001) \times 10^{-2}$
		15	$16.6 (\pm 0.65) \times 10^{-2}$
		20	$39.1 (\pm 0.15) \times 10^{-2}$
	SVD	15	18.1×10^{-2}
[a]In THF. [b]In the presence of added water (10 mM). The errors reported here are determined from a minimum of three measurements. [c]Represents a single measurement			

Table 2.24a: $Tp^{iPr}MoO(OPh)(OPMe_3)$ + MeCN					
T (°C)	T (K)	T (1/K)	$k \cdot 10^5$ $(sec)^{-1}$	lnk	$ln(kh/k_bT)$
26	299.15	0.003343	23.4	-8.36	-37.82
32	305.15	0.003277	44.6	-7.72	-37.20
38	311.15	0.003214	49.0	-7.62	-37.12
43	316.15	0.003163	89.1	-7.02	-36.54
lnA	Ea kJ/mol	$\Delta H^{\ddagger}$ kJ/mol	$\Delta S^{\ddagger}$ $(J*mol^{-1}*K^{-1})$	$\Delta G^{\ddagger}_{298}$ (kJ/mol)	
14.34	56.33	53.78	-134.29	93.92	

Table 2.24b: $Tp^{iPr}MoO(OPh)(OPEt_3)$ + MeCN					
T (ºC)	T (K)	T (1/K)	$k \cdot 10^5$ $(sec)^{-1}$	lnk	$ln(kh/k_bT)$
5	278.15	0.003595	14.6	-8.83	-38.22
11	284.15	0.003519	35.26	-7.95	-37.36
11	284.15	0.003519	34.91	-7.96	-37.37
11	284.15	0.003519	34.81	-7.96	-37.37
11	284.15	0.003519	34.00	-7.99	-37.80
16	289.15	0.003458	66.23	-7.32	-36.75
16	289.15	0.003458	63.27	-7.37	-36.79
16	289.15	0.003458	66.97	-7.31	-36.74
22	295.15	0.003388	160.77	-6.43	-35.88
22	295.15	0.003388	153.31	-6.48	-35.93
22	295.15	0.003388	153.51	-6.48	-35.93
22	295.15	0.003388	169.62	-6.38	-35.83
27	300.15	0.003332	337.26	-5.69	-35.16
32	305.15	0.003277	540.54	-5.22	-34.70
37	310.15	0.003224	1032.98	-4.57	-34.07
42	315.15	0.003173	1822.45	-4.00	-33.52
lnA	Ea kJ/mol	$\Delta H^{\ddagger}$ kJ/mol	$\Delta S^{\ddagger}$ $(J*mol^{-1}*K^{-1})$	$\Delta G^{\ddagger}_{298}$ (kJ/mol)	
32.63	95.93	93.48	18.16	88.06	

Table 2.24c: $Tp^{iPr}MoO(OPh)(OPMe_2Ph)$ + MeCN					
T (ºC)	T (K)	T (1/K)	$k \cdot 10^5$ $(sec)^{-1}$	lnk	$ln(kh/k_bT)$
5.9	279.05	0.003584	8.43	-9.38	-38.77
11.5	284.65	0.003513	25.19	-8.29	-37.70
18	291.15	0.003435	62.54	-7.38	-36.81
22.5	295.65	0.003382	124.50	-6.69	-36.14
lnA	Ea kJ/mol	$\Delta H^{\ddagger}$ kJ/mol	$\Delta S^{\ddagger}$ $(J*mol^{-1}*K^{-1})$	$\Delta G^{\ddagger}_{298}$ (kJ/mol)	
37.9	109.55	107.16	62.20	88.62	

Table 2.24d: $Tp^{iPr}MoO(OPh)(OPEt_2Ph)$ + MeCN					
T (ºC)	T (K)	T (1/K)	$k \cdot 10^5$ $(sec)^{-1}$	lnk	$ln(kh/k_bT)$
0	273.15	0.003661	8.63	-9.36	-38.73
4	277.15	0.003608	32.08	-8.05	-37.43
10	283.15	0.003532	73.812	-7.21	-36.62
17.5	290.65	0.003441	105.82	-6.85	-36.28
23.5	296.65	0.003371	222.52	-6.11	-35.56
26	299.15	0.003343	676.67	-4.99	-34.46
28	301.15	0.003321	599.52	-5.12	-34.58
lnA	Ea (kJ/mol)	$\Delta H^{\ddagger}$ (kJ/mol)	$\Delta S^{\ddagger}$ $(J*mol^{-1}*K^{-1})$	$\Delta G^{\ddagger}_{298}$ (kJ/mol)	
32.62	94.54	92.16	18.32	86.69	

Table 2.24e: $Tp^{iPr}MoO(OPh)(O(P\textit{n}\text{-}Bu)_3)$ + MeCN					
T (ºC)	T (K)	T (1/K)	$k \cdot 10^5$ $(sec)^{-1}$	lnk	$ln(kh/k_bT)$
12	285.15	0.003507	268.3	-5.92	-35.38
16	289.15	0.003458	148.4	-6.51	-35.96
21	294.15	0.0034	60.6	-7.41	-36.84
26	299.15	0.003343	26.2	-8.25	-37.66
lnA	Ea kJ/mol	$\Delta H^{\ddagger}$ kJ/mol	$\Delta S^{\ddagger}$ $(J*mol^{-1}*K^{-1})$	$\Delta G^{\ddagger}_{298}$ (kJ/mol)	
41.45	118.51	116.10	91.62	88.76	

Table 2.24f: $Tp^{iPr}MoO(OPh)(OPMePh_2)$ + MeCN					
T (ºC)	T (K)	T (1/K)	$k \cdot 10^5$ $(sec)^{-1}$	lnk	$ln(kh/k_bT)$
5	278.15	0.00360	75.76	-7.19	-36.57
10	283.15	0.00353	145.00	-6.53	-35.94
15	288.15	0.00347	276.40	-5.89	-35.31
20	293.15	0.00341	651.04	-5.03	-34.47
30	303.15	0.00330	2604.17	-3.65	-33.12
lnA	Ea kJ/mol	$\Delta H^{\ddagger}$ kJ/mol	$\Delta S^{\ddagger}$ $(J*mol^{-1}*K^{-1})$	$\Delta G^{\ddagger}_{298}$ (kJ/mol)	
36.11	100.34	97.92	47.23	83.83	

Table 2.24g: $Tp^{iPr}MoO(OPh)(OPEtPh_2)$ + MeCN					
T (ºC)	T (K)	T (1/K)	$k \cdot 10^5$ $(sec)^{-1}$	lnk	$ln(kh/k_bT)$
10	283.15	0.003532	85.30	-7.07	-36.47
16	289.15	0.003458	157.38	-6.45	-35.88
20	293.15	0.003411	383.14	-5.57	-35.02
31.5	304.65	0.003282	610.50	-5.10	-34.58
lnA	Ea kJ/mol	$\Delta H^{\ddagger}$ kJ/mol	$\Delta S^{\ddagger}$ $(J*mol^{-1}*K^{-1})$	$\Delta G^{\ddagger}_{298}$ (kJ/mol)	
21.64	67.48	65.04	-73.19	86.86	

When the activation parameters for the solvation reactions of (**1a**-**1g**) are compared, two rather unique features present themselves. First, the solvation reaction of (**1a**) and (**1f**) are distinguished by a rather large, negative entropy of activation (-134.4 and -73.2 $J \cdot mol^{-1} \cdot K^{-1}$) respectively) which contrasts the positive entropies of activation in the remaining complexes. Based upon this data, the solvation reaction appears to follow an Id-type mechanism for the majority of the series of complexes, while following an Ia-type mechanism in the case of (**1a**) and (**1f**). Secondly, despite the entropic variability across this series of complexes, the barriers to the solvated complex (**5**) fall within a relatively narrow range of ~10 kJ/mol. However, when the $\Delta\Delta G^{\ddagger}$ is compared to the $\Delta\Delta G^{o}$ values obtained from the CV, there is a two fold greater difference in the activation barrier leading to the formation of (**5**), despite rather similar relative stabilities of the intermediate complexes (range of $\Delta\Delta G^{o}$ ~4 kJ/mol). Thus the reaction coordinate for the solvation of the intermediates (**step 2**) derived from (**1**) can be approximated using the methodology presented for (**step 1**) of the reaction (**Table 2.26** and **Figure 2.16**).

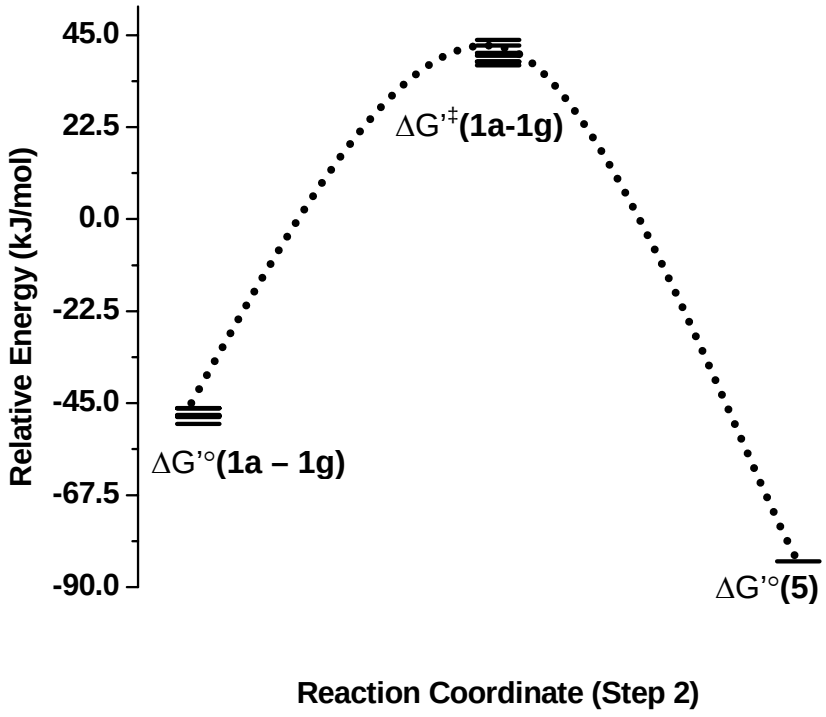

Figure 2.16: Reaction Coordinate for the solvation of (**1a-1g**) to form (**6**). $\Delta G'^{\circ}$(**1a-1g**) , $\Delta G'^{\circ}$(**5**) and $^{\circ}\Delta G'^{\ddagger}$(**1a-1g**) are defined in the text.

Table 2.26: Approximate Reaction Coordinate for the Second Step in of Reaction: Solvation of (**1a-1f**) to yield compound (**5**)				
Compound	**ΔG^o (kJ/mol)[a]**	**$\Delta G^{\ddagger}$ (kJ/mol)[b]**	**$\Delta G'^o$ (kJ/mol)[c]**	**$\Delta G'^{\ddagger}$ (kJ/mol)[d]**
$Tp^{iPr}MoO_2OPh$ **(1)**	114.2 ± 0.7	NA	0	NA
$Tp^{iPr}MoO(OPh)(OPMe_3)$ **(1a)**	64.1	90.42	-50.1	43.82
$Tp^{iPr}MoO(OPh)(OPMe_2Ph)$ **(1b)**	66.3	89.84	-47.9	40.72
$Tp^{iPr}MoO(OPh)(OPEt_3)$ **(1c)**	66.1	92.88	-48.1	39.96
$Tp^{iPr}MoO(OPh)(OP(n\text{-}Bu)_3)$ **(1d)**	67.9	93.98	-46.3	42.46
$Tp^{iPr}MoO(OPh)(OPEt_2Ph)$ **(1e)**	66.1	93.23	-48.1	38.59
$Tp^{iPr}MoO(OPh)(OPMePh_2)$ **(1f)**	68.0	94.83	-46.2	37.63
$Tp^{iPr}MoO(OPh)(OPEtPh_2)$ **(1g)**	65.8	97.46	-48.4	38.46
$Tp^{iPr}MoO(NCMe)(OPh)$ (**5**)	30.5 ± 0.3	NA	-83.7	NA
a) ΔG^o approximated from CV measurements at 298 K; b) $\Delta G^{\ddagger}$ taken from kinetics measurements at 298 K, c) $\Delta G'^o$ represents the relative energy expressed as [ΔG^o(**1-1g**)- ΔG^o(**1**)] or [ΔG^o(**5**)- ΔG^o(**1**)] d) $\Delta G'^{\ddagger}$ relative energy expressed as [$\Delta G^{\ddagger}$ (**1a-1g**) + $\Delta G'^o$(**1a-1g**)]				

Kinetics of loss of OPR_3 from $Tp^{Me2}MoO(Cl)(OPR_3)$:

Visually, this reaction proceeds from a yellow-green (**2f**, **2g)** to emerald green or gold (**2a-e**) to pale blue (**6**) and is similar to the decay of $Tp^{iPr}Mo^{IV}O(OPh)(OPR_3)$, with the noted exception that the brown species is only observable in pure benzene (the brown species was not observed in pure acetonitrile over the course of the experiment). **Table 2.27** contains the principle d-d transitions present in this complex.

Table 2.27: visible spectra of complex (**6**) $Tp^{Me2}MoOCl(NCMe)$		
$d_{xy} \rightarrow d_{xz}$ / d_{yz} (cm^{-1})	**$d_{xy} \rightarrow d_{xz}$ / d_{yz} (cm^{-1})**	**$d_{xy} \rightarrow d_{x2-y2}$ (cm^{-1})**
11500 (shoulder)	13830	26810

Table 2.28 and **Figure 2.17** provide the rate constants and kinetic parameters for the decay reaction in pure acetonitrile, while **Table 2.29** and **Figure 2.18**, contain the approximate reaction coordinate for the solvation reaction (**step 2** of the decay process).

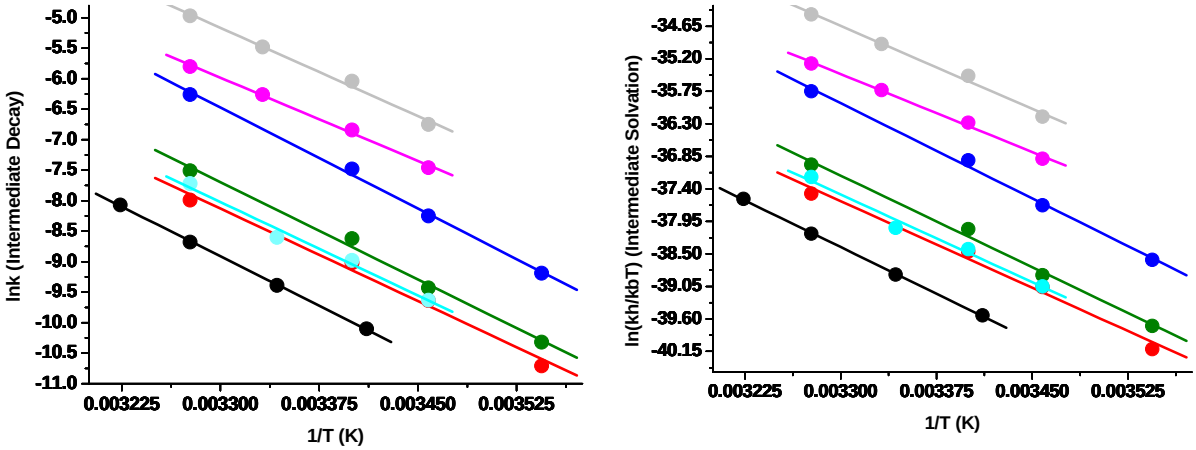

Figure 2.17: Reaction kinetics for the solvation of (**2a-2g**) to form (**6**). **Left:** Eyring Plot and **Right**: Arrhenious Plot.

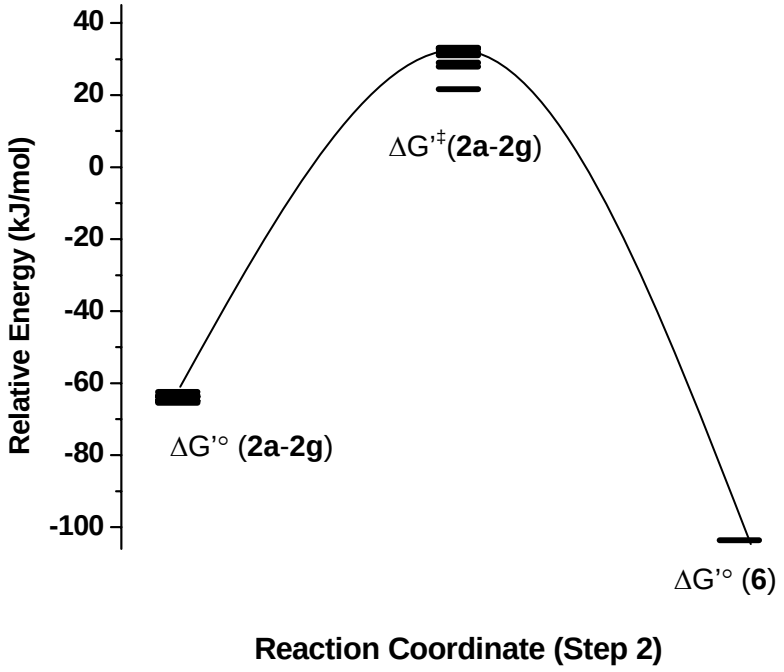

Figure 2.18: Reaction Coordinate for the solvation of (**2a-2g**) to form (**6**). $\Delta G'^{o}$(**2a-2g**) , $\Delta G'^{o}$(**6**) and $^{o}\Delta G'^{\ddagger}$(**1a-1g**) are defined in the text.

Similar to the solvation reaction of $Tp^{iPr}Mo^{IV}O(OPh)(OPR_3)$ the $\Delta\Delta G^{\ddagger}$ for solvation, when compared to the $\Delta\Delta G^{o}$ values obtained from the CV, show an approximate two fold greater difference in the activation barrier leading to the formation of (**6**). Quantitatively, this translates to an 11.06 kJ/mol range in $\Delta\Delta G^{\ddagger}$, that is paired to rather similar relative stabilities of the intermediate complexes (range of $\Delta\Delta G^{o}$ ~3 kJ/mol). Interestingly, in all cases, the activation barrier leading towards the acetonitrile adduct formation is distinguished by a $-\Delta S^{\ddagger}$, suggesting that all of these complexes decay via an associative or Ia type mechanism. To further assess this observation, the decay reaction was followed as a function of acetonitrile concentration through mixed benzene:acetonitrile solvent systems at 37 ºC, **Table 2.30 and Figure 2.19.** The linear dependence of the rate of decay upon the concentration of acetonitrile in the solution further confirms the

associative nature of the transition state leading to the acetonitrile adduct formation, and contrasts the Id mechanism that prevails in the majority of the more sterically hindered $Tp^{iPr}MoOOPh(OPR_3)$ intermediates.

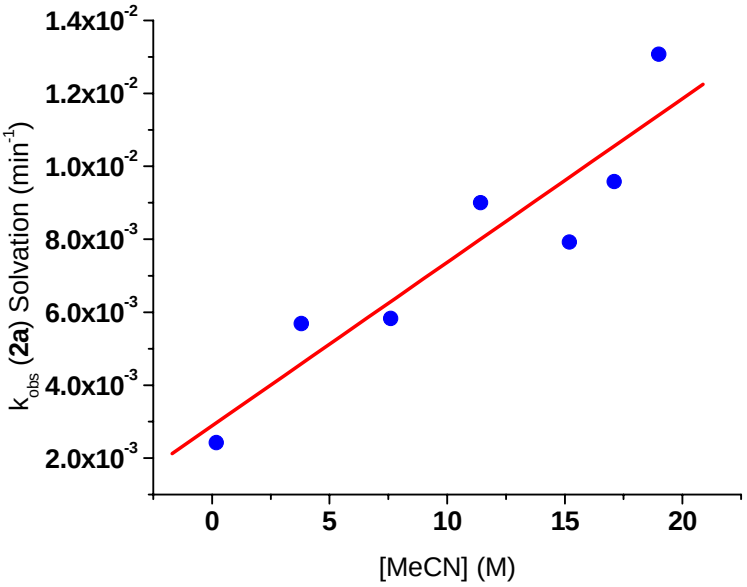

Figure 2.19: Effect of coordinating solvent concentration on the rate of solvation of (**2a**)

The order of the mechanism, with respect to acetonitrile is difficult to establish in this case as the competing dimerization reaction predominates the decay process at acetonitrile concentrations less than approximately 50X that of the $Tp^{Me2}Mo^{IV}O(Cl)(OPMe_3)$ intermediate. However, when the acetonitrile concentration exceeds ~200X the concentration of the intermediate, the reaction proceeds cleanly to the acetonitrile adduct, albeit slower than in the pure solvent. The effects of solvent concentration were not established in terms of the competing dimerization reaction.

Table 2.28a: $Tp^{Me2}MoOCl(OPMe_3)$ **(2a)** → $Tp^{Me2}MoOCl(NCMe)$ **(6)**				
T (ºC)	T (1/K)	$k \cdot 10^5$ (sec^{-1})	lnk	$ln(kh/k_bT)$
20	0.003411	4.12	-10.10	-39.54
26	0.003343	8.33	-9.39	-38.85
32	0.003277	17.00	-8.68	-38.16
37	0.003224	31.30	-8.069	-37.57
$\Delta H^{\ddagger}$	**$\Delta S^{\ddagger}$**	**$\Delta G^{\ddagger}$**	**lnA**	**Ea**
87.46± 1.6	-30.5 ± 5.3	96.6	26.8 ± 0.65	89.97± 1.6

Table 2.28b: $Tp^{Me2}MoOCl(OPEt_3)$ **(2b)** → $Tp^{Me2}MoOCl(NCMe)$ **(6)**				
T (ºC)	T (1/K)	$k \cdot 10^5$ (sec^{-1})	lnk	$ln(kh/k_bT)$
9	0.003544	2.24	-10.71	-40.11
16	0.003458	6.52	-9.638	-39.06
21	0.003400	12.1	-9.021	-38.46
32	0.003277	33.6	-7.99	-37.48
$\Delta H^{\ddagger}$	**$\Delta S^{\ddagger}$**	**$\Delta G^{\ddagger}$**	**lnA**	**Ea**
81.13± 6.3	-44.9 ± 21.6	94.5	25.0 ± 2.6	83.57± 6.3

Table 2.28c: $Tp^{Me2}MoOCl(OPPhMe_2)$ **(2c)** → $Tp^{Me2}MoOCl(NCMe)$ **(6)**				
T (ºC)	T (1/K)	$k \cdot 10^5$ (sec^{-1})	lnk	$ln(kh/k_bT)$
9	0.003544	3.30	-10.32	-39.72
16	0.003458	8.04	-9.43	-38.86
21	0.0034	18.0	-8.62	-38.08
32	0.003277	54.9	-7.51	-36.99
$\Delta H^{\ddagger}$	**$\Delta S^{\ddagger}$**	**$\Delta G^{\ddagger}$**	**lnA**	**Ea**
81.8± 7.2	-40.4 ± 24.6	93.9	25.6 ± 2.9	84.29± 7.2

Table 2.28d: $Tp^{Me2}MoOCl(OPPhEt_2)$ **(2d)** → $Tp^{Me2}MoOCl(NCMe)$ **(6)**				
T (ºC)	T (1/K)	$k \cdot 10^5$ (sec^{-1})	lnk	$ln(kh/k_bT)$
9	0.003544	10.2	-9.19	-38.60
16	0.003458	26.00	-8.25	-37.68
21	0.0034	56.6	-7.48	-36.92
32	0.003277	190.3	-6.26	-35.75
$\Delta H^{\ddagger}$	**$\Delta S^{\ddagger}$**	**$\Delta G^{\ddagger}$**	**lnA**	**Ea**
89.3 ± 3.4	-4.1 ± 11.8	91.8	29.9 ± 1.4	91.77± 3.4

Table 2.28e: $Tp^{Me2}MoOCl(OP(n\text{-}Bu)_3)$ **(2e)** → $Tp^{Me2}MoOCl(NCMe)$ **(6)**				
T (ºC)	T (1/K)	$k \cdot 10^5$ (sec^{-1})	lnk	$ln(kh/k_bT)$
16	0.003458	6.60	-9.63	-39.05
21	0.0034	12.60	-8.98	-38.42
26	0.003343	18.50	-8.60	-38.06
32	0.003277	44.60	-7.72	-37.20
$\Delta H^{\ddagger}$	**$\Delta S^{\ddagger}$**	**$\Delta G^{\ddagger}$**	**lnA**	**Ea**
82.4 ± 7.2	-39.7 ± 24.5	94.23	25.7 ± 2.9	84.9± 7.3

Table 2.28f: $Tp^{Me2}MoOCl(OPMePh_2)$ **(2f)** → $Tp^{Me2}MoOCl(NCMe)$ **(6)**				
T (ºC)	T (1/K)	$k \cdot 10^5$ (sec^{-1})	lnk	$ln(kh/k_bT)$
16	0.003458	57.50	-7.46	-36.89
21	0.0034	107.5	-6.84	-36.28
27	0.003332	190.9	-6.26	-35.73
32	0.003277	303.0	-5.80	-35.28
$\Delta H^{‡}$	**$\Delta S^{‡}$**	**$\Delta G^{‡}$**	**lnA**	**Ea**
73.0 ± 3.4	-53.8 ± 10.2	98.06	24.0 ± 1.2	75.5 ± 3.0

Table 2.28g: $Tp^{Me2}MoOCl(OPEtPh_2)$ **(2g)** → $Tp^{Me2}MoOCl(NCMe)$ **(6)**				
T (ºC)	T (1/K)	$k \cdot 10^5$ (sec^{-1})	lnk	$ln(kh/k_bT)$
16	0.003458	117.3	-6.75	-36.18
21	0.0034	237.6	-6.04	-35.49
27	0.003332	416.1	-5.48	-34.95
32	0.003277	693.4	-4.97	-34.45
$\Delta H^{‡}$	**$\Delta S^{‡}$**	**$\Delta G^{‡}$**	**lnA**	**Ea**
70.0 ± 2.6	-57.1 ± 8.7	87.0	23.6 ± 1.0	72.5 ± 2.6

Table 2.30: Acetonitrile Dependence on the Solvation of $Tp^{Me2}MoOCl(OPMe_3)$ → $Tp^{Me2}MoOCl(NCMe)$ **(6)**		
$[Tp^{Me2}MoOCl(OPMe_3)]$ (M)	[MeCN] (M)	$k \cdot 10^5$ $(M \cdot sec)^{-1}$
0.003059	0.2	5.82
0.00516	3.8	13.67
0.005736	7.6	14.02
0.004015	11.42	21.67
0.004971	15.2	19.06
0.00325	17.1	23.04
0.00516	19.0	31.45

Table 2.29: Approximate Reaction Coordinate for the Second Step in of Reaction: Solvation of (**2**) to yield compound (**6**)

Compound	**ΔG^o (kJ/mol)[a]**	**$\Delta G^{\ddagger}$(kJ/mol)[b]**	**$\Delta G'^o$(kJ/mol)[c]**	**$\Delta G'^{\ddagger}$(kJ/mol)[d]**
$Tp^{Me2}MoO_2Cl$ **(2)**	110.5 ± 0.1	NA	0	NA
$Tp^{Me2}MoOCl(OPMe_3)$ **(2a)**	46.8	96.6	-63.7	32.9
$Tp^{Me2}MoOCl(OPMe_2Ph)$ **(2b)**	45.6	93.9	-64.9	29
$Tp^{Me2}MoOCl(OPEt_3)$ **(2c)**	47.1	94.5	-63.4	31.1
$Tp^{Me2}MoOCl(OP(n\text{-}Bu)_3)$ **(2d)**	48.1	94.23	-62.4	31.83
$Tp^{Me2}MoOCl(OPEt_2Ph)$ **(2e)**	46.6	91.8	-63.9	27.9
$Tp^{Me2}MoOCl(OPMePh_2)$ **(2f)**	45.6	98.06	-64.9	33.16
$Tp^{Me2}MoOCl(OPEtPh_2)$ **(2g)**	45.1	87	-65.4	21.6
$Tp^{Me2}MoOCl(NCMe)$ **(6)**	6.9 ± 0.1	NA	-103.6	NA

a) ΔG^o approximated from CV measurements at 298 K; b) $\Delta G^{\ddagger}$ taken from kinetics measurements at 298 K;
c) $\Delta G'^o$ represents the relative energy expressed as [ΔG^o(**2-2g**)- ΔG^o(**2**)] or [ΔG^o(**6**)- ΔG^o(**2**)];
d) $\Delta G'^{\ddagger}$ relative energy expressed as [$\Delta G^{\ddagger}$ (**2a-2g**)- $\Delta G'^o$(**2a-2g**)]

Kinetics of loss of OPR_3 from $Tp^{Me2}MoO(SPh)(OPR_3)$:

Visually, this reaction proceeds from a yellow-green (**4g)** to emerald green (**4a**) to pale blue (**8**) and is similar to the decay of $Tp^{Me2}MoO(Cl)(OPR_3)$, and $Tp^{iPr}Mo^{IV}O(OPh)(OPR_3)$, with the brown species not observed in pure acetonitrile over the course of the experiment. The UV-Vis spectra of complex (**8**) can be found in **Table 2.31** contains the principle d-d transitions present in this complex.

Table 2.31: visible spectra of complex (**8**) $Tp^{Me2}MoOSPh(NCMe)$		
$\mathbf{d_{xy} \rightarrow d_{xz} / d_{yz}\ (cm^{-1})}$	$\mathbf{d_{xy} \rightarrow d_{xz} / d_{yz}\ (cm^{-1})}$	$\mathbf{d_{xy} \rightarrow d_{x2\text{-}y2}\ (cm^{-1})}$
13123	15314	24390

Table 2.32 and **Figure 2.20** provides the rate constants and kinetic parameters for the decay reaction in pure acetonitrile, while **Table 2.33** and **Figure 2.21**, contain the approximate reaction coordinate for the solvation reaction (**step 2** of the decay process).

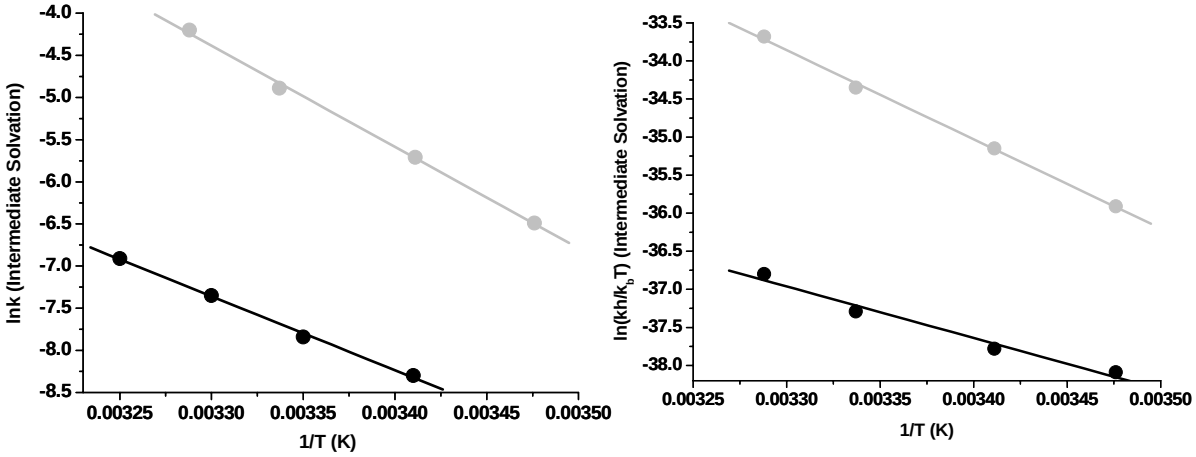

Figure 2.20: Reaction kinetics for the solvation of (**4a** and **4g**) to form (**8**). **Left:** Arrhenious Plot and **Right**: Eyring Plot.

Table 32a: $Tp^{Me2}MoO(SPh)(OPMe_3)$ **(4a)** → $Tp^{Me2}MoO(SPh)(NCMe)$ **(8)**[a]				
T (ºC)	T (1/K)	$k \cdot 10^5\ (sec^{-1})$	lnk	$ln(kh/k_bT)$
20	0.00341	24.8	-8.30	-37.76
25	0.00335	39.3	-7.84	-37.30
30	0.00330	64.5	-7.35	-36.80
35	0.00325	100.2	-6.91	-36.36
$\mathbf{\Delta H^{\ddagger}}$	$\mathbf{\Delta S^{\ddagger}}$	$\mathbf{\Delta G^{\ddagger}}$	**lnA**	**Ea**
67.8 ± 1.0	-82.5 ± 3.3	92.3	20.6 ± 0.4	70.4 ± 1.0
a) data taken from 50				

Table 32b: $Tp^{Me2}MoO(SPh)(OPEtPh_2)$ **(4f)** → $Tp^{Me2}MoOSPh(NCMe)$ **(8)**[b]				
T (ºC)	T (1/K)	$k \cdot 10^5$ (sec^{-1})	lnk	$ln(kh/k_bT)$
14.5	0.003476	151.4	-6.49	-35.91
20	0.003411	332.1	-5.71	-35.15
26.5	0.003337	754.2	-4.89	-34.35
31	0.003288	1498.2	-4.20	-33.68
$\Delta H^{\ddagger}$	**$\Delta S^{\ddagger}$**	**$\Delta G^{\ddagger}$**	**lnA**	**Ea**
107.8 ± 3.1	74.4 ± 2.5	85.64	35.2 ± 1.2	99.7 ± 2.8
b) results from this work				

Table 33: Approximate Reaction Coordinate for the Second Step in of Reaction: Solvation of (**2**) to yield compound (**6**)

Compound	**ΔG^o (kJ/mol)[a]**	**$\Delta G^{\ddagger}$(kJ/mol)[b]**	**$\Delta G'^o$(kJ/mol)[c]**	**$\Delta G'^{\ddagger}$(kJ/mol)[d]**
$Tp^{Me2}MoO_2SPh$ **(4)**	112.5 ± 0.1	NA	0	NA
$Tp^{Me2}MoO(SPh)(OPMe_3)$ **(4a)**	50.9	92.3	-63.7	30.4
$Tp^{Me2}MoO(SPh)(OPEtPh_2)$ **(4g)**	50.4	85.6	-63.8	21.8
$Tp^{Me2}MoO(SPh)(NCMe)$ **(8)**	14.4	NA	-103.6	NA

a) ΔG^o approximated from CV measurements at 298 K; b) $\Delta G^{\ddagger}$ taken from kinetics measurements at 298 K;
c) $\Delta G'^o$ represents the relative energy expressed as [ΔG^o(**4-4g**)- ΔG^o(**4**)] or [ΔG^o(**8**)- ΔG^o(**4**)];
d) $\Delta G'^{\ddagger}$ relative energy expressed as [$\Delta G^{\ddagger}$ (**4a**, **4g**)- $\Delta G'^o$(**4a, 4g**)]

Similar to the solvation reaction of $Tp^{iPr}Mo^{IV}O(OPh)(OPR_3)$ the $\Delta\Delta G^{\ddagger}$ for solvation, when compared to the $\Delta\Delta G^o$ values obtained from the CV, show an approximate two fold greater difference in the activation barrier leading to the formation of (**8**), albeit on a smaller data set. Quantitatively, this translates to an 8.6 kJ/mol range in $\Delta\Delta G^{\ddagger}$, that is paired to rather similar relative stabilities of the intermediate complexes (range of $\Delta\Delta G^o$ ~0.5 kJ/mol). Unlike the solvation of (**2a-2g**), the activation barrier leading towards the acetonitrile adduct formation is distinguished by a -

$\Delta S^{\ddagger}$, for (**2a**), suggesting that this complex solvates via an associative or Ia type mechanism, while that of (**2g**) expresses a $+\Delta S^{\ddagger}$, which suggests a dissociative or Id type mechanism of solvation.

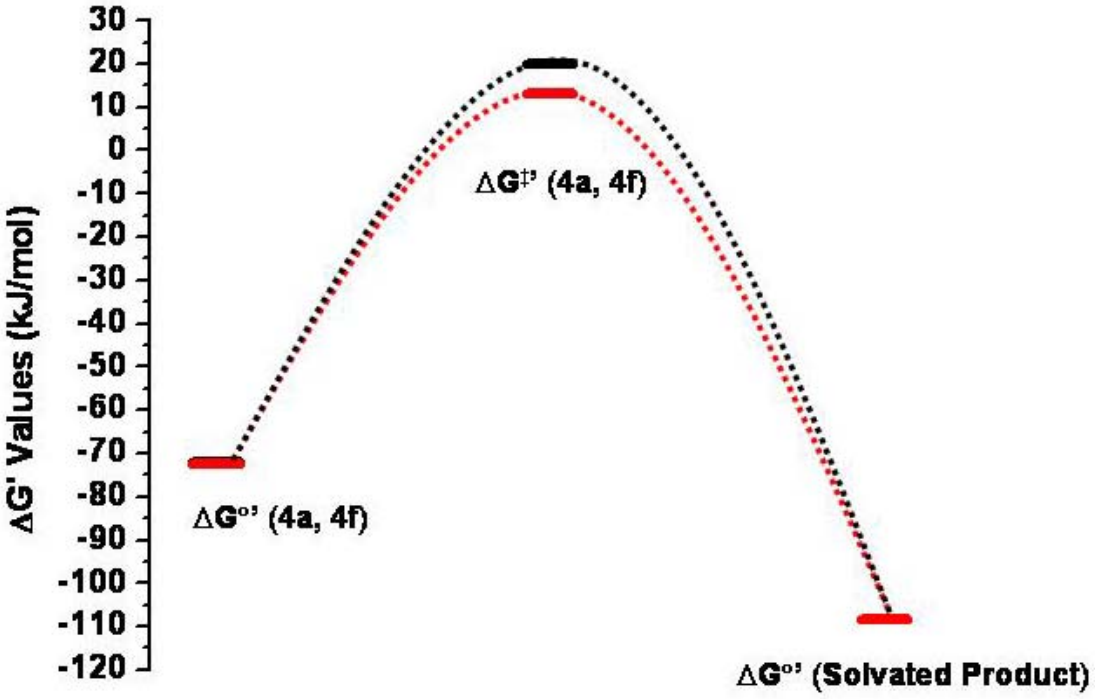

Figure 2.21: Reaction Coordinate for the solvation of (**4a)** in black and (**4g**) in red to form (**8**).

Effect of solvent:

Both the formation and the decomposition of $Tp^{iPr}MoO(OPh)(OPEt_3)$ complex has been investigated in different solvents. The formation reaction was probed in MeCN as well as in benzene that showed a strong solvent dependence. For example, at 17 °C the second-order rate constant in benzene, was found to be 2.75 x 10^{-2} M^{-1} sec^{-1} while that in MeCN was 4.72 x 10^{-2} M^{-1} sec^{-1}. Thus, the rate of the intermediate formation is approximately 2-fold faster in MeCN than it is in benzene.

The loss of $OPEt_3$ from $Tp^{iPr}Mo^{IV}O(OPh)(OPEt_3)$ was investigated in MeCN, benzene and THF. In THF, the putative d-d transitions shift ~25 cm^{-1} higher in energy relative to MeCN, which allows the observation of two processes in the lowest, presumably the $d_{xy} \rightarrow d_{xz}$ transition. For step 2 of **Figure 2.2**, a comparison of the apparent rates in MeCN and THF shows that they are equivalent within statistical error (rate constant ~ 6.3 x 10^{-2} min^{-1} at 22 °C), suggesting that this step is not affected in these two solvents. On the other hand, the second exponential, step 3 of **Figure 2.2**, was slower in THF than in it was in MeCN, indicating a solvent dependency associated with this step. For example, the rate constant for the third step, was found to be 3.49 x 10^{-3} min^{-1} at 22° C in THF, while it was 7.62 x 10^{-3} min^{-1} in MeCN under identical conditions. When MeCN solutions of $Tp^{iPr}Mo^{IV}O(OPh)(OPEt_3)$ were spiked with known amounts of water, such that the concentration of water in MeCN was ~ 10 times and 100 times the concentration of the Mo-complex, the rate of the first process remained unaffected. This observation suggests that the water present in the solvent, if any, does not influence the rate of the first step of the reaction. Interestingly, $Tp^{iPr}Mo^{IV}O(OPh)(OPEt_3)$ is stable in dry, deoxygenated pentane for hours at elevated temperatures, to days at room temperature, but decays rapidly in dry THF, or dry or wet MeCN. Unlike the observed rate for the **(1c)** to **(5)** conversion, the observed rate of the **(5)** to **(9)** conversion is strongly

influenced by the presence of water in the solvent. When water was present, an additional exponential could be seen that possibly results from the formation of a dinuclear complex other than **(9)**. The presence of this additional exponential did not allow accurate fitting of the conversion of **(5)** to **(9)** in cases when water was added.

Interestingly, when $Tp^{iPr}Mo^{IV}O(OPh)(OPEt_3)$ was dissolved in pyridine a red solution was instantly produced indicating the formation of a pyridine adduct. Complexes of this type have been structurally characterized for the hydrotris(3,5-dimethylpyrazol-1-yl)borate system.[26a] In agreement with this observation, the red colored compound could also be generated by adding pyridine to the blue MeCN solution, which suggests a higher thermodynamic stability of the pyridine coordinated complex, as expected from pyridine's high donor ability. More importantly, this experiment demonstrates that the coordinated MeCN is labile towards substitution and is consistent with MeCN self exchange and the formation of a dinuclear complex through a similar process. The rapid loss of phosphine oxide from the intermediate in pyridine also suggests that there is strong solvent assistance in this case.

Kinetics of the Dinucleation Reaction

Because the second step of the decomposition reaction (**step 3** in **Figure 2.2**) was found to be slow, the variable temperature measurements for the conversion of (**1c→9**) and (**1f→9**) were conducted at comparatively higher temperatures to facilitate data collection over five half-lives of the exponential **(Table 2.9).** The activation parameters for the dinucleation reaction for these compounds are listed in **Table 2.34**, as previously mentioned, the first step in the decay process for (**3a-3g**) was complicated by the dimerization reaction, the clean observation of the second decay step suffered from the presence of the concurrent solvation reaction. Thus, in the case of the

conversion of intermediates of (**3**) to (**11**), kinetics were not performed. In addition, the kinetics for the conversions of the intermediates of (**2**) and (**4**) to (**10**) and (**12**) were also not investigated due to the inertness of these complexes toward the dinucleation reaction under the reaction conditions. Thus for (**1c** and **1f**) the second step of **Figure 2.2** (solvation reaction) has been determined to be a dissociative process, while the third step (dinucleation reaction) is possibly a dissociative process with a positive entropy of activation.[53]

Table 2.34. Experimentally determined activation parameters for the reactions shown in Figure 2.

Reactions	$\Delta H^{\ddagger}$ kJ mol^{-1}	$\Delta S^{\ddagger}$ J mol^{-1} K^{-1}	lnA	E_a, kJ mol^{-1}	$\Delta G^{\ddagger}$ kJ mol^{-1} @298K
$Tp^{iPr}MoO_2OPh$ +PEt_3 → $Tp^{iPr}MoO(OPh)(OPEt_3)$	40.1 (±5.3)	-178.4 (±18.3)	8.96 (±2.2)	42.5 (±5.3)	93.3
$Tp^{iPr}MoO_2OPh$ + PPh_2Me → $Tp^{iPr}MoO(OPh)(OPPh_2Me)$	72.0 (±6.7)	-56.8 (±23)	21.2 (±2.8)	74.5 (±6.8)	88.9
$Tp^{iPr}MoO(OPh)(OPEt_3)$ + MeCN → $Tp^{iPr}MoO(OPh)(MeCN)$ + $OPEt_3$	93.5 (±0.9)	18.0 (±3.2)	32.6 (±0.4)	95.9 (±0.8)	88.1
$Tp^{iPr}MoO(OPh)(OPPh_2Me)$ + MeCN → $Tp^{iPr}MoO(OPh)(MeCN)$ + OPh_2Me	85.9 (±5.2)	25.0 (±16)	34.3 (±0.04)	93.3 (±5.8)	78.5
$Tp^{iPr}MoO(OPh)(MeCN)$ → Dinuclear species[a]	93.1 (±3.9)	15.0 (±13)	29.9 (±1.6)	95.6 (±3.9)	88.6

The errors reported here were derived from the regression analysis at 95% confidence limit. [a]The activation parameters were calculated using data from both $Tp^{iPr}MoO(OPh)(OPPh_2Me)$ and $Tp^{iPr}MoO(OPh)(OPEt_3)$.

Calculated structures:

Calculations have been performed on stable species and transition states that are involved in the OAT reaction and in the replacement of the phosphine oxide by the MeCN solvent. The optimized geometries of the species in this reaction are shown in **Figure 2.22.** The comparison of the geometrical data of the calculated $Tp^{iPr}MoO_2(OPh)$ reactant (REAC-C, **Figure 2.22**), with crystallographic data[54] for $Tp^{Me2}MoO_2(SPh)$ shows good agreement. Both the optimized Mo–O bond lengths (1.75 Å) and the optimized Mo–N bond lengths (2.34 Å, 2.21 Å) are slightly longer than the experimental values (1.70 Å) and (2.30 Å, 2.17 Å), respectively, while the optimized O–Mo–O angle (103.7°) is similar to the experimental angle (102.6°). In agreement with the experimental results, the Mo–N bonds trans to the strongly bonded oxo groups are longer by 0.13 Å, than the Mo–N bond trans to the more weakly bound OPh group.

The optimized geometry of the transition state (TS-IC, **Figure 2.22**) for the attack of PMe_3 on $Tp^{iPr}MoO_2(OPh)$ shows bond lengths that are intermediate between those of the reactant (REAC-C) and $Tp^{iPr}MoO(OPh)(OPMe_3)$ (INT-IC, **Figure 2.22**). The Mo–O bond under attack (1.83 Å) is slightly longer than that in the reactant (1.75 Å) but shorter than that in the intermediate (2.21 Å). The O–P bond is beginning to form in the transition state but is significantly longer in the transition state (2.15 Å) than it is in the intermediate (1.58 Å). In terms of these distances, TS-IC would be an early transition state. In our optimized structure for TS-IC, the torsion angle O–Mo–O–P is -79.6°. This value is in good agreement with previous theoretical work, that suggested an angle near ± 90° was necessary in order to occupy the correct Mo d orbital in the $2e^-$ reduction from the Mo(VI) to Mo(IV) during OAT. TS-IC has a large O–P–C_{Me} angle (153.0°), the implications of which will be discussed later. The calculated vibrational frequencies of the completely optimized transition-state

geometry show one imaginary frequency (194*i* cm^{-1}) with a motion appropriate for this transition state.

Our calculated $Tp^{iPr}MoO(OPh)(OPMe_3)$ intermediate structure (INT-IC, **Figure 2.22**), has a well formed O–P bond and a weaker Mo–$OPMe_3$ dative bond (2.21 Å). The O–P bond distance in this intermediate is 0.04 Å longer that its distance in the free ligand, $OPMe_3$, a difference that parallels the formation of a strong Mo–$OPMe_3$ dative bond (see below). In this structure the differences in the strength of the three Mo–O bonds can be seen in the trans influence on the Mo–N bonds. The calculated bond lengths are in good agreement with the experimental values[23] for $Tp^{iPr}MoO(OPh)(OPEt_3)$, the "spectator" Mo–O bond has the largest error, but its shortening from that in REAC is correctly predicted. The O–P–C_{Me} angle (109-115°) is now close to that expected for a phosphine oxide (~115°). The Mo–O–P angle (126.4°) is similar to the experimental value of 132.4°. The calculated O–Mo–O–P torsion angle is -60.5º, also in good agreement the observed values of -57.5º.

The next step in the oxo-transfer reaction, after the formation of the intermediate, is the substitution of phosphine oxide with a molecule of solvent (MeCN in this case). There are two possible "ideal" mechanisms: a dissociative mechanism where $OPMe_3$ leaves before MeCN enters; and an associative mechanism where MeCN binds to the intermediate (INT-IC) before $OPMe_3$ leaves. For the former one expects a 5-coordinate intermediate while for the latter one expects a 7-coordinate intermediate or TS.

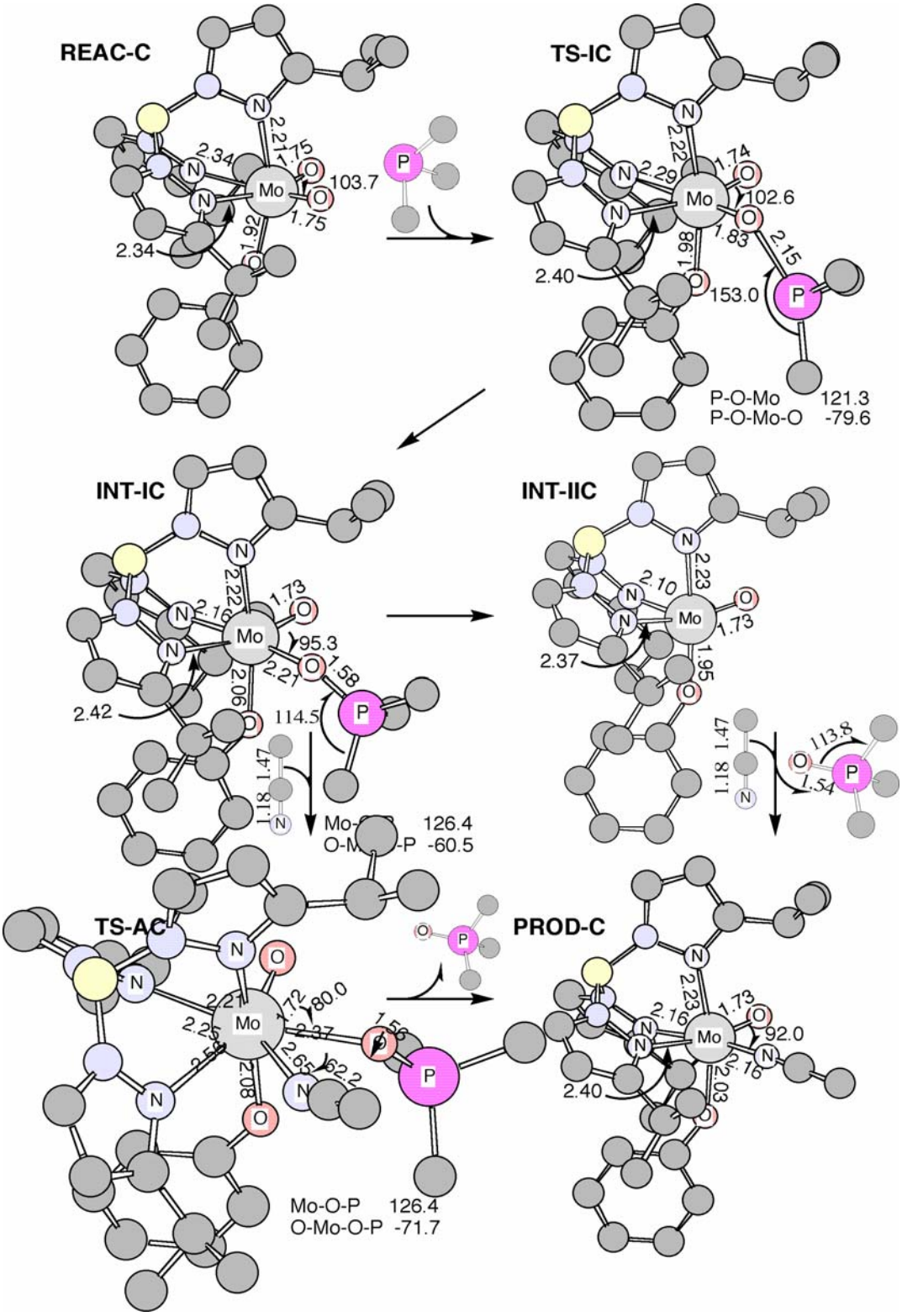

Figure 2.22 – The calculated geometries and metric parameters for the reactants, transition states, intermediates and the product for the oxygen atom transfer reaction from $Tp^{iPr}MoO_2(OPh)$ to PMe_3.

Of course, exchange pathways which are intermediate between these "ideal" situations are common. In an exchange pathway the 7-coordinate species would be expected to be a transition state with the degree of attachment of the exchanging ligands being a measure of the associative or dissociative character. In order to examine both possible pathways, we calculated the five coordinate $Tp^{iPr}MoO(OPh)$ intermediate (INT-IIC), that one expects in the dissociative mechanism and a 7-coordinate species (TS-AC) corresponding to an associative exchange mechanism. The structures are shown in **Figure 2.22**. The square pyramidal, five-coordinated $Tp^{iPr}MoO(OPh)$ intermediate (INT-IIC) has a vacant coordination site trans to one of pyrazol nitrogen donors, and this Mo-N bond is now even shorter (2.10 Å) than it was in the intermediate.

In the pathway for the associative mechanism no 7-coordinate intermediate was found but a 7-coordinate transition state (TS-AC) for exchange of $OPMe_3$ with MeCN could be located. In the optimized geometry of TS-AC there is one imaginary frequency ($64i$ cm^{-1}) corresponding to the vibration that breaks (makes) the Mo–OP bond and makes (breaks) the Mo–NC bond. The low imaginary frequency is indicative of a very “loose” transition state, where both $OPMe_3$ and NCMe are nearly dissociated. The Mo–OP bond is longer (2.37 Å) and the O–P bond is shorter (1.56 Å) than those in the intermediate. The Mo–NC bond is longer (2.65 Å) than that of the product (PROD-C) where MeCN is fully coordinated. In this 7-coordinate TS-AC the weakest Mo–N (pyrazole) bond, trans to oxo ligand becomes even longer (2.56 Å).

In the structure of the MeCN substituted product (PROD-C, **Figure 2.22**), the Mo–NC bond is completely formed with a Mo–NC bond length of 2.16 Å. The Mo–N bond length trans to MeCN is similar to that in the intermediate. This similarity in trans influence of $OPMe_3$ and MeCN suggest similarities in their Mo-ligand bond strength.

Calculated Energies:

The computed reaction energies in **Table 2.35** and **Figure 2.23** are all relative to the energy of the reactant (REAC-C) plus the energy of both PMe_3 and MeCN. Gas-phase enthalpies and free energies, and solvation corrected free-energies for MeCN at standard conditions are given in **Table 2.35**. **Figure 2.9** shows the free-energy profile for the predictions in MeCN, which will be described in detail below. The PMe_3 substrate reacts by crossing the transition state, TS-IC, to form the intermediate, INT-IC. For TS-IC, the B3LYP gas-phase enthalpic barrier ($\Delta H^{\ddagger}$) is 37.6 kJ/mol.

Table 2.35 Calculated energies in kJ/mol. Values in parenthesis are estimated as discussed in the text.

	ΔH^{o}(Gas Phase)	ΔG^{o}(Gas Phase)	ΔG^{o}_{solv}(MeCN)
REAC-C	0.00	0.00	0.00
TS-IC	37.59	85.49	95.00
INT-IC	-90.25	-37.98	-41.02
TS-AC	-12.86	84.74	101.49
(TS-IIC)		(71.95)	(68.91)
INT-IIC	19.68	13.42	-11.42
(TS-IIC')		(61.54)	(35.14)
PROD-C	-56.84	-14.99	-41.39

Gas-phase corrections for the loss in entropy on forming this transition state produce a free-energy barrier ($\Delta G^{\ddagger}$) of 85.5 kJ mol^{-1}. Solvation corrections increase the free-energy barrier ($\Delta G^{\ddagger}_{solv}$(MeCN)) to 95.0 kJ mol^{-1}. Additional corrections for the reduction in entropy due to restricted motion of the separated species in solution[55] were not made. The enthalpy of formation ($\Delta H°$) of INT-IC is –90.9 kJ mol^{-1} and the free-energy, $\Delta G^{\ddagger}_{solv}$(MeCN) of –41.0 kJ mol^{-1} favors its formation, however, the entropy does not. As a result, the intermediate (INT-IC) is found to be quite stable.

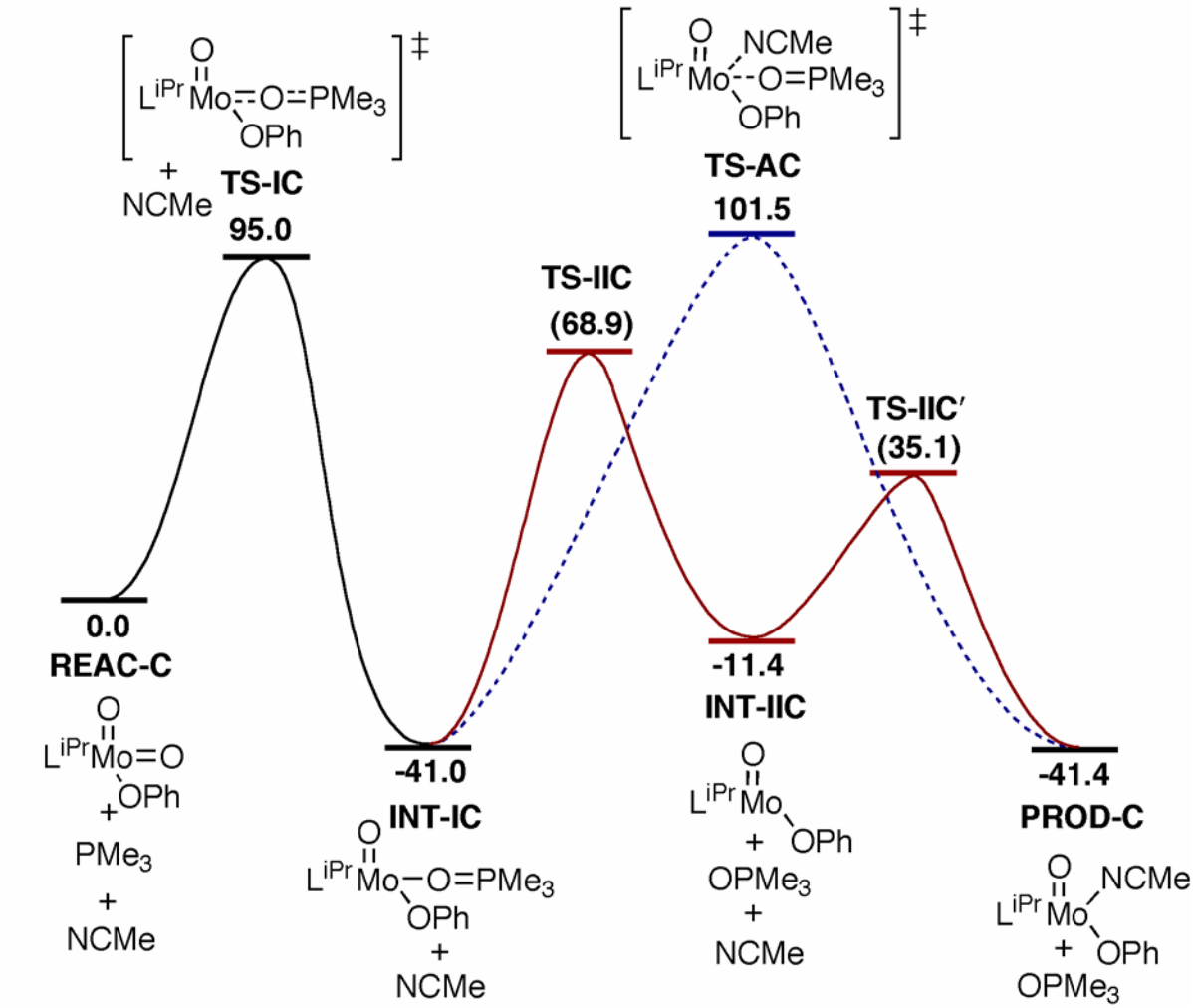

Figure 2.23. The reaction path for REAC-C + PMe_3 + MeCN $\rightarrow$ PROD-C + $OPMe_3$. A solid (dashed) line is used to represent the dissociative (associative) path for the decomposition of INT-IC. All energies are solvent corrected (MeCN) free energies in kJ/mol. Values in parenthesis are estimated as discussed in the text

Energies for the replacement of the $OPMe_3$ ligand in INT-IC by MeCN were determined for both a dissociative and an associative path. The barrier for the dissociative path was taken to

be the dissociation energy of the $OPMe_3$ ligand. The enthalpic differences correspond to a Mo-$OPMe_3$ bond energy of 109.9 kJ mol^{-1}. In this dissociative reaction the entropy is higher as two species are produced. However, this increase in entropy only occurs after most of the enthalpic barrier is achieved. In summary, in determining the free-energy barriers for the dissociative mechanism, the free-energy of the dissociative intermediate species (INT-IIC) cannot be used as the barrier. Thus, the maximum free-energy barrier for the dissociative route corresponds to the enthalpic barrier of 109.9 kJ mol^{-1}. After formation of INT-IIC, MeCN must overcome an entropic barrier to coordinate to INT-IIC and form the product (PROD). In this "forward" reaction we assume that the full entropic barrier is encountered before the enthalpic stabilization from the formation of the new Mo–NCMe bond reduces the energy to that of the product. For both of these estimated dissociative transition states the solvation corrections, like the entropic corrections, corresponds to the associative precursor, INT-IC and PROD-C, respectively.

On the associative path, TS-AC has an enthalpic barrier (from the intermediate, INT-IC) of 77.4 kJ mol^{-1}. Gas-phase entropic corrections and solvent corrections produce a free-energy barrier ($\Delta G^{\ddagger}_{solv}$(MeCN)) of 142.5 kJ mol^{-1}, a barrier that is ~33 kJ mol^{-1} higher than the highest barrier on the dissociative path. The enthalpic data (uncorrected for solvent) suggest that the Mo-$OPMe_3$ bond is ~ 43 kJ mol^{-1} stronger than the Mo–NCMe bond. However, the large dipole moment of $OPMe_3$ leads to a large solvation correction favoring the replacement of the phosphine oxide by MeCN, an overall reaction which is now favored by ~1.6 kJ mol^{-1} (0.4 kcal/mol). The high concentration of MeCN further favors formation of this substituted product (PROD-C).

Discussion.

The results presented in the preceding sections demonstrate that the reactions of tertiary phosphines with $Tp^{iPr}MoO_2(OPh)$, $Tp^{Me2}MoO_2Cl$, $Tp^{Me2}MoO_2(OPh)$, $Tp^{Me2}MoO_2(SPh)$, and proceed through multiple transition states; in this case three transition states have been experimentally defined. The first transition state involves the formation of a phosphine oxide-coordinated intermediate, the second one is due the formation of a solvent coordinated complex, and the last one is due to the formation of a dinuclear compound. In the context of biological OAT reactions, the formation of a dinuclear species is not pertinent, but the other two transition states are relevant and significant. Within the scheme of events the rate-limiting step has also been defined, for the reactions of $Tp^{iPr}MoO_2(OPh)$ and $Tp^{Me2}MoO_2(SPh)$, to be the first nucleophilic attack step for all phosphines tested with the exception of PMe_3 as shown in **Table 2.36**.

Table 2.36: Formation and Solvation Rates of Intermediate Complexes (**1a-1g**) and Formation and Solvation of (**4a**) and (**4g**).

Intermediate	**k_f $(sec)^{-1}$ x 10^5 (Step 1)**	**k_s $(sec)^{-1}$ x 10^5 (Step 2)**	**k_f/k_s x 10^3 [f]**
$Tp^{iPr}MoO(OPh)(OPMe_3)$ **(1a)**	92.0[a]	23.4[b]	3900
$Tp^{iPr}MoO(OPh)(OPMe_2Ph)$ **(1b)**	92.0[b]	124.5	739
$Tp^{iPr}MoO(OPh)(OPEt_3)$ **(1c)**	23.9[b]	160.8[b]	150
$Tp^{iPr}MoO(OPh)(OP(n\text{-}Bu_3))$ **(1d)**	14.2[c]	60.6[c]	230
$Tp^{iPr}MoO(OPh)(OPEt_2Ph)$ **(1e)**	28.5[d]	222.5[d]	130
$Tp^{iPr}MoO(OPh)(OPMePh_2)$ **(1f)**	8.76[c]	651.0[e]	13
$Tp^{iPr}MoO(OPh)(OPEtPh_2)$ **(1g)**	3.65[a]	383.14[e]	9.5
$Tp^{Me2}MoO(SPh)(OPMe_3)$ **(4a)**	35.1[e]	24.8[e]	1415
$Tp^{Me2}MoO(SPh)(OPEtPh_2)$ **(4g)**	23.8[e]	332.1[e]	741

a) recorded at 22° C. b) recorded at 26° C. c) recorded at 21° C. d) recorded at 23.5° C. e) recorded at 20° C. f) when $k_f = k_s$, ratio would be noted as 1000

*Mechanism of formation of **(1a-1g)**, **(3a-3g)** and **(4a** and **4g)**.*

As expected, the reactions of $Tp^{iPr}Mo^{VI}O_2(OPh)$, $Tp^{Me2}MoO_2(OPh)$, $Tp^{Me2}MoO_2(SPh)$, and presumably $Tp^{Me2}MoO_2(Cl)$, follows a second-order process when reacting with tertiary phosphines. This reaction proceeds as the tertiary phosphine approaches the Mo-center, followed by the nucleophilic attack by the tertiary phosphine and the transfer of two electrons to the Mo-center. The reaction results in the formation of intermediate species, which are either isolatable or observed *in situ*. The reaction is dependent on the nature of the phosphine, as well as the starting molybdenum complex, as evidenced from the comparison of the experimentally determined rates of the reaction as shown in **Table 2.37.**

Table 2.37: Comparison of the Formation Rates of Intermediate Complexes (**1a-1g**), (**3a-3g**) and (**4a** and **4g**).

Reactant	**k_f $(sec)^{-1}$ x 10^5 (1a-1g)**	**k_f $(sec)^{-1}$ x 10^5 (3a-3g)**	**k_f $(sec)^{-1}$ x 10^5 (4a** and **4g)**
PMe_3	92.0[a]	15.1[a]	35.1[e]
PMe_2Ph	92.0[b]	20.5[a]	**ND**
PEt_3	23.9[b]	9.8[d]	**ND**
$P(n\text{-}Bu_3)$	14.2[c]	**ND**	**ND**
PEt_2Ph	28.5[d]	4.8[d]	**ND**
$PMePh_2$	8.76[c]	3.17[a]	**ND**
$PEtPh_2$	3.65[a]	1.24[b]	23.8[e]

a) recorded at 22° C. b) recorded at 26° C. c) recorded at 21° C. d) recorded at 23.5° C. e) recorded at 20° C.
ND = not determined

It is immediately evident that two features distinguish the reactivity in these systems, which are consistent with the observations presented in **Chapter 1** and **Chapter 3** of this work. As such the first distinguishing feature involves substrate effects, while the second involves the nature of the

starting Mo complex. The substrate effects can be exemplified when the reactivity of (**1**), (**3**) and (**4**) with $PEtPh_2$ are compared to their corresponding reactivity with PMe_3 where, in all cases, PMe_3 generally leads to faster intermediate formation. On the surface, this slower reaction is consistent with both the lower pK_a of $PEtPh_2$ (6.25), relative to that of PMe_3 (8.65) as well as greater steric bulk of $PEtPh_2$ (Tolman Cone Angle = 136º) relative to that of PMe_3 (118°).

However, this difference in reactivity is also dependant upon the starting Mo complexes, such that the general order of increasing reactivity towards PMe_3 are as follows: (**3**) < (**4**) < (**1**). Interestingly, the reactants follow a different order of increasing reactivity towards $PEtPh_2$ such that: (**3**) < (**1**) < (**4**). Thus (**3**) is expected to be the least reactive metal complex, while (**1**) has a large variability in reactivity and appears to have the greatest specificity towards phosphines. On the other hand, it appears that (**4**) exhibits a smaller degree of substrate variability while expressing the least substrate specificity. This selectivity is most accentuated by the comparison of the reactivity ratios (k_{PMe3}/k_{PEtPh2}) of (**1**) with a ratio of 25.2, (**3**) with a reactivity ratio of 12.1, and (**4**) which is only slightly more reactive towards PMe_3 than $PEtPh_2$ with a 1.5 reactivity ratio. Thus, with the noted exception of (**4**), the rate of the reaction leading to intermediate formation is strongly influenced by a combination of the relative basicity of the attacking phosphine as well as the size of the phosphine. More specifically, these results may suggest that the Mo-oxo ligand has sufficient acidity to react faster with stronger bases, which have relatively small cone angles.

On the other hand, the substitution of the oxo-phenolate ligand in (**3**) with a sulfur thiolate ligand in (**4**) results in a significant increase in reactivity towards phosphines such that the $k_{(4)}/k_{(3)}$ ratio is 2.3 for PMe_3 and 19.2 for $PEtPh_2$. At this point the origins of the higher reactivity in the sulfur verses oxygen comparison remain unknown, with future work directed towards understanding these observations. However a more detailed discussion on the reactivity of phosphorous

compounds in oxidation reactions, especially in the reactions of (**1**) with phosphines, can be found in **Chapter 3** of this work.

Accordingly, when the differences between the enthalpic barriers are compared, (**Table 2.38**) there is a significant substrate effect in the reactions of (**1**) such that the greatest difference arises between PMe_2Ph and $PEtPh_2$ (39.1 kJ/mol), while the difference between PMe_3 and $PEtPh_2$ are surprisingly smaller (7.9 kJ/mol), given their difference in pka and size. Even more surprising is the comparison of these same effects in (**3**) and (**4**). The reactions of (**3**) reflect a trend that is nearly opposite of (**1**) such that the difference between PMe_3 and $PEtPh_2$ represent one of the greatest differences (21.3 kJ/mol), and are expressed in the opposite order (the enthalpic barrier for $PEtPh_2$ is lower than that of PMe_3 for (**3**)). Furthermore, greatest difference for (**3**) arises between $PMePh_2$ and PMe_3 (24.6 kJ/mol), whereas this difference not significant (1.3 kJ/mol) in the reactions of (**1**), despite the similarity between the PMe_3 ethalpic barriers for these two complexes (0.7 kJ/mol). However, the reactions of (**4**) with PMe_3 and $PEtPh_2$ are surprisingly similar to those of (**1**) with a (7.8 kJ/mol) difference in these ethalpic barriers.

Furthermore, when the entropic contributions to the barrier to intermediate formation are compared, across all substrates, the reactions of (**1**) and (**3**) share a similar average contribution such that $T\Delta S^{\ddagger}$ contributes 27.7 ± 16 percent in (**1**) and 26.9 ± 7 percent in (**3**) towards $\Delta G^{\ddagger}_{298}$. On the other hand, the reactivity of the two substrates measured for (**4**) suggest that there is a two fold increase in the entropic contribution to the barrier relative to the average contribution in (**1**) and (**3**). For example, the average entropic contribution for reactions with PMe_3 expresses an average contribution in (**1**) and (**3**) of 19.5 ± 2.8 percent, while that of (**4**) is 56.5 percent.

Table 2.38: Enthalpy and % Entropic Contribution (298.15 K) to the Barrier for the First Step in the Reaction: Reduction of (**1**), (**3**) and (**4**) with Phosphines to Yield Compounds (**1a-1g**), (**3a-3g**), (**4a** and **4g**).

Reactant	**$\Delta H^{\ddagger}$ (kJ/mol)[a] (1)**	**$\Delta H^{\ddagger}$ (kJ/mol)[a] (3)**	**$\Delta H^{\ddagger}$ (kJ/mol)[a] (4)**
PMe_3	74.6 (17.5)	73.9 (21.5)	40.1 (56.5)
PMe_2Ph	43.1 (52)	59.7 (36.2)	**ND**
PEt_3	48.4 (48)	66.0 (30.3)	**ND**
P(*n*-Bu_3)	66.8 (28.4)	**ND**	**ND**
PEt_2Ph	83.2 (11.5)	58.1 (16.1)	**ND**
$PMePh_2$	73.3 (22.7)	49.3 (29.7)	**ND**
$PEtPh_2$	82.5 (15.4)	52.6 (27.7)	47.9 (48.4)

a) the number in parenthesis indicates the percent contribution of $T\Delta S^{\ddagger}$ (298.15K) to the $\Delta G^{\ddagger}_{298}$

Taken together, the enthalpic barrier to the reactivity of (**1**) resembles that observed in the reactivity of (**4**), while the entropic contributions are closer in the reactivity of (**1**) and (**3**). However, when the additive effects of the enthalpic and entropic contributions to the barrier of activation are considered the reactivity of (**4**) and (**1**) appear more closely related than those of (**1**) and (**3**). For example, the entire reaction coordinate for the reaction of (**1**) and (**4**) with PMe_3 result in a nearly identical barrier to (**1a**) and (**4a**) formation when referenced to (**3**) (**Table 2.39** and **Figure 2.24**). In contrast, the reaction of (**3**) with PMe_3 results in an approximate 10 kJ/mol increase in the barrier to the formation of (**3a**) relative the barriers to (**1a**) and (**4a**) formation. In general, the predominant effect upon the reaction barrier, in the case of the oxygen ligated complexes (**1**) and (**3**), appears to be of enthalpic origins while the sulfur containing (**4**) appears to have a more uniform enthalpic and entropic contribution to reaction with phosphines.

Table 2.39: Approximate Reaction Coordinate for the First Step in the Reaction: Reduction of (**1**), (**3**) and (**4**) with Phosphines to Yield Compounds (**1a-1g**), (**3a-3g**), (**4a** and **4g**) Relative to (**3**)			
Reactant	**$\Delta G'^{\ddagger}$ (kJ/mol)[d] (1)**	**$\Delta G'^{\ddagger}$ (kJ/mol)[d] (3)**	**$\Delta G'^{\ddagger}$ (kJ/mol)[d] (4)**
	-8.8[c]	0[c]	-10.5[c]
PMe_3	81.6	94.27	81.5
PMe_2Ph	81.0	93.57	**ND**
PEt_3	84.1	94.65	**ND**
$P(n\text{-}Bu_3)$	85.2	**ND**	**ND**
PEt_2Ph	84.4	69.23	**ND**
$PMePh_2$	86.0	70.09	**ND**
$PEtPh_2$	88.7	72.69	82.2
c) $\Delta G'^{o}$ represents the energy relative to (**3**) expressed as [ΔG^{o}(**1-4**)- ΔG^{o}(**3**)]; d) $\Delta G'^{\ddagger}$ energy relative to (**3**) expressed as {$\Delta G^{\ddagger}$ [**(1-4)a-(1-4)g**] + $\Delta G'^{o}$(**1-4**)}.			

When the effects of solvent were examined for the reaction of PEt_3 with $Tp^{iPr}Mo^{VI}O_2(OPh)$ it was found that the rate was 1.7 times faster in acetonitrile than in benzene. The calculations indicate that the reactant has a larger dipole moment than the transition state. If the solvent effect was purely due to the dielectric constant of the solvent one would expect the opposite of what is seen experimentally. Actual solvent effect calculations parallel this expectation as the barriers in solution are calculated to be larger than those for the gas phase and the barrier in benzene is lower than that calculated for acetonitrile. Therefore, acetonitrile may be involved in the first step of the OAT reaction of this system to the degree that standard "bulk" solvent corrections fail to predict this behavior.

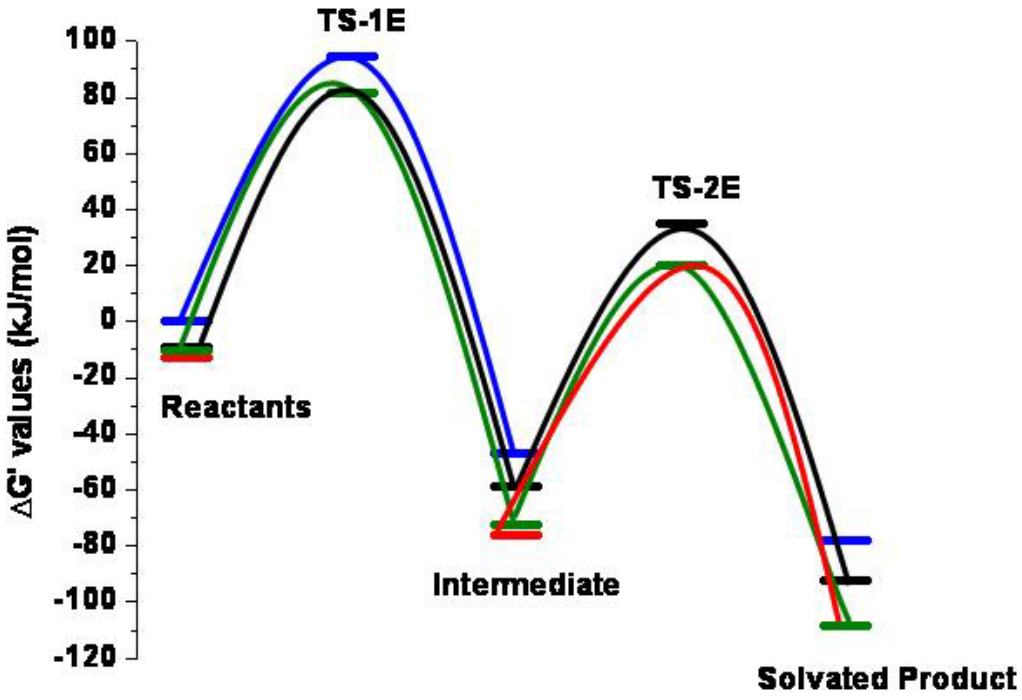

Figure 2.24: Experimental Reaction Pathway for the Reaction of (**1**) (Black Lines), (**2**) Red Lines, (**3**) Blue Lines and (**4**) Green Lines with PMe_3. All Reaction Coordinates are Reference to the Energy of (**3**) as Detailed in the Text.

In all cases the first step of the formation of intermediates (**1a-1g**), (**3a-3g**), and (**4a** and **4f**) proceed via an associative mechanism as evidenced by the rather large negative entropies of activation. Furthermore, the enthalpy of activation generally dominates the barrier and suggests that there is a significant degree of bond breaking and forming in the transition state for each series of complexes, with the exception of (**4**). Lastly the general higher entropic contributions present in the reactions of (**4**) suggest that the transition states leading to the formation of (**4a**) and (**4g**) are more ordered than those leading to (**1a**), (**1g**), (**3a**) and (**3g**). The greater order in the transition state for (**4**) counteracts the lower enthalpic demands required for the formation of (**4a**) and (**4g**) and leads to a free energy of activation that is similar to that observed in the reactions of (**1**).

Moreover, the relatively broad ranges for the enthalpy of activation, $\Delta\Delta H^{\ddagger} \approx 40$ kJ/mol in the case of (**1**), reflects a difference in basicity of the phosphines coupled with differences in steric interactions in the transition state. Some support for this argument can be found in the reactions of the less sterically hindered (**3**) which provides a much smaller range in $\Delta\Delta H^{\ddagger} \approx 22$ kJ/ mol. The reactions of (**4**) suggest that sulfur donors coupled with the smaller steric effect further reduce the enthalpic contributions to a near constant 40 kJ/mol.

The calculations, which predict an associative transition state with a solvent-corrected free-energy barrier of 95.0 kJ/mol for the reaction of the simplest substrate, PMe_3, are in reasonable agreement with these experimental results ($\Delta G^{\ddagger}$ = 90.4 (**1a**), 94.3 (**3a**) and 92.0 (**4a**) kJ/mol). The calculated structure for this first transition state, TS-IC, suggests that there are two components to its electronic structure. Usually, the attack on the M=O bond by a substrate is thought of as the attack of a nucleophile (the substrate) on the π^* M=O orbital forcing a $2e^-$ reduction of the metal center. Ultimately, of course, this is the final outcome. However, the metal-based oxygen may also act as a nucleophile and attack an empty orbital on the substrate. The surprisingly the large O–P–C_{Me} angle (153.0°) suggests that some of this "role reversal" is taking place in TS-IC. If the attack of PMe_3 on the Mo=O bond only involved the P lone pair attacking the Mo=O π^*, one would expect the 3-fold axis of PMe_3 to be aligned with the axis of attack, P→O. This alignment would produce an O–P–C_{Me} angle of ~115°. On the other hand, if the O were the nucleophile and it attacked the P through the P–C_{Me} σ^* orbital, the P would become a hypervalent trigonal bipyramid (surrounded by 5 electron pairs) with its own lone pair in an equatorial TBP site. In this alternative, the O–P–C_{Me} angle would be 180°. Thus, the calculated angle of 153.0°, which is nearly halfway between the two extremes, suggests an intermediate situation with nearly equal mixtures of the two types of

nucleophilic attack. As the system proceeds to the intermediate, the O–P–C_{Me} angle decreases to that expected for $OPMe_3$.

Mechanism of loss of OPR_3 from $Tp^{iPr}MoO(OPh)(OPR_3)$:

It has been established that there are three spectrally distinct species (**1c**, **5** and **9**) present during the decomposition of (**1c**); two of which are major spectral contributors and one that is a minor spectral contributor within the observed reaction time. More explicitly, the two principal components account for over 95% of the observed spectral variation, the remaining 5% being accounted for by the third species and spectral noise vectors. The spectrum of $Tp^{iPr}MoO(OPh)(OPEt_3)$ (**1c**), constructed through SVD analysis, follows a single exponential decay with a half-life of 49 minutes at 11 °C. Another important result was that the spectrum of the second species (**9**), which was blue in color, could be assigned as the MeCN bound species $Tp^{iPr}MoO(OPh)(MeCN)$, whose temporal vectors could also be fit as a single exponential decay with a half-life of approximately 55 minutes at 11 °C. Lastly, SVD predicted that a third (**9**), minor component increased comparatively slowly over time with a single exponential halftime of 400 minutes at 11 °C. The brown species (**9**) has been assigned as an oxo-bridged dinuclear complex in analogy to a hydrotris(3,5-dimethylpyrazol-1-yl)borate ligand, $[(Tp^{Me2}MoOCl)O(Tp^{Me2}MoCl(MeCN)]$. Interestingly, the relatively large extinction coefficient of a dinuclear species, at ~500 nm, suggests that small amounts of the dimer will result in a physically observable color change due to the ~ 10-fold more intense LMCT. Furthermore, concurrent with the growth of the intense 500 nm band was a loss of 680 nm and 910 nm transitions. Thus a new high intensity band developed and the low intensity bands decreased which resulted in the readily observed color change when small amounts of the dinuclear product were present. Taken together

the loss of phosphine oxide from the intermediate proceeds through more than one transition state (**TS-IIE**, **TS-IIC**, **TS-IIC'**, and **TS-IIIE**), the first three may be involved in the formation of a solvated species while the last one is associated with the formation of a dinuclear species. The natures of two of the four transition states have been defined experimentally.

The loss of phosphine oxide from (**1a-1g**), (**2a-2g**) and (**4a** and **4g**) follows a first-order process with respect to the concentration of the intermediate complex. The absence of an observable solvent dependence (no differences were observed in the solvation rates in tetrahydrofuran or acetonitrile) upon the rate of the reaction was consistent with this proposal. However, the decay reaction of (**2a**) in mixed benzene/acetonitrile solutions shows a linear dependence of the solvation rate with respect to acetonitrile concentration. This then suggests that under normal reaction conditions, the rate of solvation is saturated and appears to depend only upon the concentration of the intermediate. However, the rate of conversion from the solvated product, **(5)** in the case of acetonitrile**,** to (**9)** is strongly influenced by the nature of the solvent such that the reaction proceeds twice as fast in acetonitrile than in THF, suggesting acetonitrile is a better leaving group.As observed in the first step of the reaction, the solvation step is influenced both by the nature of the phosphine oxide leaving group and the ligand system of the metal complex, as indicated in **Table 2.40**.

Table 2.40: Comparison of the Solvation Rates of Intermediate Complexes (**1a-1g**), (**2a-2g**) and (**4a**) and (**4g**).

Reactant	k_s **(sec)$^{-1}$ x 10^5 (1a-1g)**	k_s **(sec)$^{-1}$ x 10^5 (2a-2g)**	k_s **(sec)$^{-1}$ x 10^5 (4a** and **4g)**
PMe_3	23.4[a]	4.1[f]	24.8[f]
PMe_2Ph	124.5[b]	18.0[d]	**ND**
PEt_3	153.5[c]	12.1[d]	**ND**
$P(n\text{-}Bu_3)$	148.4[d]	12.6[d]	**ND**
PEt_2Ph	222.5[e]	56.6[d]	**ND**
$PMePh_2$	651.0[f]	107.5[d]	**ND**
$PEtPh_2$	383.1[f]	237.6[d]	332.1[f]

a) recorded at 26° C. b) recorded at 22.5° C. c) recorded at 22° C. d) recorded at 21° C. e) recorded at 23.5° C. f) recorded at 20.0° C.
ND = not determined

The leaving group dependence of the solvation reaction can be demonstrated by comparing the rate of solvation of (**1a**) and (**1g**), which shows at least a 16-fold increase in the solvation reaction of (**1g**) relative to that observed in (**1a**) if temperature differences are ignored. Moreover the greatest difference in solvation rates occurs between the solvation reactions of (**1a**) and (**1f**) which approaches a 28-fold increase in the solvation rate of (**1f**) relative to that of (**1a**). Interestingly the solvation reations of (**4a**) and (**4g**) display an approximate 13-fold increase in rate, and is similar to the differences observed in the solvation of (**1a**) and (**1g**). Lastly, this leaving group dependence is further accentuated by the comparison of (**2a**) and (**2g**) which display an approximate 58-fold increase in the solvation of (**2g**).

When the dependence of the metal ligand architecture is examined, there are nearly identical rates for the solvation of for both the (**1a;4a**) and (**1g;4g**) pairs, despite the differences observed in the formation step of these species. However when all complexes are compared, the overall rates of the solvation reaction can be arranged in increasing order as follows: (**2a-2g**) < (**1a-1g**) ~ (**4a** and **4g**).

The enthalipic and entropic contributions to the solvation reaction also reflects leaving group dependence, and for (**1a-1g**), reflect trends similar to those observed in the formation reaction. For example when PMe_3 and $PEtPh_2$ are compared, there is an approximate 8 kJ/mol higher enthalpic contribution in the barrier leading to free $OPEtPh_2$ relative that of free $OPMe_3$. In addition, the greatest enthalpic difference mirrors that in the formation reaction and occurs between PMe_2Ph and $PEtPh_2$ with an approximately 40 kJ/mol higher enthalpic contribution in $PEtPh_2$. More specifically there is a relatively broad range in the enthalpic contributions when (**1a-1g**) are taken together such that $\Delta H^{\ddagger}_{avg}$ = 67.4 ± 15.9 kJ/mol and spans from 43.1 to 83.2 kJ/mol in PMe_2Ph and PEt_2Ph respectively. However, the most interesting feature of this series is related to the entropic contributions to the barrier, which are distinguished in two ways. First, the entropy of activation for both the solvation of (**1a**) and (**1g**) are show a marked difference in that they are both negative. This is in stark contrast to the remaining complexes (**1b-1f**), which express positive entropy of activation. The second feature regarding entropic contributions is that, when only the positive entropies are considered, there is an extremely broad range expressed that $T\Delta S^{\ddagger}_{298}$ spans from 5.4 kJ/mol (PMe_3) to 27.3 kJ/mol ($P(n\text{-}Bu_3)$) and a percent $T\Delta S^{\ddagger}_{avg}$ = 16.0 ± 10.4 kJ/mol at 298 K.

In contrast, the solvation of (**2a-2g**) shows a much more uniform enthalpic contribution with $\Delta H^{\ddagger}_{avg}$ = 80.7 ± 7.1 kJ/mol, and spans from 89.3 to 70.0 kJ/mol in PEt_2Ph and $PEtPh_2$ respectively. When (**2a**) and (**2g**) are compared, the difference in the enthalpic contributions to solvation show a

17.5 kJ/mol lower barrier to the solvation of (**2g**), which is an opposite trend relative the same comparison in (**1a;1g**) and (**4a;4g**). Unlike the solvation of (**1a-1g**), the entropic contribution is marked by a negative values in all cases, but expressed a similar percent $T\Delta S^{\ddagger}_{avg}$ = 12.3 ± 5.8 kJ/mol at 298 K.

Lastly, complexes (**4a**) and (**4g**) show a difference in enthalpic barriers of 40 kJ/mol, and represent the largest difference for the loss of $OPMe_3$ and $OPEtPh_2$ that has been observed. However, the solvation of (**4a**) also represents the lowest enthalpic contribution that was found for the release of $OPMe_3$ while that of (**4g**) represents the greatest enthapic contribution observed for the release of $OPEtPh_2$. In terms of the entropic barrier, the solvation of the two intermediates of (**4**) are quite similar to that observed in (**1a**) and (**1g**) in that one reaction shows positive entropy while the other shows negative entropy. However, unlike (**1g**), which expresses negative entropy, the solvation of (**4g**) expresses positive entropy. Interestingly, the entropic contributions to the barrier for both the solvation of (**4a**) and (**4g**) provide a constant contribution to $\Delta G^{\ddagger}_{298.}$

Table 2.41: Enthalpy and % Entropic Contribution [100*($T\Delta S^{\ddagger}/\Delta G^{\ddagger}$)] to the Barrier for the Second Step in the Reaction: Solvation of (**1a-1g**), (**2a-2g**), (**4a** and **4g**) to yield (**5**), (**6**) and (**8**) respectively.

Reactant	**$\Delta H^{\ddagger}$ (kJ/mol)[a] (1)**	**$\Delta H^{\ddagger}$ (kJ/mol)[a] (2)**	**$\Delta H^{\ddagger}$ (kJ/mol)[a] (4)**
PMe_3	74.6 (42.6)	87.5 (9.4)	67.8 (26.6)
PMe_2Ph	43.1 (20.1)	81.8 (12.8)	**ND**
PEt_3	48.4 (6.1)	81.1 (14.0)	**ND**
$P(n\text{-}Bu_3)$	66.8 (30.8)	82.4 (1.3)	**ND**
PEt_2Ph	83.2 (6.3)	89.3 (12.4)	**ND**
$PMePh_2$	73.3 (16.8)	73.0 (16.4)	**ND**
$PEtPh_2$	82.5 (25.1)	70.0 (19.6)	107.8 (25.9)

a) the number in parenthesis indicates the percent contribution of $T\Delta S^{\ddagger}$ (298.15K) to the $\Delta G^{\ddagger}_{298}$

Taken together, the reaction coordinate for the solvation of the reaction intermediates resulting from (**1**), (**2**) and (**4**) reflect the complexity that was observed in the formation of these same intermediates, when referenced to (**3**). For example, the barrier to the solvation of (**1a-1g**), expressed as $\Delta G_2'^{\ddagger}$ (**Table 2.42**) shows a surprisingly narrow range with $\Delta G_2'^{\ddagger}_{avg}$ = 32.2 ± 2.0 kJ/mol at 298 K. That same barrier in (**2a-2g**) solvation is somewhat lower and broader with $\Delta G_2'^{\ddagger}_{avg}$ = 12.9 ± 6.0 while the solvation of (**4a**) and (**4g**) reflect this trend as well. In fact, when the reaction coordinate is referenced to (**3**), the solvation of (**2a**) and (**4a**) present an identical barrier, while that of (**1a**) is 15kJ/mol higher. This suggests that, in the solvation reaction, the more sterically encumbered intermediates of (**1**), result in overall greater kinetic stability despite their relatively lower thermodynamic stability: ΔG^{o}(**1a**) = 64 kJ/mol, verses ΔG^{o}(**2a**) = 46.8 kJ/mol and ΔG^{o}(**4a**) = 50.9 kJ/mol; ΔG^{o}(**1g**) = 65.8 kJ/mol, verses ΔG^{o}(**2g**) = 45.1 kJ/mol and ΔG^{o}(**4g**) = 50.4 kJ/mol.

Table 2.42: Approximate Reaction Coordinate for the Second Step in the Reaction: Solvation of (**1a-1g**), (**2a-2g**), (**4a** and **4g**) to yield (**5**), (**6**) and (**8**) respectively relative to (**3**)			
Reactant	**$\Delta G_2'^{\ddagger}$ (kJ/mol)[a] (1)**	**$\Delta G_2'^{\ddagger}$ (kJ/mol)[a] (2)**	**$\Delta G_2'^{\ddagger}$ (kJ/mol)[a] (4)**
	-8.8[b]	-12.5[b]	-10.5[b]
PMe_3	35.0	20.4	20.2
PMe_2Ph	31.9	6.9	**ND**
PEt_3	31.2	7.7	**ND**
$P(n\text{-}Bu_3)$	33.7	10.0	**ND**
PEt_2Ph	29.8	15.4	**ND**
$PMePh_2$	33.8	20.7	**ND**
$PEtPh_2$	29.7	9.1	13.04
NCMe	-92.5[c]	-116.1[c]	-108.6[c]
a) $\Delta G_2'^{\ddagger}$ energy relative to (**3**) expressed as {$\Delta G_2^{\ddagger}$ [**(1-4)a-(1-4)g**] + $\Delta G'^{o}$[(1-4)**a-(1-4)g**]). b) $\Delta G'^{o}$ represented as the energy relative to (**3**) expressed as [ΔG^{o}(**1-4**)- ΔG^{o}(**3**)]; c) $\Delta G'^{o}$ represented as the energy relative to (**3**) expressed as [ΔG^{o}(**5-8**)- ΔG^{o}(**3**)];			

At 5 °C in MeCN, the rate of decomposition of $Tp^{iPr}MoO(OPh)(OPEt_3)$ is approximately seven times slower than that of $Tp^{iPr}MoO(OPh)(OPPh_2Me)$, suggesting that there is a strong dependence on the leaving group. This leaving group dependence is most clearly expressed in the enthalpy of activation of the two processes, which favors formal loss of $OPEt_3$ by ~30 kJ/mol. More explicitly, the enthalpy of activation for ligand ($OPEt_3$) dissociation is 34% smaller than that for $OPPh_2Me$, which may reflect the bond strength of the two intermediate molecules. It is important to point out that the crytallographically determined Mo—OP bond distances in $Tp^{iPr}MoO(OPh)(OPEt_3)$ and in $Tp^{iPr}MoO(OPh)(OPPh_2Me)$ are 2.157(3) Å and 2.172(3) Å, respectively, thus suggesting that this bond is weaker in the $OPPh_2Me$ than in the $OPEt_3$ complex.

The weakness of the Mo-OP bond in (**1f**) relative to (**1c**) is further supported by the CV data which expresses an ~ 2 kJ/mol greater instability for (**1f**). Taken together these results suggest an early transition state in the solvation of (**1c**) which would be more reactant like, while a late transition state in (**1f**) would be more product-like. More specifically, (**1c**) with its stronger Mo-OP bond, would have little breakage in the transition state while the same bond in (**1f**) would be mostly ruptured. Despite this strong enthalpic dependence, with respect to the leaving group, there is a 29 $J/mol^{-1}K^{-1}$ difference in the entropy of activation. In addition, at 298 K, the entropic term ($T\Delta S^{\ddagger}$) contributes significantly towards the free energy of activation accounting for approximately 6% in (**1c**) and 16% in (**1f**) towards the total free energy. However, the entropy of activation for both leaving groups is positive and indicates an overall dissociative mechanism.

This case generally holds for the solvation of the intermediates of (**1**) with the noted exceptions of (**1a**) and (**1g**), where the activation parameters are marked by strong negative entropies of activation thus indicating an associative type mechanism.

Interestingly, when the solvations of the intermediates of (**2**) are considered, negative entropies of activation are expressed in all cases suggesting an associative type mechanism is persistent. Although the solvation of (**4a**) is entropically consistent with its analogues (**1a** and **2a**), the solvation of (**4g**) is not. Thus the solvation of (**4g**) appears to follow a dissociative type mechanism as determined by its positive entropy of activation, and is in contrast to the (**1g**) and (**2g**) analogue complexes.

The DFT calculations predict that the dissociative route through the 5-coordinate intermediate (INT-IIC) is favored over the associative route by ~33 kJ/mol. However, our model system (**1a**) fails to account for the experimentally determined associative type mechanism in this complex. We also calculated a triplet state for the five-coordinated intermediate on the dissociative

path. The geometry of this state is trigonal bipyramidal. The calculations predict this structure to be several kJ/mol more stable than the singlet. However, it is known that the B3LYP method overestimates the stability of triplet states.[56] Furthermore, no indication of any contribution by a triplet state was observed in the experiments. Thus, we believe that the triplet is less stable than the singlet and hence, it is not important in this reaction.

Although it is clear that the first step of the decomposition of the intermediate complexes of (**1**) (i.e., step 2 in **Figure 2.9**) generally follows a dissociative type mechanism, the activation parameters alone cannot distinguish between an dissociative interchange or a pure dissociative mechanism for either of the $Tp^{iPr}MoO(OPh)(OPR_3)$ complexes. Furthermore, in the cases of an associative type mechanism (**1a**), (**1g**), (**2a-2f**) and (**4a**), it is also impossible to distinguish an associative interchange or pure associative mechanism. Thus, as the calculations predict, the dissociation of the phosphine oxide is the lowest energy path and if it is assumed that this path is the only pathway operative we can look to the Hammond postulate for justification. For a pure dissociative mechanism to be operative, the Mo-center would need to pass through a penta-coordinate (INT-IIC, **Figure 2.22**) species prior to solvent coordination. In order for a dissociative interchange (I_d) mechanism to be operative, the formation of Mo—solvent bond has to start before the Mo—OP bond is completely broken, thus stabilizing the transition-state by never allowing the metal center to become truly penta-coordinated. Positive entropy of activation suggests that in the transition state bond breaking is more important than bond making. In a non-coordinating solvent, such as benzene or hexane, making a bond with a solvent molecule is unlikely, and the reaction proceeds directly to a dinuclear species. These observations are further supported through conducting the decomposition reaction in pyridine, where the reaction proceeds rapidly with no detectable dinuclear product. The calculations support a dissociative mechanism from the predicted

high stability of the 5-coordinate intermediate and the calculated higher energy associative reaction path, but as with the experimental results, the calculations cannot really distinguish between a true dissociative mechanism and a dissociative interchange one, as this choice will be very solvent and substrate dependent. The calculations find a pure dissociative free energy barrier of 109.9 kJ/mol, which is 16 kJ/mol higher in energy than the experimental value (93.9 kJ/mol). The larger calculated free energy barrier, compared to the experimental value, is an indication that the loss of phosphine oxide in a solution of MeCN may be better described by an interchange mechanism.

Thus, a third possibility remains that may explain all of the findings such that in any reaction, in its transition state, that must more completely break the Mo-OP bond prior to solvation would express positive entropies of activation and be defined as an early transition state. On the other hand, any reaction that involves a larger degree of solvent coordination in the transition state, would express negative entropies of activation and be defined as a late transition state. More clearly, the case of the early transition state would appear as a more pure dissociative mechanism, with bond breaking dominating the energetics such that a transition state structure should appear more intermediate-like with an extremely long Mo-OP bond (the structure would lie between INT-IIC and the starting intermediate). In the case of the late transition state, the Mo-OP bond has weakened to the point of dissociation, but bond formation with the solvent becomes dominant in the energetics such that the transition state structure should appear more product-like (solvated complex) with a well formed bond to solvent and a completely dissociated phosphine oxide (the structure would lie between INT-IIC and the solvated complex).

Under the experimental conditions, the dinucleation of $Tp^{iPr}MoO(OPh)(MeCN)$ appears to follow a first-order kinetics with respect to the concentration of the intermediate, where the rate is dependent on the initial concentration of the complex. The absence of an observed solvent

concentration dependence on the rate of the dinucleation, suggests that there is equilibrium between the coordinated and bulk MeCN. Once the coordinated solvent molecule dissociates, the penta-coordinated species combines with another molecule of $Tp^{iPr}MoO(OPh)(MeCN)$ resulting in a dinuclear complex. Support for this proposed mechanism can be seen in the lack of a statistical difference in the observed rate of dinucleation in solutions of 3 mM or 9 mM $Tp^{iPr}MoO(OPh)(OPEt_3)$, which is expected to approximately triple for a second-order dependency. Further support of this proposal can be derived through the observation of a solvent dependent rate. For example, in a solution of $Tp^{iPr}MoO(OPh)(OPEt_3)$ at 22º C, the rate of dinucleation in THF is 3.49×10^{-3} min^{-1} while that in MeCN is $7.62.0 \times 10^{-3}$ min^{-1}. Lastly, when the full reaction coordinate of (**1c**) and (**1f**) (as referenced to the reaction coordinate for (**3**)) are considered, the inclusion of the dinucleation step reveals that it most likely originates from the solvated species (**Figure 2.25 and Table 2.43**).

Table 2.43: Approximate Full Reaction Coordinate for the Formation and Solvation of (**1c**) and (**1f**), to yield (**5**), and subsequently form (**9**) relative to (**3**)

Reactant	**ΔG' (kJ/mol) (1c)**	**ΔG' (kJ/mol) (1f)**
Dioxo Complex (**1**)	-8.8[a]	-8.8[a]
$[MoO\text{-}OPR_3]^{\ddagger}$	84.1[b]	86.0[b]
INT	-56.9[c]	-55.0[c]
Dinucleation of INT	31.7[d]	33.6[d]
$[MoO(OPR_3)(NCMe)]^{\ddagger}$	31.2[e]	28.8[e]
Mo-NCMe	-92.5[f]	-92.5[f]
Dinucleation of Mo(NCMe)	-3.9[g]	-3.9[g]

a) $\Delta G'^{o}$ represented as the energy relative to (**3**) expressed as $[\Delta G^{o}(\mathbf{1}) - \Delta G^{o}(\mathbf{3})]$;
b) $\Delta G_1'^{\ddagger}$ energy relative to (**3**) expressed as $\{\Delta G_1^{\ddagger}[\mathbf{(1c),(1f)}] + \Delta G'^{o}[(\mathbf{1})]\}$.
c) $\Delta G'^{o}$ represented as the energy relative to (**3**) expressed as $[\Delta G^{o}[(\mathbf{1c}),(\mathbf{1f})] - \Delta G^{o}(\mathbf{3})]$;
d) $\Delta G_3'^{\ddagger}$ energy relative to (**3**) expressed as $\{\Delta G_3^{\ddagger}[\mathbf{(1)c,(1)f}] + \Delta G'^{o}[(\mathbf{1c}),(\mathbf{1f})]\}$.
e) $\Delta G_2'^{\ddagger}$ energy relative to (**3**) expressed as $\{\Delta G_2^{\ddagger}[\mathbf{(1)c,(1)f}] + \Delta G'^{o}[(\mathbf{1c}),(\mathbf{1f})]\}$.
f) $\Delta G'^{o}$ represented as the energy relative to (**3**) expressed as $[\Delta G^{o}(\mathbf{5}) - \Delta G^{o}(\mathbf{3})]$;
g) $\Delta G_3'^{\ddagger}$ energy relative to (**3**) expressed as $\{\Delta G_3^{\ddagger}[\mathbf{(1)c,(1)f}] + \Delta G'^{o}[(\mathbf{5})]\}$.

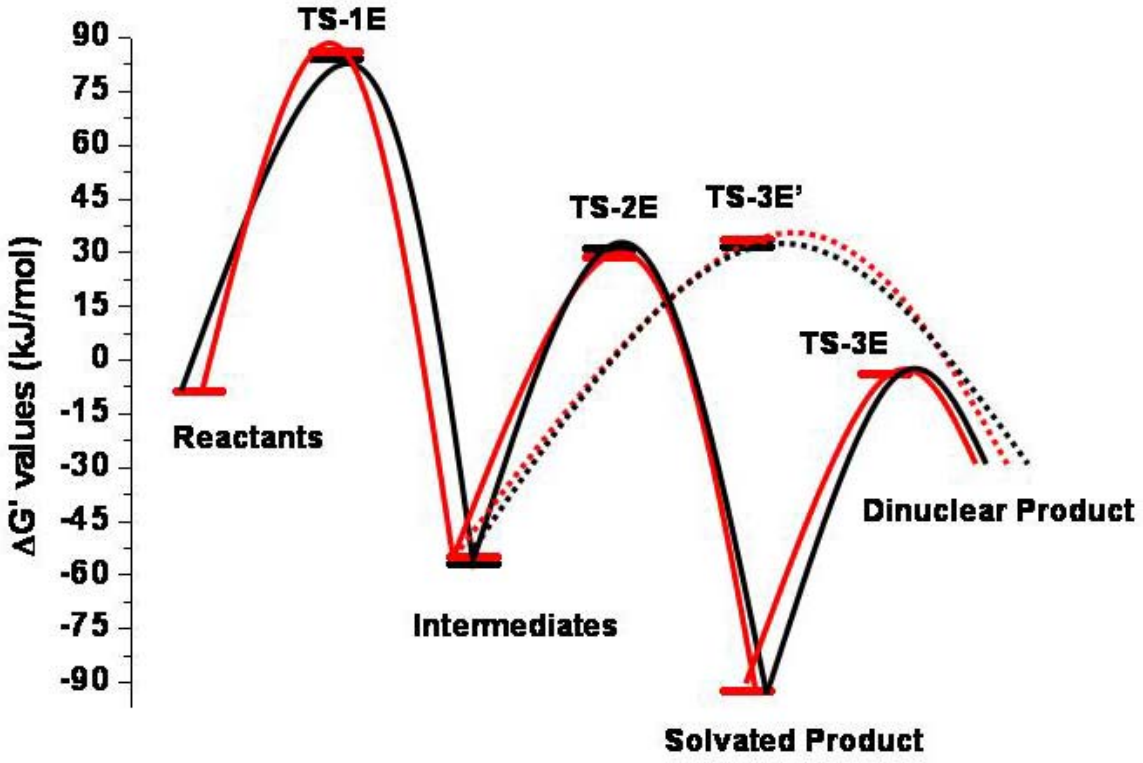

Figure 2.25: Experimental Reaction Pathway for the Reaction of (**1**) with PEt_3 (Black Lines) and $PMePh_2$ (Red Lines). Solid Lines Represent the Primary Pathway, while Dotted Lines Represent an Alternative Pathway to the Dinuclear Product. The Energies were determined as presented in the text.

For the dinucleation of (**1c**) and (**1f**) there are two distinct pathways, the first of which orginates from the intermediate species and the second originates from the solvated complex. When the $\Delta G^{\ddagger}$ of the dinucleation reaction, which is the same for both (**1c**) and (**1f**), is added to both the $\Delta G°$ of the intermediate (INT) and the solvated product (Mo-NCMe) it becomes apparent that the dinuclear product is easier to form from the solvated product. However, for (**1c**) it appears that it is thermodynamically equally as likely to proceed to the dinuclear complex from either the INT or the Mo-NCMe complex. This suggests that, in the case of (**1c**), the formation of the solvated complex is kinetically controlled, and that the dinuclear species arises from the acetonitrile adduct. Moreover, in the case of (**1f**), the reaction path leading to the formation of the solvated product is favored by ~

5 kJ/mol over the direct conversion to the dinuclear species. Thus since the rate constants for the formation of the dinuclear species are identical for (**1c**) and (**1f**) it becomes clear that the only energetically equivalent path that is available results from the solvated complex.

Unlike $Tp^{iPr}MoO(OPh)(OPEt_3)$ the change in the low energy band (900 nm) for $Tp^{iPr}MoO(OPh)(OPPh_2Me)$ showed a double exponential behavior from which the rate of dimerization was determined. In this system, at 10 ºC a rate constant of 1.10 x 10^{-3} min^{-1} was observed. When these rate constants were included in the Eyring or Arrhenius plots for $Tp^{iPr}MoO(OPh)(OPEt_3)$ the linearity was maintained. From the combined data set the activation parameters were determined. Although the relatively high errors associated with the activation parameters do not allow unambiguous description of the mechanism, a close to zero entropy of activation suggests that bond breaking might be more important.

3. The overall reaction profile.

Schematically, using $Tp^{iPr}Mo^{VI}O_2(OPh)$ as a model, the experimental reaction path is shown in **Figure 2.26**. When the reaction is viewed in its entirety, $Tp^{iPr}Mo^{VI}O_2(OPh)$ to $Tp^{iPr}Mo^{IV}O(OPh)(OPR_3)$ to $Tp^{iPr}Mo^{IV}O(OPh)NCMe$ to $[(Tp^{iPr}MoO(OPh)MoOTp^{iPr}(NCMe))]O$, two important features associated with the reaction can be noted. The first feature pertains to the effect of the substrate upon the rate-limiting step of the reaction. Although these seven substrates are similar in their geometry about the central phosphorus atom, P(*n*-Bu)$_3$ and PEt_3 are expected to have a higher conformational flexibility and lead to a greater entropic penalty. On the other hand, PPh_2Me and PPh_2Et have a lower basicity due to the electron withdrawing effects of the phenyl rings and are more sterically encumbered, which should result in a higher enthalpic contribution and a retarded rate of reaction.

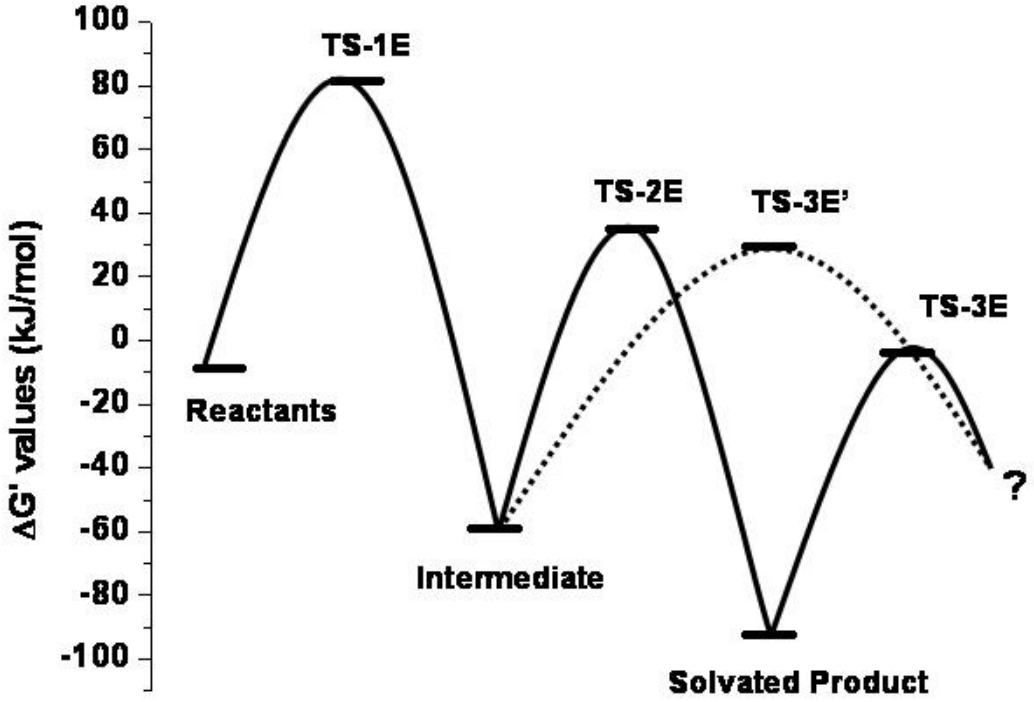

Figure 2.26: Experimental Reaction Pathway for the Reaction of (**1**) with PMe_3. Solid Lines Represent the Primary Pathway, while Dotted Lines Represent an Alternative Pathway to the Dinuclear Product. The Energies were determined as presented in the text.

In both (**1**) and (**4**), the loss of the phosphine oxide is the rate-limiting step when PMe_3 is considered (k_f/k_s (**1a**) = 3.9; k_f/k_s (**4a**) = 1.4), while for the remaining complexes of (**1**) and complex (**4g**), the formation step is rate limiting (k_f/k_s ranges from 0.74 (**1b**) and (**4g**) to 0.0095 in (**1g**)). When the reaction between (**1**-**4**) and PMe_3 and $PEtPh_2$ are compared, as referenced to the reaction coordinate for (**3**), several subtle features of the reaction come to light, as shown in **Figure 2.24, Figure 2.27** and **Table 2.44**.

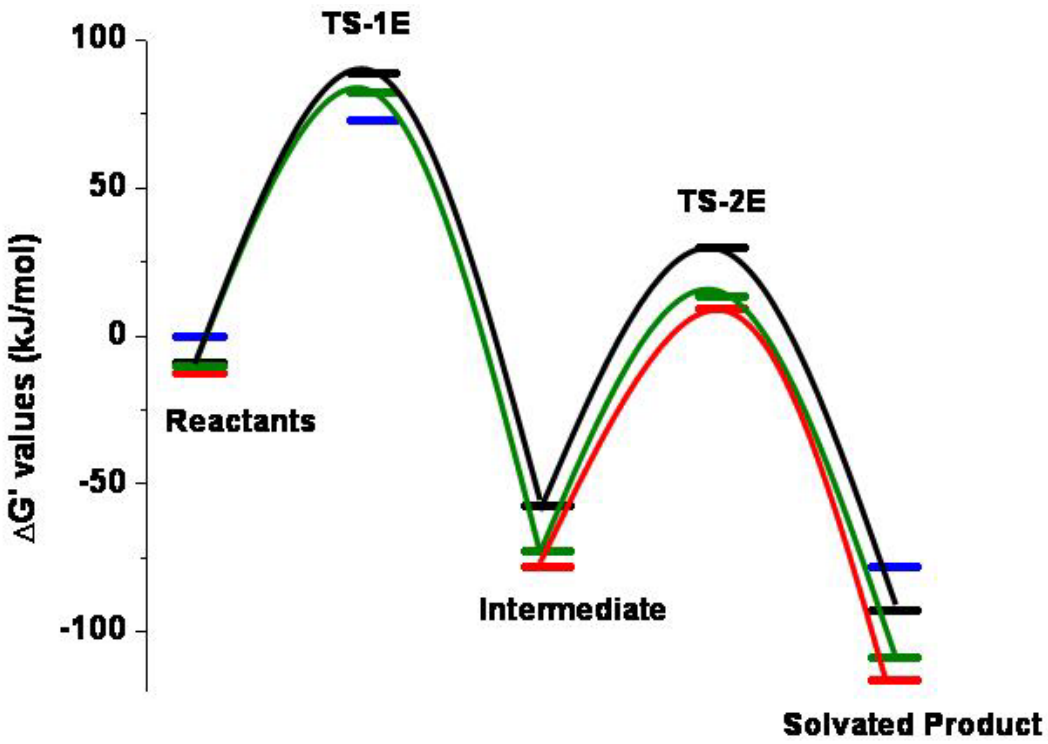

Figure 2.27: Experimental Reaction Pathway for the Reaction of (**1**) (Black Lines), (**2**) Red Lines, (**3**) Blue Lines and (**4**) Green Lines with $PEtPh_2$. All Reaction Coordinates are Reference to the Energy of (**3**) as Detailed in the Text.

First, when the reactions of (**1**) and (**4**) are compared it becomes evident that the first nucleophilic attack step, with PMe_3 and $PEtPh_2$, are energetically similar when referenced to the reaction coordinate for (**3**). More specifically, the barrier to formation of (**1a**) is equal to the barrier of formation of (**4a**), while the barriers to (**1g**) and (**4g**) are separated by 6 kJ/mol, despite a 2 kJ/mol difference in their starting energies. Thus, in terms of overall reactivity, the sulfur containing (**4a**) and (**4g**) are more easily solvated by 15 to 16 kJ/mol than (**1a**) and (**1g**) respectively, despite the fact that (**4a**) and (**4g**) are approximately 14 kJ/mol more thermodynamically stable. Furthermore, the resultant solvated complexes (**5**) and (**8**) are also energetically separated by ~ 15 kJ/mol, with (**5**) being more unstable. Taken together, the substitution of a sulfur ligand (**4**) for a oxygen ligand (**1**) results in an overall reduction of the reaction coordinate by ~15 kJ/mol, and

results in a more reactive species. However, a more true comparison of the effect of sulfur (**4a**) for oxygen substation arises when the formation of (**3a**) is considered, and is immediately evidenced by a large (~26 kJ/mol) increased stabilization of (**4a**). This stabilization carries over to the solvated products as well with (**7**) being ~31 kJ/mol less stable than (**8**). Lastly, when the solvation of (**2a**) and (**2g**) are considered, the barrier to solvation of (**2a**) is equal to that of (**4a**), while the barriers for (**2g**) and (**4g**) show an approximate 4 kJ/mol higher barrier for (**4g**).

Table 2.44: Approximate Reaction Coordinate for the First and Second Steps in the Reaction: Formation of (**1a-1g**), (**3a-3g**), (**4a** and **4g**) and the Solvation of (**1a-1g**), (**2a-2g**), (**4a** and **4g**) to yield (**5**), (**6**) and (**8**) respectively relative to (**3**)

Complex	**ΔG' (kJ/mol) (1)**	**ΔG' (kJ/mol) (2)**	**ΔG' (kJ/mol) (3)**	**ΔG' (kJ/mol) (4)**
Dioxo-Complex	-8.8[a]	-12.5[a]	0[a]	-10.5[a]
[MoO-O-PMe_3]‡	81.6[b]	**ND**	94.3[b]	81.5[b]
Intermediate (**a**)	-58.9[c]	-76.2[c]	-46.9[c]	-72.1[c]
[MoO-($OPMe_3$)(NCMe)]‡	35.0[d]	20.4[d]	**ND**	20.2[d]
Solvated Complex	-92.5[e]	-116.1[e]	-77.7[e]	-108.6[e]
Dioxo-Complex	-8.8[a]	-12.5[a]	0[a]	-10.5[a]
[MoO-O-$PEtPh_2$]‡	88.7[b]	**ND**	72.7[b]	82.2[b]
Intermediate (**g**)	-57.2[c]	-77.9[c]	**ND**	-72.6[c]
[MoO-($OPEtPh_2$)(NCMe)]‡	29.7[d]	9.1[d]	**ND**	13.0[d]
Solvated Complex	-92.5[e]	-116.1[e]	-77.7[e]	-108.6[e]

a) $\Delta G'^{o}$ represented as the energy relative to (**3**) expressed as [ΔG^{o}(**1-4**)- ΔG^{o}(**3**)];
b) $\Delta G_1'^{\ddagger}$ energy relative to (**3**) expressed as {$\Delta G_2^{\ddagger}$ [**(1-4)a-(1-4)g**] + $\Delta G'^{o}$[(**1-4**)**a-(1-4)g**]).
c) $\Delta G'^{o}$ represented as the energy relative to (**3**) expressed as [ΔG^{o}[**(1-4)a-(1-4)g**] - ΔG^{o}(**3**)];
d) $\Delta G_2'^{\ddagger}$ energy relative to (**3**) expressed as {$\Delta G_2^{\ddagger}$ [**(1-4)a-(1-4)g**] + $\Delta G'^{o}$[(**1-4**)**a-(1-4)g**]).
d) $\Delta G'^{o}$ represented as the energy relative to (**3**) expressed as [ΔG^{o}(**5-8**)- ΔG^{o}(**3**)];

In a biologically catalyzed OAT reaction, the formation of the intermediate complex from the dioxo-Mo(VI) complex can be viewed as a successor complex. Under this scheme, the dissociation of the phosphine oxide would be the product release step, then a water molecule would coordinate to the metal center, regenerating the catalytically competent active site by coupled proton electron transfer process. Indeed, such an intermediate molecule, where the metal center is coordinated by a substrate molecule, has been crystallographically characterized for DMSO reductase.[57] In addition, the crystal structure of chicken liver sulfite oxidase showed a sulfate molecule close to the first coordination sphere of the metal ion.[58] These reports provide direct evidence for the formation of an intermediate complex, similar to those described herein.

Kinetic investigation by Bray and his coworkers demonstrated that the formation of the enzyme-substrate complex for DMSO reductase is found to be rate-limiting at pH 5.5, while at pH 8.0 the oxo-transfer step has been proposed to be rate limiting.[59] Similarly, the OAT reactions of W-substituted DMSO reductase have been interpreted where the rate-limiting step is proposed to be the first electron transfer step i.e., the formation of the intermediate.[60] Brody and Hille have investigated the atom transfer chemistry of sulfite oxidase (SO) with sulfite and dimethyl sulfite as substrates.[61] Their interpretation was that the nucleophilic attack, and not the product dissociation, was the rate-limiting step. In general, the kinetic studies on the enzymes were focused on the catalytic cycle and thus information on the kinetics of the individual steps of the cycle is not available. However, it is clear that the rate-limiting step can be modulated by the nature of the substrate and the catalytic site, underscoring the importance of subtle perturbations to the reaction mechanism. While the parallel is compelling it is not comprehensive as enzymatic systems are investigated under catalytic conditions and current work did not focus on establishing a saturation behavior.

Summary.

The mechanistic details of the oxygen atom transfer reactivity from a dioxo-Mo(VI) center have been investigated. The reactivity has been investigated in solution by a combination of spectrophotometry coupled with singular value decomposition analysis. In addition mass spectrometric and spectroscopic methods have been used to characterize the products. The kinetic measurements were conducted at several wavelengths and at variable temperatures. The species on the proposed reaction paths have also been defined computationally by density functional theory. Moreover, the solvent effect on the reaction has been investigated both experimentally and computationally. The overall reaction has been described in terms of elementary steps that have been experimentally defined.

The first step in the overall reaction mechanism involves an intermediate situation between a more conventional nucleophilic attack by the phosphine to the Mo=O π^* orbital and nucleophilic attack by the terminal oxo group to the P—C σ^* orbital, which is illustrated through the large O—P—CMe angle (153.0^o) in TS-IC. The reaction proceeds through an associative transition state forming an intermediate where the phosphine oxide remained coordinated to the metal center. Computationally, the transition state geometry has been defined, and experimentally the associative nature of the reaction has been established through variable temperature rate measurements. Next, a solvent molecule replaces the phosphine oxide leading to the formation of a solvent coordinated complex. Kinetically the reaction most likely proceeds through a dissociative transition state (positive entropy of activation) following a dissociative interchange pathway. However, negative values can be obtained for the entropy of activation in a substrate dependent manner and most likely reflect the early and late transition state in accord with the Hammond Postulate. Computational results reveal that the associative transition state is ~33 kJ/mol higher in energy than the dissociative

transition state and further support the findings that both positive and negative entropies of activation can be achieved as a function of substrate and relative earliness or lateness of the transition state. The Mo-$OPMe_3$ bond is enthapically more stable than the Mo-NCMe bond, but the high solvent (MeCN) concentration and the large stabilization of the polar product, $OPMe_3$, drives the reaction. Thus the solvation reaction generally kinetically favored over the formation of the dinuclear species, but has a marginal degree of thermodynamic support in a leaving group dependent manner. The MeCN coordinated species and the 5-coordinate intermediate that are in equilibrium with each other then undergo dinucleation.

The reactivity was examined with seven different phosphines and in most cases, the rate-limiting step found to be the initial nucleophilic attack step, which is in agreement with the DFT calculations. However, when the reactions are conducted with PMe_3, the rate limiting step becomes the solvation step, which can only be supported experimentally. At 298K the maximal experimental free energy difference ($\Delta\Delta G^{\ddagger}_{298}$) between all of the substrates in (**1**) is 7.6 kJ/mol, in (**3**) is 26.0 kJ/mol, while no statistical difference was found in the two substrates used with (**4**), for the nucleophilic attack step. For the following solvation step, the maximal experimental free energy differences between all substrates in (**1**) were found to be 5 kJ/mol, while those of (**2**) were found to be 11 kJ/mol, and 6.7 kJ/mol was found for (**4**). The unequal difference in the two steps confirms that it is possible to alter the rate-limiting step of the reaction through a suitable choice of substrate. In light of the kinetic investigation on DMSO reductase, where rate-limiting steps were noted to be different at different pH, the present work provides a parallel in discrete oxo-molybdenum complexes.

Appendix 2.1: Singular Value Decomposition

Singular Value Decomposition

Time traces obtained during the decomposition of (**1c**) were scrutinized using singular value decomposition (SVD) as described below. All matrix manipulations on the data arrays were completed using 'matlab student edition' mathematical software with supplemental mathematics computed on 'mathcad 8.0 professional edition'. Upon completion of the SVD analysis, the right singular vectors were fitted in 'Origin 6.1' and subsequently used to define the overall rate of the reaction, as based on our previously proposed mechanisms. Difference spectra were calculated by subtracting the final trace from each subsequent trace such that:

$$S_{A(t)} = S_{Ai} - S_{Af} \qquad \textbf{Equation A2.1-1}$$

Where $S_{A(t)}$ refers to the difference spectrum at time (t).

Due to the great uncertainty associated with the reaction mechanism, this system was deemed a prime candidate for data analysis using the least-squares minimizing properties of singular value decomposition (SVD). Although a complete discussion of the SVD algorithm has been reviewed elsewhere[62,63] and lies beyond the scope of this text, a brief summary of the mathematics is essential to the understanding of the methodology applied to the spectral data analysis. Two immense advantages arise from the application of the SVD algorithm in that it first provides a method for reducing the magnitude of the data set [A], while secondarily; it offers the best least-squares approximation to the number of spectrophotometrically significant components contributing to the observed data set. Mathematically the SVD algorithm views the spectra data matrix [A] as a woven fabric of two orthoganally situated types of eigenvectors termed the left and right singular vectors (U and V respectively) such that **Equation A2.1-2** is maintained.

$$[A] = \{[U]*[S]*[V^T]\} \qquad \textbf{Equation A2.1-2}$$

In addition, the eigenvalues obtained during the calculation of the SVD of [A] (singular values of A) present information as to the relative spectral importance of its associated columns of U and V as a function of their overall contribution to sum of the spectral traces contained in [A]. Here, left singular vectors represent the basis spectral vectors associated with the matrix [A] such that when multiplied by the corresponding singular value, a purely mathematical representation of the pure component species is attained. In hand with this, the corresponding right singular vectors (columns of V) are representative of the overall spectral amplitude of a given basis spectrum. Thus when the U*S product is assessed with respect to its column of V it then becomes possible to predict several features contained within the data matrix. Three of the most important features that can be expressed are the shape of the pure species spectrum, the relative contribution of that spectrum to the overall spectrum and the degree of change of a given basis species spectrum during the course of measurements. Another advantage of using SVD is that since the matrix [A] can be decomposed into the three separate matrices, defined in **Equation A2.1-2**, it then becomes possible to reconstruct the data matrix as:

$$[A_i] = \{[U_i]*[S_i]*[V_i^T]\} \qquad \textbf{Equation A2.1-3}$$

such that:

$$|A - A_i|^2 = m*n*\sigma^2 < \sum_{i=r}^{n} (S_{ij})^2 \qquad \textbf{Equation A2.1-4}$$

is minimized[64]. Here, m and n are represented as the physical magnitude of the measured parameters such that if [A] is m x n then m is the number of rows in the data matrix and n is the number of columns in the data matrix. The inherent importance of this is that the value of σ^2 (the distance between [A] and [A_i]) provides a gauge for how much of the original spectral data set contains useful information such that vectors that either are noise or contain mostly noise can be discarded. Thus once SVD has been performed on a data matrix, a new reduced noise version of that data matrix can be constructed that contains all of the important information that was contained in the original matrix. In addition, SVD also lends to ease of analysis in that a compact form of the original matrix with reduced numeric bulk is produced that is only a fraction of the size of the "raw" data matrix.

Several available methods for calculating the significance of the data-output obtained from the application of the SVD algorithm primarily focus on the calculation of auto-correlations in the columns of U and in the columns of V. In addition, screening methods have also been based on the previously described numerical distance, **Equation A2.1-2**, and the magnitude of the singular values corresponding to columns of U and V. The autocorrelations in U and V are defined as:

$$C_{Uj} = \sum_{i=1}^{m-1} u_{ij} * u_{i+1,j} \qquad \textbf{Equation A2.1-5}$$

Shrager has established that values of C_{Uj} should be well above +0.5 and further defines the upper and lower limits as 1 and –1 respectively. When the columns of U and V are thus independently scrutinized, all of those that express autocorrelation values below 0.5 are to be discarded. Additional constraints are placed on the results through the application of **Equation A2.1-4** such that any distance that is not less than the sum of the singular values squared should also be discarded. On the

other hand, Henry and Hofrichter have established a cross-correlation method, which may be applied to tease lesser components from those that are mainly noise such that the auto-correlations in equation 6 are maximized as expressed in **Equation A2.1-6**.

$$C_{Uj,k} = \sum_{i=1}^{m-1} u_{ij} * u_{i+1,k}$$ **Equation A2.1-6**

Thus the application of this method defines a matrix $[X_{ij}]$ whose eigenvectors form the vectors of a rotation matrix $[R_{ij}]$. This $[R_{ij}]$ matrix which, when multiplied by the original source vector, produce new signal optimized vectors $[U^R_i]$ from U_i or $[V^R_i]$ from V_i and filter noise to the remaining vectors $[U^R_{i+1}]$ and $[V^R_{i+1}]$ as defined in the following:

$$[U_{kl}]*[R_{kl}] = [U^R_{kl}]$$ **Equation A2.1-7**

and:

$$[A_{ij}] = [(U_{ij})*(S_{ij})*(U^R_k)*(S_k)*(V^T_{ij})*(V^{RT}_k)]$$ **Equation A2.1-8**

One notable result of performing the rotation procedure defined in **Equation A2.1-7** is the loss of orthonganality in the columns of V and U which is remedied through the implementation of **Equation A2.1-8**, followed by a second processing by SVD.

Once the columns of U, S and V have been calculated, the next step is to fit the columns of V to the fewest number of kinetic equations, usually smallest number of summed exponentials required to account for the observed amplitude change such that:

$$V_i(t) = \sum_{j=1}^{k} F_{ij} * e^{(-t/\tau)}$$ **Equation A2.1-9**

Here F_{ij} represents the change in amplitude of the i^{th} basis spectrum accompanying the j^{th} relaxation, with zero-time as the time in which maximum amplitude is observed in V_1. In such a fitting process, the data set becomes further reduced to a set of (e) exponential decay rates, (f) values of F_{ij} and (b) basis spectra. Additional Utility in this procedure can be found in that a procedure now exists for the determination of the sample spectrum prior to a specific decay such that:

$$D_k(\lambda) = \sum_{j=k} \sum_{i=1} [U_i(\lambda) * S_i * F_{ij}]$$ **Equation A2.1-10**

In this equation, U_i (λ) represents the basis spectra of a given component and S_i represents its singular value.

Lastly, by applying a derived rate law it then becomes possible to predict the concentrations of each component at any time (t) along the reaction pathway.

References

1) Taube, H. *ACS Symposium Series* **1982**, *198*, 151-179.

2) Sharpless, K.B. *Tetrahedron*, **1994**, *50*, 4235-4258.

3) Holm, R.H. *Chem. Rev.* **1987**, *87*, 1401-1449.

4) Woo, L.K. *Chem. Rev.* **1993**, *93*, 1125-1136.

5) Espenson, J.H. *Adv. Inorg. Chem.* **2003**, *54*, 157-202.

6) Lane, B. S.; Burgess, K. *Chem. Rev*., **2003**, *103*, 2457-2473.

7) Nugent, W. A.; RajanBabu, T. V.; Burk, M. J. *Science* **1993**, *259*, 479-483.

8) *The Chemistry of Phosphorous,* John Emsley and Dennis Hall. Harper and Row publishers, N.Y. 1976

9) Holm, R.H *Coord. Chem. Rev.*, 1990, **100**, 183.

10) Enemark, J.H. and Young, C.G. *Adv. Inorg. Chem.*, 1993, **40**, 1.

11) Enemark, J. H.; Cooney, J. J. A.; Wang, J-J.; Holm, R. H.. *Chem. Rev.,* **2004**, *104*, 1175-1200.

12) Young, C.G. "Biomimetic Chemistry of Molybdenum," in *Biomimetic Oxidations Catalyzed by Transition Metal Complexes*; B. Meunier, Ed., Imperial College Press, **2000**, Chapter 9, pp. 415–459.

13) Schultz, B. E.; Hille, R.; Holm, R. H. *J. Am. Chem. Soc.*, **1995**, *117*, 827-828.

14) Stewart, L. J.; Bailey, S.; Collison, D.; Morris, G. A.; Preece, I.; Garner, C. D. *ChemBioChem,* **2001**, *2*, 703-706.

15) (a) Barral, R.; Bocard, C.; Seree de Roch, I.; Sajus, L. *Tet. Lett*. **1972**, 1693-1696. (b) Reynolds, M. S.; Berg, J. M.; Holm, R. H. *Inorg. Chem.* **1984**, *23*, 3057-3062.

16) (a) Das, S. K.; Chaudhury, P. K.; Biswas, D.; Sarkar, S. *J. Am. Chem. Soc.* **1994**, *116*, 9061-9070. (b)Oku, H.; Ueyama, N.; Kondo, M.; Nakamura, A. *Inorg. Chem.* **1994**, *33*, 209-216.

17) (a) Sung, K-M.; Holm, R.H. *J. Am. Chem. Soc.,* **2002**, *124*, 4312-4320. (b) Sung, K-M.; Holm, R. H. *J. Am. Chem. Soc.*, **2001**, *123*, 1931-1943. (c) Donahue, James P.; Goldsmith, Christian R.; Nadiminti, U.; Holm, R. H. *J. Am. Chem. Soc.* **1998**, *120*, 12869-12881.

18) Lim, B. S.; Holm, R. H. *J. Am. Chem. Soc.*, **2001**, *123*, 1920-1930.

19) (a) Xiao, Z.; Young, C. G.; Enemark, J. H.; Wedd, A. G. *J. Am. Chem. Soc.*, **1992**, *114*, 9194-9195. (b) Xiao, Z.; Bruck, M.A.; Enemark, J.H.; Young, C.G.; Wedd, A. G. *Inorg. Chem.* **1996**, *35*, 7508-7515.

20) Nemykin, V.N.; Davie, S.R.; Mondal, S.; Rubie, N.; Kirk, M.L.; Somogyi, A.; Basu, P. *J. Am. Chem. Soc.,* **2002**, *124*, 756-757.

21) Pietsch, M. A.; Hall, M. B. *Inorg. Chem.,* **1996**, *35*, 1273-1278.

22) Rappé, A. K.; Goddard, W. A., III. *J. Am. Chem. Soc.* **1982**, *104*, 3287-3294.

23) Smith, P. D.; Millar, A. J.; Young, C. G.; Ghosh, A.; Basu, P. *J. Am. Chem. Soc.* **2000**, *122*, 9298-9299.

24) Millar, A.J.; Doonan, C.J.; Smith, P.D.; Nemykin, V.N.; Basu, P.; Young, C.G. *Chem. Eur. J.*, in press.

25) Nemykin, V.N.; Laskin, J.; Basu, P. *J. Am. Chem. Soc.*, **2004**, *126*, 8604.

26) (a) Xiao, Z.; Bruck, M. A.; Enemark, J. H.; Young, C. G.; Wedd, A. G. *Inorg. Chem.,* **1996**, *35*, 7508-7515. **(**b**)** Xiao, Z.; Young, C. G.; Enemark, J. H.; Wedd, A. G. J. Am. Chem. Soc., **1992**, *114*), 9194-9195.

27) Webster, C.E.; Hall, M.B. *J. Am. Chem. Soc.*, **2001**, *123*, 5820.

28) Ralford, D.S.; Fisk, L.C.; and Becker, E.D. *Anal.Chem*. **1979**, 51, 2050.

29) Henry, E.R.; Hofrichter, J. *Methods in Enzymology,* **1992**, *210*, 129-191.

30) Shrager, R.I.; Hendler, R.W. *Anal. Chem.*, **1982**, *54*, 1147-1152.

31) Sengar, R.S., Nemykin, V.N., and Basu, P. *New. J. Chem.* **2003**, 27, 1115-1123

32) Becke, A. D. *J. Chem. Phys.* **1993,** *98*, 5648. C. Lee, W. Yang, and R. G. Parr, *Phys. Rev. B* **1988**, *37*, 785.

33) Parr, R.G.; Yang, W. *Density-functional theory of atoms and molecules* Oxford Univ. Press, Oxford (1989).

34) Frisch et al., Gaussian 03, Revision B5, Gaussian, Inc., Pittsburgh PA, 2003.

35) Cossi, M.; Rega, N; Scalmani, G.; Barone, V. *J. Chem. Phys.*, **2002**, *117*, 43.

36) Dunning Jr., T.H.; Hay, P.J. in *Modern Theoretical Chemistry*, Ed. H. F. Schaefer III, Vol. 3 (Plenum, New York, 1976) 1-28.

37) Hay, P.J.; Wadt, W.R. *J. Chem. Phys.*, **1985**, *82*, 299.

38) Couty, M.; Hall, M.B. *J. Comp. Chem.* **1996**, *17*, 1359.

39) Hay, P.J.; Wadt, W.R. *J. Chem. Phys.*, **1985**, *82*, 270.

40) Huzinaga, S. *Guassian Basis Sets for Molecular Calculations*, Elsevier, Amsterdam, 1984.

41) Becke, A. D. *J. Chem. Phys.* **1993,** *98*, 5648. C. Lee, W. Yang, and R. G. Parr, *Phys. Rev. B* **1988**, *37*, 785.

42) Parr, R.G.; Yang, W. *Density-functional theory of atoms and molecules* Oxford Univ. Press, Oxford (1989).

43) Frisch et al., Gaussian 03, Revision B5, Gaussian, Inc., Pittsburgh PA, 2003.

44) R. S. Mulliken, *J. Chem. Phys.* **1955**, 23, 1833.

45) a)J. E. Carpenter and F. Weinhold, *J. Mol. Struct. (Theochem)* **1988,** 169, 41. b)J. E. Carpenter, PhD thesis, **1987**, University of Wisconsin (Madison, WI),. c) J. P. Foster and F. Weinhold, *J.*

Amer. Chem. Soc. **1980,** 102, 7211. d) A. E. Reed and F. Weinhold*, J. Chem. Phys.* **1983**, 78, 4066. e) A. E. Reed and F. Weinhold*, J. Chem. Phys.,* **1983**, 1736. f)A. E. Reed, R. B. Weinstock and F. Weinhold, *J. Chem. Phys*. **1985**, 83, 735. g) A. E. Reed, L. A. Curtiss and F. Weinhold, *Chem. Rev.* **1988,** 88, 899 h) F. Weinhold and J. E. Carpenter, "The Structure of Small Molecules and Ions," Plenum, **1988**, 227.

46) a) B. H. Besler, K. M. Merz, Jr. and P. A. Kollman, *J. Comp. Chem*. **1990**, 11, 431.b) U. C. Singh and P. A. Kollman, *J. Comp. Chem*. **1984**, 5, 129.

47) a) P. W. Abegg, *Mol. Phys.* **1975**, 30, 579. b) M. W. Wong, M. J. Frisch and K. B. Wiberg, *J. Amer. Chem. Soc.* **1991**, 113, 4776. c) M. W. Wong, K. B. Wiberg and M. J. Frisch, *J. Amer. Chem. Soc.* **1992**, 114, 523. d) M. W. Wong, K. B. Wiberg and M. J. Frisch, *J. Chem. Phys*. **1991**, 95, 8991.e) M. W. Wong, K. B. Wiberg and M. J. Frisch, *J. Amer. Chem. Soc.* **1992**, 114, 1645. f) J. G. Kirkwood, *J. Chem. Phys.* **1934**, 2, 351. g) L. Onsager, **1936**, 58, 1486.

48) Frisch et al., Gaussian 03, Revision B5, Gaussian, Inc., Pittsburgh PA, 2003.

49) a) Tolman, C.A. *Chem. Rev.* **1977**, 77, 313-348; b) Tolman, C.A. *J.Am.Chem.Soc*. **1970**, 92, 2953; c) Tolman, C.A., Seidel, W.C. and Glosser, L.W. *J.Am.Chem.Soc*. **1974**, 96, 53.

50) Raghvenda Singh Sengar, Ph.D. Thesis. 2004. Duquesne University

51) Nemykin, V.N.; Basu, P manuscript in preparation.

52) Nemykin, V.N.; Basu, P. *J. Chem. Soc., Dalton Trans,* **2004**, 1928-1933.

53) The large errors involved in the activation parameters for the last step (step 3 in Figure 3) cautions in reaching definitive conclusions.

54) Xiao, Z, Bruck, M.A.; Doyle, C.; Enemark, J.H.; Grittini, C.; Gable, R.W.; Wedd, G.; Young, C.G. *Inorg. Chem.*, **1995**, *34*, 5950.

55) Yu, Y.B. *J. Phys. Chem. B* **2003**, *107*, 1721.

56) Fan, Y; Hall, M.B. *Chem. Eur. J.* **2004**, *10*, 1805.

57) McAlpine, A. S.; McEwan, A. G.; Bailey, S. *J. Mol. Biol.* **1998**, *275*, 613-623.

58) Kisker, C.; Schindelin, H.; Pacheco, A.; Wehbi, W. A.; Garrett, R. M.; Rajagopalan, K. V.; Enemark, J. H.; Rees, D. C. *Cell* **1997**, *91*, 973-983.

59) Adams, B.; Smith, A. T.; Bailey, S.; McEwan, A. G.; Bray, R. C. *Biochemistry* **1999**, *38*, 8501-8511.

60) Stewart, L. J.; Bailey, S.; Collison, D.; Morris, G. A.; Preece, I.; Garner, C. D. *ChemBioChem* **2001**, *2*, 703-706.

61) Brody, M.S.; Hille, R. *Biochem. Biophys. Acta*, **1995**, *1253*, 133-135.

62) Hofrichter, J.; Henry, E.R.; Sommer, J.H.; Deutsch, R.; Massao Ikeda-Saito; Yonetani, T.; and Eaton, W.A." *Biochemistry*, **1985,** 24, 2667-2679.

63) Henry, E.R; and Hofrichter, J *Methods in Enz.* **1992**, 210, 129-191.

64) Shrager, R.I.; and Hendler, R. W. *Anal Chem.* **1982**, 54, 1147-1152.

Chapter 3

Reactivity of Phosphorous in Oxygen Atom Transfer Chemistry with Implications toward Nitrogen and Sulfur Donors

Chapter 3

Reactivity of Phosphorous in Oxygen Atom Transfer Chemistry with Implications toward Nitrogen and Sulfur Donors

Abstract:

The interpretation of the relationships that exist between the chemical reactivity of metal catalysts and the physico-chemical properties of substrates has been of interest for well over 60 years. In general, the bulk of this work has been centered upon phosphorous (III) substrates, generally as phosphines or phosphites, which act as ligands to metal complexes. To this end, it has been established that there are three main physico-chemical parameters that contribute to the reactivity of phosphorous (III) compounds, two of which are electronic and the third is of steric origin. More specifically, it is commonly accepted that these reactions involve a σ-basicity component, a π-acidity component and a steric/size component. However, there has been little investigation into the reactivity of the analogue oxo-phosphorous (V) compounds which are typically generated during oxygen atom transfer reactions (OAT) when the parent phosphorous (III) compounds act as nucleophiles toward oxygen. With this in mind, this chapter will explore the current concepts associated with reactivity, the origin of reaction parameters and the general applicability of phosphorous (III) parameters toward reactions that evolve phosphorous (V) products. In addition, the foundations of the current established parameters for nitrogen and sulfur oxidation reactions will be eluded through a comparison with phosphorous (III) compounds.

Introduction:

Over the past 20 to 25 years, research on oxygen atom transfer chemistry (OAT) has lent to great advances in the understanding of catalytic oxidation processes. This research spans through biological, biomemetic, organometallic and fuel chemistry fields and continues to provide a promising area of research. Of particular interest in the study of atom transfer chemistry are the possible substrates that serve as oxygen donors and oxygen acceptors, which have been dominated by three major classes, defined by the element with actively accepts or donates oxygen. The first and most prominent of these are the organo-phosphorous compounds that contain either phosphorous (III) or an oxo-phosphorous (V) center. Typically the phosphorous (III) compounds are phosphines or phosphites, while the phosphorous (V) compounds are typically the corresponding oxide. The second major classe of oxygen atom donors are the sulfur containing compounds that contain sulfur (II), an oxo-sulfur (IV) or occasionally dioxo-sulfur (VI) element. As such the sulfur donor compounds with sulfur (II) are well represented by organo-sulfur compounds in the form of thiols and thioethers, while the organo sulfur (IV) compounds are represented by the sulfoxides and the organo sulfur (VI) compounds are represented by the sulfones. In addition, inorganic sulfur as sulfur (VI) can be in the form of sulfate as a donor or sulfur (IV) in the form of sulfite as the acceptor. Furthermore, the organo-nitrogen based oxygen donors and acceptors that either contains nitrogen (V) or nitrogen (III) respectively. This group of compounds is typified by the N-oxy amines and amines. In addition to the organo-nitrogen compounds, inorganic nitrogen (V) as nitrate and nitrogen (III) as nitrite have also been used as the oxygen atom donor and acceptor, respectively.

In general, these compounds have been shown to participate in OAT chemistry when reacted with a variety of metal complexes ranging from, but not limited to, Iron, Molybdenum, Tungsten, Ruthenium, Rhenium, and Chromium. Moreover, the metal complexes range from discrete mononuclear and di-nuclear complexes to large multinuclear metal systems. As the focus of this chapter is upon the reactivity of the non-metal donor and acceptors in OAT chemistry, the metal complex reactivity will only surface when needed. However, there have been many comprehensive reviews written over the years which discuss the OAT reactivity of the complexes of the aforementioned metals and the reader is referred to the works of Holm[1], Wu[2], Enemark[3], and Espenson[4] as well as **Chapter 1** of this work.

When this bulk of research is taken together, several patterns emerge regarding the rates of the reactions of the N, S and P compounds based upon three general physico-chemical parameters: size, π-bonding ability and basicity/ acidity. In an attempt to understand the relationship of these effects with reactivity, the most well characterized complexes; the PR_3 complexes will be used and will serve as a model for the nitrogen and sulfur compounds. In general, the size and electronic factors are quite similar in nature to the factors that influence the stability and reactivity of many metal coordination complexes and as such have been explored in great detail. Tolman[5] has shown through elegant work with $Ni(CO)_3PR_3$ complexes that the vibrational frequency of a CO trans to the phosphine can be shifted through variable substitution at phosphorous. This shift in IR frequency can be attributed to the π-backbonding ability of the phosphine, such that phosphines with electron donating groups induce greater interactions between metal dπ

and ligand π* orbitals. In the case of electron withdrawing groups, interactions between the metal dπ and ligand π* orbitals are reduced. The end results of these interactions are interpreted in a two ways. First a charge in an experimentally observable parameter such as the vibrational frequency in a trans-ligand is quantitated, and second, through variable substitution at phosphorous, the electronic properties of phosphorous can be approximated. This observation lead to the theory that there is an electronic parameter as well as a geometric parameter that contributes to the resultant infrared spectrum of a phosphine-substituted complex when compared to the un-substituted compound or reference phosphine-substituted compound. Another result of this work is that Tolman's electronic parameter χ, correlates very well with the experimentally determined pK_a of phosphines, and represents an alternative method of pK_a estimation as shown in **Figure 3.1a**. Along the lines of the Tolman electronic parameters are those presented by the Kamlet-Taft (β-π* and α scales)[6] and Hammett[7] (σ and ρ) constants, which provide a measure of substituent effects upon the basicity of a parent protonated complex.

Drago[8] has established an electrostatic-covalent bond model (E and C model) to describe the reactivity of substituted phosphines through a linear combination of weighting factors, E_B and C_B parameters and E_A and C_A parameters. The main focus of the E_B and C_B parameters was to provide a separation of electronic effects into a portion derived through covalent bonding interactions (σ-basicity) with the metal and a portion derived from electronic interactions (π-acceptor properties) between the phosphine and the metal.

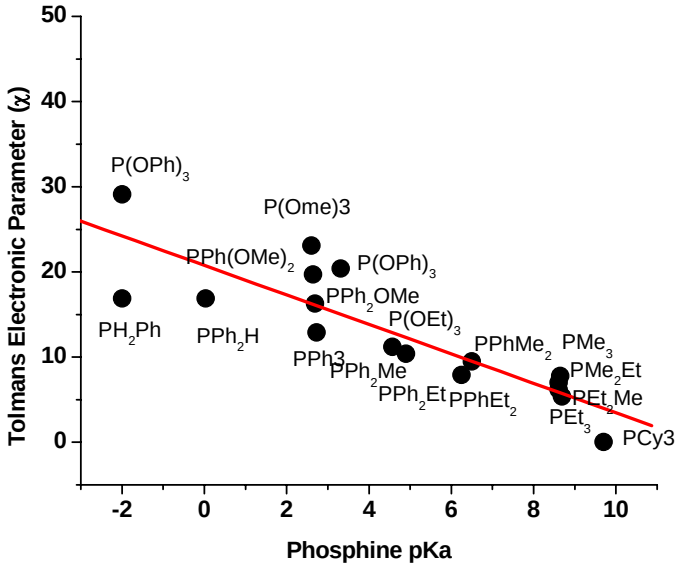

Figure 3.1a: Tolmans electronic parameter verses phosphine pK_a. R^2 = -0.866, N= 17, slope= -1.73 ± 0.25, intercept = 20.80 ± 1.50

Later, these E_B and C_B parameters were refined for phosphines to the E_B* and C_B* parameters[9], but still express the same goal of attempting to quantify the electronic effects of phosphine complexes. More concretely, E and C model presents a method of understanding the role of σ-basicity towards reactivity without the inclusion of steric effects. Interestingly, both the C_B and C_B* parameters correlate well with the phosphine pK_a and Tolman's electronic parameter shown in **Figure 3.1b- Figure 3.1e.**

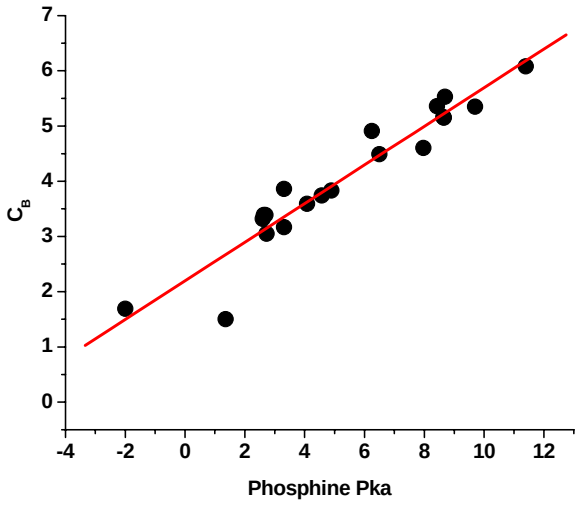

Figure 3.1b: Drago C_B parameter verses phosphine pK_a. $R^2 = 0.955$, N= 20, slope= 0.350 ± 0.026, intercept = 2.19 ± 0.16

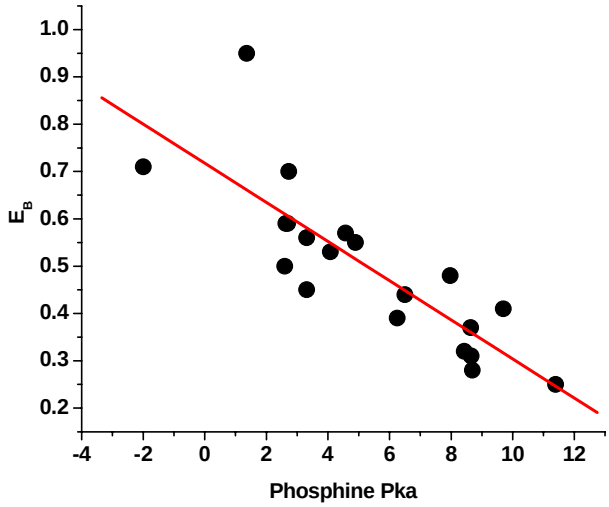

Figure 3.1c: Drago E_B parameter verses phosphine pK_a. $R^2 = 0.830$, N= 20, slope= -0.041 ± 0.007, intercept = 0.718 ± 0.041

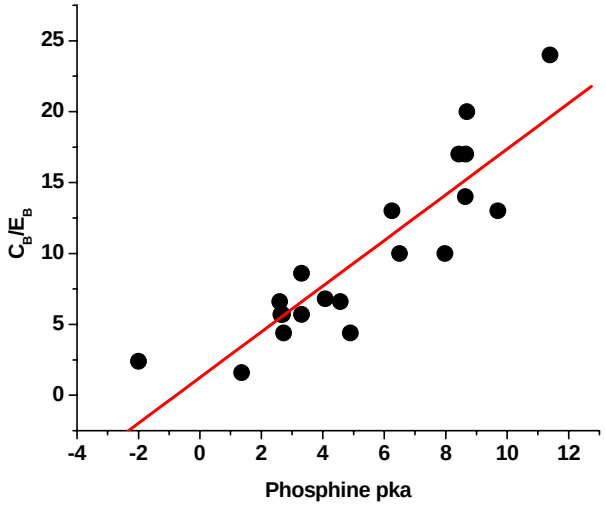

Figure 3.1d: Drago C_B/E_B Ratio verses phosphine pK_a. R^2 = 0.891, N= 20, slope= 1.61 ± 0.19, intercept = 1.24 ± 1.21

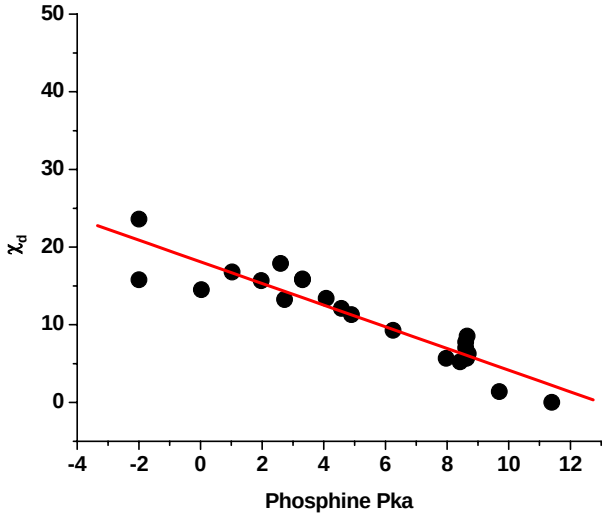

Figure 3.1e: QALE χd verses phosphine pK_a. R^2 = -0.928, N= 22, slope= -1.40 ± 0.13, intercept = 18.12 ± 0.79

Others have also developed similar relationships between electronic parameters that focus upon the pK_a of the phosphine in terms of $pK_a'\sigma$, $pK_a'\pi$, molecular electrostatic potentials, χ_d, and π_p in attempt to estimate both the σ-basicity and π-bonding ability of phosphines. Along these same lines, the experimental[10] and theoretical[10b], protonation energies of phosphourous (III) compounds have been determined as well as ionization potentials in hopes of understanding reactivity. Others have established correlations between the ^{31}P chemical shift of oxo-phosphorous (V) complexes and the reactivity of the related phosphorous (III) compounds, which provided a basis for electronic effects in OPR_3 complexes[11]. Based upon this intense investigation of phosphorous (III) complexes, it is easy to see that steric and electronic factors influence the reactivity and that these parameters should also participate in the reactivity of N and S compounds. Indeed, the cone angle description of steric effects in phosphines has been applied to sulfur complexes in terms of a fractional cone angle[12,5]. Furthermore, QALE analysis (Quantification of Ligand Effect) has been employed to introduce this concept of a linear combination of steric and electronic parameters into the reactivity of N and S compounds, as well as further investigate the P compounds[13]. Taken together, the combined work of these, and other authors, represents a common goal of predicting reactivity through linear free energy relationships (LFER), which arise through the implementation of physico-chemical parameters in data analysis. In the sections to follow, a more detailed description of the general parameters involved in understanding reactivity, π-back-bonding ability and basicity/ acidity, will be provided in terms of oxygen atom transfer chemistry to phosphorous.

Physico-Chemical Properties

General Steric Effects

The most widely evoked steric parameter, for PR_3 complexes, is the Tolman Cone Angle (Θ). Θ was established for applications involving the binding of phosphines to metals as ligands, but has also been used to describe the reactivity of phosphines toward oxygen atom donation or abstraction. The cone angles of phosphines were first produced from CPK models of the phosphine complexes, with the ligands bent to create maximal steric interactions with a point located 2.28 Å from the central phosphorous atom. Accordingly, the cone angle can be defined in two ways. First, for symmetric phosphines (tri-substituted phosphines with three identical substituents) the cone angle is defined as the solid angle formed from the periphery of the ligands when placed a distance of 2.28 Å from the coordinated metal **(Figure 3.2)**.

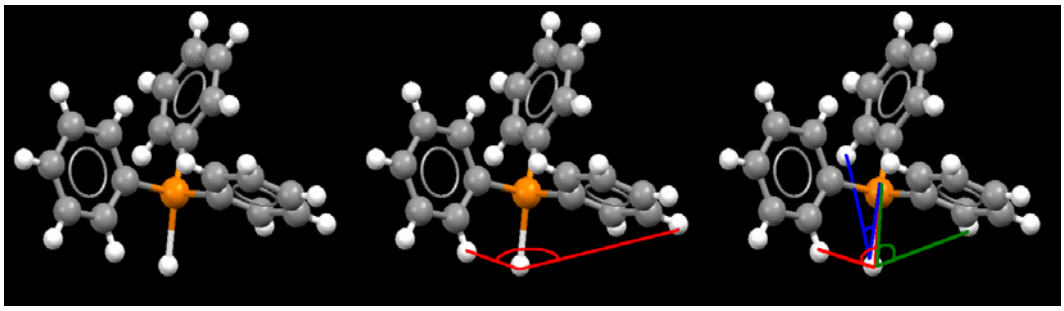

Figure 3.2. left panel: PPh_3 from the Cambridge Crystal Database. **Middle panel**: shows the measured Tolman Cone Angle Θ, for symmetric ligands about phosphorous. **Right panel**: shows the Tolman Partial Angles θ_1 , θ_2, and θ_3 for unsymmetric ligands on phosphorous.

Secondly, for asymmetric phosphines, (tri-substituted phosphines with one, two or three different substituents) the cone angle is defined by **Equation 3.1**, such that the sum of half-angles produced is minimized (**Figure 3.2**).

$$\Theta = \frac{2}{3}\sum_{i=1}^{3}\frac{\theta_i}{2} \qquad \textbf{Equation 3.1}$$

Here Θ is the cone angle and θ_i is the half-angle as described in **Figure 3.2**. One critical assumption inherent is the cone angle description is that the phosphine ligands should be arranged to introduce the greatest steric interaction with the metal, and that this interaction does not induce undue strain upon phosphorous. In other words, the manipulation of the phosphine ligands in this way is assumed to approximate an energetically favorable orientation of the ligands without causing undo strain upon the central phosphorous atom. A second critical assumption is that the phosphorous to metal bond is approximately 2.28 Å. Lastly, a third critical assumption is that the metal based ligand-metal-phosphorous angle remains 180º when a metal-based ligand trans to the phosphine is considered. In light of these assumptions, the use of the Tolman cone angle has been the subject of scrutiny in the recent past, as the number of crystollographically-characterized structures involving metal-phosphine bonds has increased. The predominant reason for such skepticism results from four key points. First, it is difficult to validate the use of static solid angles for the prediction of dynamic reactivity in solution. Second, the metal to phosphorous bond length is largely dependent upon the metal and can deviate significantly from 2.28 Å and as such constricts or expands the measured cone angle as a function of bond length. Thirdly, many crystal structures show

deviations from 180º for the metal-based ligand-metal-phosphorous angle, especially when phosphine oxides are considered. Lastly, a frequently encountered problem is that is there is significant cone angle variation within multiple crystal structures containing the same phosphine ligand[14]. This variation occurs partially through variations in the previously mentioned bond lengths and angles, as well as a limitation in the assumption that maximized steric interactions results in an energetic minimum for the orientation of the phosphines ligands. Thus a free or coordinated phosphine in a low energy conformation breaks the inferred symmetry about phosphorous in the "symmetric" phosphines defined above. For example, the reported Tolman cone angle of $P(OMe)_3$ is 107°, but measuring the cone angle of a sample coordination complex, found in the Cambridge Crystal Database[15], provides a cone angle of only 60.3° when considered as an unsymmetric complex. If it is assumed that the compound is symmetric, based only upon the fact that three OMe groups are bonded to the central phosphorous, and the largest partial angle is assumed to be equivalent to the remaining three angles, the net cone angle is raised to 114.9°. An even more interesting discrepancy arises when the cone angle of $P(OMe)_3$ is calculated from the optimized geometry which leads to a cone angle of 121°, when considered to be asymmetric. (**Figure 3.3).**

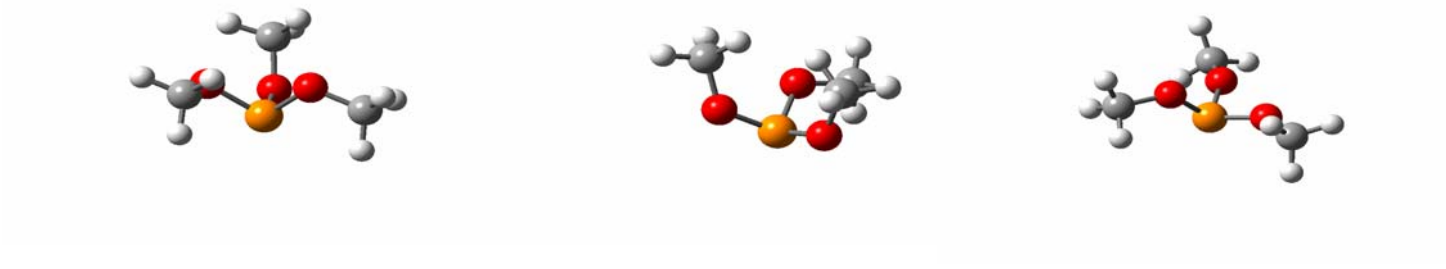

Figure 3: **Left panel**: optimized geometry of $P(OMe)_3$ with a volume of 118.65 cm^3/mol, radius of 4.47 Å and cone angle of 121º. **Middle Panel**: coordinated $P(OMe)_3$ with metal and metal based ligands removed from the structure volume of 74.53 cm^3/mol, radius of 3.90 Å and a cone angle of 60.3º. **Left panel**: $P(OMe)_3$ constructed with the minimized sum of half-angles at 108 (107 reported) with a volume of 82.24 cm^3/mol and a radius of 4.02 Å

At first this may be surprising, but can be explained, at least partially, by changes in the geometry about phosphorous. In a tri-substituted phosphine, the central phosphorous atom adopts a trigonal pyramidal geometry (tp) with an R-P-R' angle of ~107°, which must change upon oxidation or coordination to a tetrahedral geometry (td) and an R-P-R' angle of ~109°. The change from tp to td geometry should cause the average ligand-phosphorous-ligand angle to expand by ~2 degrees and result in an overall reduction in the observed cone angle, **Table 3.1,** by allowing for greater flexability in the R-groups through less constriction about phosphorous.

Table 3.1: Cone angles of phosphines verses those of the related oxide				
Phosphine	**Cone angle[a] PR_3**	**Cone angle[b] OPR_3**	**Volume PR_3**	**Volume OPR_3**
PMe_3	118 (100.3)	62.9 (64.8)	77.081	84.52
PMe_2Ph	122 (96.9)	73.6 (76.9)	94.351	99.15
PEt_3	132 (110.6)	91.5 (87.4)	131.30	120.86
P(*n*-Bu_3)	132/136 (128.4)	(86.5)	221.96	174.63
PEt_2Ph	136 (109.3)	(88.0)	169.08	147.86
$PMePh_2$	136 (113.5)	(89.0)	179.22	146.01
$PEtPh_2$	140 (118.5)	96.7 (99.6)	132.52	195.48
PPh_3	145 (120.4)	99.5 (99.2)	214.21	208.81
P(*p*-F-C_6H_4)$_3$	145		195.8	223.30
$P(OMe)_3$	107 (121.5)	95.5 (99.5)	118.65	104.51
$P(OEt)_3$	109 (117.3)	122	129.75	
$P(OPh)_3$	128 (128)	144.6	238.75	242.96
$P(OMe_2)Ph$	120	(86.8)	134.97	121.36
a) Experimental cone angles were taken from the literature[16,5]; number in parenthesis indicates cone angle of optimized geometry. b) Cone angles calculated from Cambridge Crystal database crystal structures; number in parenthesis indicates cone angle of optimized geometry				

This introduces yet another question, which has been raised by others[17], as to the applicability of cone angles to the reactivity of complexes because the cone angle does not reflect the lowest energy state of the phosphine, or a realistic model of a coordinated phosphine. The general consensus with regards to the variability in cone angles, as previously mentioned by Poë is that the Tolman Cone Angle represents one of the many accessible energetic conformations of the phosphine and may vary as a function of the phosphines role in the reaction, as well as the metal with which it interacts. This has resulted in a generally accepted revision of the cone angle to provide "best fits" to experimental data and has resulted in the adjustment of the original Tolman Cone Angles of P(*n*-Bu)$_3$ from 132º to 136º and $P(OMe)_3$ from 107º to 102º.

Regardless of the possible unrealism inherent with the concept of a solid phase angles capability of representing the dynamic environment of solution chemistry, there

exists a strong correlation between cone angles and reactivity[18], using Tolman's Equation, **Equation 3.2**.

$$property = a + b \cdot (\chi) + c \cdot (\Theta) \qquad \textbf{Equation 3.2}$$

Where, *a* is a constant, *b* and *c* are weighting factors, Θ is the cone angle and χ is Tolman's electronic parameter as defined by the shift in the A^1 frequency for νCO of $Ni(CO)_3PR_3$ complexes, referenced to P(*t*-Bu)$_3$, while Θ is defined in **Equation 3.1**.

One possibility for the observed correlations of the cone angle with reactivity may simply be derived from the idea that knowledge of the absolute number is less important than the trends established from estimates in that number.

Later, Tolman's Equation was adapted to introduce a new form of steric effects as defined in the LFER analysis technique known as QALE analysis, provided in **Equation 3.3**.

$$property = (a \cdot \chi_d) + (b \cdot \Theta) + (b' \cdot (\Theta - \theta_{st}) \cdot \lambda) + (c \cdot E_{ar}) + (d \cdot \pi_p) + e \qquad \textbf{Equation 3.3}$$

Here, *a*, *b*, *b'*, *c*, and *d* are weighting factors, *e* is a constant, χ_d is the electronic parameter, E_{ar} is an aryl effect parameter and π_p is a π-acid/base term, all of which will be discussed in detail in the sections to follow. However, of special importance to this section are the Θ and $(\Theta-\theta_{st})\lambda$ parameters which express the contribution of steric effects in the property of interest. Although the steric parameter Θ was previously discussed, the model introduces the concept of a steric threshold[18,19], which is defined as the value of Θ

at which steric effects become dominant, $(\Theta-\theta_{st})\lambda$, and is mathematically controlled by the switching function λ. The term switching function refers to its formal definition in that for all $\Theta < \theta_{st}$, λ is zero and for all $\Theta > \theta_{st}$, λ is unity, and acts to simplify the regression analysis in the absence of an observable threshold. In this the model accounts for steric sensitivity in the property of interest simply as a change in the property with a corresponding change in the cone angle after the steric threshold is achieved. More importantly, the concept of the steric threshold allows for the gradual inception of steric effects to appear in a given reaction. The remaining parameters of this equation will be discussed in detail in the following section on electronic effects parameters.

Electronic effects

As mentioned in the introduction, the second component that is typically evoked in the reactivity of phosphorous, nitrogen and sulfur compounds is some measure of electronic effects. These electronic effects are generally represented by some electronic parameter and are expressed in the form of a linear free energy relationship (LFER), such that some physically measurable property can be explained. The simplest measure of electronic effects is gauged by the pK_a of the compound as shown in **Table 3.2** for selected phosphines. Tolman introduced first true electronic parameter for phosphorous, referred to as simply the electronic parameter or Tolmans electronic parameter (χ of **Equation 3.2**), which was intended as a measure of the σ-basicity of a phosphine, and is similar in concept proposed by the Kamlet-Taft scale (β-π^*) and Hammet (σ) constants which provides a series of reactivity constants for selected substituents. Over the years, other models were derived which utilized single parameters to measure the donor

strength, with steric effects and π-back bonding envoked to describe deviations of reactivity from the donor strength parameter. Later, Drago introduced the E and C model (also referred to as the ECW model) that is defined in **Equation 3.4** in its simplest form:

$$\Delta\chi = E_A E_B + C_A C_B + W \qquad \textbf{Equation 3.4}$$

Here, $\Delta\chi$ is a physicochemical property observed during the reaction, the E_A and C_A represent the dual parameter σ-basicity scale for the acceptor and E_B and C_B are the dual parameters for the donor, while W is a weighting constant for the reaction. More explicitly, the C term is designed to parallel the tendency of a reactant to undergo covalency or frontier controlled reactions while the E term is designed to parallel the tendency for the reactants to undergo charge controlled or electrostatic interactions. The E and C model follows with the ideas of Tolman, and is less reliant upon steric parameters and π-back bonding contributions as the parameters were derived from compounds that lack these interactions. Interestingly, the C_B and E_B terms (combined or taken individually) correlates approximately as well as the Tolman electronic parameters correlate with the pK_a of the phosphine **(Figure 3.1b – Figure 3.1e).** However, the E and C model represents a divergence from the more traditional one-parameter systems for σ-basicity and provides for an important vehicle into the development of more sophisticated multi-parameter reactivity models.

Table 3.2: Selected cone angles and pK_a values of reported phosphines[5,16]

Phosphine	Cone Angle (Θ)	pK_a
$P(OCH_2)Et$	101	1.74
$P(OMe)_3$	107	2.6
$P(OEt)_3$	109	3.31
PMe_3	118	8.65
$P(OMe)_2Ph$	120	2.64
PMe_2Et	123	8.61
PMe_2Ph	122	6.5
PPh_2H	126	0.03
PEt_2Me	127	8.61
$P(OPh)_3$	128	-2
$P(n\text{-}Pr)_3$	132	8.64
PPh_2OMe	132	2.69
PEt_3	132	8.69
$P(n\text{-}Bu)_3$	132(136)	8.43 (9.26)
PEt_2Ph	136	6.25
PPh_2Me	136	4.57
PPh_2Et	140	4.9
$P(p\text{-}F\text{-}C_6H_4)_3$	145	1.97
$P(p\text{-}Cl\text{-}C_6H_4)_3$	145	1.03
PPh_3	145	2.73
PBz_3	165	6
$P(m\text{-}Me\text{-}C_6H_4)_3$	165	3.3
PCy_3	170	9.7
$P(O\text{-}t\text{-}Bu)_3$	172	4.5
$P(t\text{-}Bu)_3$	182	11.4
$P[(2,6\text{-}MeO)_2C_6H_3)_3]$	184	9.33
$P[2,4,6\text{-}MeO)_3\ C_6H_2)_3$	184	11.02
$P(o\text{-}Me\text{-}C_6H_4)_3$	194	3.08
$P(2,4,6\text{-}Me_3\text{-}C_6H_2)_3$	212	7.3

Drago further expanded the E and C model over the years to include families of compounds whose E and C values were not known by introducing **Equation 3.5**.

$$\Delta\chi^X = d^E \Delta E^X + d^C \Delta C^X + \Delta\chi^H \qquad \textbf{Equation 3.5}$$

Here, $\Delta\chi^X$ is the measured property of the molecule containing substituent X, $\Delta\chi^H$ is the same measured property for the proton-substituted compound, ΔE^X and ΔC^X are dual parameter analogues of the Hammett values and d^E and d^C are the dual parameter analogues of the Taft constant and relate to the E and C terms in **Equation 3.4**. Drago has effectively used the E and C model in the descriptions of hundreds of reactions and electronic properties of acid-base interactions, and has suggested that single parameter σ-basicity scales result in the inappropriate introduction of steric effects in acid-base interactions. However, the E and C model has two substantial drawbacks with hinder its utility in understanding reactivity. First, when a reaction involves steric interactions, π-back bonding, or expresses significant entropic effects that are uncorrelated to bond strength, the E and C model fails. Thus the ECW model is limited to the study of sterically unhindered complexes and donor atoms that function in a predominately σ-donor fashion. Secondly, the requirement of prerequisite knowledge of the E and C parameters for the catalyst, as well as the substrate, limits the utility of the model to compounds that have been parameterized within the conscript of the model. Thirdly, the E and C parameters were initially developed upon gas phase and non-interacting solvent ΔH data, and cannot be applied to reactions involving strong solvent interactions that are expressed in terms of an enthalpic contribution to the overall reactivity. The inherent problems with the ECW model have been discussed elsewhere[20] that highlights its limitations as a model phosphorous reactivity.

As mentioned earlier, a second model for LFER determinations entitled quantitative analysis of ligand effects (QALE) involves a combination of parameters that are similar to those of the E and C model, and based upon Tolmans Equation, with the

added utility of allowing for the inclusion of steric effects, as previously defined in **Equation 3.2** and **Equation 3.3** on page 3-10.

$$property = (a \cdot \chi_d) + (b \cdot \Theta) + (b'\cdot(\Theta - \theta_{st}) \cdot \lambda) + (c \cdot E_{ar}) + (d\pi_p) + e \qquad \textbf{Equation 3.3}$$

Here, χ is an electronic parameter[21], Θ (Tolmans cone angle) and $(\Theta - \theta_{st})\lambda$ (Tolman angle at the steric threshold) are steric parameters, and E_{ar} is an aryl effect parameter[20,21,22]. The χ_d parameter, essentially a σ-basicity parameter derived from the shift in the A^1 frequency of ν_{CO} for substituted $Ni(CO)_3PR_3$ complexes, follows in the line of other defined σ-basicity parameters in that it nicely approximates the pK_a of the phosphine of interest (**Figure 3.1e**), and as such is quite similar to E_B, C_B while being directly related to Tolmans electronic parameter through its method of inception. However, one critical assumption is made with regards to the definition of χ_d, such that the property of interest is assumed to be linear over the entire range of compounds studied. Furthermore, the χ parameter renders the QALE model as a single parameter σ-basicity scale, despite the inclusion of the other non-steric parameters. Because of this limitation, the E_{ar} parameter was initially presented and originally represented an aryl effect parameter originally derived from the number, n = 1-3, of aromatic substituents upon phosphorous by Giering and Prock[22] and adapted by Brown but later revised[23] to include all electron withdrawing and electronegative substituents that are bonded to phosphorous. The π_p term, resulted from the desire to escape the intrinsic unreliability of single parameter σ-basicity scales, and represents an attempt at accounting for the π-acidity of a donor and resembles in concept the E parameter of the Drago Equation,

Equation 3.5. However, the π_p term has only been parameterized for a small subset of complexes, and appears centered upon the alkyl and aryl phosphites. Lastly, the e-term in the equation acts as a measure of the standard reactivity of the system and relates to the W-factor of the E and C model (all lines must have an intercept), but unlike W, the e-term is usually non-zero. Furthermore, an analogue to **Equation 3.3**, has been developed specifically for associative reactions of $Ru_3(CO)_{12}$ and P-donor nucleophiles[24] using the QALE methodology, as defined in **Equation 3.6**.

$$\log k_2 = \alpha + \beta \cdot (pK'_a + 4) + \gamma \cdot (\theta - \theta_{th}) \cdot \lambda + \delta \cdot E_{ar} + \phi \cdot (pKa'(\pi)) \quad \textbf{Equation 3.6}$$

Here α, β, γ, and δ are weighting factors, pK_a' is the σ-basicity parameter, and is closely related to χ_d, other basicity parameters and the pK_a of the phosphine, and is defined as dependent upon β, a dimensionless logarithmic term, that provides for a measure of the extent of bond-making in the transition state. The $pK_a'(\pi)$ term represents a measure of the π-acidity of the phosphorous compound, and is governed by the dimensionless quantity ϕ, which acts as a measure of transition state stabilization due to π-backbonding. Here the $pK_a'(\pi)$ and π_p terms are closely related by the relation described in **Equation 3.7**.

$$pK_a'(\pi) = -1.10 + 1.78 \cdot \pi_p \quad \textbf{Equation 3.7}$$

In analogy with **Equation 3.3**, the a-term represents a measure of the standard reactivity, thus resembling the W-term in the E and C model, and the θ and $(\theta - \theta_{th})\lambda$ terms are

identical in meaning and interpretation to those defined previously. Similar to the unmodified QALE analysis, the $pK_a'(\pi)$ is not defined for all phosphines and as such is generally uninvolved in reactions with alkyl, aryl and mixed alkyl-aryl phosphines. The QALE model suffers somewhat from its inherent complexity, but expresses much greater versatility than the E and C model in at least two distinct ways. First, compounds that have had their parameters developed for QALE are transferable to related compounds. For example, reactions involving As and Sb can be directly taken from the existing parameters for phosphorous. Secondly, there is no inherent reliability upon the catalysts parameters (E_AC_A in Drago's equation) such that individual reactions need not be conducted over a closely related family of catalysts. However, the QALE equation may suffer limitations through the presence of an increased weight of the steric parameters and lead to possible over-estimation of its importance. Moreover, the apparent inception of the $pK_a'(\pi)$ parameter was based upon the latter possible weakness in the QALE model such that its incorporation was to allow for steric effects when electronic parameters alone could not account for an observed reactivity.

More recently, the idea of using density functional, ab-initio and semi-emperical theories has gained interest and includes examples of reactivity parameters based upon electrostatic potentials, computed heats and free energies of donor protonation[25], as well as free energy changes associated with the computed reaction coordinate.[26] Thus, the list of parameters used to define the reactivity in these systems would present an impossible list, and this paper will focus upon σ-basicity parameters (pK_a) that have been previously defined.

A Critical Look into Steric and Electronic effects in atom transfer chemistry

Electronic Effects in Oxygen Atom Transfer Chemistry

As noted in the previous sections, the two main themes of reactivity in phosphorous complexes (and presumably N and S complexes) are predominantly centered upon the interplay of electronic effects and steric effects. However despite the abundance of parameters for phosphorous most, if not all, are based upon P(III) and as such present several critical problems with respect to atom transfer chemistry. The first problem arises with respect to σ-donation and π-back bonding; namely that a relatively electron rich P(III) compound should be more efficient than the analogue P(V) complex (regardless of the presence of an oxo-group) at both σ-donation and π-back bonding to electron deficient metals. This is evidenced by the rather large range of pK_a values that have been assigned to P(III) complexes when compared to the narrow range of basicity, pk_{BH}, values for the related P(V) complexes[27]. The second problem arises as an extension of the first in that, although similar in concept, the phosphorous atom does not directly interact with the metal as described in the current parameters. More explicitly, the transition state in atom transfer chemistry reflects an oxo-bridged metal to phosphorous interaction that may either be described as involving the formation of a P=O bond or as cleaving of a M-O bond. This issue becomes even more pronounced when the average M-P(III) bond is compared to the average P(V)-O bond added to the average M-O(P(V)) bond. Even by assuming that the M-OP(V) and M-P(III) bonds are equivalent, any interaction between the metal and the weaker σ-donor and π-back bonding P(V) compound would need to be sustained over an additional ~1.5 Å. Thus the nucleophilic attack of phosphorous on the metal-based oxygen atom most likely involves σ-donor

ability, but its release from the metal as an oxide cannot involve direct π-back bonding of phosphorous to the metal.

Geometric Effects in Oxygen Atom Transfer Chemistry

Equally as problematic are the reported cone angles of the P(III) and P(V) complexes with regard to the Tolman definition and shares many features with the problems associated with electronic effects. The greatest problem with the cone angle arises from it being defined as arising through a direct phosphorous-metal bond, which is absent in atom transfer chemistry. A second problem then arises in the initial nucleophilic attack of phosphorous upon the metal-based oxygen, which for reasons of orbital symmetry, cannot occur along a 180° M-O-P angle. More specifically, the lone pairs of the oxygen atom are in the p_x and p_y orbitals and as such are oriented 90° relative to that defined by the traditional Tolman cone angle. Furthermore the incoming phosphorous nucleophile must then approach the oxygen atom as close as possible to 90° to allow for maximal overlap between the phosphorous and oxygen orbitals. The phosphorous atom, initially with tp symmetry, will change to a td symmetry upon nucleophilic attack at oxygen and result in a R-P-R' angle of ~109°, while oxygen will adopt a more water-like bent-structure after phosphorous attack such that the M-O-P angle must pass through 104°, before forming the final P=O bond (M-O-P ~180). The end result of these interactions is a L-M-O-P torsion that places the phosphorous atom at both a considerably longer distance from the metal and at a "un-Tolman-like" angle, especially in the transition state. Support of this argument can be found through a survey of the phosphine oxide crystal structures showing metal coordination, **Table 3.3** and **Figure 3.4**, in which

the average M-O-P angle, ψ, is highly variable (155.8 ± 14º; n = 43 angles, single coordinated $OPPh_3$; 144.16 ± 3.6º; n=9 angles, single coordinated $OPMe_3$) when compared to the average O-P-R angle of the coordinated phosphine oxide (110.2 ± 1.5º; n = 27 angles).

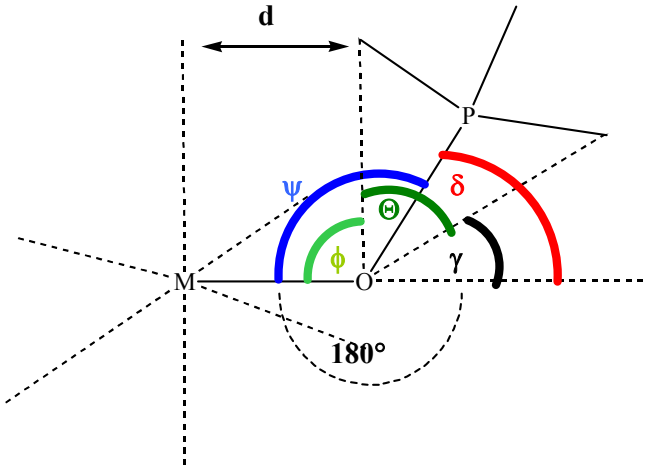

Figure 3.4: Bond angle variability in $P(Me)_3$. Here ψ is the M-O-P angle, and Θ is the Tolman cone angle, relative to oxygen. ψ and Θ, together create three other angles (ϕ, γ, and δ) when 180° is considered the maximum M-O-P bond angle. ϕ represents the effective cone angle that places the ligands of the phosphine at a distance, d, from the metal ligands. γ is the tilt angle with respect to 180°, while δ is the counter-part of ψ which produces the maximum M-O-P angle.

Table 3.3: X-ray structural measurements of coordinated phosphine oxides (CSD Search 03-20-2006)

Phosphine Oxide	Mean P=O	Mean M-O	Mean M-O-P (Ψ)	Mean O-P-R_n	# Obs
$OPMe_3$	1.52 ± 0.04	2.07 ± 0.04	145.9 ± 7.9	111.1 ± 2.4	9
$OPEt_3$	1.53 ± 0.01	2.05 ± 0.004	142.1± 7.2	110.2 ± 2.2	2
$OPMe_2Ph$	1.51 ± 0.01	2.04 ± 0.06	147.4 ± 9.0	111.4 ± 2.1	9
$OPEt_2Ph$	1.53	2.06	153.6	109.6 ± 1.5	1
$OP(n\text{-}Bu)_3$	1.51 ± 0.02	2.34 ± 0.03	159.4 ± 18.3	112.9 ± 4.0	3
$OP(t\text{-}Bu)_3$	1.51 ± 0.03	2.05 ± 0.03	170.1 ± 9.3	107.7 ± 0.6	5
$OPCl_3$	1.46	2.29	142.7	113.3 ± 1.9	1
$OPCy_3$	1.52	2.05	145.5	109.6 ± 3	1
$OP(OPh)_3$	1.50	1.51	134.9	111.1 ± 3.4	1
$OPPh_3$	1.51 ± 0.03	2.16 ± 0.22	157.6 ± 11.3	111.0 ± 2.5	42

Although steric arguments cannot explain the deviations in the M-O-P angle, they may be explained through the insightful theoretical paper by Chestnut[28], that offers the electron localized function description of the P=O bond and adds an electron density derived argument for the partial ionic character of the oxygen to phosphorous double bond, as previously described by Cotton and Wilkinson[29]. The main point of Cotton and Wilkinson can be seen in **Figure 3.5**, where low lying phosphorous d_π orbitals were described as participating in Op_π-Pd_π back bonding which results in a three-fold resonance hybrid view of the phosphorous oxygen bond, described as having single (similar to R_3N^--O^+), double and triple bond character. Chestnuts results show that the oxygen p-orbitals, in the phosphine oxide, are "banana-shaped", with electron density of the electron pairs oriented towards phosphorous and are consistent with the $R_3P^-\equiv O^+$ view of the bonding interaction. Through this argument, if phosphorous were the only atom effectively interacting with the oxygen atom, in d_π-p_π or p_π-p_π interactions, then the P=O-M bond angle would approach 104°.

However, the metal is also interacting with the oxygen, and Holm has reviewed the concept of oxo-functional groups in transition metal chemistry. Accordingly, the metal-oxo groups can be geometrically classified upon two criteria, the first is by the number of oxo-groups and the second is by the number of d-electrons in the metals valence shell. Under these classifications, the geometric considerations of a d^0 metal with two oxo-groups and a d^2 metal with two oxo-groups can be visualized in **Table 3.4** and **Figure 3.5**. Here, the multiple-bond character of the M-O bond depends upon the π-

acceptor ability of the three metal dπ orbitals and the geometric position of the oxygen atoms.

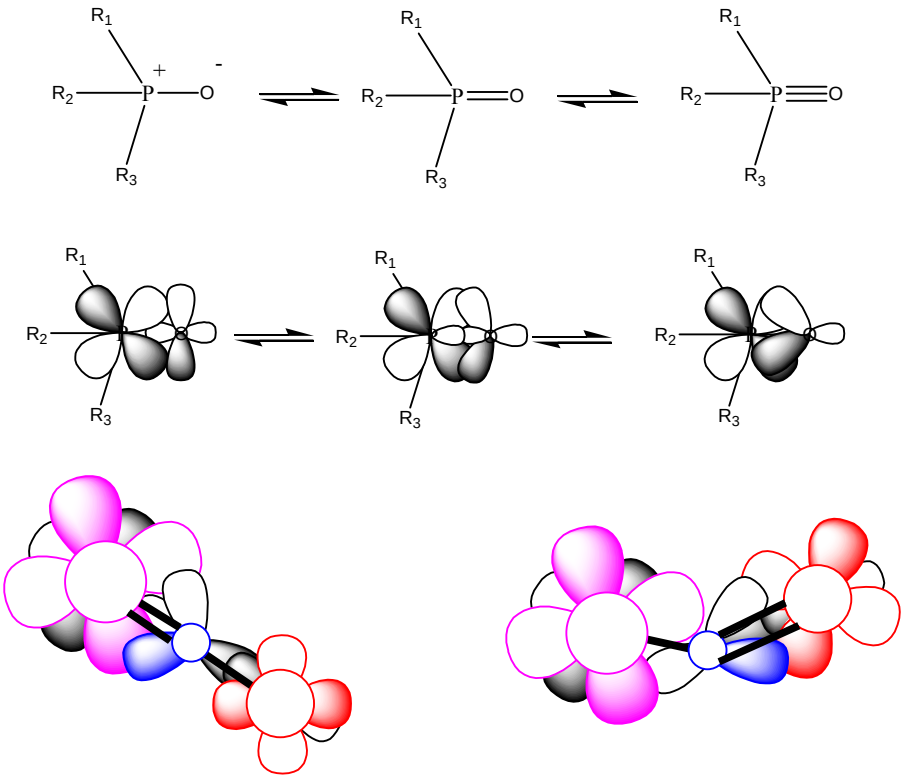

Figure 3.5: **Top:** Phosphorous (V) resonance structures in the P=O bond. **Middle:** Chesnut's orbital[28] description of the P=O bond, combined with Cotton's[29].**Bottom:** Possible explination of the ψ angle of M-O-P bonding.

Table 3.4: Selected Bond Distances and Angles in Oxo and Dioxo-Metal Complexes			
M=O			
Metal (Oxidation State)	**$M=O_{avg}$, [n] (Å)**	**$O=M=O_{avg}$, [n] (°)**	**Electronic Configuration**
Mo (IV)	1.66 ± 0.01 , [2]	NA	$[Kr]3d^2 4s^2$
Mo(VI)	1.64, [1]	NA	$[Kr]3d^0 4s^2$
W (IV)	1.70 ± 0.02 , [2]	NA	$[Kr]3d^2 4s^2$
W (VI)	1.70 ± 0.05 , [2]	NA	$[Kr]3d^0 4s^2$
Re(V)	1.768 ± 0.01 , [3]	NA	$[Xe]4f^{14}5d^2 6s^0$
$M=(O)_2$			
Metal (Oxidation State)	**$M=O_{avg}$, [n] (Å)**	**$O=M=O_{avg}$, [n] (°)**	**Electronic Configuration**
Mo (IV)	1.834, [1]	180, [1]	$[Kr]3d^2 4s^2$
Mo (VI)	1.71 ± 0.01 , [13]	108.6 ± 7.5 , [12]	$[Kr]3d^0 4s^2$
W (VI)	1.72 ± 0.01 , [3]	116.3 ± 8.3 , [2]	$[Kr]3d^0 4s^2$

This suggests that if the terminal oxo-groups are interacting with the metal, the O-M-O angle should be ~112° in the d^0 metal and ~180° in a d^2 metal. Thus, a Cambridge Crystal Database search was limited to structures that possessed a terminal oxo-group and a single coordinated phosphine oxide as well as the crystal data of the known tris-pyrazolyl borate, mono-oxo phosphine oxide intermediates, **Table 3.5** and **Figure 3.6**, in attempt to examine whether the oxygen of the coordinated phosphine oxide behaves as an oxo-group. However, the only examples of a d^2 with both a terminal oxo-group and a single coordinated phosphine oxide in the Cambridge Data Base are limited to Re complexes which appear to function similar to an oxo-group and express O-Re-O(P) angles that approach 180° (172.12 ± 3.2°; n=7 structures). Furthermore the Re-O bond (1.66 ± 0.02 Å) and Re-O(P) bond (2.10 ± 0.04 Å) lengths of and are slightly shorter and slightly longer than the average mono-oxo Re-O bond (1.77 ± 0.01 Å) respectively. This suggests that the Re-O bond has considerably greater triple bond character than the mono-oxo Re-O bond, while the Re-O(P) bond can be classified as a single bond.

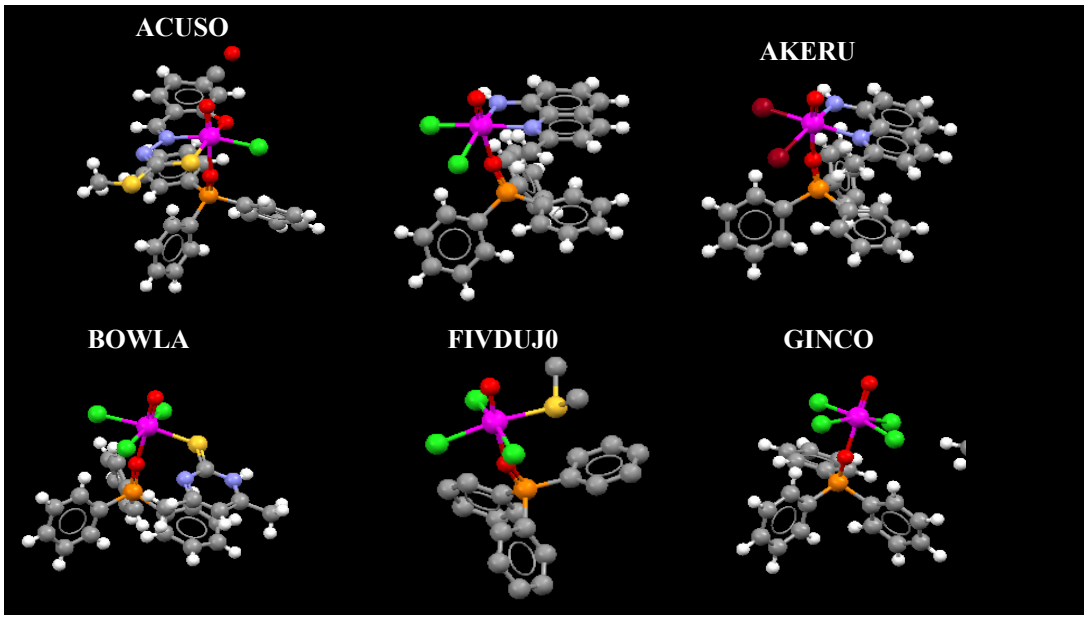

Figure 3.6: Crystal structures taken from the Cambridge Crystal Database containing a single phosphine oxide and a terminal oxo-group

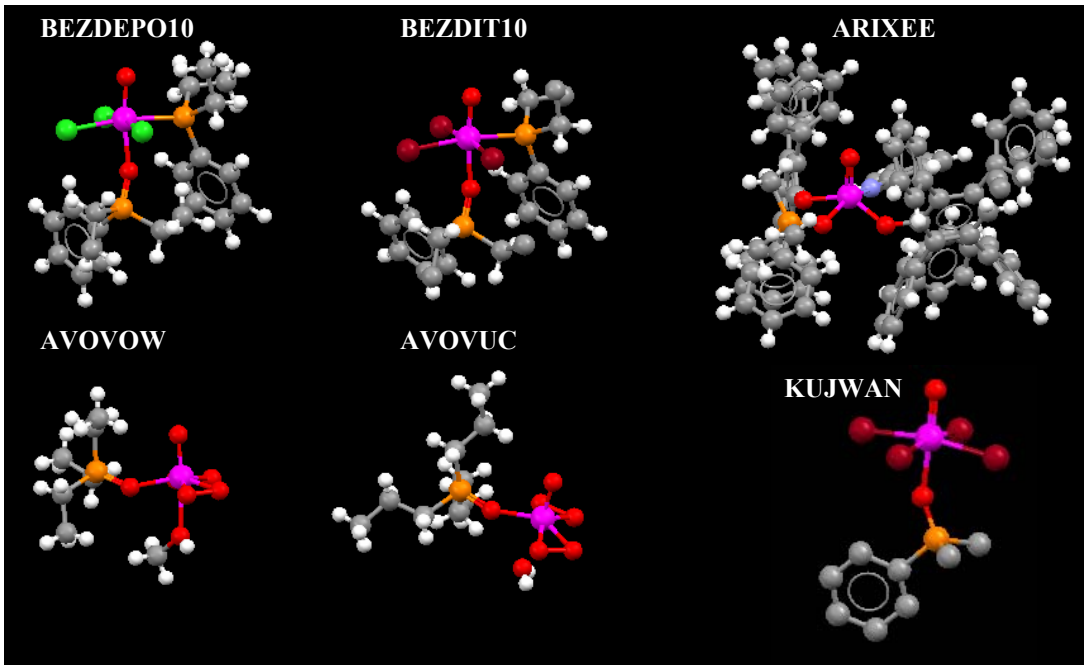

Table 3.5: Structural Parameters for Mono-oxo Metal Complexes With Single Phosphine Oxide Coordination

structure	phosphine	M-O(P) (Å)	P=O (Å)	$M\text{-}O_t$ (Å)	M-O-P (°)	O-M-O(P) (°)	Electronic Configuration	C.N	Geom[f]	Ox State
ARIXEE[a]	$OPMe_3$	2.117	1.506	1.694	137.4	97.95	$[Kr]3d^04s^2$	5	SqP	W(VI)
AVOVOW[a]	$OPEt_3$	2.048	1.536	1.68	137.1	96.04	$[Kr]3d^04s^2$	7	PBP	Mo(VI)
AVOVUC[a]	$OPEt_3$	2.043	1.527	1.672	147.2	93.82	$[Kr]3d^04s^2$	7	PBP	Mo(VI)
BEZDIT10[a]	$OPMe_2Ph$	2.054	1.514	1.663	158.9	172.58	$[Xe]4f^{14}5d^26s^0$	6	Oh	Re(V)
KUJWAN[a]	$OPMe_2Ph$	2.109	1.528	1.677	152.1	176.65	$[Kr]3d^04s^2$	6	Oh	W(VI)
BEZDEP10[a]	$OPEt_2Ph$	2.063	1.525	1.672	153.6	172.77	$[Xe]4f^{14}5d^26s^0$	6	Oh	Re(V)
ACUSOG[a]	$OPPh_3$	2.181	1.449	1.667	156.4	176.39	$[Xe]4f^{14}5d^26s^0$	6	Oh	Re(V)
AKEROX[a]	$OPPh_3$	2.117	1.502	1.669	167.5	167.41	$[Xe]4f^{14}5d^26s^0$	6	Oh	Re(V)
AKERUD[a]	$OPPh_3$	2.126	1.499	1.666	166.6	167.91	$[Xe]4f^{14}5d^26s^0$	6	Oh	Re(V)
BOWLAA[a]	$OPPh_3$	2.087	1.494	1.621	172.5	174.62	$[Xe]4f^{14}5d^26s^0$	6	Oh	Re(V)
FIVDUJ01[a]	$OPPh_3$	2.072	1.509	1.651	164.0	173.14	$[Xe]4f^{14}5d^26s^0$	6	Oh	Re(V)
GINCOV[a]	$OPPh_3$	2.05	1.603	1.728	156.2	179.05	$[Kr]3d^04s^2$	6	Oh	W(VI)
$Tp^{iPr}MoO(OPPh_3)Cl$[b]	$OPPh_3$	2.159	1.498	1.749	146.7	98.52	$[Kr]3d^24s^2$	6	Oh	Mo(IV)
$Tp^{Me2}MoO(OPMe_3)Cl$[c]	$OPMe_3$	2.158	1.503	1.724	134.1	96.61	$[Kr]3d^24s^2$	6	Oh	Mo(IV)
$Tp^{Me2}MoO(OPMe_3)Cl$-2[d]	$OPMe_3$	2.138	1.491	1.726	133.6	96.35	$[Kr]3d^24s^2$	6	Oh	Mo(IV)
$Tp^{Me2}MoO(OPMe_2Ph)Cl$[c]	$OPMe_2Ph$	2.148	1.462	1.908	144.0	97.04	$[Kr]3d^24s^2$	6	Oh	Mo(IV)
$Tp^{Me2}MoO(OPMe_3)$(p-$OMe\text{-}C_6H_4S$)[e]	$OPMe_3$	2.174	1.501	1.684	133.41	99.79	$[Kr]3d^24s^2$	6	Oh	Mo(IV)
$Tp^{Me2}MoO(OPMe_3)SPh$ [e]	$OPMe_3$	2.154	1.504	1.687	136.76	99.25	$[Kr]3d^24s^2$	6	Oh	Mo(IV)

(a) structural data taken from the Cambridge Crystal Database[15] (b) taken from reference 42 (c) taken from reference 30 (d) unpublished result
(e) taken from reference [31] (f) SqP = square pyramidal; PBP = pentagonal bipyramidial; Oh = octahedral

The examples of the d^0 metals that fit the previously mentioned criteria are limited to W and Mo, which exhibit more complex behavior. For example, the Cambridge structures with $OPMe_3$ and $OPEt_3$ coordinated to either W-d^0 or Mo-d^0 (3 total) place the phosphine in the equatorial plane with an average O-M-O(P) angle of 95.9 ± 2.1°, which is significantly smaller than that observed in dioxo, W-d^0 (116.3 ± 8.3°) or Mo-d^0 (108.6 ± 7.5°) complexes. However, the Mo-O bond (1.68 ± 0.01 Å) and the W-O bond (1.69 Å) lengths are in good agreement with a mono-oxo Mo(VI) or W(VI) center, while the Mo-O(P) bond (2.05 ± 0.00 Å) and the W-O(P) bond (2.12 Å) lengths or considerably longer than the expected W=O and Mo=O bond length (~1.72 Å). On the other hand, the structures of W-d^0 with coordinated $OPPh_3$ and W-d^0 with coordinated $OPMe_2Ph$, show an average O-W-O(P) angle of 177.8 ± 1.8°, and suggests that there is little $O_{p\pi}$ to $M_{d\pi}$ interaction between the metal and the phosphine oxide oxygen. In addition the average W-O bond (1.70 ± 0.04 Å), and the average W-O(P) bond (2.08 ± 0.04 Å) length in these complexes agree well with the bond lengths observed through equatorial phosphine oxide coordination. Finally, when the phosphine oxide intermediates of the general formula $Tp^RMo(IV)O(OPR'_3)X$, (where Tp is hydrotris-pyrazol-1yl borate, R = 3 5- dimethyl or 3-isopropyl, R' = Me, Ph and X = Cl or SPh), were considered, an average O-M-O(P) angle of 97.9 ± 1.5° was found, which is surprisingly consistent with the d^0 Mo and W complexes from the Cambridge Database (95.9 ± 2.1°). Furthermore, the average Mo-O bond (1.71 ± 0.03 Å) and the average Mo-O(P) bond (2.16 ± 0.01 Å) lengths in these complexes are also in good agreement with bond lengths observed in the d^0 Mo and W complexes. However, the average Mo-O bond

in these complexes appear intermediate in length between the mono-oxo d^2 Mo-O bond (1.66 ± 0.01 Å) and the dioxo d^2 M-O bond (1.83 Å) length, while the average M-O(P) bond is consistent with a slightly elongated Mo-O single bond.

This M-O(P) data presents a picture of the coordinated phosphine oxide which is similar to the metal-oxygen interactions that prevail in other oxygen containing ligands[32], such as alkoxides, phenolates, and carbonyls. In ligands such as alkoxides and phenolates containing a C-O single bond, the M-O(C) bond angle bond typically ranges from 110° to 140°, while carbonyls with C=O double bond ranges from 140° to 170°. More importantly, the ranges in these M-O-C bond angles have been attributed to the variability of π-donation to the metal as well as the metals π acceptor ability. Taken together, the variability of the M-O(P) angle can be attributed to at least four distinct features namely, the geometry of the metal, the oxidation state of the metal, the π-donor ability of the oxygen, and the π-acceptor ability of the metal.

Octahedral Metal Complexes with Tetragonal Compression.

The data suggests that when an octahedral, d^2, dioxo-metal center participates in OAT chemistry, the resultant phosphine oxide complex is somewhat destabilized by weak, yet significant interactions between the filled, non-bonding oxygen p orbitals and the filled metal d_{xy} orbital (**Figure 3.7, Figure 3.8** and **Figure 3.9a).** As a result, the complex can attempt to alleviate this destabilization in two ways. First, by placing the coordinated phosphine oxide in a trans position, relative to the terminal oxo-group, similar to the interactions observed in the octahedral, d^2 $Re(V)O(OPR_3)$ and $Mo(IV)O_2$ complexes, the oxygen p orbitals are placed orthogonal to the filled metal d_{xy} orbital.

Secondly, the M-O(P) angle can be decreased such that the non-bonding, oxygen p-orbitals are placed in a nearly orthogonal position relative to the metal d_{xy} orbital.

The first case, in terms of a coordinated oxo-ligand, suggests that the strength of the M-O(P) σ-donor interaction is similar to that found through coordination of a carbonyl oxygen. Here the M-O(P) bond strength, through σ-donor interaction, is expected to be greater as the M-O-P angle approaches 180° and that the predominant oxygen pπ interactions would involve the phosphorous dπ orbitals. The predominance of this effect in the d^2 Re(V) complexes is not surprising since the ligand architectures allow for relatively easy isomerism with respect to the group that is positioned trans to the terminal oxo-group. The second case, the M-O-P bond angle appears to result from a σ-donor interaction that is similar to that found in coordinated alkoxides and phenolates. However, the tridentate, facially coordinating Tp ligand does not allow for isomerism between a pyrazol nitrogen and phosphine oxide oxygen such that the σ-donor interaction between the d^2 metal and the phosphine oxide is sacrificed to elevate destabilization of the metal d_{xy} orbital by the oxygen pπ orbitals. Accordingly, it is expected that the M-O(C) bond weakens as the M-O-P angle is reduced. These conclusions are consistent with both the slightly elongated M-O(P) bond as well as the previously mentioned intermediate M-O bond length.

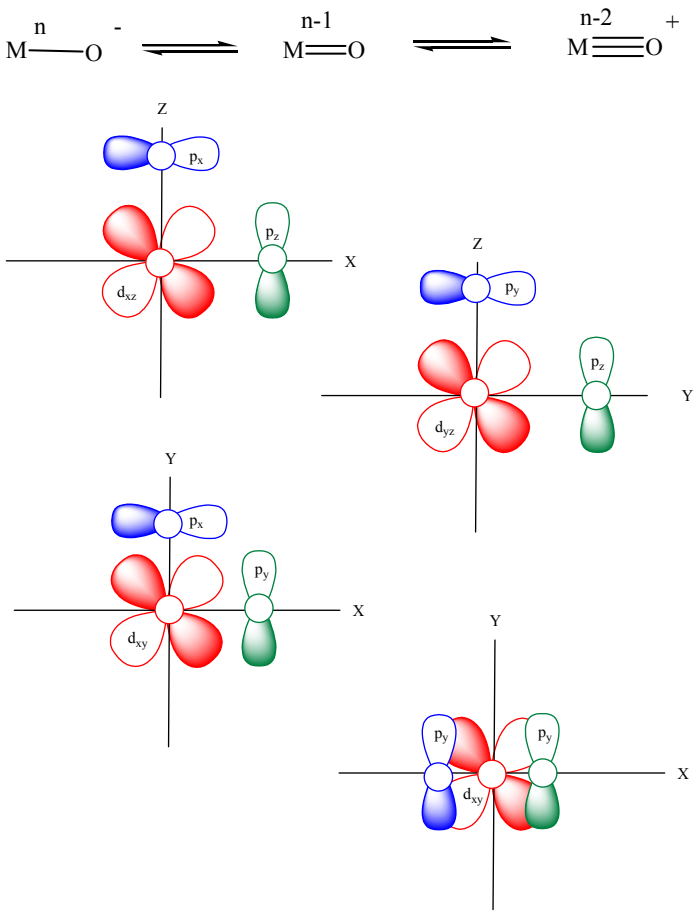

Figure 3.7: **Top:** Metal-Oxygen interactions with oxygen as a ligand. **Bottom:** Possible metal dπ, oxygen π and phosphorous dπ interactions involved in metal oxygen multiple bonding

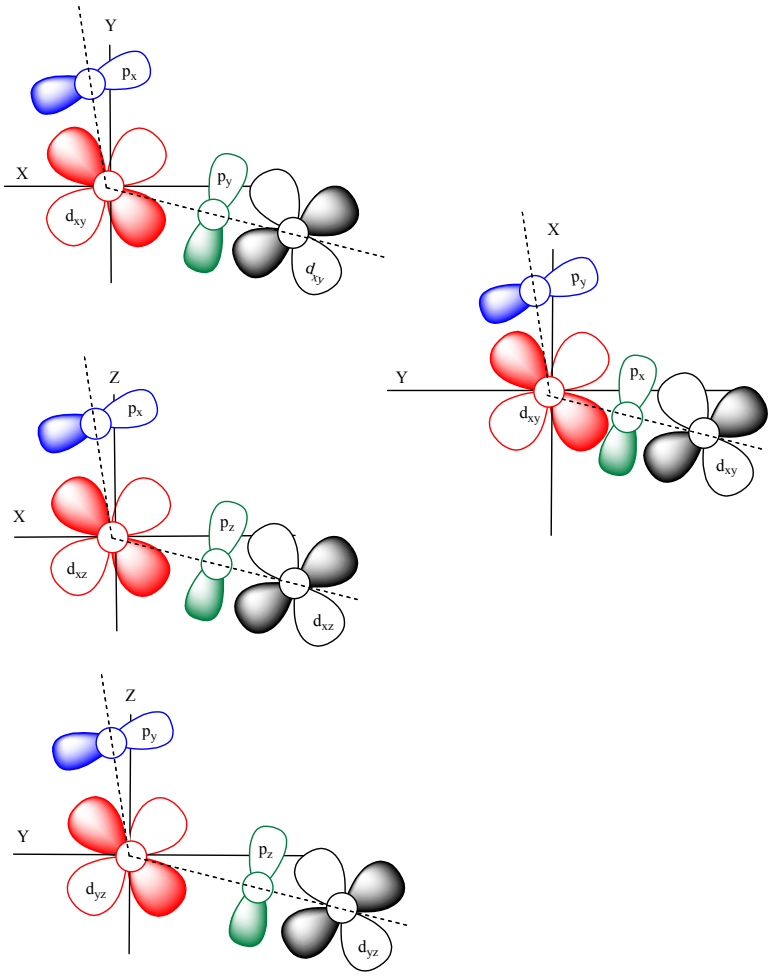

Figure 3.8: Possible metal dπ, oxygen π and phosphorous dπ interactions during OAT from a dioxo-metal center.

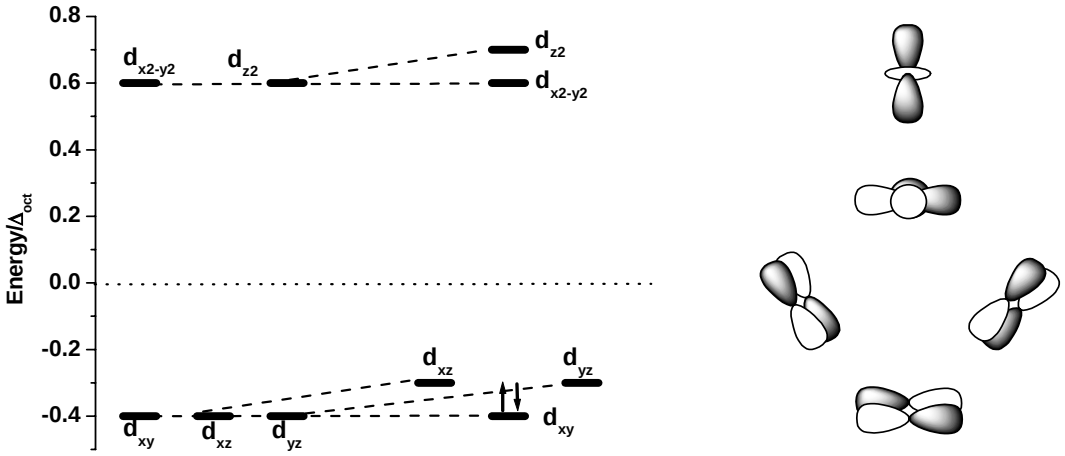

Figure 3.9a:**Left panel:** Relative ligand field energy diagram for an octahedral metal complex and an octahedral complex with tetragonal compression due to the terminal oxo-group. **Right panel:** Representation of the atomic d-orbitals presented to the left.

The weakness of the M-O(P) interaction is further supported by the two crystallographically characterized W(VI) complexes (KUJWAN and GINCOV). Formally, these complexes should exist with the oxygen atoms positioned cis to one another if it were a true dioxo species. However, the fact that the M-O-P angles in these complexes approaches 180°, suggests that there is little $M_{d\pi}$ to $O_{p\pi}$ interaction, relatively stronger M-O σ interactions and stronger $P_{d\pi}$ to $O_{p\pi}$ interaction. . Additionally the relatively elongated M-O(P) bond distance of (2.11 ± 0.05 Å), is suggestive of a formal M-O single bond.

We have observed a similar situation arising in the cis and trans geometric isomers of the d^1, Mo(V) complexes of (3-tert-butyl 2-hydroxy-5-methylphenyl)bis(3,5-dimethylpyrazolyl)methane) and the related (2-hydroxy-5-methylphenyl)bis(3,5-

dimethylpyrazolyl)methane), and is described in greater detail in **Chapter 4** of this work. However, a short description of their behavior that is relevant to this discussion is that a statistical mixture of equatorial and axial phenolate oxygens are achieved during synthesis of the complex (cis = equatorial oxygen and trans = axial oxygen). Upon standing in solution the pure cis complex will spontaneously isomerize to the trans complex via an intermolecular twist mechanism, due to the intereactions between the partially filled metal d_{xy} orbital and the oxygen pπ orbitals.

Square pyramidal and Pentagonal bipyramidal Metal Complexes

In both of the non-distorted geometries, the metal d_{xy} orbital is generally higher in energy than the degenerate d_{xz}, d_{yz} pair by ~ 0.35 Δ_{oct} for square pyramidal and by ~ 2.5 Δ_{oct} for pentagonal bipyramidal.[33]

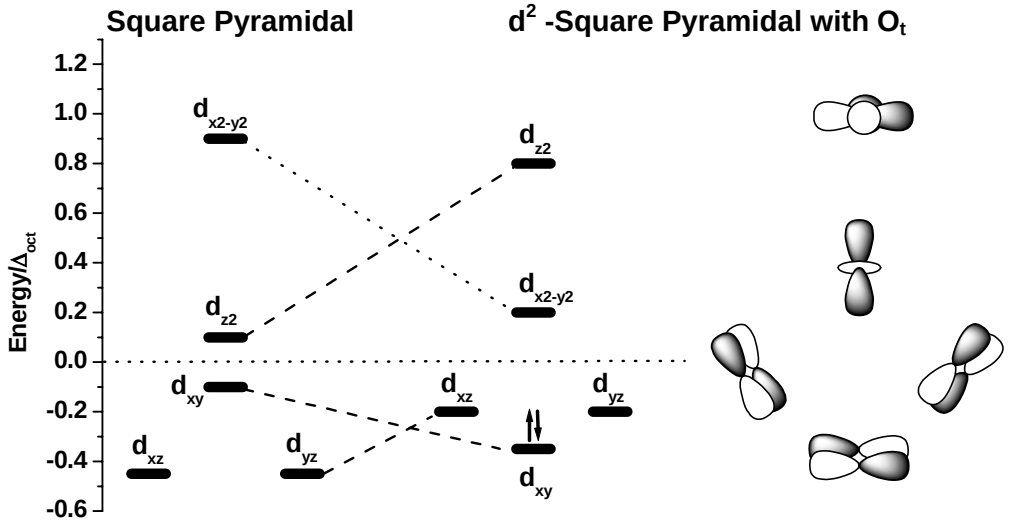

Figure 3.9b: **Left panel:** Relative ligand field energy diagram for a square pyramidal metal complex and a square pyramidal complex with compression along the z axis due to the terminal oxo-group. **Right panel:** Representation of the atomic d-orbitals presented to the left.

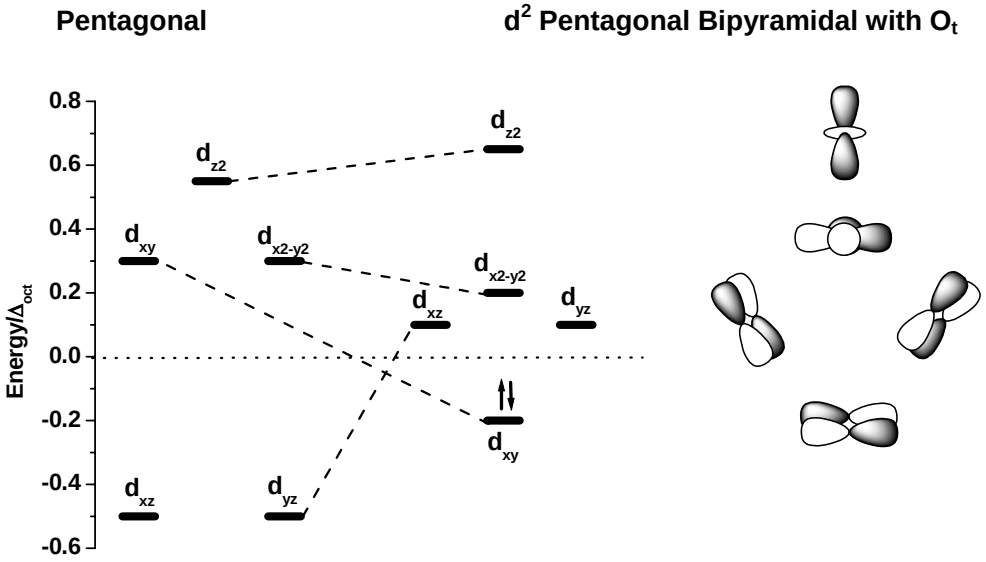

Figure 3.9c:**Left panel:** Relative ligand field energy diagram for a pentagonal bipyramidal metal complex and a pentagonal bipyramidal complex with compression along the z axis due to the terminal oxo-group. **Right panel:** Representation of the atomic d-orbitals presented to the left.

Thus in cases involving Jahn-Teller distortions, produced by a terminal oxo-group in the z-plane, the d_{xy} orbital become lower in energy than both of the degenerate dπ orbitals. Thus the electron pair in a d^2 complex, in either of these geometries, should reside in the (d_{xy}) orbital, **Figure 3.9b**and **Figure 3.9c.** Interestingly, the destabilization that was produced in the equatorial plane of the compressed octahedral systems via the d_{xy} orbital (resulting from oxygen pπ orbitals interaction) appears to be of less influence in the square pyramidal and pentagonal bipyramidal metal complexes. However, the higher energy of the dπ orbitals in the distorted pyramidal and trigonal bipyramidal systems possibly offers greater destabilization such that the coordinated phosphine oxide remains single bonded to the metal in the equatorial plane. The end result is that the interaction between the d_{xz} and d_{yz} orbitals and the electron density of the oxygen pπ

orbitals is minimized. These interactions in turn produce a situation that whose end result is similar to that seen in the octahedral complexes with the Tp ligand, with reduced σ-donation from oxygen to the metal expressed as a small M-O-P bond angle less than 98°.

A second result of this electronic tug-of-war between the metal on the phosphorous atom is a tendency of the M-O-P angle to approach an intermediate structure that is neither bent (both M-O and P-O single bonds should have water-like geometry and 104.5° angle) nor linear (a strong M-O bond and P-O bonds should approach 180°) such that the M-O-P angle deviates from 180° by an angle δ, **Figure 3.4.** This in turn creates a much larger effective cone angle, Θ_{eff}, of the phosphine oxide, which is mathematically equal to: $\Theta_{eff} = \Theta + [180-(\Psi+½\Theta)]$

Combining Geometric and Electronic Effects in Oxygen Atom Transfer

Regardless of its origin, one of the defining events in the atom transfer reaction cannot correlate with the formal definition of the cone angle for two reasons. First, the metal to phosphorous distance is indeterminate, or at best the sum of the P=O bond distance, **Table 3.6**, and the M=O distance (3.2-3.5 Å), and the angle of maximal steric interaction does not necessarily occur at 180°. For example, the average M-O bond length in 74 structures, shown in **Table 3.3**, was found to be 2.06± 0.22 Å, while the average coordinated P=O bond, in $OPPh_3$, was found to be 1.503 ± 0.028 Å (n=43 structures), and the average P=O bond of the free phosphine oxide was found to be 1.485 ± 0.039 Å (n=74 structures). However, as previously mentioned, a strong correlation has been observed between the Tolman cone angle and the reactivity of phosphorous compounds, generally with phosphine in the role of entering, leaving or stationary ligand. In attempt

to understand correlation to reactivity phenomenon, the phosphines geometry may be viewed in two ways.

Table 3.6: X-ray structural measurements of free phosphine oxides (CSD Search 03-20-2006)

Phosphine oxide	Mean P=O	Mean O-P-R_n	Number of Observations
$OPMe_3$	1.49	111.1 ± 1.1	1
$OPEt_3$	1.51 ± 0.01	111.5 ± 1.0	2
$OPEtPh_2$	1.48	112.5 ± 1.3	1
$OP(n\text{-}Pr)_3$	1.50	112.6 ± 1.0	1
$OP(OEt_3)$	1.44 ± 0.002	116.9 ± 1.9	2
OP(OMe)MePh	1.48 ± 0.01	114.1 ± 3.9	2
$OP(OMe)_2Me$	1.47	114.6 ± 1.3	1
$OP(p\text{-}OMe\text{-}C_6H_4)_3$	1.48 ± 0.003	114.1 ± 3.8	2
$OP(p\text{-}Cl\text{-}C_6H_4)_3$	1.48 ± 0.003	112.2 ± 0.7	3
$OP(C_6F_5)_3$	1.46 ± 0.00	112.9 ± 1.8	2
$OP(Ph)(C_6F_5)_2$	1.47 ± 0.01	112.6 ± 1.5	2
$OPPh_3$	1.49 ± 0.02	111.8 ± 1.2	74

First, when the trends in the tp phosphine cone angle are plotted verses trends in both the geometry optimized phosphine oxide and phosphine cone angles; it is evident that the tp trends are mirrored by trends in the td phosphorous cone angle as well as the theoretical phosphine cone angle, **Figure 3.10**

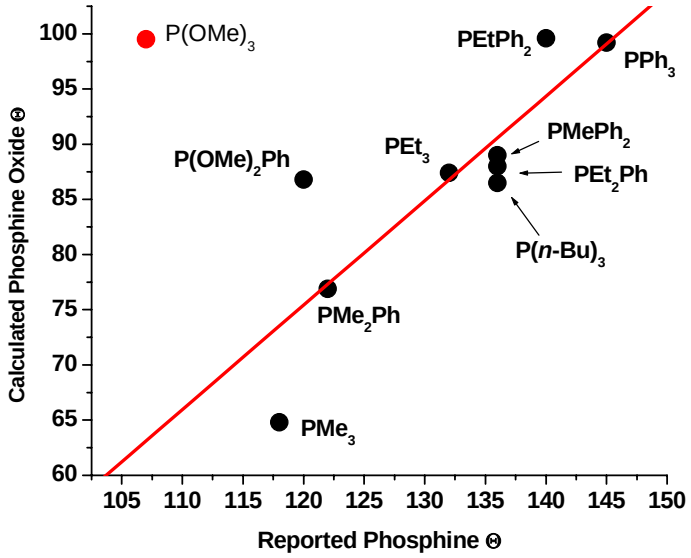

Figure 3.10: Plot of the reported PR_3 cone angle (tp) geometry verses the calculated OPR_3 cone angle with td geometry. $R^2 = 0.845$ with $P(OMe)_3$ considered as an outlier.

Thus suggests that, for a given system, the relative trends in the angles are more important than the absolute angle. Second, the phosphine can be viewed as existing in three or four discrete states: 1) the Tolman Configuration, 2) the optimized configuration, 3) the free crystal configuration and 4) the coordinated crystal configuration. Once the state of interest is constructed, it may then be rotated in three dimensions to carve out a spherical volume of possible steric interaction **(Figure 3.11a – Figure 3.11c).** This concept, of rotating a molecule in three dimensions, is similar to the solvation model described by Onsager[34] in which a dipole (solute) is rotated about its center of mass to produce a spherical volume that interacts with the bulk solvent.

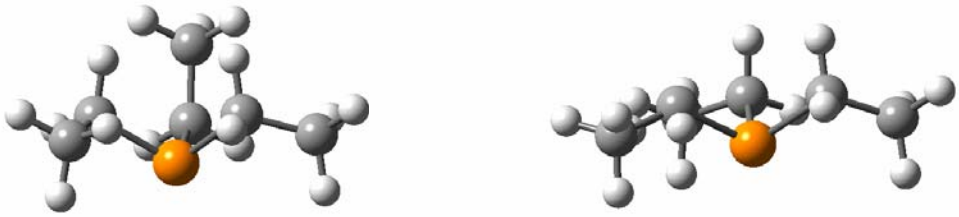

Figure 3.11a: Right: B3P86/6-311G(d,p) optimized PEt_3 geometry (cone angle = 121.84). Left: PEt_3 geometry with maximal steric interations (cone angle = 137.79

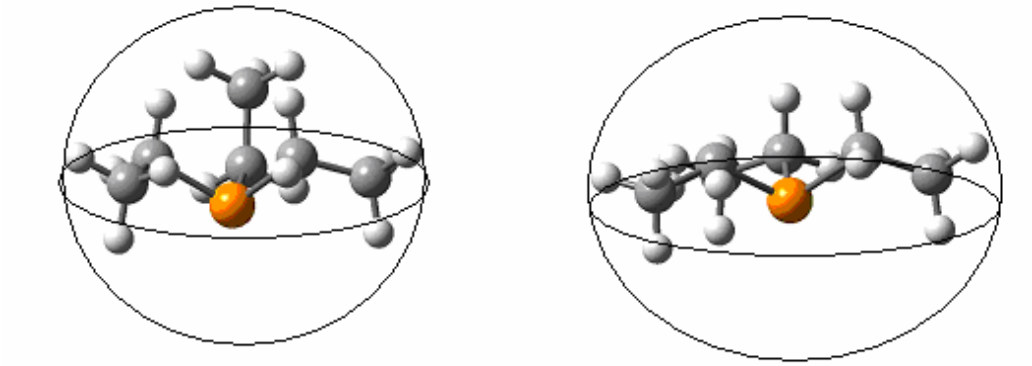

Figure 3.11b: Representation of the Onsager Volume of PEt_3 in **Right:** Geometry Optimized (radius = 4.41 Å; Volume = 113.067 cm^3/mol) and **Left:** Tolmans Configuration (radius = 4.37 Å, Volume = 110.022 cm^3/mol). Here a difference of 15.9° in the cone angle (11.6% difference) translates to a difference in radius and volume of 0.04Å or 3 cm^3/mol (2.7% difference) respectively.

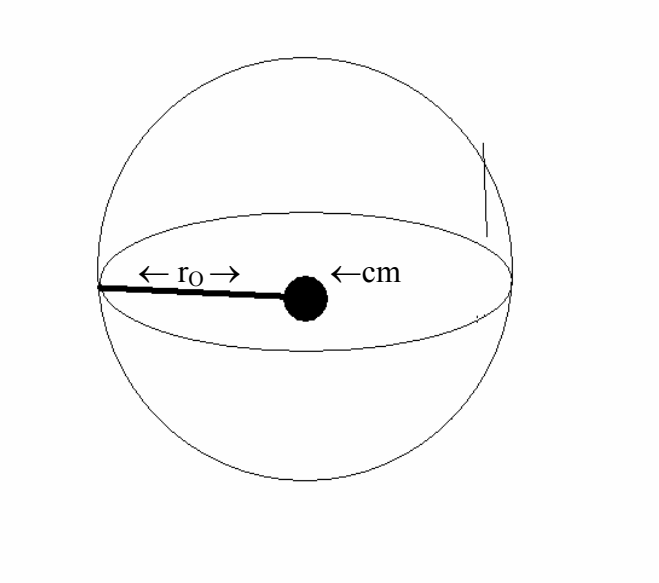

Figure 3.11c: Generalized view of the Onsager Volume calculation (cm = center of molecular mass, r_O = radius of molecule from center of mass, V_O = volume of molecule upon rotation about the center of mass, and π is of usual significance.

When a similar procedure is conducted for all of the geometric states, followed by referencing to the optimized structure a remarkable pattern in **Figure 3.12** emerges in which the three dimensional steric interaction-volume shows an amazingly small deviation in magnitude relative to the large deviation in cone angle. Furthermore the relationship between the reported cone angle and the Onsager volume becomes clearer in **Figure 3.13**, which is relatively linear with an R^2 of 0.792 for 14 phosphines. As previously stated, despite the volume of data that is present for phosphines, there is surprisingly little data with regards to the related phosphine oxides. With such limited data on both the reactivity of phosphine oxides and the limited incorporation of coordinated phosphine oxides in crystal structures, we must be reliant upon the parameters derived for the parent phosphine for trends in reactivity.

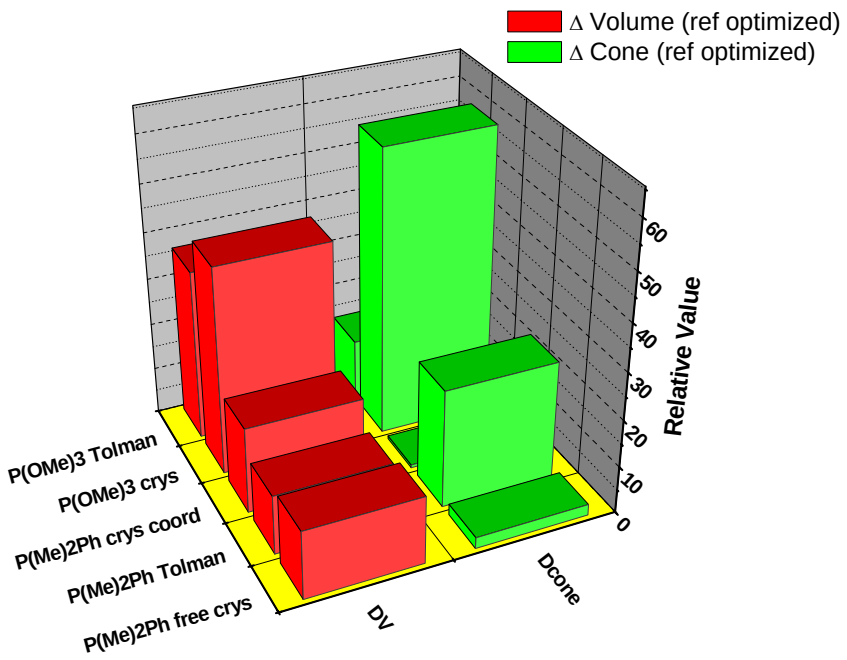

Figure 3.12: Depiction of small ΔV associated with large Δcone

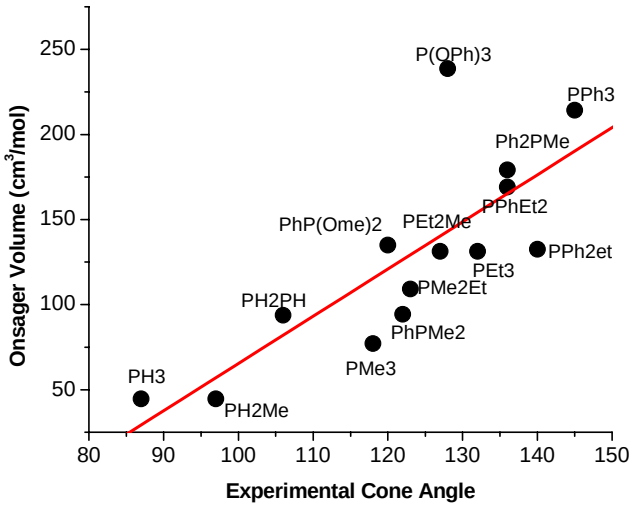

Figure 3.13: Graph of linear correlation between Tolman Cone Angles and Onsager molar volumes (R^2 = 0.793; N=14)

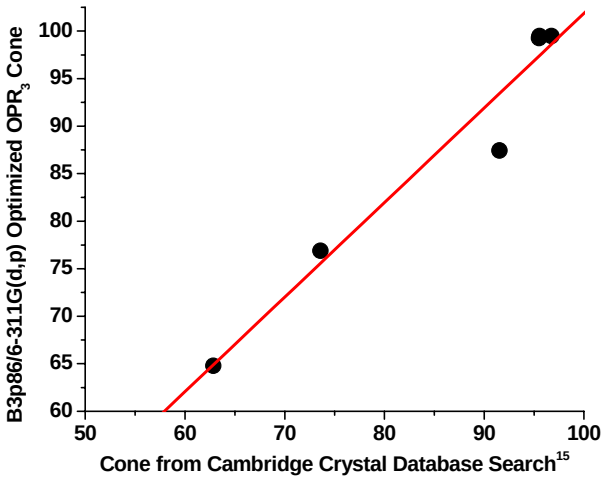

Figure 3.14: Plot of the cone angle taken from the B3P86/6-311G(d,p) optimized geometry verses the cone angle determined for the free phosphine oxide in the Cambridge Crystal Database Structures. $R^2 = 0.998$; slope = 0.995 ± 0.11; intercept = 2.4 ± 9.3; N = 5 observations.

On the other hand, when the corresponding phosphine-oxides are examined, there is a good correlation ($R^2 = 0.978$) between the calculated and experimentally observed phosphine cone angles, **Figure 3.14**. In this sense, it becomes possible to assign a Tolman cone angle to the phosphine oxides through theoretical calculations, which appear to predict the actual cone angles precisely, albeit in the strictest Tolman sense ($M\text{-}O_{avg}$ taken as 1.90Å, L-M-O-P assumed 180º and calculated with **Equation 3.1**).

Phosphorous in Atom Transfer Chemistry

The reactivity of phosphorous compounds as both organometallic ligands and oxygen atom abstracting agents in atom transfer chemistry represents the most thoroughly studied class of donors and acceptors known. The most commonly studied

classes of phosphorous compounds are the phosphorous (III) alkyl, aryl and mixed alkyl-aryl phosphine complexes bearing the three of such substituents (PR_3). The second most studied class of phosphorous (III) complexes are the alkoxy, phenoxy and mixed alkoxy-phenoyl phosphines (phosphites or simply $P(OR)_3$), which are constituted analogously to the previously mentioned PR_3 compounds. In addition to the PR_3 and $P(OR)_3$ complexes, their related, oxo-phosphorous V complexes, OPR_3 and $OP(OR)_3$ respectively, represent the predominant oxygen atom donor in OAT chemistry. Although these classes of compounds predominate the literature involving oxygen atom transfer, there are also examples of tri-halogenated phosphines, the most common of which is PCl_3 as well as phosphorous (III) analogue compounds such as $As^{III}Ph_3$ and its related $OAs^{V}Ph_3$. Understanding the chemistry of the latter class of complexes has significant implications into the biogeochemical cycling of arsenic, as well as in understanding the feasibility of potential remediation strategies of arsenic contaminated aquifers. As eluded to in the introduction, phosphorous complexes represent a unique class of compounds in the understanding of atom transfer catalysis, based on the principle that when the PR_3 and $P(OR)_3$ compounds are considered together, a diverse range of solvents becomes available which spans in dielectric constant from benzene 2.274 to water 80. Secondly, the large availability of R-groups presents a unique opportunity to study the electronic effects in OAT, by creating a pK_a range of ~ 4 to ~ 9 as a function of substitution in the PR_3 complexes and a pK_a range of ~ -2 and ~ 4.5 in the $P(OR)_3$ phosphorous compounds. However, the last point of interest produced by variable substitution at phosphorous is that it presents the possibility of investigating steric effects in addition to electronic effects. Although a full discussion of steric properties can be found in the preceeding, an

example of steric variability can be found in the alkyl phsophines whose pK_a falls narrowly in the range of ~8.5 to 9, but encompasses a reasonable large steric variability in terms of the Tolaman cone angle of ~108º (PMe_3) to ~136º (P*n*-Bu_3) as shown in **Table 3.1**.

Despite the variety in phosphorous physico-chemical properties, the number of phosphines and phosphine oxides used in oxidation and reduction reactions appears relatively limited and has generally been contained to $P(OMe)_3$, PEt_3, PEt_2Ph, $P(OMe_2)Ph$, $PEtPh_2$, PPh_3, and $P(OPh)_3$, especially in the arena of metal centered catalysis. Furthermore, the principle volume of phosphine oxidation research has been limited to the reactivity of only a small subset of these compounds with a given oxygen atom donor such that there are no large datasets that encompass a single donor with a large variety of phosphines. However, three significant pieces of information can be extracted from the trends in phosphine reactivity with multiple oxygen donors and an important subset of this data can be found in **Table 3.7.** First, when the reactivity of neutral $TpRe^{V}OCl_2$ is compared with that of the mono-cationic analogue $[Tp^*Re^{V}OCl_2]^+$, (defined in **Table 3.7**) towards PPh_3, a macroscopic charge effect upon the rate of the reaction is observed in that the mono-cation is ~776x more reactive than the neutral species. Here the term macroscopic charge effect refers to the readily physically observable difference in charge between the Re^{V} complexes. In this example the rate increase can only arise through charge differences in the catalyst because two isosteric catalysts have been employed with the same phosphine.

Table 3.7: Oxygen Atom Transfer Chemistry to Phosphorous						
Compound Acceptor	**Reactant**	**Rate x10^5 ($M^{-1}s^{-1}$)**	**$\Delta H^{\ddagger}$ ($kJ \cdot mol^{-1}$)**	**$\Delta S^{\ddagger}$ ($J \cdot mol^{-1} \cdot K^{-1}$)**	**$\Delta G^{\ddagger}$ ($kJ \cdot mol^{-1}$)**	**Ref**
$Mo^{VI}O_2$(ssp)	PPh_2Et	7.1	65.2	-86.5	91.0	35
$[Tp^*Re^{V}OCl_2]^+$	PPh_3	970	56 ± 2	-79.4 ± 8.4	78.8	36
$TpRe^{V}OCl_2$	PPh_3	1.25	71.5 ± 2	-82.4 ± 1.7	-82.4 ± 1.7	36
$[Mo^{VI}O_2(mnt)_2]^{2-}$	PPh_3	934	62.7	95.3	62.7	37
$[Mo^{VI}O_2(mnt)_2]^{2-}$	PEt_3	417	-54.3	78.9	46	37
$Mo^{VI}O_2$(*t*BuL-NS_2)	PEt_3	49	-117.4	80.9	40.1	38
ssp= [2-(salicylindenamino)benzethiolate]$^{2-}$; Tp*= hydrotris(pyrazol-1yl)methane; Tp= [hydrotris(pyrazol-1yl)borate]$^{1-}$; mnt= [*cis*-1,2-dicyano-1,2-ethylenedithiolate]$^{2-}$; *t*BuL-NS_2 = {*tert*-butyl[2,6-bis(2,2-dipphenyl-2thioethyl)pyridinate]}$^{2-}$						

In terms of reactivity models, Θ, E_{ar} and χ_d of the QALE model are identical and, if added data were present, would provide for an interesting analysis when the two complexes are compared. On the other hand, the E and C model would suggest that the E_B and C_B values would be the same with different E_A and C_A values for each complex. However, the presence of a net charge on the $[Tp^*Re^{V}OCl_2]^+$complex may lend to failure of this model provided that the charge produces a solvation-based enthalpy contribution in the transition state. A second trend in the data can be seen when the reaction of di-anionic $[Mo^{VI}O_2(mnt)_2]^{2-}$ is examined with two different phosphines, there is a clear substrate effect in that PEt_3 is approximate twice as reactive than PPh_3. Again, the E and C would predict an EA and CA value for the catalyst, which could be compared with other similar complexes, while the QALE model would essentially provide a similar-minded profile of the reaction. Unfortunately, the prospect of enthalpy contributions arising from solvation of the charged reactant could present problems for the E and C model. Lastly, there is a donor atom dependence that arises from the metal based ligands such that $Mo^{VI}O_2$(*t*BuL-NS_2) having an NS_2 donor set is 7x more reactive with PEt_3 than $Mo^{VI}O_2$(ssp), having an O,N and S donor set, with $PEtPh_2$. Although the phosphines in

this example are different, the earlier example with $[Mo^{VI}O_2(mnt)_2]^{2-}$, suggests that this difference should only account for a 2-fold increase in rate and thus the remaining increase can possibly be attributable to donor-ligand effects. Regardless of the differences in the rates of these reactions, there remain three similarities in terms of the mechanism and energetic barriers of phosphine oxidation. First, in all cases, the entropy of activation is negative and suggests an overall associative mechanism for the OAT reaction involving the formation of phosphine oxide with a $\Delta S_{avg}^{\ddagger}$ = -95.7 ± 35 J•mol^{-1}•K^{-1}. Secondly, the $\Delta G^{\ddagger}$ of all of these reactions falls within a surprising narrow window of $\Delta G_{avg}^{\ddagger}$ = 85.2 ± 6.9 kJ•mol^{-1}, despite a nearly 1000-fold difference in the rate constants. Lastly the overall trends in $\Delta H_{avg}^{\ddagger}$ = 59.9 ± 12 kJ•mol^{-1}, suggest a broad enthalpic contribution (21% difference when compared to the average) to $\Delta G^{\ddagger}$ which is partially compensated (8% difference when compared to the average) by an even broader entropic contribution (37% difference when compared to the average). One interesting side note of that comes from this analysis is an example of the intrinsic instability of a single parameter estimation of a property, in this case $\Delta H^*(1/T)+\Delta S$ is essentially equal to logk. In this case, the expected error in the intercept (ΔS term) would contain approximately 3x the error in the slope term (ΔH), if the experiment were conducted for a single reaction[39]. Thus in this example we see a similar propagation of the single reaction error in the combined analysis of multiple reactions. Thus as previously eluded in the electronic effects discussion of this paper, a single parameter estimation of reactivity would suffer from this same error.

Application of LFER to Oxygen Atom Transfer Reactivity

Tables 3.8a and 3.8b show the reactions of $[Mo^{VI}O_2(mnt)_2]^{2-}$, $[W^{VI}O_2(mnt)_2]^{2-}$ and $[Mo^{VI}O_2(S_2CNEt)_2]^{2-}$ with the available phosphine data, along with the QALE parameters for the reaction (the E and C model was excluded due to the presence of a charge on the catalysts and its subsequent rejection by Poë). Upon first inspection, the phosphines used in these reactions appear to require very different parameters for establishing the reactivity, however QALE analysis of the $[Mo^{VI}O_2(mnt)_2]^{2-}$ and $[W^{VI}O_2(mnt)_2]^{2-}$ data was problematic. First, the lack of data points (phosphines used in the reaction) provided a difficult situation for finding a steric threshold, however **Figure 3.15b** suggests that a threshold existed at approximately 117.5º.

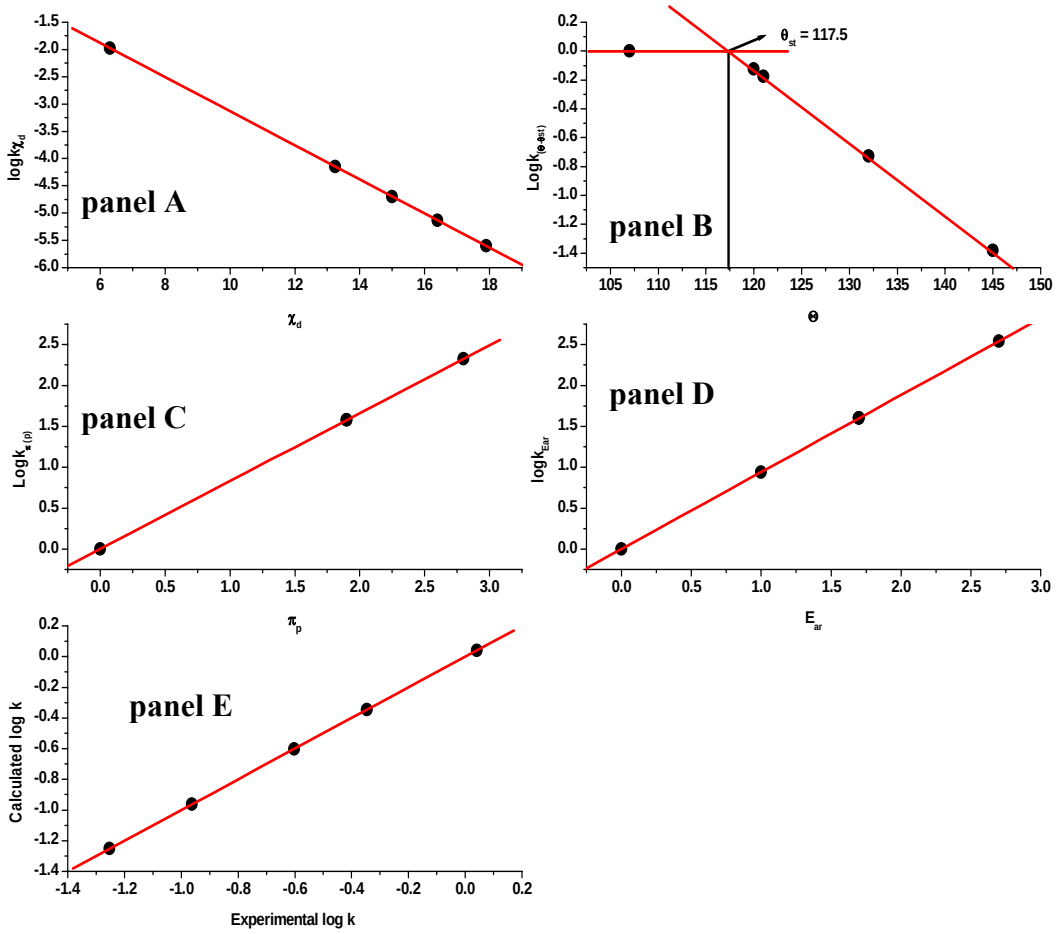

Figure 3.15: Results of the QALE anlysis of $[Mo^{VI}O_2(mnt)_2]^{2-}$. **panel a**) $\log k\chi_d$ verses χ_d; **panel b)** $\log k_\Theta$ verses Θ, **panel c)** $\log k_{\pi p}$ verses π_p **panel d)** $\log k_{Ear}$ verses E_{ar} and **panel e)** logk calculated verses logk experimental (R^2 =1; m=1 ± $1.8E^{-5}$; b= $-6.5E^{-6}$± $1.4E^{-5}$)

Table 3.8a

$[Mo^{VI}O_2(mnt)_2]^{2-} + PR_3 \rightarrow [Mo^{IV}O(mnt)_2]^{2-} + OPR_3$

phosphine	Log k (oxidation)	χ_d	π_p	θ	$(\theta-\theta_{th})\lambda$	E_{ar}	θ_{th}
$P(OMe)_3$	-0.60206	17.9	2.8	107	14.5	1	117.5
$P(MeO)_2Ph$	-0.3467875	14.8	0.9	132	27.5	2.3	
PEt_3	-0.9625735	6.3	0	132	2.5	0	
PPh_3	-1.2525882	13.25	0	145	0	2.7	
$P(OEt)_2Ph$	0.041393	15	1.9	121	3.5	1.7	

References: 37, 40

$[W^{VI}O_2(mnt)_2]^{2-} + PR_3 \rightarrow [W^{IV}O(mnt)_2]^{2-} + OPR_3$

phosphine	Log k (oxidation)	χ_d	π_p	θ	$(\theta-\theta_{th})\lambda$	E_{ar}	θ_{th}
PPh_3	-3.34679	13.25	0	145	27.5	2.7	117.5
$P(OMe)_3$	-5.01323	17.9	2.8	107	0	1	
$PhP(OMe)_2$	-3.34679	16.4	1.9	120	2.5	1.7	
$P(OEt)_2Ph$	-2.46852	15	1.9	121	3.5	1.7	

References: 37

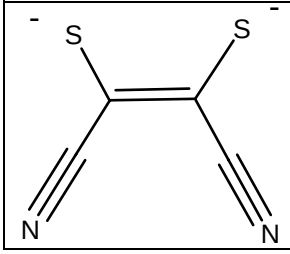

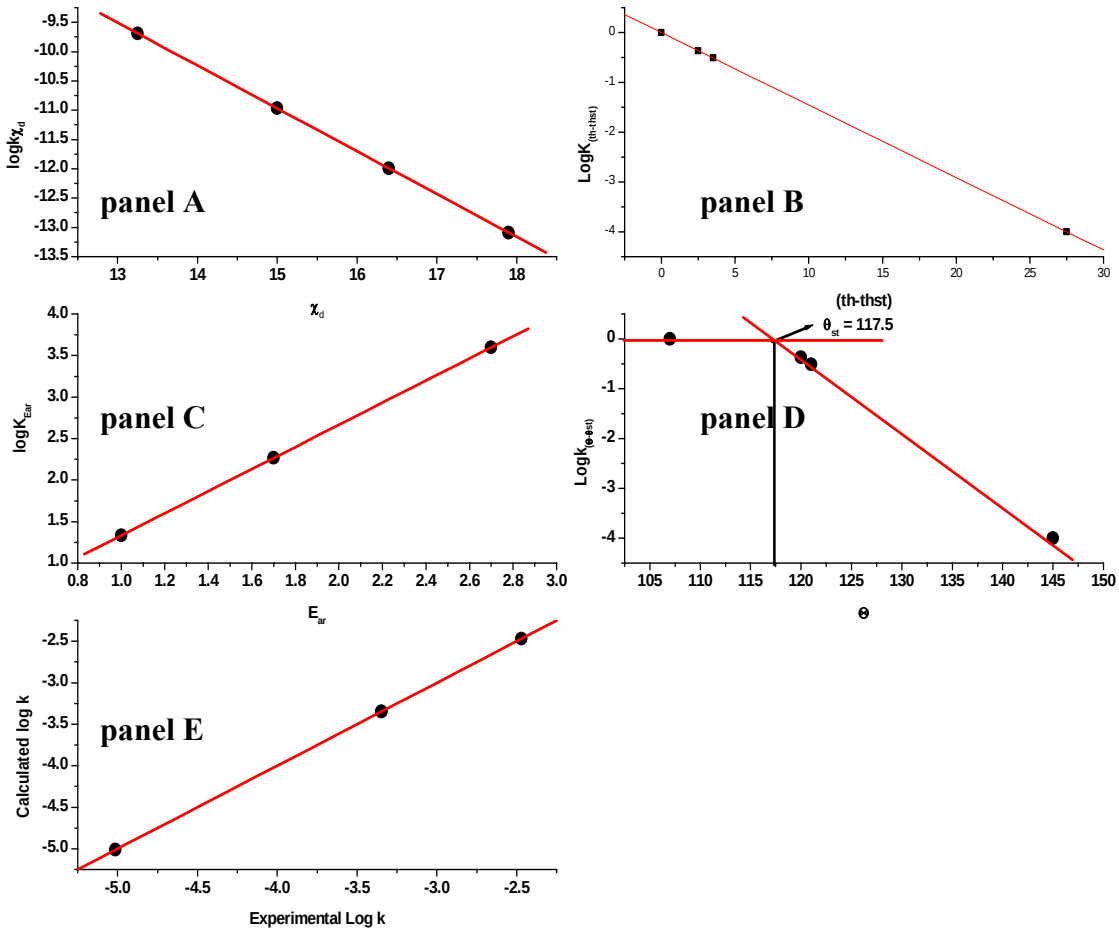

Figure 3.16: Results of the QALE anlysis of $[W^{VI}O_2(mnt)_2]^{2-}$. **panel a**) $logk\chi_d$ verses χ_d; **panel b)** $logk_{(\Theta-\theta th)}$ verses $(\Theta-\theta_{th})$; **panel c)** $logk_{Ear}$ verses E_{ar}; **panel d)** $logk_{\Theta}$ verses Θ; **panel e)** logk calculated verses logk experimental (R^2 =1; m=0.99 ± $1.5E^{-5}$; b= $-1.9E^{-5}$± $4.9E^{-5}$)

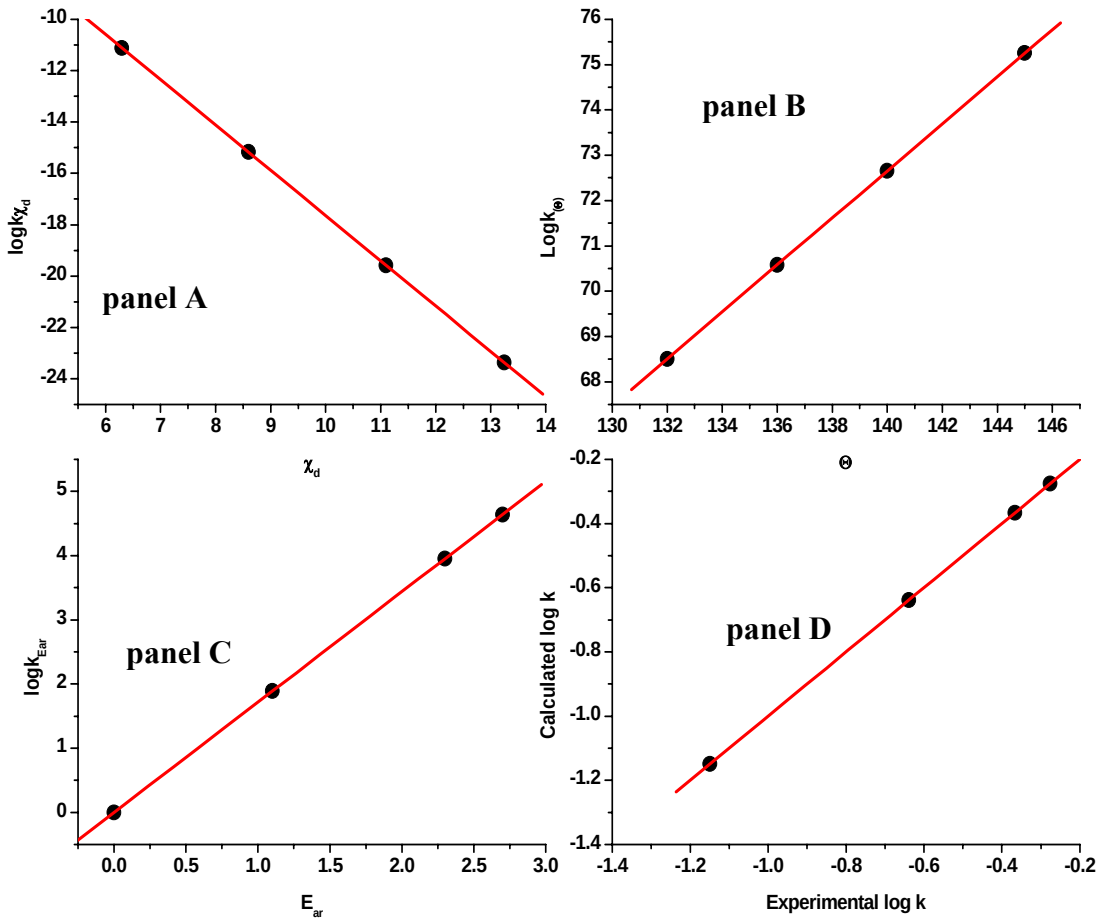

Figure 3.17: Results of the QALE anlysis of $[Mo^{VI}O_2(S_2CNEt_2)_2]^{2-}$. **panel a**) $\log k\chi_d$ verses χ_d; **panel b)** $\log k_\Theta$ verses Θ **panel c)** $\log k_{Ear}$ verses E_{ar}; **panel e)** logk calculated verses logk experimental (R^2 =1; m=1 ± 2.4E^{-5}; b= -1.6E^{-4}± 1.7E^{-5})

Table 3.8b							
$[Mo^{VI}O_2(S_2CNEt)_2]^{2-}$ + PR_3 → $[Mo^{IV}O(S_2CNEt)_2]^{2-}$ + OPR_3							
phosphine	Log k (oxidation)	χ_d	π_p	θ	$(\theta-\theta_{th})\lambda$	E_{ar}	θ_{th}
PEt_3	-0.27572	6.3	0	132	0	0	Not detected
PEt_2Ph	-0.36653	8.6	0	136	0	1.1	
PPh_2Et	-0.63827	11.1	0	140	0	2.3	
PPh_3	-1.14874	13.25	0	145	0	2.7	
References: 41							
$Et_2NCS_2^-$							

The choice for maintaining steric threshold in this system is based upon the concept of an energetic pocket that is formed by sterically encumbering ligand architecture about a central reactive metal,[42] such that the overall contribution of steric effects should be low. Thus the final fit, provided in **Figure 3.15e,** for the $[Mo^{VI}O_2(mnt)_2]^{2-}$ series of reactions could be described by **Equation 3.8:**

$$\log k = 1.74 - (0.313 \cdot \chi_d) + (0.83 \cdot \pi_p) + [0.0502 \cdot (\Theta - \theta_{st}) \cdot \lambda] + (0.94 \cdot E_{ar}) \quad \textbf{Equation 3.8}$$

In addition the following contributions were found: σ-basicity term, (χ_d = 51.8 %) steric effects (Θ = 18.6 %), the πp term (πp = 10.3%) and the aryl effect term, (E_{ar} = 19.4 %). The analysis of the $[W^{VI}O_2(mnt)_2]^{2-}$ data was much more difficult, most likely due to the even smaller data set available for this complex. When the πp term was included in the analysis, strong correlations between the πp term and the E_{ar} term were identified and as such the πp term was rejected from the analysis. However, a steric threshold was detected

in the same location as in the molybdenum analogue and as such a threshold angle of 117.5° was used. Thus the final fit, provided in **Figure 3.16e,** for the $[W^{VI}O_2(mnt)_2]^{2-}$ series of reactions could be described by **Equation 3.9:**

$$\log k = 6.74 - (0.731 \cdot \chi_d) + [0.145 \cdot (\Theta - \theta_{st}) \cdot \lambda] + (1.33 \cdot E_{ar}) \qquad \textbf{Equation 3.9}$$

In addition the following contributions were found: σ-basicity term, (χ_d = 59.7 %) steric effects (Θ = 26.7 %), and the aryl effect term, (E_{ar} = 13.6 %). Unfortunately the lack of sufficient data in these data sets does not allow for proper statistical analysis of the reaction in both cases with the mnt ligand. However when the plots of the individual parameters were compared for both complexes, **Figure 3.15a - Figure 3.15d and Figure 3.16a - Figure 3.16d,** showed similar trends in both the $\log k_{\chi d}$ verses χ_d plots and the $\log k_{(\Theta-\theta st)\lambda}$ verses Θ plots. Thus in reactions with mnt complexes of Mo and W, the rate of the reaction decreases with decreasing phosphine basicity and decreases with increasing cone angle, while increasing with increasing E_{ar}. Lastly, plots of logk (calculated) verses logk (experimental) **(Figure 3.15e and Figure 3.16e)** were found to be linear for both complexes with R^2 values of 1, but may reflect the underdetermined nature of the data sets.

On the other hand, the QALE analysis of the reaction of $[Mo^{VI}O_2(S_2CNEt)_2]^{2-}$ with phosphine complexes proceeded much more amiably, with no detectable steric threshold, and only the σ-basicity term, the phosphine cone angle, and the aryl effect term, present. The apparent lack of the threshold term in this complex suggests that the added flexibility present in the diethyl-amine tail of the ligand produces a stronger steric

effect in this ligand when compared to the flatter, more ridged mnt ligand. Thus the final fit, provided in **Figure 3.17e,** for the $[Mo^{VI}O_2(S_2CNEt)_2]^{2-}$ series of reactions could be described by **Equation 3.10:**

$$\log k = 57.7 - (0.1.76 \cdot \chi_d) + (0.519 \cdot \Theta) + (1.72 \cdot E_{ar}) \qquad \textbf{Equation 3.10}$$

In addition, the analysis produced a fit that was very similar to that observed in both the $[W^{VI}O_2(mnt)_2]^{2-}$ and $[Mo^{VI}O_2(mnt)_2]^{2-}$complexes, as shown in **Figure 3.15e, Figure 3.16e**, and **Figure 3.17e,** with an R^2 value of 1**.** On the surface, the contributions from each term seemed very similar to the mnt based reaction in that the σ-basicity term accounted for 56 %, the phosphine cone angle consisted of a 37 % contribution, while the aryl effect term was significantly smaller at ~7 %. The individual parameter profiles **Figure 3.17a- Figure 3.17c** , the χ_d term showed that each term contributed in the same manner towards the overall reactivity such that the rate of reaction decreased as a function of decreasing basicity, and that this decrease was more dramatic for the $[Mo^{VI}O_2(S_2CNEt_2)_2]^{2-}$ complex (χ_d = 56%) relative to the $[Mo^{VI}O_2(mnt)_2]^{2-}$ complex (χ_d ~ 52%), but represented the predominant effect in both reactions. Similarly, the trends in the E_{ar} term acted to increase the rate of the reaction, albeit much less for $[Mo^{VI}O_2(S_2CNEt_2)_2]^{2-}$ (E_{ar} = 7%) than $[Mo^{VI}O_2(mnt)_2]^{2-}$ (E_{ar} =22.5%). However, when the individual parameter profiles for Θ were plotted there was a significant difference in the reactivity such that steric effects accelerated the rate of the $[Mo^{VI}O_2(S_2CNEt_2)_2]^{2-}$ (Θ = 37%) reaction, but decelerated the rate of the $[Mo^{VI}O_2(mnt)_2]^{2-}$ reaction by one-half

that magnitude (Θ = 18.6%). Experimentally, this comparison manifested in $[Mo^{VI}O_2(S_2CNEt_2)_2]^{2-}$ being 5 times more reactive towards PEt_3 than $[Mo^{VI}O_2(mnt)_2]^{2-}$, but essentially equally reactive (1.3 times more reactive) towards PPh_3 than $[Mo^{VI}O_2(mnt)_2]^{2-}$. These experimental observations are not quite justified by the results of the QALE analysis and leave three possible explanations for the observed trends. First it is a possibility that the parameters derived for phosphorous III compounds cannot be directly extended towards phosphorous V compounds. The second is that, although the $\Delta S^{\ddagger}$ of reaction reflects an associative transition state, the observed $\Delta S^{\ddagger}$ represents a reaction that involves more than just phosphorous or the compounds exhibit different rate limiting steps. Lastly, the third possibility is that the limited amount of data makes the analysis suspect.

Testing Phosphorous III Parameters in Oxo-phosphorous V Systems involving Metal-Coordinated Imtermediates.

To test the possible weaknesses of employing the P(III) parameters to reactions that generate P(V), the reaction of various PR_3 species with *t*-BuO_2H was scrutinized independently, **Table 3.9,** and compared with the results obtained by Geiring, as well as the reactions between $Tp^{Me2}MoO_2OPh$ and $Tp^{iPr}MoO_2OPh$ and various phosphines, **Table 3.10a- Table 3.10c**.

Table 3.9: Quale Analysis of for the Oxidation of Phosphines by an Organic Peroxide							
***t*-Bu-OOH + PR_3 → *t*-Bu-OH + OPR_3**							
phosphine	Log k (oxidation)	χ_d	π_p	Θ	$(\Theta-\theta_{th})\lambda$	E_{ar}	θ_{th}
$P(OMe)_3$	-1.17783	17.7	2.8	107	0	1	128°
$P(OEt)_3$	-0.9914	15.8	2.9	109	0	1.1	
$PPh(OMe)_2$	-0.36051	16.4	1.9	120	0	1.7	
$P(OPh)_3$	-2.18046	23.6	4.1	128	0	1.3	
$P(i\text{-}OPr)_3$	-1.10237	13.4	2.9	130	2	1.3	
PEt_3	0.76716	6.3	0	132	4	0	
$PPh_{2(}OMe)$	0.10721	14.8	0.9	132	4	2.3	
$P(n\text{-}Bu)_3$	0.79239	5.25	0	136	8	0	
$P(p\text{-}MeO\text{-}C_6H_4)_3$	0.21219	10.5	0	145	17	2.7	
$P(p\text{-}Me\text{-}C_6H_4)_3$	-0.04096	11.5	0	145	17	2.7	
PPh_3	-0.27003	13.25	0	145	17	2.7	
$P(p\text{-}F\text{-}C_6H_4)_3$	-0.55129	15.7	0	145	17	2.7	
$P(p\text{-}Cl\text{-}C_6H_4)_3$	-0.6216	16.8	0	145	17	2.7	
$PPh_2(C_6F_5)$	-1.59688	20.4	0	158	30	3.2	
References:43,13							

In the first case, the peroxide reaction results in the production of the analogous phosphine oxide and represents a test to the application of phosphorous (III) parameters to phosphorous (V) species evolution while the results were identical to those obtained by Geiring as shown in **Equation 3.11**.

$$\log k = (1.68 \pm 0.1175) - (0.0867 \cdot \chi_d \pm 0.0158) + ((\Theta - 128) \cdot \lambda) + (0.166 \pm 0.0661 \cdot E_{ar}) + (0.519 \cdot \pi_p \pm 0.0685)$$

Equation 3.11

Table 3.10a						
$Tp^{iPr}MoO_2OPh + PR_3 \rightarrow Tp^{iPr}MoO(OPR_3)OPh$						
phosphine	Log k_1 (oxidation)	χ_d	Θ	$(\Theta-\theta_{th})\lambda$	E_{ar}	θ_{th}
PMe_3	-3.0362	8.55	118	0	0	127.5°
PEt_3	-3.0334	10.5	122	0	1	
PMe_2Ph	-3.6216	6.3	132	4.5	0	
PEt_2Ph	-3.8477	5.25	136	8.5	0	
$P(n\text{-}Bu)_3$	-3.5452	8.6	136	8.5	1.1	
$PMePh_2$	-4.0573	12.6	136	8.5	2.2	
$PEtPh_2$	-4.4379	11.1	140	12.5	2.3	

Table 3.10b						
$Tp^{Me2}MoO_2OPh + PR_3 \rightarrow Tp^{Me2}MoO(OPR_3)OPh$						
phosphine	Log k_1 (oxidation)	χ_d	Θ	$(\Theta-\theta_{th})\lambda$	E_{ar}	θ_{th}
PMe_3	-3.91229	8.55	118	0	0	127.5°
$PPhMe_2$	-3.87718	10.5	122	0	1	
PEt_3	-3.90729	6.3	132	4.5	0	
$PPhEt_2$	-4.54351	8.6	136	8.5	1.1	
$PMePh_2$	-4.73915	12.6	136	8.5	2.2	
$PEtPh_2$	-5.1872	11.1	140	12.5	2.3	

The results of the peroxide analysis are shown in **Figure 3.17a - Figure 3.17f**, with an excellent overall fit to the experimental data with χ_d = 20% Θ= 35% θ_{th} = 128°, $\pi(p)$ = 42% and Ear = 3% for an overall R^2 of 0.994. The parameter plots show that the

Table 3.10c						
$Tp^{iPr}MoO_2OPh + PR_3 \rightarrow Tp^{iPr}MoO(OPR_3)OPh \rightarrow Tp^{iPr}MoO(NCMe)OPh + OPR_3$						
phosphine	Log (k_1/k_2) (oxidation)	χ_d	Θ	$(\Theta-\theta_{th})\lambda$	E_{ar}	θ_{th}
PMe_3	0.594572	8.55	118	0	0	(127.5 and 0)
PEt_3	-0.12854	10.5	122	0	1	
PMe_2Ph	-0.82382	6.3	132	4.5 (0)	0	
PEt_2Ph	-0.63018	5.25	136	8.5 (0)	0	
$P(n\text{-}Bu)_3$	-0.89252	8.6	136	8.5 (0)	1.1	
$PMePh_2$	-1.87092	12.6	136	8.5 (0)	2.2	
$PEtPh_2$	-2.02125	11.1	140	12.5 (0)	2.3	

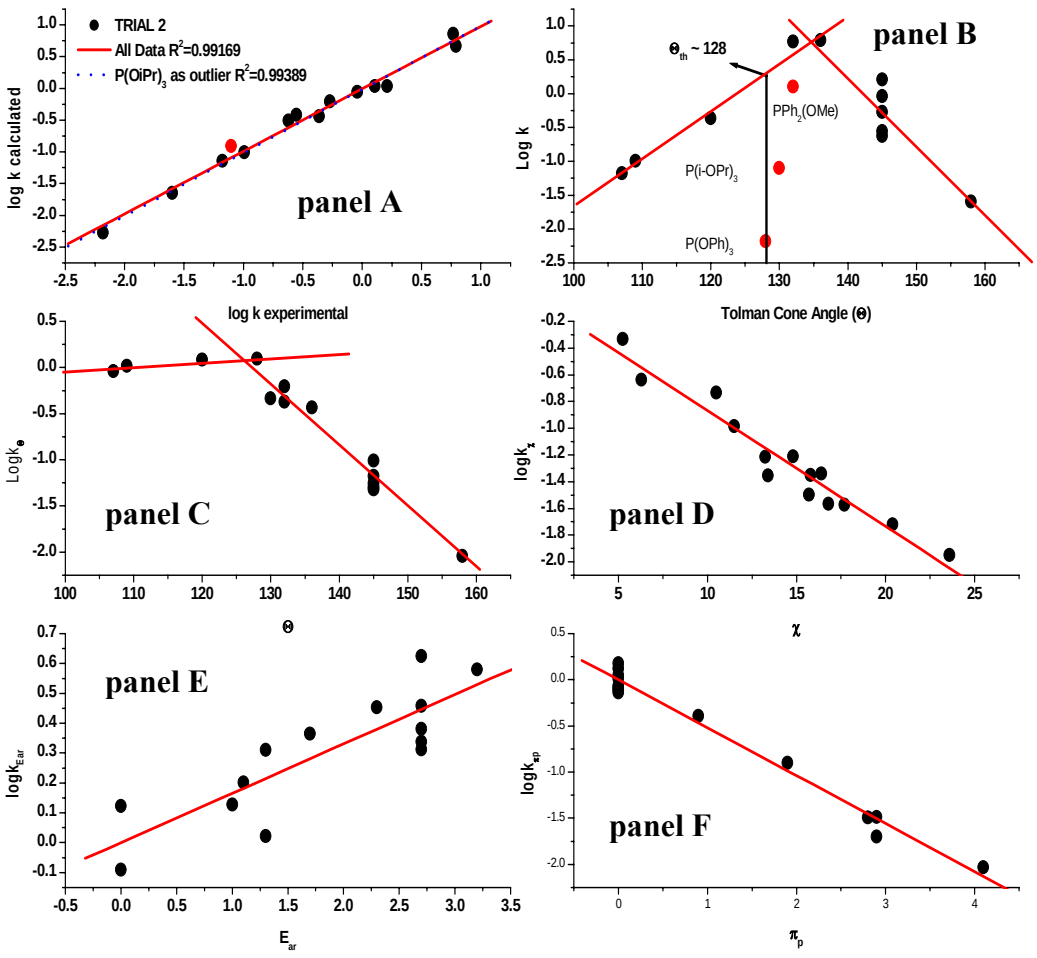

Figure 3.17: Results of the QALE anlysis of *t*-BuOOH reactions. **panel a)** logk calculated verses logk experimental **panel b)** logk verses Θ; **panel c)** $\log k_{\Theta}$ verses Θ; **panel d**) $\log k\chi_d$ verses χ_d; **panel e)** $\log k_{Ear}$ verses E_{ar}; **panel f)** $\log k_{\pi p}$ verses π_p

rate of the oxidation decreases with decreasing σ-basicity, as observed in both the mnt and S_2CNEt_2 reactions but with an approximately 50% lower magnitude. In addition, the peroxide reaction appeared similar to the mnt reaction in terms of steric effects which act in reducing the overall reactivity after the steric threshold, but a share similar magnitude

(Θ= 35%) of steric effects with the S_2CNEt_2 reaction (Θ= 37%). Furthermore, it appears that the rate of the overall reaction is accelerated in the t-BuOOH data at cone angles less than the steric threshold and as such share commonality with the acceleration evidenced in the S_2CNEt_2 reaction. Additional similarity to both reactions was found in the Ear plot, which showed that aryl effects have an accelerating effect on the reaction but the magnitude (Ear = 3%) of these effects were more similar to the S_2CNEt_2 reaction (E_{ar} = 7%) than that of the mnt reaction (E_{ar} = 13.6 %). Lastly, the π_p term, dominated in terms of reaction influence (π_p = 42%), but contributed to an overall reduction in reaction rates which is opposite to its role in the mnt reaction (π_p = 10.3%). Thus it appears that these parameters are transferable to phosphorous oxidation reactions, but the differences in the reactivity that were observed between the mnt and the S_2CNEt_2 reactions still remain unclear, and are quite possibly less clear when the *t*-BuOOH oxidation is considered.

In the second set of tests, both the $Tp^{Me2}MoO_2OPh$ and $Tp^{iPr}MoO_2OPh$ complexes are known to produce isolatable intermediate species of the type $Tp^RMoO(OPR_3)OPh$ and provide a gauge for both an increased steric demand and a reaction known to proceed through at least two transition states. Unfortunately, it was impossible to deconvolute any of the $Tp^RMoO(OPR_3)OPh$ reactions in terms of a "good-fit" or with reliable statistics despite a clear steric threshold at 127.5°. Furthermore only when both the steric threshold and full cone parameters are included in the reduction scheme can the experimental rate constant be reproduced reasonably well, albeit at full disregard for reliable statistics (see **Table 3.11a** and **Table 3.11b** for complete details).

Table 3.11a: $Tp^{iPr}MoO_2OPh + PR_3 \rightarrow Tp^{iPr}MoO(OPR_3)OPh$						
Constant	Coef of χ_d	Coef of Θ	Coef of $(\Theta-\theta th)\lambda$	Coef of E_{ar}	R^2	R^2 $(\log k_{calc})/(\log k_{exp})$
-2.46 ± 1.9	-0.07 ± 0.24	*****	-0.12 ± 0.08	0.16 ± 0.76	0.895	0.947
3.27 ± 9.1	-0.01 ± 0.31	-0.05 ± 0.06	*****	-0.08 ± 0.93	0.859	0.927
0.36 ± 10.0	-0.13 ± 0.35	-0.02 ± 0.08	-0.10 ± 0.11	-0.32 ± 1.07	0.899	0.948
***** indicates that this variable was not used in the analysis as described in the text						

Table 3.11b: $Tp^{Me2}MoO_2OPh + PR_3 \rightarrow Tp^{Me2}MoO(OPR_3)OPh$						
Constant	Coef of χ_d	Coef of Θ	Coef of $(\Theta-\theta th)\lambda$	Coef of E_{ar}	R^2	R^2 $(\log k_{calc})/(\log k_{exp})$
-2.5 ± 1.2	-0.15 ± 0.15	*****	-0.12 ± 0.05	0.25 ± 0.49	0.970	0.984
-4.8 ± 9.4	0.16 ± 0.32	0.00 ± 0.06	*****	-0.79 ± 0.96	0.894	0.945
-9.9 ± 0.14	-0.01 ± 0.00	0.05 ± 0.00	-0.16 ± 0.01	-0.16 ± 0.00	0.948	0.999
***** indicates that this variable was not used in the analysis as described in the text						

However, when the rate constant (k_1) for the formation of the $Tp^{iPr}MoO(OPR_3)OPh$ complexes was considered with its solvation rate constant (k_2), as either $\log(k_1/k_2)$ or (k_2/k_1), the reaction could be fit quite well using QALE analysis **(Figure 3.18a- Figure 3.18c).** When the reaction is considered as $\text{Log}(k_1/k_2)$ (**Table 3.12a** and **Table 3.12b**)it represents the steady state concentration of B, as Log(d[B]/dt), for a reaction defined by **Equation 3.12**, and **Equation 3.13**.

$$A + B \xrightarrow{k_1} C \xrightarrow{k_2} D \qquad \textbf{Equation 3.12}$$

$$\frac{d[C]}{dt} = \frac{k_1}{k_2}[A][B] \qquad \textbf{Equation 3.13}$$

and produces reactivity trends that were observed in both of the mnt reactions and the *t*-BuOOH reaction. Interestingly, when considered in this manner, the once clear steric threshold disappears and the experimental data set could be well reproduced when fit with only χ_d and Θ as shown in **Equation 3.14**.

$$\log\frac{k_1}{k_2} = 13.2 \pm 1.6 - (0.145 \cdot \chi_d \pm 0.038) - (0.0976 \cdot \Theta \pm 0.012) \qquad \textbf{Equation 3.14}$$

Here χ_d contributes 40% to the overall reactivity while Θ contributes 59.9% to the observed reactivity. Thus when the data is manipulated in this way, the contribution from

the χ_d term is much higher than observed in *t*-BuOOH (χ_d = 20%), and slightly lower than observed in the $[Mo^{VI}O_2(S_2CNEt_2)_2]^{2-}$ complex (χ_d = 56%), the $[Mo^{VI}O_2(mnt)_2]^{2-}$ complex (χ_d ~ 52%), and the $[W^{VI}O_2(mnt)_2]^{2-}$ complex (χ_d = 59.7%).

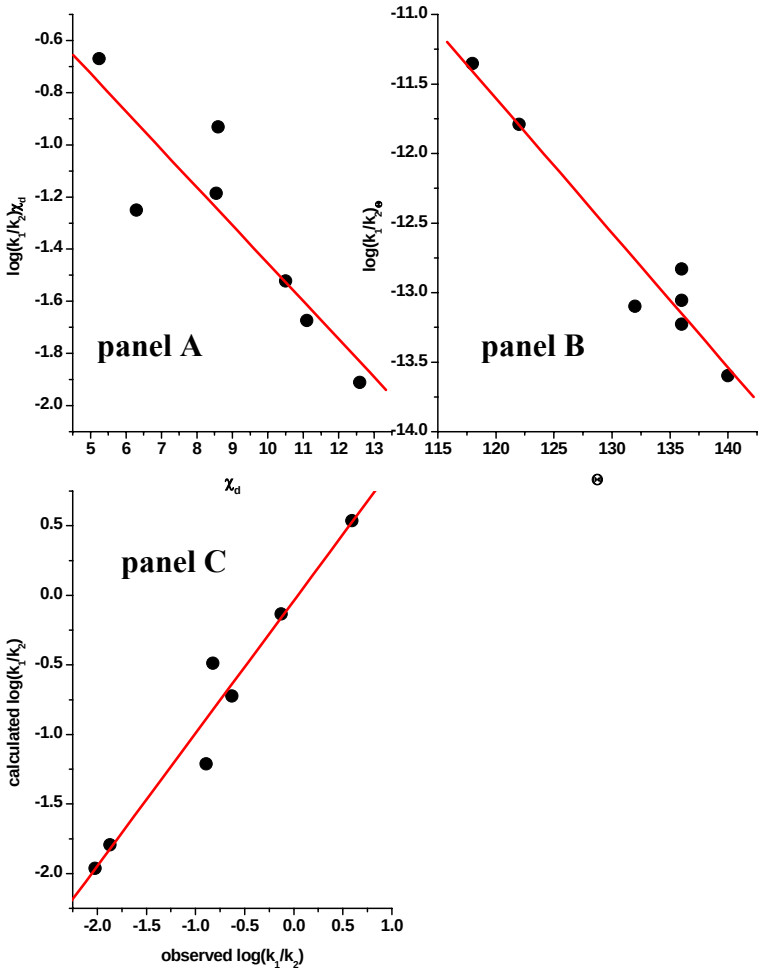

Figure 3.18: Results of the QALE anlysis of $Tp^{iPr}MoO_2OPh$ reactions taken as $\log(k_1/k_2)$ as described in the text. **panel a**) $\log k\chi_d$ verses χ_d; **panel b)** $\log k_\Theta$ verses Θ; **panel c)** logk calculated verses logk experimental (R^2 =0.974; m=0.95 ± 0.01; b= 0.07 ± 0.14)

In all cases, the χ_d term contributes to an overall decrease in reactivity with decreases in the σ-basicity of the phosphine. Conversely, the presence of steric effects is more

significant in the overall formation/solvation of $Tp^{iPr}MoO(OPR_3)OPh$ (Θ = 59.9%), relative to the *t*-BuOOH (Θ = 35%), the $[Mo^{VI}O_2(S_2CNEt_2)_2]^{2-}$ complex (Θ = 37%), the $[Mo^{VI}O_2(mnt)_2]^{2-}$ complex (Θ = 18.6 %), and the $[W^{VI}O_2(mnt)_2]^{2-}$ complex (Θ = 26.7 %). Thus, the analysis suggests that the rate determining step in the reactions of the $[Mo^{VI}O_2(mnt)_2]^{2-}$, $[W^{VI}O_2(mnt)_2]^{2-}$ and the $Tp^{iPr}MoO_2OPh$ complexes, with tertiary phosphines and phosphites possibly share a common rate determining step in the overall reaction leading towards free phosphine oxide production. This comparison has validity through the theoretical identification of an intermediate in the reaction of $[Mo^{IV}O(mnt)_2]^{2-}$ with trimethylamine-N-oxide, which suggested the presence of $[Mo^{IV}O(ONCH_3)(mnt)_2]^{2-}$ situated in a shallow energetic well between two transition states (the intermediate was ~7 kJ/mol lower in energy than both of the transition states)[44]. In another theoretical investigation, the reaction of $[Mo^{IV}O(mnt)_2(OMe)]^-$ with Me_2SO found a similar, but deeper energetic well (~31 kJ/mol lower than TS1 and 63 kJ/mol lower than TS2) for the $[Mo^{IV}O(OSMe_2)(mnt)_2(OMe)]^-$ intermediate on the reaction path towards Me_2S production[45]. As discussed in **Chapter 1** of this work, we have shown both experimentally and theoretically that the $Tp^{iPr}MoO(OPMe_3)OPh$ intermediate that arises from the reaction of the $Tp^{iPr}MoO_2OPh$ complexe with PMe_3 sits in a similar energetic well along the reaction coordinate towards free $OPMe_3$ production (~26.6 kJ/mol lower in energy than TS1 and ~29.8 kJ/mol lower in energy than TS2)[46]. Furthermore the more sterically encumbered $Tp^{iPr}MoO_2OPh$ complex suffers in overall reactivity due to the increased weight of steric effects, relative to the sterically less hindered $[Mo^{VI}O_2(mnt)_2]^{2-}$ and $[W^{VI}O_2(mnt)_2]^{2-}$ complexes.

Table 3.12a						
$Tp^{iPr}MoO_2OPh + PR_3 \rightarrow Tp^{iPr}MoO(OPR_3)OPh \rightarrow Tp^{iPr}MoO(NCMe)OPh + OPR_3$						
phosphine	Log (k_1/k_2) (oxidation)	χ_d	Θ	$(\Theta-\theta_{th})\lambda$	E_{ar}	θ_{th}
PMe_3	0.594572	8.55	118	0	0	(127.5 and 0)
PEt_3	-0.12854	10.5	122	0	1	
PMe_2Ph	-0.82382	6.3	132	4.5 (0)	0	
PEt_2Ph	-0.63018	5.25	136	8.5 (0)	0	
$P(n\text{-}Bu)_3$	-0.89252	8.6	136	8.5 (0)	1.1	
$PMePh_2$	-1.87092	12.6	136	8.5 (0)	2.2	
$PEtPh_2$	-2.02125	11.1	140	12.5 (0)	2.3	

Table 3.12b: $Tp^{iPr}MoO_2OPh + PR_3 \rightarrow Tp^{iPr}MoO(OPR_3)OPh \rightarrow Tp^{iPr}MoO(NCMe)OPh + OPR_3$						
Constant	Coef χ_d	Coef Θ	Coef $(\Theta-\theta th)\lambda$	Coef E_{ar}	R^2	R^2 $Log(k_1/k_2)_{calc}/Log(k_1/k_2)_{exp}$
0.76 ± 1.5	0.014 ± 0.19	*****	0.047 ± 0.06	0.17 ± 0.61	0.887	0.942
-8.1 ± 3.7	0.20 ± 0.12	0.06 ± 0.02	*****	-0.38 ±0.37	0.961	0.980
-4.5 ± 0.73	0.08 ±0.02	0.039 ± 0.01	*****	*****	0.948	0.974
0.34 ± 0.25	0.07 ± 0.03	*****	0.063 ± 0.01	*****	0.884	0.940
***** indicates that this variable was not used in the analysis						

In attempt to reverse the rate-limiting step of the reaction, the Tp^{iPr} reaction was investigated as $\log(k_2/k_1)$ using the QALE methodology.

When viewed in this way the results were very similar to those obtained through QALE analysis of $\log(k_1/k_2)$ and the reaction could only be fit using χ_d and Θ as defined in **Equation 3.15**.

$$\log\frac{k_2}{k_1} = 1.92 \pm 0.246 - (0.0214 * \chi_d \pm 0.006) - (0.0139 * \Theta \pm 0.002) \qquad \textbf{Equation 3.15}$$

Here the contributions are nearly identical to those found for the $\log(k_1/k_2)$ analysis such that χ_d contributes 40.5% to the overall reactivity while Θ contributes 59.5%. Moreover, the trends in the contributions are also the same such that as both χ_d and Θ increase, the rate of the reaction decreases.

Lastly, the difference in the trends that are observed between the $[Mo^{VI}O_2(S_2CNEt_2)_2]^{2-}$ complex and the other previously discussed reactions can possibly be attributed to a difference in the rate determining step or mechanism of the reactions that have been documented for this complex. However, attempts to validate this proposal were not successful and thus the possibility that the deviant behavior of the $[Mo^{VI}O_2(S_2CNEt_2)_2]^{2-}$ complex results from a small data set cannot be ruled out.

Discussion and Summary

In this chapter we have investigated the principle contributors to chemical reactivity with phosphorous (III) and (V) reactants. Based upon a survey of the literature, three general physico-chemical properties have been associated with reactivity and suggest that a linear combination of σ-basicity, π-acidity and steric effects contribute to chemical reactivity. These same parameters have been extended to the reactivity of nitrogen, silicone, sulfur, arsenic and carbon compounds with the same level of success that has been achieved with phosphorous compounds, and as such further solidifies their implementation into the understanding of chemical reactivity. In general, all σ-basicity and π-acidity terms are quite similar in nature and represent a pseudo-pK_a type parameter, which suggests that nearly any of the previously discussed parameters may be used as a σ-basicity parameter in a LFER, provided that the same parameter is used consistently. Furthermore, the most widely accepted steric parameter is the cone angle Θ, (Tolman's cone angle), and its two ligand variants which are extensions of cone angle definition.

The most widely parameterized and successful model in the understanding of chemical reactivity is the QALE model, despite the fact that parameters such as E_{ar} and π_p appear relatively subjective. The strongest advantage to the QALE analysis is the inclusion of a steric threshold, which improves upon the reactivity models produced by Tolman, Drago, Taft and others, by allowing for the gradual inception of steric effects into reactions where steric effects are not important for all reactants.

In attempt to validate the use of chemical parameters developed for predicting the reactivity of P(III) compounds in reactions that produce oxo-phosphorous (V)

compounds, 5 sets of data were analyzed which are known to produce oxo-phosphorous (V) from phosphorous III reactants. In most cases, the P(III) parameters were found to be viable predictors of P(V) generating reactions, with the notable exception of reactions involving isolatable intermediates. However, when the two rate constants that define the formation and solvation of the intermediate were considered as a single rate constant produced by the k_1/k_2 ratio, the parameters allowed for reasonable fits of the kinetic data. Further validation of this concept was produced through reasonable and justifiable contributions of both the χ_d and Θ parameters toward reactivity as well as through the trends in each parameter.

Lastly, when the data from **Chapter 2** is considered in full, the results with the intermediates further suggest that the production of phosphine oxides from both the *cis*-1,2-dicyano-1,2-ethylenedithiolate and dithiocarbamate complexes most likely reflect a two step reaction. The grounds for this statement are based upon two observations. First, when a single sulfur ligand is substituted for a single oxygen ligand, the rate of intermediate formation (k_1) appears to approach the rate of solvation (k_2) and release of the coordinated phosphine oxide. Furthermore, the general trend in the reactivity follows that k_1 (intermediate formation) is the rate limiting step of the complete atom transfer reaction, while k_2 (solvation and phosphine oxide release) is comparably much faster, especially when the oxygen acceptor is not PMe_3. Secondly, by extending the concept of oxygen for sulfur substitution to a nitrogen (Tp ligand) for sulfur substitution (*cis*-1,2-dicyano-1,2-ethylenedithiolate or dithiocarbamate ligand) it may be possible to enhance the rate of solvation of a hypothetical intermediate species to the degree that $k_2 >>> k_1$ such that $k_{obs} \cong k_2$. Under this light, it is not surprising that the results produced by the

k_1/k_2 ratio of the Tp^{iPr} complexes can be described by the same parameters used in the analysis of the $[Mo^{VI}O_2(mnt)_2]^{2-}$, $[W^{VI}O_2(mnt)_2]^{2-}$ and $[Mo^{VI}O_2(S_2CNEt_2)_2]^{2-}$ complexes.

Appendix 3.1: Theoretical Details

The geometries of all structures were fully optimized by the B3LYP[47] DFT[48] method as implemented in Gaussian 98 or Gaussian 03.[49] Analytical harmonic frequencies have been calculated for all stationary points to confirm the nature of these points, for the zero point energies, and for the thermodynamic properties, **Table A3.1-1**. The results reported in this work have been obtained using the standard 6-31G* basis set[50] for the phosphine oxides and the standard 6-311G(d,p) basis set for the phosphines. Onsager volume calculations were performed on all complexes with 6-311G(d,p) basis set. Cone angles were established using **Equation 3.2**, at a fixed 1.84 Å distance from oxygen for the phosphine oxides, while a fixed distance of 2.28 Å was used for the phosphines.

Absolute energies for the multiple conformations of $P(OMe)_3$ and $OP(OMe)_3$ are tabulated in **Table A3.1-2,** and are provided with zero point energy corrections.

Table A3.1-1: Experimental and Calculated properties of phosphine oxides

Phosphine oxide	υP=O (cm^{-1})	P=O (Å)	O-P-R (°)	$\delta^{31}P$ (ppm) verses H_3PO_4	Cone Angle (Θ°)	Molar Volume (cm^3/mol)
OPH_3	1277.3	1.485	117.61 ± 0.00	NR	60.8	26.56
OPH_2Ph	1260.3	1.493	117.09 ± 0.70	NR	74.3	31.47
OPH_2Me	1257.0	1.487	116.62 ± 0.64	NR	62.2	53.73
$OPMe_3$	1244.7 (1174)	1.498 (1.488)	114.27 ± 0.00 (112.76 ± 1.05)	35.05 (35.6)♦	64.8 (62.9)	84.52
$OPMe_2Ph$	1239.4 (1194)*	1.499	113.31 ± 1.14	39.49 (28.9)♦	76.6 (73.6)	99.15
$OPEt_3$	1214.9	1.502 (1.505 ± 0.01)	113.31 ± 0.47 (111.50 ± 1.04)	58.40 (48)♠ (48.9)♦	87.4 (91.5)	120.86
$OP(n\text{-}Bu)_3$	1210.5	1.500	113.22 ± 0.56	54.05 (43)♠(42.1)♦	85.2	174.63
$OPEt_2Ph$	1219.7	1.502	112.44 ± 0.85	(45.5)♦	88.1	147.86
$OPMePh_2$	1231.9 (1206)*	1.500	112.76 ± 1.79	39.04 (32.4)♦	89.0	146.01
$OPEtPh_2$	1226.7	1.500 (1.483)	112.76 ± 1.55	46.32 (31.9)♦	99.3 (96.7)	195.48
$OPPh_3$	1225.8 (1195)	1.500 (1.489 ± 0.02)	(112.89 ± 2.03) (111.78 ± 1.23)	(25)♠	92.6 (95.5)	208.81
$OP(p\text{-}F\text{-}C_6H_4)_3$	1195.5	**ND**	**ND**	**ND**	**ND**	223.30
OPTA	1204.3	**ND**	**ND**	**ND**	(61.2)	122.89
$OP(OMe)_3$	1303.2 (1278)*	1.478	116.24 ± 0.02	(2)♠	94.8 (95.5)	104.51
$OP(OEt)_3$	**ND**	(1.443 ± 0.03)	(116.89 ± 1.93)	(-1)♠	(122.0)	**ND**
$OP(OEt)_2Ph$	1269.7	1.486	115.36 ± 3.1	**ND**	86.2	185.33
$OP(OPh)_3$	1306.9 (1290)*	1.475	117.21 ± 0.06	(-18)♠	139.1 (144.6)	**ND**
$OP(OMe_2)Ph$	1289.6 (1258)*	1.483	115.6 ± 1.84	**ND**	96.6	121.37
$OP(OMe)Ph_2$	1259.2 (1238)*	1.491	114.7 ± 2.65	**ND**	89.6	**ND**
$OPCl_3$	1317.3 (1300)	1.469	114.8 ± 0.00	**ND**	76.8	**ND**

Experimental numbers are in parenthesis, * calculated from $\upsilon_{P=O}/cm^{-1} = 930 + 40\sum\pi$ from reference51. ♠ Values taken from[52] ♦ values taken from **Chapter 2.**

Table A3.1-2 Selected Differences in the Parameters between $OP(OMe)_3$ and $P(OMe)_3$ in either the optimized geometry, the crystallographically determined geometry or the Tolman Geometry.						
	ΔG^o kcal/mol	ΔH^o kcal/mol	ΔS^o cal/mol·K	ΔVolume (cm^3/mol)	ΔRadius (Å)	ΔCone degrees
$OP(OMe)_3$ crys - $OP(OMe)_3$ opt	+203.02	+189.52	-45.27	-10.63	-0.36	-3.95
$P(OMe)_3$ Tolman - $P(OMe)_3$ opt	+39.25	+27.27	-38.66	-36.33	-0.45	-13
$P(OMe)_3$ opt - $OP(OMe)_3$ opt des-ox	+73.33	+73.59	+0.886	+1.90	+0.24	-2.79
$P(OMe)_3$ Tolman - $P(OMe)_3$ crys	+19.49	+17.17	-7.77	-11.55	-0.15	+12.46
$P(OMe)_3$ opt - $P(OMe)_3$ crys	+19.76	+10.55	-30.89	+ 44.13	+0.57	+60.7
$P(OMe)_3$ Tolman- $OP(OMe)_3$ opt des-ox	+112.57	+101.31	-37.77	-20.28	-0.27	+5.72
$P(OMe)_3$ crys- $OP(OMe)_3$ opt des-ox	+93.09	+84.14	-30.00	-28.08	-0.39	-41.98
$OP(OMe)_3$ opt - $P(OMe)_3$ opt	-75.34	-87.05	-39.29	-14.12	+0.06	-21.51
$OP(OMe)_3$ opt - $P(OMe)_3$ Tolman	-114.59	-114.77	-0.629	-22.18	-0.51	+8.51
$OP(OMe)_3$ crys - $P(OMe)_3$ Tolman	+88.43	+74.75	-45.90	-11.55	-0.15	+12.46
Crys = crystallographically determined geometry, Tolman = geometry with Tolman's Cone Angle, opt = the optimized geometry, opt des-ox = geometry optimized then all other calculations were performed after removal of the oxygen from the phosphine oxide.						

Appendix 3.2: Applied QALE Analysis

In this document, all rate constants were either obtained from the literature or taken from **Chapter 2** of this document under similar reaction conditions, such as temperature, solvent, etc. Plots of log k for each reaction were constructed against the QALE phosphorous parameters, with special attention to the plot of log k verses Θ. The importance of log k verses Θ, is that breaks the linearity of the plot indicate the presence of a steric threshold, while the lack of apparent breaks suggest that the steric threshold is not operative with the phosphorous species studied in the reaction. Once the plots were completed and the presence/absence of the steric threshold was determined, the data were analyzed by multi-component linear regression analysis, with a full set of QALE parameters, using Mini-Tab 14[53]. A general, non-statistical description of fitting in this way can be found in **Equation A3.2-1.**

$$[\log k] = [A] \cdot \overrightarrow{C} \qquad \textbf{Equation A3.2-1}$$

Here, logk can be represented as a matrix [logk] which equals the parameter matrix [A], when multiplied by a vector of coefficients C. Thus through the application of matrix theory, a coefficient vector can be found that allows [A] to approximate [logk].

The results of the analysis were interpreted by two criteria. The first set of criteria was that the resultant equation could effectively produce a data set ($logk_{calc}$) that closely approximated the experimental data ($logk_{exp}$), with the residual and R^2 value of $logk_{calc}$ verses $logk_{exp}$ plots as an indicator of a good fit. The second set of criteria was based upon the statistical analysis of each coefficient that was retrieved from the analysis, in

terms of standard errors at the 95% confidence limit as provided in the Mini-Tab 14 program. Thus a "good fit" was determined by R^2 values that approached unity and small standard errors in the coefficients of each parameter employed. The most common criteria for the rejection of a set of parameters in the analysis resulted from the observation of excellent R^2 values and small residuals in the $\log k_{calc}$ verses $\log k_{exp}$ plots, but large standard errors and overall poor statistical support for such a description of the reactivity. In these cases, the parameter with the single greatest statistical error was removed from the parameter list and the "fitting" was again resumed with the remaining parameters in an iterative process until a "best fit" condition was met that provided good R^2 and small residuals as well as the best statistical support for the parameter choice (set of parameters whose coefficients could be determined with the best accuracy). By performing the analysis in this way, the minimal set of parameters could be found that could accurately model the observed trends in reactivity. Once accurate coefficients of each parameter were established, the percent contribution of each parameter was generated as outlined in reference 13.

References

[1] a) Holm, R.H. *Chem. Rev*. **1987**, 87, 1401-1449. b) Holm, R.H. *Chem. Rev*. **2004**, 104, 1175-1200

[2] Woo, K.L. *Chem. Rev*. **1993**, 93, 1125-1136

[3] Enemark, J.H. and Cooney, J.J.A. *Chem. Rev.* **2004**, 104, 1175-1200

[4] Espenson, J.H. *Coord.Chem.Rev.* **2005**, 249, 329

[5] a) Tolman, C.A. *Chem. Rev*. **1977**, 77, 313-348, b) Tolman, C.A. J.Am.Chem.Soc. **1970**, 92, 2953, c) Tolman, C.A., Seidel, W.C. and Glosser, L.W. J.Am.Chem.Soc. **1974**, 96, 53.

[6] a) Kamlet, J.M. and Taft, R.W. *J.Am.Chem.Soc*. **1976**, 98, 377-383. b) Taft, R.W., and Kamlet, J.M. *J.Am.Chem.Soc*. **1976**, 98, 2886-2894. c) Taft, R.W. *J.Am.Chem.Soc* **1953**, 4538-4539.

[7] a) Hammett, L.P. *J.Am.Chem.Soc*. **1928**, 50, 2666-2673. b) Hammett, L.P. *J.Am.Chem.Soc* **1937**, 59, 96-103.

[8] a) Drago, R.S. and Wayland, B. B. *J.Am.Chem.Soc*. **1965**, 87, 3571.b) Niedzielski, R.S., Drago, R.S. and Middaugh, R.L. *J.Am.Chem.Soc*. **1964**, 86 c) Joesten, M.D. and Drago, R.S., *J.Am.Chem.Soc*. **1962**, 84, 3817. Drago, R.S., Vogel, G.C., and Needham, T.E. *J.Am.Chem.Soc* **1971**, 93, 6014-6026.

[9] a) Doan, P.E., and Drago, R.S. *J.Am.Chem.Soc* **1982**, 104, 4524-4529. b) Drago, R.S. *Organometallics*, **1995**, 14, 3408-3417.c) Drago, R.S. and Joerg, S. *J.Am.Chem.Soc* **1996**, 118, 2654-2663. d) Joerg, S., Drago, R.S., and Sales, J. *Organometallics*, **1998**, 17, 589-599.

[10] a) Streuli, C.A. *Anal.Chem.* **1960**, 32, 985. b) Bush, R.C., and Angelici, R.J. *Inorg.Chem.* **1988**, 27, 681.

[11] Derencsényi, T.T. Inorg.Chem. **1981**, 20, 655-670.

[12] Fernandez, A.L., Reyes, C., Lee, T.Y., Prock, A., Giering, W.P., Haar, C.M. and Nolan, S.P. *Perkin Trans.* **2000,** 2, 1349

[13] http://www.bu.edu/qale/

[14] a) Müller, T.E. and Mingos, D.M.P. *Transit. Met. Chem.* **1995**, 20, 533. b) Smith, J.M., Coville, N.J., Cooke, L.M and Boeyens, J.C.A. *Organometallics*, **2000**, 19, 5273. c) Smith, J.M., Coville, N.J. *Organometallics*, **2001**, 20, 1210. d) Bunten, K.A., Chen, L., Fernandez, A.L., and Poë, A.J. *Coord.Chem.Rev***. 2002**, 233-234, 41-51.

[15] Allen, F.H., Kennard, O., Taylor, R. *Acc.Chem.Res.* **1983**, 16, 145 (Search date 3-20-2006)

[16] Cook, G.A.; Mason, G. W. *J.Org.Chem*. **1972**, 37, 3342

[17] a) Alyea, E.C., Dias, S.A., Fergusson, G., and Restino, R. *Inorg.Chem*. **1977**, 16, 2329. b) Fergusson, G., Robert, P.J., Alyea, E.C. and Khan, M. *Inorg.Chem*. **1978**, 17, 2965.c) Farrar, D.H. and Payne, N.C. *Inorg.Chem*. **1981**, 20, 821. d) Immirzi, A., and Musco, A. *Inorg.Chim.Acta*, **1977**, 25, L41. e) White, D., Taverner, B.C., Leach, P.G.L. and Coville, N.C. *J.Comp.Chem* **1993**, 36, 1042. f) White, D., and Coville, N.J. *Adv. Organomet. Chem*. **1994**, 36, 95.

[18] a) Zizelman, P.M., Amatore, C., and Kocki, J.K. *J.Am.Chem.Soc*. **1984**, 106, 3771. b) Golovin, M.N., Rahman, M.M., Belmonte, J.E., Giering, W.P. *Organometallics,* **1985**, 4, 1981. c) Dahlinger, K., Falcone, F., and Poë, A.J. *Inorg.Chem*. **1986**, 25, 2654.

[19] Lui, H.-Y., Eriks, K., Prock, A, and Giering, W.P. *Organometallics*, **1990**, 9, 1758.

[20] Fernandez, A.L., Lee, T.Y., Reyes, C., Prock, A. and Giering, W.P. *Organometallics,* **1998**, 17, 3169

[21] a) Fernandez, A.L., Lee, T.Y., Reyes, C., Prock, A., Giering, W.P., Haar, C.M. and Nolan, S.P.: *J. C. S. Perkin Trans*. **1999,** 2, 2631 b) Fernandez, A.L., Reyes, C., Prock, A. and Giering, W.P.: *Perkin Trans* **2000**, 2, 1033.

[22] Wilson, M.R., Wokasa, D.C., Prock, A., Giering, W.P. *Organometallics,* **1985**, 14, 869

[23] Wokasa, D., Prock, A. and Giering, W.P. *Organometallics*, **2000**, 19, 4629

[24] Babij, C., Chen, H., Chen, L. and Poë, A.J. *Dalton. Trans*, **2003**, 3184.

[25] a) Rodima, T.; Kaljurand, I.;Pihl, A.;Maemets, V.; Leiti, I.; Koppel, I.A. *J.Org.Chem.* **2002**, 67, 1873. b) Streitwieser, A., McKeown, A.E., Hasanayn, F. and Davis, N. *Organic Lett*. **2005**, 7, 1259

[26] a) Brown, T.L. Inorg.Chem. **1992**, 31, 1286-1294; b) Caffery, M.L. and Brown, T. L. *Inorg.Chem.* **1991**. 30, 3907. c) White, D.P. and Brown, T.L. *Inorg.Chem.* **1995**, 34, 2718. d) Choi, M-G. and Brown, T.L. *Inorg.Chem.* **1993**, 32, 1548. e) Lee, K.J.. and Brown, T.L. *Inorg.Chem.* **1992**, 31, 289. f) Choi, M-G. and Brown, T.L. *Inorg.Chem.* **1993**, 32, 5603. g) Choi, M-G., White, D. and Brown, T.L. *Inorg.Chem.* **1994**, 33, 5591.

[27] Cook, G.A. and Mason, G.W. *J.Org.Chem.* **1972,** 21, 3342

[28] Chesnut, D.B. *J.Am.Chem.Soc*, **1999**, 122, 2335.

[29] Cotton, A.F. and Wilkinson, G.W. in *Advanced Inorganic Chemistry*, 4th Ed. **1980**, John Wiley and Sons, New York, page 440.

[30] Nemykin, V.N.; and Basu, P. *Inorg.Chem*. **2005**, 44, 7494

[31] Senger, R. S.; and Basu, P. *New J. Chem*. **2003**, 27, 1115.

[32] Holm, R.H.; Kennepohl, P.; and Solomon, E.I. *Chem. Rev*. **1996**, 96, 2239.

[33] Housecroft, C.E. and Sharp, A.G. in *Inorganic Chemistry*. 2nd Ed. 2005, Prentice Hall, New York, page 563.

[34] a) Onsager, L. *J.Am.Chem.Soc,* **1936**, 18, 1486. b) Onsager, L. *J. Phys. Chem*, **1939**; 43, 189.

[35] a) Topich, J. Lyon, J.T., III.. *Inorg.Chim. Acta*. **1983**, 80, L41, b) Topich, J. Lyon, J.T., III. *Polyhedron*, **1984**, 3, 61. c) Topich, J. Lyon, J.T., III. *Inorg.Chem*. **1984**, 23, 3202. d) Boyd, I.W.; Spence, J.T. *Inorg. Chem.* **1982**, 21, 1602

[36] Seymore, S. B.and Brown, S.N. *Inorg.Chem*. **2000**, 39, 325

[37] Lorber, C.; Plutino, M.R.; Elding, L.I.; Norlander, E. *J.Chem.Soc., Dalton Trans.* **1997**, 3997

[38] Schultz, B.E. and Holm,R. H. *Inorg.Chem* **1993**, 32, 4244

[39] Cornish-Bowden, A. *J.Biosci***, 2002**, 27, 121

[40] Tucci, G.C.; Donahue, J.P.; Holm, R.H. *Inorg.Chem.* **1998**, 37, 1602

[41] Reynolds, M.S.; Berg, J.M.; Holm, R.H. *Inorg.Chem.* **1984**, 23, 3057.

[42] Millar, A.J., Doonan, C.J., Smith, P.D., Nemykin, V.N., Basu, P. and Young, C.G. *Chem. Eur. J.* **2005,** 11, 3255.

[43] J. I. Shulman, *J. Org. Chem.* **1977**, *42*, 3970

[44] Thapper, A.; Deeth, R. J.; Nordlander, E. *Inorg.Chem.* **2002**, 41, 6695-6702

[45] Angew.Chem.Int.Ed. **2004**, 43, 546-549.

[46] Kail, B.W., Pérez, L.M., Zarić, S.D., Millar, A.J., Young, C.G., Hall, M.B. and Basu, P. Accepted *Chem. Eur. J*. **2006**

[47] Becke, A. D. *J. Chem. Phys.* **1993,** *98*, 5648. C. Lee, W. Yang, and R. G. Parr, *Phys. Rev. B* **1988**, *37*, 785

[48] Parr, R.G.; Yang, W. *Density-functional theory of atoms and molecules* Oxford Univ. Press, Oxford **1989**.

[49] Gaussian 98 Revision: A11 Gaussian 03, Revision B5, M. J. Frisch, G. W. Trucks, H. B. Schlegel, G. E. Scuseria, M. A. Robb, J. R. Cheeseman, J. A. Montgomery, Jr., T. Vreven, K. N. Kudin, J. C. Burant, J. M. Millam, S. S. Iyengar, J. Tomasi, V. Barone, B. Mennucci, M. Cossi, G. Scalmani, N. Rega, G. A. Petersson, H. Nakatsuji, M. Hada, M. Ehara, K. Toyota, R. Fukuda, J. Hasegawa, M. Ishida, T. Nakajima, Y. Honda, O. Kitao, H. Nakai, M. Klene, X. Li, J. E. Knox, H. P. Hratchian, J. B. Cross, C. Adamo, J. Jaramillo, R. Gomperts, R. E. Stratmann, O. Yazyev, A. J. Austin, R. Cammi, C. Pomelli, J. W. Ochterski, P. Y. Ayala, K. Morokuma, G. A. Voth, P. Salvador, J. J. Dannenberg, V. G. Zakrzewski, S. Dapprich, A. D. Daniels, M. C. Strain, O. Farkas, D. K. Malick, A. D. Rabuck, K. Raghavachari, J. B. Foresman, J. V. Ortiz, Q. Cui, A. G. Baboul, S. Clifford, J. Cioslowski, B. B. Stefanov, G. Liu, A. Liashenko, P. Piskorz, I. Komaromi, R. L. Martin, D. J. Fox, T. Keith, M. A. Al-Laham, C. Y. Peng, A. Nanayakkara, M. Challacombe, P. M. W. Gill, B. Johnson, W. Chen, M. W. Wong, C. Gonzalez, and J. A. Pople, Gaussian, Inc., Pittsburgh PA, 2003.

[50] a) R. Ditchfield, W. J. Hehre and J. A. Pople, J. *Chem. Phys.* **1971,** 54, 724 b) W. J. Hehre, R. Ditchfield and J. A. Pople, , *J. Chem. Phys*. **1972**, 56, 2257. c) P. C. Hariharan and J. A. Pople, Mol. Phys. **1974**, 27, 209 (). d) M. S. Gordon, Chem.

Phys. Lett. **1980**, 76, 163. e) P. C. Hariharan and J. A. Pople, Theo. Chim. Acta. **1973**, 28, 213.

[51] "The Chemistry of Phosphorous" Emsley, J. and Hall, D. **1976**, Harper and Row Publishers, N.Y.

[52] Derencsenyi, T.T. *Inorg. Chem.* **1981**; *20*, 665.

[53] http://www.minitab.com

Chapter 4: Geometric Rearrangement in Mononuclear Molybdenum (V) Complexes: The Serine Gated Electron Transfer Hypothesis.[‡]

[‡] Parts of this work have been published: Kail, B.W.; Nemykin, V.N.; Davie, S.R.; Carrano, C.J.; Hammes, B.; Basu, P. *Inorg. Chem*. **2002**, 41, 1281-1291. Carrano, C.J.; Balwant, C.S.; Hammes, B.S.; Kail, B.W.; Nemykin, V.N.; Basu, P. *Inorg. Chem*. **2003,** 42, 5999-6007. Kail, B.W. and Basu, P. *J.C.S. Dalton Trans.*, **2006**, 11, 1419-1423**.**

Chapter 4: Geometric Rearrangement in Mononuclear Molybdenum (V) Complexes: The Serine Gated Electron Transfer Hypothesis.

Abstract:

Many mononuclear molydenum enzymes are believed to function via catalytic oxygen atom transfer (OAT) reactions as either oxygen atom acceptors with a Mo(IV) metal center or as oxygen atom donors with a Mo(VI) metal center. Moreover, the regeneration of a catalytically active enzyme, after formal OAT has occurred, is believed to involve two, one electron/ one proton transfer steps that result in a formal Mo(V) intermediate. Although the crystal structures of the fully oxidized Mo(VI) and fully reduced Mo(IV) forms of the enzyme have been reported, no crystal structure exists for the enzyme in a transient 5+ state. To this end we have synthesized, and fully characterized a series of monooxo-Mo(V) complexes in attempt to model the transient Mo(V) state of the enzyme. Furthermore we show that these complexes can be isolated as two discrete isomers with respect to the position of a heteroatom donor relative to the oxo-group and have detailed the kinetics of isomerization and electronic structure of these complexes. Based upon our findings we have postulated a serine gated electron transfer hypothesis (SGET) to provide a possible explanation for the role of isomerism in the regeneration step of a catalytically active protein. Lastly, we have also investigated the role of solvent in the isomerization process in attempt to model the effects of a "protein-like" dielectric environment on the overall transformation rate and mechanism.

Introduction

Dimethyl sulfoxide reductase (DMSO reductase) is a pyranopterin-bound mononuclear molybdenum enzyme that catalyzes the reduction of dimethyl sulfoxide (DMSO) to dimethyl sulfide (DMS).[1,2,3] This reductive process is important in the biogenic sulfur cycle by way of the biogeochemical cycling of sulfur in aquatic environments. The most common source of biogenic sulfur in these environments is dimethylsulfoniopropionate (DMSP), which originates mainly from the algal osmolyte. DMSP can then be cleaved to produce acrylate and dimethyl sulfide (DMS), a volatile organo sulfur compound that has been associated with a counteractive effect on global warming.[4] Moreover, DMS can be oxidized photochemically and biologically to DMSO. DMSO can function as a terminal electron acceptor for respiration in anaerobic marine organisms that express DMSO reductase, and as such allow for sulfur cycling through "reclaiming" oxidized DMS. DMSO reductase is a pterin-bound mononuclear molybdenum enzyme that catalyzes the two-electron reduction of DMSO to DMS with the corresponding two-electron oxidation of the molybdenum center from +4 to +6. Among the known DMSO reductases, the molybdenum center from three bacterial species has been intensely investigated. Two were isolated from photosynthetic species; *Rhodobacter sphaerodies*[5] and *R. capsulatus*[6], while the third was isolated from *E. coli*.[7] Unlike the majority of the mononuclear molybdenum enzymes, DMSO reductases from *Rhodobacter spheroides* and *R. capsulatus* have the molybdenum center as the sole prosthetic group. The absence of other prosthetic groups has allowed detailed spectroscopic investigations to probe the active site directly. Thus, DMSO reductases

have been investigated by extended X-ray absorption fine structure (EXAFS) spectroscopy at the K-edge of the molybdenum center,[8,9] resonance Raman (rR) spectroscopy,[10,11,12] magnetic circular dichroism (MCD) spectroscopy,[13] and electron paramagnetic resonance (EPR) spectroscopy.[14] In addition, the enzymes isolated from both organisms have been studied by X-ray crystallography.[5a,6c,15] Enzymes isolated from these sources exhibit a high degree of sequence similarity (77% identity and 93.5% similarity) and are localized in the periplasmic space.

The first crystallographic investigation on DMSO reductase isolated from *R. sphaeroides* was carried out in the oxidized form as well as on the dithionite reduced form.[15a] On the basis of the crystallographic results, a novel mechanism involving an oxygen-atom transfer reaction between a monooxo-Mo(VI) center and a desoxo-Mo(IV) center was proposed. Subsequently, crystal structures of the *R. capsulatus* protein described more conventional dioxo-Mo(VI) and monooxo-Mo(IV) centers.[6c,15] Although there are major differences in the active-site descriptions, the structural reports reveal a close similarity with respect to the folding of the protein, the presence of two pyranopterin cofactors, and a single coordinated serine per molybdenum atom. The diversity in the DMSO reductase family has lead Boyington *et al*. to suggest that the coordination of the different amino acids to the bis-ditholene coordinated metal imparts substrate specificity among the members of the DMSO reductase family.[16] Among the differences are the number of coordinated pyranopterin ene-1,2-dithiolate donors, the mode of their coordination (i.e., bidentate or monodentate), and the number of terminally coordinated oxo groups (O_t). Detailed EXAFS and rR data on the *R. sphaeroides* enzyme suggest a monooxo-Mo(VI) center coordinated by four sulfur donors. A similar EXAFS

investigation on the *R. capsulatus* enzyme suggested that the fully oxidized state had a dioxomolybdenum center. A high-resolution (1.3 Å) crystal structure of the *R. sphaeroides* enzyme that shows that the active site is disordered, existing as a mixture of hexa-and pentacoordinated molybdenum centers,[5a] has recently been reported. It has also been suggested that such structural disorders may be a result of different crystallization or protein-handling conditions. Indeed, by varying the preparative conditions, different forms of the *R. capsulatus* enzyme have been generated.[17] Another in-depth rR investigation on *R. capsulatus* raised the possibility of sulfeinic units resulting from the dithiolene moiety. While these investigations have provided insight into the structure and biochemistry of DMSO reductase, it appears that the reduced and catalytically competent molybdenum center is desoxo-Mo(IV), while the fully oxidized state is a monooxo-Mo(VI) center. Similar reactivities with discrete inorganic complexes have recently been discovered.[18,19,20]

The current understanding of this transient state relies heavily upon spectroscopy.[21] In addition to the possibility of sulfeinic units, based on spectroscopic features of the metal center, it has also been suggested that ene-dithiolene dissociation from the metal center may lead to different forms of the enzyme.[17a] However, this dissociation may also be possibly attributed to preparative, handling or crystallization conditions. One possible argument for a preparative-based dissociation is through understanding the possible effects of altering the internal dielectric constant at the protein active site. For example, it has been reported that the pK_a of histidine residues are reduced inside a protein when exposed to increasing salt concentrations. This has been established in studies on *Staphylococcal nuclease*, where the pK_a's of histidine residues

in were shown to exhibit anion-specific effects and lowering of the pK_a (from that of free histidine) was found to be different with different anions under equivalent ionic strength.[22] Moreover, recent investigations of dielectric environments of the protein interior suggest that the dielectric constant can be higher than the commonly assumed value of 4. Once again, *Staphylococcal nuclease* was studied and the experimental pK_a of the buried Lys-66 and Glu-66 residues were indicative of an apparent dielectric constant of ~10 as reflected by pK_a values of 5.7 and 8.8 respectively[23]. Furthermore, the dielectric constant may be as high as 12 in the environment of the protein interior.[24] Taken together, these results suggest that it is possible to lower the pK_a of a coordinated residue as a function of anion such that the basicity of the donor atom can be altered to favor dissociation from the metal ion.

A detailed inspection of the DMSO reductase crystallographic data, and that of a related enzyme trimethylamine N-oxide reductase (TMAOR), reveals a wide variation in the reported O_t -Mo-O_{ser} angle, which ranges from 77-146° **(Figure 4.1)**.[5a,6c,15,18] A similar comparison for an O(terminal)-Mo-S(cysteine) angle can be made from the crystal structure of chicken liver sulfite oxidase[25] and *Desulfovibrio desulfuricans* nitrate reductase[26] where the O(terminal)-Mo-S(cysteine) angles are 72.8° and 55°, respectively. The magnitudes of the angles are clearly suggestive of a preference for the sulfur donors in the equatorial position as opposed to an axial oxygen donor.

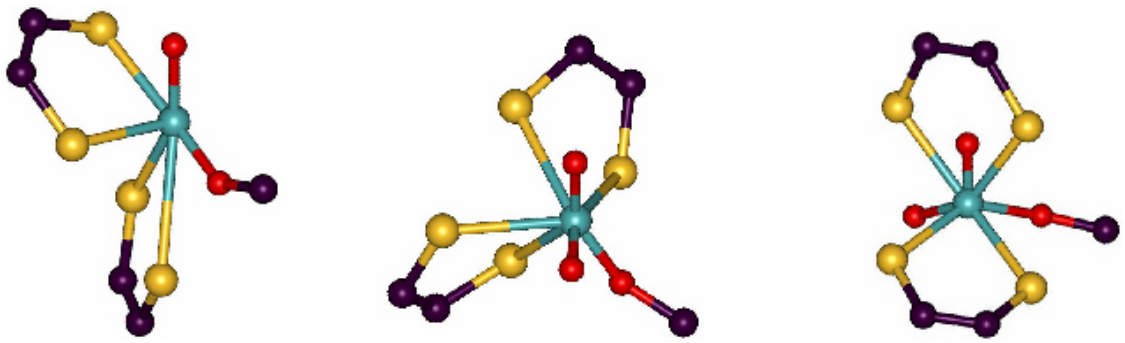

Figure 4.1
Active- site structures of (A) DMSO reductase from *R. sphaeroides*,[5b] (B) TMAO reductase from *Shewanella massilia*,[1] and (C) DMSO reductase from *R. capsulatus*. The Ot -Mo-O_{ser} angles are (A) 109°, (B) 146 and 90°, and (C) 77 and 93°.

Analog chemistry has played an invaluable role in understanding the structure and mechanism of metalloproteins including mononuclear molybdoenzymes[27,28,29,30]**.** For example, detailed work using the symmetric tris(pyrazolyl)borate Tp^R ligands, as a platform, has resulted in oxo-molybdenum(V) systems that provided valuable insight to spectroscopic signature of the enzymes[31]. Indeed, this early work has given us one of the first forays into the reactivity and spectroscopy of isostructural [$(Tp^R)MoOX_2$] derivatives where (X) OPh-, OMe-, and SPh-). Polyfunctional, facially coordinating tridentate ligands used in this study contain two pyrazole groups with two nitrogen donors, and another donor atom such as the thiolato sulfur or phenolato oxygen that provides an asymmetric donor set. More specifically, these heteroscorpionate ligands, $(pz)_2CHX$, produce coordination environments that are similar to that offered by (TpR)- with the same topology and charge, but allowing for a difference in one donor atom. Therefore, through the comparison of $(pz)_2CHX$ tripodal ligands, where X contains O or S donors, with the well studied (Tp^R) allows a direct understanding of the influence of structure on the reactivity of Mo(V)-oxo complexes. To this end, we describe our work with the Mo(V)-oxo complexes of three heteroscorpionate ligands $(L1O)^-$, $(LO)^-$ and

$(L3S)^-$ and their properties (**Figure 4.2**)[32]. In attempt to understand the chemical significance of the angular variability in DMSOR and TMAOR, we have reported the synthesis of two geometric isomers: *cis*-$(L1O)Mo^{V}OCl_2$ and *trans*-$(L1O)Mo^{V}OCl_2$ (where L1OH) (3-tert-butyl-2hydroxy-5-methylphenyl)bis(3,5-dimethylpyrazolyl) methane) (**Figure 4.2**). Here the cis and trans notations refer to the position of the phenolato oxygen (O_p) relative to that of the terminal oxo (O_t) ligand.

In general, there are two possible mechanisms for the isomerization of octahedral metal complexes[33], although such investigations on oxo-molybdenum complexes are rare[34]. The first possible mechanism is a bond dissociation mechanism in which either one of the equivalent equatorial chlorine, nitrogen or the oxygen donor could briefly dissociate from the metal center and then reattach upon geometric rearrangement of $(L1O)Mo^{V}OCl_2$. Such dissociation may reflect the inherent plasticity at the metal center, similar to that discussed earlier with respect to high salt concentrations. The second possible mechanism is a twist mechanism, in which involves a 120º rotation of a plane containing the terminal oxo-group and two equatorial chlorine atoms of $(L1O)Mo^{V}OCl_2$. Furthermore, in this chapter, demonstrate the effects of ligand sterics upon the rate of the isomerization by exploring *cis*-$(LO)Mo^{V}OCl_2$ (where LOH) (2-hydroxy-5-methylphenyl)bis(3,5-dimethylpyrazolyl) methane) (**Figure 4.2**). Using these well-defined, discrete molecules, we suggest that by varying the O_t -Mo-O_p angle the electronic structure and consequently the reduction potential could be modulated[35].

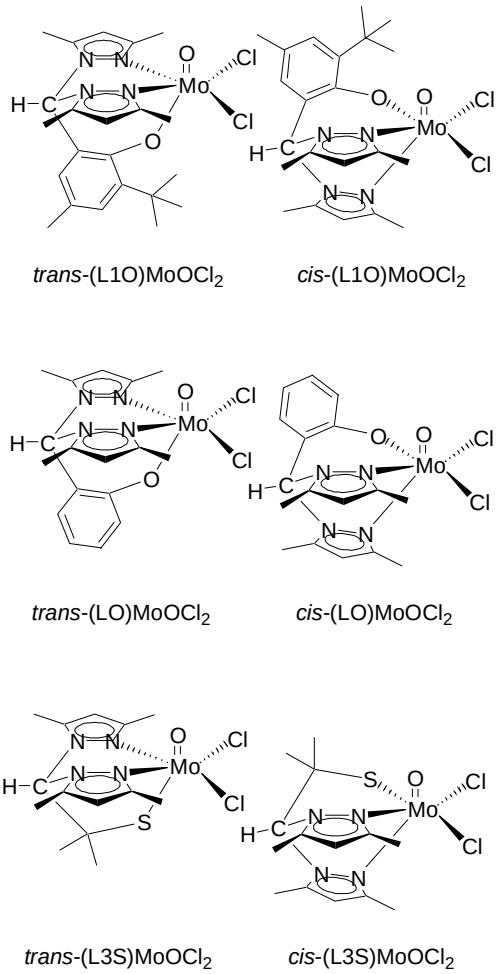

Figure 4.2
Schematic representations of the *cis* and *trans*-isomers of the heteroscorpionate ligands (top) *cis*-(L1O)$Mo^{V}OCl_2$ and *trans*-(L1O)$Mo^{V}OCl_2$ complexes, (middle) *cis*-(LO)$Mo^{V}OCl_2$ and *trans*-(LO)$Mo^{V}OCl_2$ and (bottom) *cis*-(L3S)$Mo^{V}OCl_2$ and *trans*-(L3S)$Mo^{V}OCl_2$ complexes.

On the basis of these findings, we hypothesized that a "serine-gated electron-transfer" process may be important in the catalytic mechanism of DMSO reductase. The details of the isomeric transformation, the electronic structure of the two isomers, and the details of the serine-gated electron-transfer hypothesis and its mechanistic implication to

DMSO reductase[36] are also discussed. We describe a similar angular variation in nitrate reductase and TMAO reductase through the cis and trans isomers of the (L3S)H ligand (methyl-thiol)bis(3,5-dimethylpyrazolyl) methane); (**Figure 4.2)**. In addition, we also explore the effects of a variable dielectric constant upon the isomerization reaction of *cis*-(L1O)$Mo^{V}OCl_2$ and have found that the mechanism of the transformation is very sensitive to the solvent used[37]. Lastly, we show that the g-values of the complex can change as a function of the isomer and as such present a "high" and "low" g form of $[(L1O)Mo^{V}O]^{3+}$ cores. The results are presented in light of the known geometric preference of the active sites of the mononuclear molybdenum enzymes.

Experimental Section

All syntheses were carried out in oxygen-free, dry argon atmospheres using dry and distilled solvents following standard Schlenk techniques.

Materials and Supplies.

All chemicals were purchased from commercial sources such as Aldrich Chemical Company and Acros Chemical Company. The solvents were purified as follows: acetonitrile from CaH_2 followed by Na_2CO_3 -$KMnO_4$ and finally from P_2O_5; dichloromethane from CaH_2; toluene and tetrahydrofuran (THF) from sodium benzophenone. The ligands, (L1O)H and (LO)H, were synthesized as reported and obtained from Prof. Carl Carrano, while the (L3S)$MoOCl_2$ complex was also synthesized by his group at San Diego State University.

Spectroscopy and Electrochemistry.

Infrared spectra were recorded on a Perkin-Elmer FT-IR 1760X using KBr pellets. The electronic spectra were recorded on a Cary 14 spectrophotometer with an OLIS 14 version 2.6.99 operating system connected to a constant-temperature circulator. The kinetic measurements were performed at a series of seven temperatures ranging from 20 to 55 °C with a 5 °C increment in dry, oxygen-free acetonitrile. All kinetic data were transferred to a personal computer and processed using Origin 6.1 software from Microcal. Electrochemical measurements were carried out in a Bioanalytical Systems (BAS) model CV-50W. Voltammograms were recorded with a standard three-electrode system consisting of a Pt-disk working electrode, a Ag/Ag^+ reference electrode, and a Pt-wire auxiliary electrode. All voltammograms were internally referenced with ferrocene, and the potentials are reported with respect to the Fc^+/Fc couple without junction correction. Electrospray mass spectra (ESI MS) were collected on a Micromass ZMD mass spectrometer, with acetonitrile solutions injected via syringe pump at a flow rate of 0.1 mL/min. X-band EPR spectra were acquired using a Bruker-300 spectrometer equipped with an Oxford ESR-910 liquid helium cryostat and Bruker bimodal cavity. All samples for the EPR spectroscopy investigations were dissolved in a dry, degassed, 50:50 toluene:chloroform mixture and immediately cooled to –77 ^oC until analyzed. The quantification of all signals was relative to a CuEDTA spin standard and the spectra were obtained with a field modulation of 1 mT_{pp} at 100 KHz. In addition, the magnetic field was calibrated with a NMR gaussmeter while the microwave frequency was measured with a frequency counter.

The isotropic g and A values were calculated by simulating the room temperature spectra of the two samples, using custom written software**,** that diagonalizes the Hamiltonian shown in **Equation 4.1**:

$$\mathbf{H = \beta B(g_{xx}\hat{S}_x + g_{yy}\hat{S}_y + g_{zz}\hat{S}_z) + h(A_{XX}\hat{S}_X\hat{I}_X + A_{YY}\hat{S}_Y\hat{I}_Y + A_{ZZ}\hat{S}_Z\hat{I}_Z)} \qquad \textbf{Equation 4.1}$$

Where the axes of the g-tensor (x, y, z) are not always coincident with the axes of the A-tenzor (X, Y, Z). As a result, three Euler angles (α_{xy}, β_{xz}, and γ_{yz}) were included to transform the A-tensor into the g-tensor axes system. The calculated isotropic g and A values were then used as input to specify the average values of the g and A tensor. Thus this method enabled two of the three variables, in the g and A tensors, to float while the third parameter adjusted automatically to keep the average constant. The EPR spectra were recorded and simulated by Prof. Michael Hendrich at Carnegie Mellon Univeristy.

Details in the Geometry Optimization

Optimized geometries for the *cis* and *trans*-isomers of (L1O)$MoOCl_2$, (LO)$MoOCl_2$ and (L3S)$MoOCl_2$ were obtained by using the B3LYP exchange-correlation functional with a 3-21G* basis set for all atoms under the unrestricted formalism. For all DFT calculations, the molybdenum atom was represented by DGauss full-electron double-Z basis sets with polarization having a (18s,12p,9d)f[6s,5p,3d] contraction scheme[38], while a standard 6-311G* basis set[39] was used to describe all other atoms, unless otherwise noted. All single point and geometry optimized DFT calculations were performed using the Gaussian 98 program family running under a Windows or a

Linux operating system[40]. The percent contribution from the atomic orbitals, to their respective molecular orbitals, was calculated using the VMOdes program[41].

Computational Mechanistic Investigation

The X-ray crystal geometries have been used for the *cis*-(L1O)$MoOCl_2$ and *trans*-(L1O)$MoOCl_2$ complexes. In the case of the twist mechanism, the trigonal face containing the O_t and two chlorine atoms was rotated about the pseudo-threefold axis in 10° increments. The single-point energies for each of the rotamers were calculated and plotted as a function of the angle of rotation. The rotational barrier was calculated as the energy difference between *cis*-(L1O)$MoOCl_2$ and the most unfavorable conformer, a 60° rotation of the trigonal face leading to an eclipsed conformation.[42,43] To understand the steric contribution to the twist mechanism of cis-trans isomerization, model calculations were carried out using a simplified structure obtained by deleting the extraneous alkyl groups. The rotational barrier in this set of calculations was determined in a manner similar to that described above. These calculations were performed at the semiempirical level with the PM3 Hamiltonian[44] implemented in the Hyperchem software package[45]. In addition, single-point calculations for *cis*-(L1O)$MoOCl_2$, *trans*-(L1O)$MoOCl_2$, and eclipsed-(L1O)$MoOCl_2$ complexes were performed at the DFT level using Becke's three-parameter hybrid-exchange functional[46] and Perdew's nonlocalcorrelation functional[47] (B3P86) in the borders of the unrestricted and restricted-open Hartree-Fock formalism without symmetry restrictions. The B3P86 exchange-correlation functional was chosen because previous research has shown that this functional gives similar, and at times superior, results compared to those from the Becke three-parameter hybrid-exchange

functional and the Lee-Yang-Parr non-local correlation functional (B3LYP)[48] when energies profiles are calculated.[49,50] All single point DFT calculations were performed using the Gaussian 98 program family running under a Windows or a Linux operating system.[40]

Computational Derivation of EPR Parameters:

Both the known crystal structures and the density functional theory-based (DFT) optimized geometries of *cis*- and *trans*-(L1O)$Mo^{V}OCl_2$ were used for the electronic structure calculations. Furthermore, for computational ease, the three-methyl groups located distal to the metal center were omitted from the model due to their insignificant contribution towards the overall steric and electronic environment at the metal center. In all cases, relativistic effects were excluded from the calculations. In the case of X-ray determined geometry of (L1O)$Mo^{V}OCl_2$, the Mo=O bond distance was fixed at 1.68 Å, while the Mo – Cl bond was fixed at 2.34 Å as there was a disorder between the chlorine and oxygen atoms. The following basis sets were used in the single-point DFT calculation of EPR parameters: 1) a modified DGauss full electron double-ζ basis set with polarization, DZVP for molybdenum; 2) The 6-311G(d) basis set for chlorine, oxygen, and nitrogen atoms; 3) The 6-31G(d) basis set for all carbon atoms and 4) the 3-21G* basis set for all hydrogen atoms. In each case, the B3P86 exchange-correlation functional was used. Furthermore, two different modifications to the DZVP basis set (denoted as basis set 1 and basis set 2) were used for the preliminary calculations. Once the preliminary calculations were complete, relativistic effects were included in calculations using DFT optimized geometries. Basis set 1 included the relativistic

elimination of small components (RESC) scalar relativistic core Hamiltonian. All DFT calculations were performed using the Gaussian 98 or Gaussian 03 program family running on either a Windows or Linux operating system. Mulliken charges for all atoms of interest were calculated using the standard procedures that are implemented into the Gaussian family software package. The percent contribution that atomic orbitals lend to their respective molecular orbitals was calculated by using the VMOdes program.[41]

Because the theory of the calculation of the EPR parameters for the transition-metal complexes using the DFT framework has already been covered in the numerous books and original publications, only the basic formulas are described here. In the DFT approach utilized in the Gaussian program, g-tensors are calculated as a correction to the free-electron value in **Equation 4.2a, 4.2b** and **4.2c**:

$$g_1 = g_e + \Delta g_{xx} \qquad \textbf{Equation 4.2a}$$

$$g_2 = g_e + \Delta g_{yy} \qquad \textbf{Equation 4.2b}$$

$$g_3 = g_e + \Delta g_{zz} \qquad \textbf{Equation 4.2c}$$

The three contributions are considered when Δg is calculated: i) relativistic corrections; ii) diamagnetic contributions to g; iii) paramagnetic contributions to g. As a result, the Δg value can be calculated by **Equation 4.3:**

$$\Delta g_{uv} = \Delta g^{relativistic} + \Delta g^{diamagnetic} + \Delta g^{paramagnetic} \qquad \textbf{Equation 4.3}$$

The calculation of the different contributions to the Δg, can be done within GIAO formalism implemented in Gaussian 03 software. The principal values of the A^{Mo} tensor can be calculated as the sum of isotropic (Fermi contact term) and anisotropic (spin dipolar term) contributions as given in **Equations 4.4a, 4.4b** and 4.**4c**:

$$A_{11} = A_F + T^{Mo}{}_x \qquad \textbf{Equation 4.4a}$$

$$A_{22} = A_F + T^{Mo}{}_y \qquad \textbf{Equation 4.4b}$$

$$A_{33} = A_F + T^{Mo}{}_z \qquad \textbf{Equation 4.4c}$$

Since the Fermi contact term is directly proportional to the spin density at the molybdenum nucleus it can be estimated by **Equation 4.5**:

$$A_F(Mo) = 8\pi/3\, g_e g_{Mo} \beta_e \beta_{Mo} \sum_{\mu,\lambda} P^{\alpha-\beta} \langle \chi_\mu | \delta(r_{Mo}) | \chi_\lambda \rangle \qquad \textbf{Equation 4.5}$$

Where $P^{\alpha-\beta}$ is the spin density matrix; χ_μ and χ_λ are atomic basis functions; $r_{Mo} = r - R_{Mo}$ (R_{Mo} is the position of the molybdenum nucleus); β_e and β_{Mo} are Bohr and nuclear magnetons, respectively; g_{Mo} is the ratio of molybdenum magnetic moment (in units of β_{Mo}) and molybdenum nucleus total spin. The components of the symmetric and traceless anisotropic hyperfine coupling tensor T^{Mo} reflect the asymmetry of the spin density around molybdenum nucleus and can be estimated by **Equation 4.6:**

$$T_{uv}(Mo) = g_e g_{Mo} \beta_e \beta_{Mo} \sum_{\mu,\lambda} P^{\alpha-\beta} \langle \chi_\mu | r^{-5}_{Mo} (r^2_{Mo} \delta_{uv} - 3 r_{Mo,u} r_{Mo,v}) | \chi_\lambda \rangle \quad \textbf{Equation 4.6}$$

Since all molecules presented in this paper have point group C_s or C_1, after diagonalization, T^{Mo} has the form of **Equation 4.7:**

$$T^{Mo}_x \neq T^{Mo}_y \neq T^{Mo}_z. \quad \textbf{Equation 4.7}$$

Kinetic Analysis.

The kinetic measurements were carried out in dry, degassed acetonitrile solutions prepared under an argon atmosphere using standard Schlenk techniques. Measurements were performed in 1 cm path-length quartz cuvettes placed in an isothermal cell holder. Due to the relatively slow rate of isomerization and wide range of solvent boiling points, variable temperature data were collected over the range of 25 to 40 °C in 5 to 10 degree increments. In each case, the first data point was collected within one minute of dissolution of the solid sample. A typical assay consisted of rapidly dissolving 1-2 mg (2 to 4 μmoles) of the molybdenum complex in 1 ml of thermally equilibrated solvent, followed by immediate data collection. Assays were conducted by monitoring the changes in the absorption ca. 340nm - 350 nm. The reason this range was chosen is based upon the solvochromatic shift observed in *cis*-(L1O)$MoOCl_2$ and a slight shift in the principle absorption band for *cis*-(L1O)$MoOCl_2$ relative to that of *cis*-(LO)$MoOCl_2$. The rate constants were determined from **Equations 4.8a** or **4.8b**,

$$d[\textit{cis}\text{-(L1O)}MoOCl_2]\,)dt = A_0 + [\textit{cis}\text{-(L1O)}MoOCl_2] \exp(-t/\tau) \quad \textbf{Equation 4.8a}$$

d[*cis*-(LO)$MoOCl_2$])dt = A_0 + [*cis*-(L1O)$MoOCl_2$] exp(-t/τ) **Equation 4.8b**

where A_0 is the initial absorbance, t is the time in minutes, and τ is the half-life of the reaction. In all cases, the data were fit to the above single-exponential with R^2 of 0.99 or better, with the residual absorbances an order of magnitude lower than the measured ones. From the variable-temperature experiments, the activation parameters were calculated using the Arrhenius and Eyring equations (**Equations 4.9a** and **4.9b**)

$$\ln k = \ln A \cdot e^{\frac{-Ea}{RT}} \qquad \textbf{Equation 4.9a}$$

$$\ln \frac{kh}{k_b T} = -\frac{\Delta H^*}{RT} + \frac{\Delta S^*}{R} \qquad \textbf{Equation 4.9b}$$

Synthesis of cis-(L1O)$MoOCl_2$ and trans-(L1O)$MoOCl_2$.

$MoCl_5$ (280 mg, 1.03 mmol) was placed in a dry 25 mL Schlenk flask, and 10 mL of dry degassed THF was added at -78 °C using an acetone-dry ice bath with stirring for 1 h. The temperature of the resulting slurry was raised to ~0 °C by placing the reaction flask in an ice bath. To this greenish-brown solution was added 375 mg (1.02 mmol) of the (L1O)K (offered from Professor Carl Carrano through collaborative arrangements) under argon atmosphere, and the reaction mixture was stirred overnight on ice. The color of the solution changed to dark brown. The solution was filtered and washed with acetonitrile, and the residue was extracted with dichloromethane. The resulting solution was combined with the filtrate, evaporated to dryness, dissolved in dichloromethane, and

chromatographed on silica gel using chloroform as the eluent. The target compound eluted from the column as the second pink band. Yield: 200 mg (37%).

From the column described above, a yellow band was eluted as the fourth band and was found to be the trans isomer. Yield: 100 mg (18%). The first yellow band (minor) was due to the (L1O)MoO_2Cl, while the third brown band was determined to be a mixture of the cis and trans isomers, accounting for ~100 mg of the product. Thus, the total yield of the two isomers was 400 mg (74%).

Synthesis of cis-(LO)$MoOCl_2$ and trans-(LO)$MoOCl_2$

Due to the lower steric hindrance of the (LO)K ligand, we anticipated the synthesis of *cis*-(LO)$MoOCl_2$ may require lower temperature to get similar yields. Interestingly, at room temperature, the reaction of $MoOCl_3(THF)_2$ with LOH yields only the trans isomer.[13] With these concerns in mind, *cis*- and *trans*-(LO)$MoOCl_2$ were synthesized following a modified procedure reported for *trans*-(LO)$MoOCl_2$. First, Solid $MoCl_5$ (1 mmol) was added to a 100 ml Schlenk flask and cooled in a dry-ice acetone bath for 30 min. Once cooled, 20 ml of THF was added drop-wise with rapid stirring and the reaction mixture was allowed to slowly warm to room temperature and resulted in the formation of green $MoOCl_3(THF)_2$. Once formed, the $MoOCl_3(THF)_2$ was returned to the acetone-dry ice bath for an additional 30 minutes. In parallel, anhydrous sodium acetate (1 mmol) was dissolved in ~20 ml dry THF in a dry box and 1mmol of (LO)H[51] was added with rapid stirring. Next the (LO)H/sodium acetate mixture was sealed, removed from the drybox and cooled in dry-ice acetone with rapid stirring for 30 minutes. Once cooled, the LOH/sodium acetate solution was added to the green $MoOCl_3(THF)_2$ solution

via cannula and immediately produced a brown color. The reaction mixture was allowed to react for 45 minutes in the dry-ice acetone bath, followed by rapid quenching by the addition of cold hexane to yield fine brown precipitate and yellow orange mother liquor. The precipitate was collected via vacuum filtration resulting in a soluble orange-yellow fraction and a fine brown solid, both of which were dried overnight under vacuum (yield 444 mg). Pure cis and trans isomers were obtained by flash chromatography on a silica stationary phase, in a cold room with dry-ice acetone cooled 10% acetonitrile/chloroform as the mobile phase. The first pinkish-red band was found to be the *cis*-complex (m/z =514 (M+Cl); $\upsilon_{Mo=O}$ 964 cm^{-1}, λ_{max} = 282 nm chloroform ~42% yield), while the second yellow-green band was found to be the trans-complex (m/z=514 (M+Cl); $\upsilon_{Mo=O}$ 944 cm^{-1}, λ_{max} = 340 nm chloroform: ~18% yield).All fractions were collected in a dry-ice acetone bath, and like fractions were combined and evaporated to dryness under high vacuum.

Results:

Synthesis of cis-(L1O)-$MoOCl_2$ and trans-(L1O)-$MoOCl_2$

The oxo-Mo(V) dichloride complex of the hydrotris-(pyrazolyl)borate ligand has been synthesized using $MoCl_5$ as the source of molybdenum. Initially, pure *cis*-(L1O)$Mo^{V}OCl_2$ was synthesized following a similar procedure. However, the kinetic investigation demonstrates that the cis isomer spontaneously converts to the more-stable trans isomer (vide infra), suggesting that a higher yield of the *cis*-(L1O)$Mo^{V}OCl_2$ could be obtained by conducting the synthesis at low temperatures. Using this modification, we have synthesized the *cis*-(L1O)-$Mo^{V}OCl_2$ as the kinetically controlled product in a higher yield. Statistically, the cis isomer should be the major (67%) product, and the trans

isomer should be the minor (33%) product. The experimentally obtained yield follows this statistical distribution (37% cis and 18%trans), indicating that very little of the cis isomer had isomerized to the trans isomer. The cis complex is highly soluble in common chlorinated organic solvents such as chloroform and dichloromethane, while the yellow *trans*-compound shows lower solubility under the same conditions. The molecular composition of the two compounds was confirmed by electrospray ionization mass spectrometry (ESI MS) of acetonitrile solutions of the complexes. Slow evaporation of a dichloromethane or an acetonitrile solution of the cis compound afforded X-ray-quality single crystals; however, disorder in the crystal did not allow us to determine the geometry unequivocally. Both isomers exhibit well-defined Mo=O vibrations in the IR spectra. The Mo=O stretching frequency of the cis isomer appears at 961 cm^{-1}, while the same vibration appears at 947 cm^{-1} for the trans isomer. The cis complex has a low-energy charge-transfer band that originates from the phenolic oxygen-to-molybdenum transition (vide infra). This charge-transfer band precludes the observation of the ligand field transition. No such low-energy charge-transfer band could be observed for the trans isomer, which would allow the observation of the ligand-field transition[52].

Synthesis of cis-(LO)-$MoOCl_2$ and trans-(LO)-$MoOCl_2$

Because the heteroscorpionate ligand, (LO)H, is sterically less hindered than the (L1O)H, we anticipated the synthesis of *cis*-(LO)$MoOCl_2$ may require lower temperature control to get similar yields. Interestingly, at room temperature, the reaction of $MoOCl_3(THF)_2$ with (LO)H yields only the trans isomer. In the present case, we have conducted the reaction at a low temperature and the chromatographic separation was

performed inside a cold room. Thus, $MoCl_5$ was reacted with (LO)H in THF following the previously described protocol. *cis*-(LO)$MoOCl_2$ was separated by adsorption chromatography on silica gel using pre-cooled acetonitrile-chloroform as the eluent. *cis*-(LO)$MoOCl_2$ compound eluted first as a pinkish band which was evaporated under vacuum yielding the target compound in solid state. The *trans*-(LO)$MoOCl_2$ compound followed as a greenish yellow band, which was also evaporated to get the pure *trans*-(LO)$MoOCl_2$ in the solid state. The *cis*-(LO)$MoOCl_2$ was isolated in a higher yield (42 %) than the *trans*-(LO)$MoOCl_2$ (18%) indicating that very little of the cis compound has isomerized to the trans geometry. In addition, the electronic spectra of *cis* and *trans*-(LO)$MoO^{V}Cl_2$ are very similar to those of the *cis* and *trans*-(L1O)$MoO^{V}Cl_2$ complexes.

Electrochemistry of cis-(L1O)-$Mo^{V}OCl_2$ and trans-(L1O)-$Mo^{V}OCl_2$:

The redox chemistry of the two isomers was investigated by cyclic voltammetry in acetonitrile solution, which is depicted in **Figure 4.3**. Both compounds exhibit well-defined one-electron reductive couples that can be attributed to the reduction of Mo(V) to Mo(IV), with the half-wave potentials of -934 and -1150 mV (vs Fc^{+}/Fc) for the trans and the cis isomers, respectively. The peak-to-peak separations (83 and 62 mV, respectively, for the cis and trans isomers) are indicative of the quasi-reversible one-electron nature of the process.

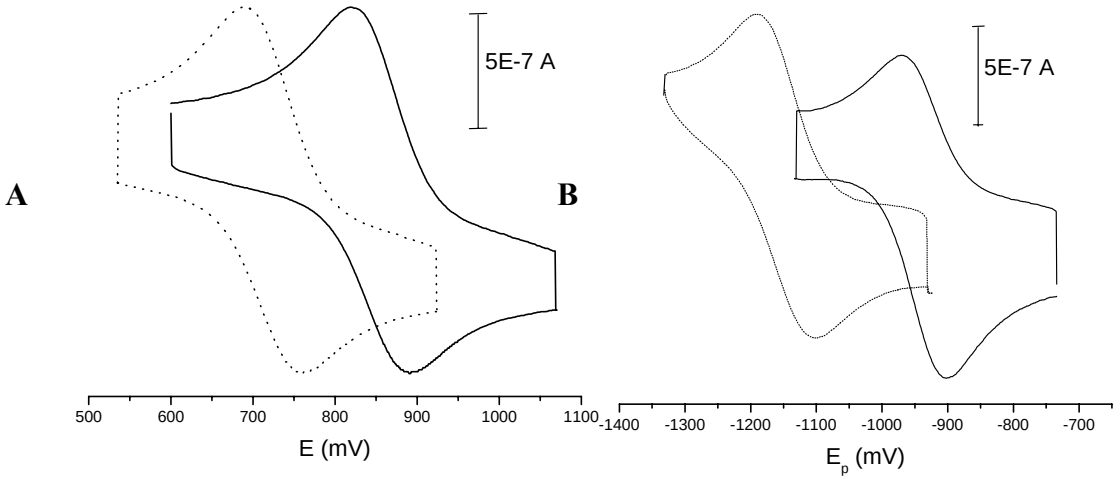

Figure 4.3. Cyclic voltammograms of *cis* and *trans*-(L1O)Mo$O^{V}Cl_2$: cis (dashed line). For both isomers, panel A represents the oxidative couple and panel B represents the reductive couple.

In addition, both isomers exhibit well-defined one electron oxidative couples for the oxidation of Mo(V) to Mo(VI); (**Table 4.1)**. The cis isomer is easier to oxidize ($E_{1/2}$= 726 mV vs Fc^{+}/Fc; ΔEp) 70 mV) than the trans isomer ($E_{1/2}$ = 861 mV vs Fc^{+}/Fc; ΔEp 65 mV). For both couples, the peak currents follow linear relationships with the square root of the scan rate. Interestingly, the separation between the two couples is larger in the cis isomer (1876 mV) than in the trans isomer (1795 mV). Although a similar reductive couple at -250 mV (vs Ag/AgCl) has been observed for $Tp^{Me2}Mo^{V}OCl_2$ (where Tp^{Me2} is the hydrotris(3,5-dimethylpyrazolyl)borate ligand), no oxidative couple was detected for this complex[31a].

Electrochemistry of cis-(LO)-$Mo^{V}OCl_2$ and trans-(LO)-$Mo^{V}OCl_2$

Most importantly, the redox potentials indicate that *trans*-(LO)$MoOCl_2$ is more stable than *cis*-(LO)$MoOCl_2$ by 4.3 kcal/mol whereas the difference in the (L1O)$MoOCl_2$ system is ~5 kcal/mol. Thus, the presence of an alkyl group slightly reduces the thermodynamic driving force of the isomerization reaction. The redox properties of the *cis* and *trans*-(LO)$MoOCl_2$ and (L1O)$MoOCl_2$ complexes, and the *cis*-(L3S)$MoOCl_2$ complex[53], complex are tabulated in **Table 4.1.** Interestingly the *cis*-(LO)$MoOCl_2$ isomer is the most difficult complex to oxidize ($E_{1/2}$ $Mo^{VI/V}$ of 864mV), while *trans*-(LO)$MoOCl_2$ undergoes irreversible oxidation. On the other hand, *cis*-(LO)$MoOCl_2$ is easier to reduce than *cis*-(L1O)$MoOCl_2$ by ~119 mV, presumably due to the electron releasing t-butyl group in the former ligand. In keeping with this, the most easily reduced complex was found to be the *cis*-(L3S)$MoOCl_2$ isomer, (~330mv easier than (LO)$MoOCl_2$ and ~450mV easier than (L1O)$MoOCl_2$) which does not possess the phenyl ring but does contain a more easily polarized sulfur donor.

Table 4.1. Electrochemical data [a] recorded in acetonitrile; [b] recorded in CH_2Cl_2.

Compound	**$E_{1/2}$ ($Mo^{VI/V}$)mV; (ΔE_p, mV)**	**$E_{1/2}$ ($Mo^{V/IV}$),mV, (ΔE_p, mV)**
cis-(LO)$MoOCl_2$	864 (89) [a]	-1031 (72) [a]
trans-(LO)$MoOCl_2$	Irreversible [a]	-841 (-85) [a]
cis-(L1O)$MoOCl_2$	726 (70) [a]	-1150 (83) [a]
trans-(L1O)$MoOCl_2$	861 (65) [a]	-934 (62) [a]
cis-(L3S)$MoOCl_2$	Irreversible [b]	-700 (62)[b]

Isomerization Kinetics:

The cis isomer spontaneously isomerizes to the trans isomer, which is associated with distinctive changes in the optical spectra. The difference spectra of the isomer transformation are provided in **Figure 4.4** and exhibit tight isosbestic points at 466 and 316 nm. The rates of the isomeric conversions have been followed spectrophotometrically at 347 nm. In each case, the reaction was monitored for 3-5 half-lives to ensure that the process had neared completion. In an attempt to provide the best possible approximation to the theromodynamic parameters associated with the conversion, the reaction rate was measured over seven different temperatures ranging from 25 to 55 °C. The isomerization follows a first-order process, indicating a unimolecular reaction.

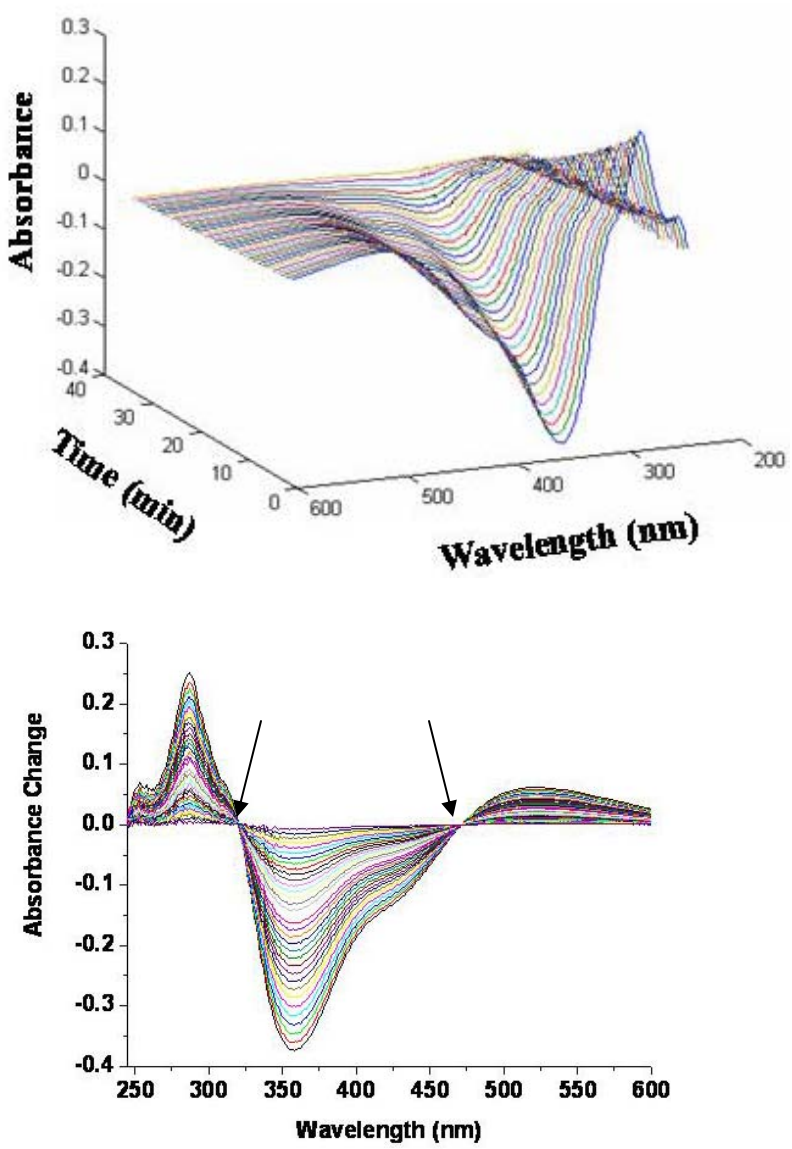

Figure 4.4. Top: Three-dimensional optical difference spectra in the cis-trans isomerization for (L1O)$MoOCl_2$ in acetonitrile at 20º C. **Bottom:** Same spectra in two-dimensions, clearly showing isosbestic points.

All thermodynamic data and k_{obs} at 40 °C, tabulated in **Table 4.2**, with a representative fit shown in **Figure 4.5.** These first-order rate constants, obtained from the fits, were used to determine the activation parameters.

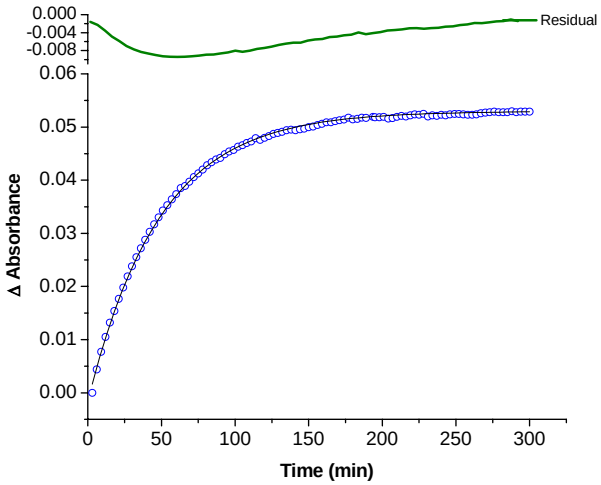

Figure 4.5. Optical spectral change at 347nm for the conversion of *cis*-(L1O)$MoOCl_2$ to the *trans*-(L1O)$MoOCl_2$ complex.

Solvent effects in the cis-(L1O)$MoOCl_2$ and cis-(LO)$MoOCl_2$ isomerization.

Acetonitrile solutions of *cis*-(LO)$MoOCl_2$ and *cis*-(L1O)$MoOCl_2$ spontaneously isomerize to the trans isomer. Single wavelength assays, for (LO)$MoOCl_2$, were performed at 347 nm in the temperature range 40 – 61 °C. For the *cis*-(LO)$MoOCl_2$ complex, single wavelength assays were performed at 340 nm over the temperature range of 35 - 50 °C. The isomerization reaction of *cis*-(L1O)$MoOCl_2$ was examined in solvents with a wide range of physical and chemical properties that included, but are not limited to, different dielectric constants, densities, viscosities and donor atoms. The single

wavelength assays were conducted over a range of 340 nm to 352 nm, depending upon the solvent, due to a small yet significant solvochromatic shift in the principle charge transfer transition in the *cis*-(L1O)$MoOCl_2$ and *trans*-(L1O)$MoOCl_2$ complexes. In all cases, the reactions followed a first order process depending only on the concentration of the complex. From the variable temperature rate data the activation parameters were calculated using the Eyring and Arrhenius equations. The rate constants at 40 °C and activation parameters are listed in **Table 4.2**.

Table 4.2. Kinetic parameters for cis→ trans geometric rearrangement

complex	**Solvent**	**Visc. mPa[54]**	**μ, D [62]**	**ε [62]**	**$Ea^{‡}$ kJ mol^{-1}**	**lnA**	**$\Delta H^{‡}$ kJ mol^{-1}**	**$\Delta S^{‡}$ J $mol^{-1}K^{-1}$**	**k_{obs} 40°C min^{-1}**
(L1O)$MoOCl_2$	MeCN	0.284	3.924	37.5	94.8	27	92.2	-31.7	2.40×10^{-3}
	DMF	0.624	3.82	38.3	98.7	30	96.0	-21.2	2.29×10^{-3}
	DMSO	1.29	3.96	46.7	48.4	11	51.1	-50.9	2.58×10^{-2}
	THF	0.359	1.63	7.5	87.6	25	90.2	69.4	1.93×10^{-2}
	Benzene	0.335	0	2.28	110.5	34	107.8	30.4	1.69×10^{-2}
	Ethylacetate	0.325	1.78	6.02	137.1	43	140.6	222.2	1.23×10^{-2}
(LO)$MoOCl_2$	MeCN	0.284	3.924	37.5	78.8	23	76.3	-45.2	2.86×10^{-2}
Solvent properties where taken from reference 62, while the activation parameters are taken from reference 38.									

The negative entropy of activation for the isomerization of *cis*-(LO)$MoOCl_2$ suggests the presence of a twist mechanism. However, when the rates of isomerization in acetonitrile of the two cis compounds are compared, the less sterically hindered (LO)$MoOCl_2$ complex isomerizes ~12 times faster than the (L1O)$MoOCl_2$ complex. This observed rate increase can be attributed to a $\Delta\Delta H^{‡}$ of ~15 kJ/mol higher for the

(L1O)$MoOCl_2$ complex which is only partially compensated by a slightly less negative entropy of activation ($\Delta\Delta S^{\ddagger}$ ~3.5kJ/mol at 298 K). Thus the end result of reducing the steric bulk of the phenolate ring in the *cis*-(LO)$MoOCl_2$ complex generates an ~12 kJ/mol lower $\Delta G^{\ddagger}$ for the process. The enthalpy of activation spans from 50 -140 kJ/mol while **Figure 4.6** depicts the observed positive entropy for non-polar solvents and the negative entropy in polar solvents. The mechanism was further investigated by mass spectrometry.

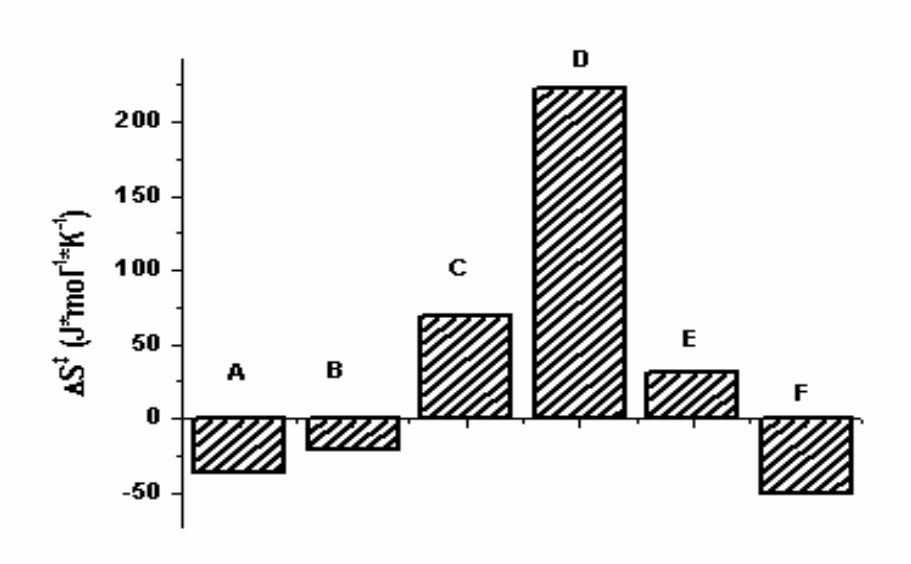

Figure 4.6. The entropy of activation for the isomerization of the *cis*-[(L1O)$MoOCl_2$] to the *trans*-[(L1O)$MoOCl_2$] complex in different solvents. From left to right, a) acetonitrile, b) DMF; c) THF; d) ethyl acetate; e) benzene; and f) DMSO.

Mass Spectrometry:

The kinetic results were complemented by ESI MS on (L1O)MoO_2Cl, with and without the addition of excess tetraalkylammonium salts (R_4NX, where R = *n*Bu, X = F or I and where R = Et, X = Br). The results of the ESI MS with and without tetraalkylammonium salts present are displayed in **Figure 4.7** and **Chart 4.1**.

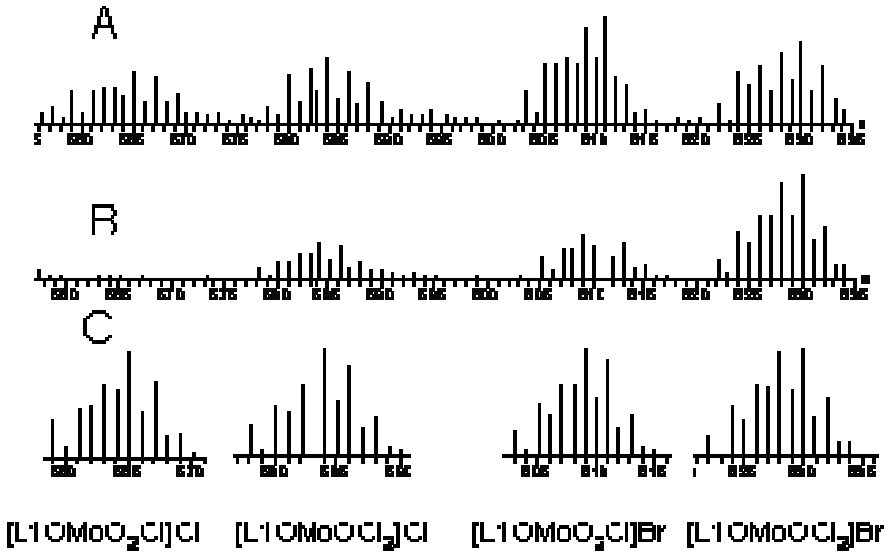

Figure 4.7. Negative -mode ESI mass spectra of (A) *cis*-(L1O)$MoO^{V}Cl_2$ and (B) trans-(L1O)$MoO^{V}Cl_2$ after incubation with 2-fold excess of Et_4NBr. Calculated distributions modeling the observed peaks are shown in (C).

All Mo(V) species discussed below gave good-quality ESI MS, which were observed only in the negative-ion mode. These experiments were performed by incubating 2.3 mmol of the *cis*-(L1O)MoO_2Cl in acetonitrile containing 4.8 mmol of R_4NX at 24 °C for 4 h with 2.4 mmol of the *trans*-(L1O)MoO_2Cl incubated under the same conditions as those used in a control experiment. An additional control was introduced through incubation of equimolar concentrations of the cis and trans isomers in

acetonitrile at 24 °C for 4 h. The experiments without R_4NX demonstrate that both isomers exhibit, in addition to their molecular-ion peaks, peak clusters due to the formation of (L1O)MoO_2Cl. With the exception of the fluoride salt, the experiments with R_4NX exhibit four additional peak clusters whose mass-to-charge ratios were well-matched to those expected for [(L1O)MoO_2Cl]X^-, [(L1O)MoO_2Cl]Cl^-, [(L1O)$MoOCl_2$]X^-, and [(L1O)$MoOCl_2$]Cl^-. Additional identification of each peak cluster was made through the simulation of the experimentally observed isotopic distribution pattern. Under similar experimental conditions (e.g., concentration, spectrometer parameters, flow rate, etc.), the intensity of the signal due to the oxidized Mo(VI) species was higher for the *cis*-(L1O)$MoOCl_2$ complex than that for the trans isomer. In the case of the dioxo (L1O)$MoOCl_2$ species, the comparison with the mass spectra of an authentic dioxo complex confirmed its presence in the *cis*-(L1O)$MoOCl_2$ and *trans*-(L1O)-$MoOCl_2$ spectra. The basis for the latter experiments is that tertiary phosphines are well-known, selective, oxo-abstracting agents in which a terminal oxo group may be abstracted from a dioxo species but not from a monooxo species. We have recently shown that mass spectrometry is a powerful tool for studying the oxygen-atom transfer reaction by probing the intermediates of the process.[29a] In accord with this result, when the authentic dioxo complex and the cis and trans isomers were reacted with excess PPh_3, a peak cluster due to a phosphine adduct could be detected in all cases, further confirming the presence of a dioxo species in solution.

Chart I. ESIMS of (L1O)$MoOCl_2$(base peaks are shown in parenthesis)

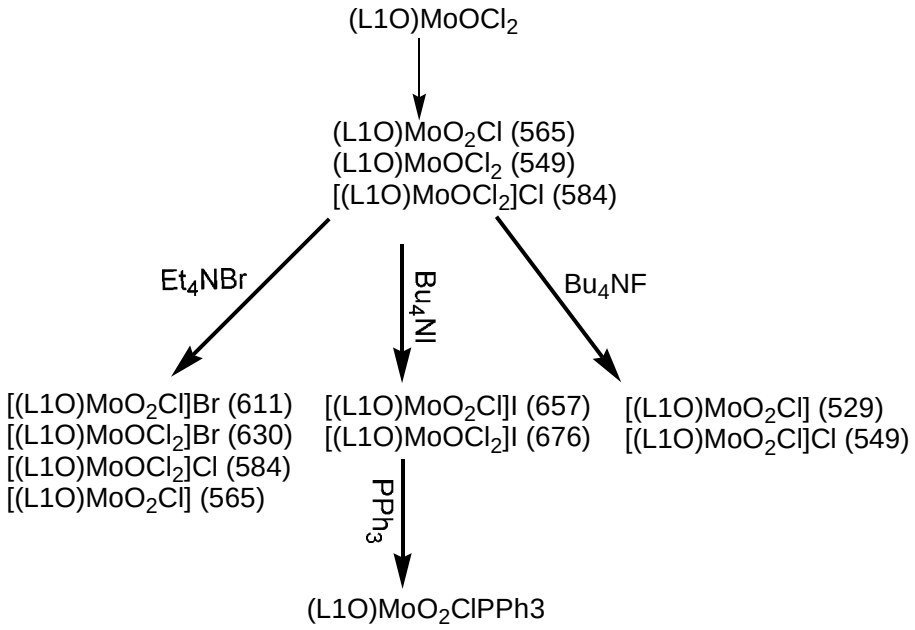

Chart 4.1. Mass spectral chart showing base peaks obtained from the *cis* [(L1O)$MoOCl_2$] to the *trans*-[(L1O)$MoOCl_2$] Isomerization in the presence of excess tetraalkyl Ammonium Salts

Electronic Structure, Stability and Mechanistic Calculations in cis- and trans-(L1O)$MoOCl_2$

The effects of the observed geometries on the electronic structure were investigated computationally. The electronic structure calculations for *cis*-, *trans*-, and *eclipsed*-(L1O)$MoOCl_2$ geometries were carried out at the unrestricted DFT B3P86 level. For computational purposes, the three-methyl groups (those distal to the metal center) were omitted from the model **(Figure 4.8)** as they do not significantly affect the steric requirement at the metal center. The DFT calculations on a possible twist reaction

pathway suggest that there is a decrease in the dipole moment of an eclipsed conformation at 11.6 D , relative to the dipole moment of the starting cis-complex 12.7D and the trans product 13.4D. The energy-level diagram and orbital compositions are presented in **Figure 4.8a, Figure 4.8b** and **Table 4.3**. In general these calculations show that the metal d orbitals are strongly destabilized by strong antibonding interactions with the terminal oxo group as well as with the donor atom trans to the terminal oxo group (i.e., phenolic oxygen for the trans isomer and pyrazolyl nitrogen for cis isomer). These interactions raise the energy of an orbital that is primarily composed of the metal d_z^2 orbital that is higher than any of the other d orbitals. In all compounds, large contributions from the equatorial ligands to the d_x^2-$_y^2$ orbital that lead to strong L$^{\sigma}$- Mo antibonding interactions have been observed. In each case, the displacement of the molybdenum atom from the equatorial plane (containing two chlorine, one nitrogen, and one oxygen or nitrogen atom) leads to an effective movement of the d_x^2-$_y^2$ orbital away from the Mo-Cl, Mo-N, or Mo-O bond vectors. Such movement of the metal away from the equatorial plane reduces the Lπ-Mo overlap and stabilizes the d_x^2-$_y^2$ orbital more than it does the d_z^2 orbital. The molecular orbital containing the metal d_x^2-$_y^2$ orbital contains several pyrazole π orbitals **(Figure 4.8a** and **Figure 4.8b).** Thus, the contribution to this orbital from the pyrazole π orbitals is greater in the trans isomer than in the cis. In addition to the previously discussed orbital interaction, the terminal oxo group contributes to a predominantly metal-centered lowest unoccupied molecular orbital (LUMO) and to LUMO + 1 orbitals through strong Oπ-Mo(d_{xz}, d_{yz}) antibonding interactions. As expected, the lowest-energy d orbital is the d_{xy} orbital, which is the

highest occupied molecular orbital (HOMO) and is half-filled for the molybdenum(V) state.

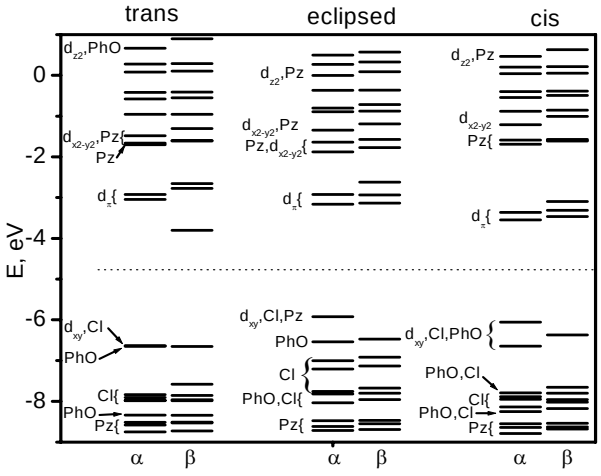

Figure 4.8a. Molecular Orbital diagram of the cis, trans and eclipsed (L1O)MoO^{V}Cl$_2$ geometries. Spin-unrestricted calculations were carried out using the B3P86 DFT

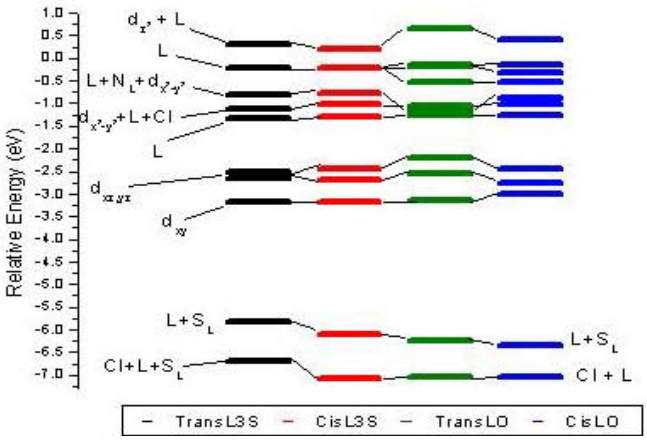

Figure 4.8b. Molecular orbital diagram for (LO)MoO^{V}Cl$_2$ and (L3S)MoO^{V}Cl$_2$ cis and trans isomers.

In all cases, one orbital that is predominantly due to the phenolic group could be located below the metal manifold. This orbital and the HOMO are well-separated from the other occupied π orbitals that are predominantly localized on the chlorine and the (L1O)- pyrazole or phenolic groups. The differences in energy between HOMO and HOMO - 1 are 0.02 and -0.6 eV for the trans and cis (also the eclipsed) geometries, respectively.

Table 4.3. Composition of the α-spin $(L1O)Mo^{V}OCl_2$ -complexes molybdenum d manifold.

Orbital	**Geometry**	**E, eV**	**%Mo**	**%O_t**	**%Cl**	**%OPh**	**%Pz**	**%L1O**
d_{xy}	trans	-6.63446	64.62	0.01	29.51	0.76	4.63	5.39
	cis	-6.05921	51.48	0.94	11.42	34.19	1.55	35.78
	eclipsed	-5.92587	58.03	3.14	14.25	13.88	8.47	23.29
d_{xz}	trans	-3.04525	69.42	14.23	2.58	9.55	3.54	13.09
	cis	-3.54703	66.94	15.70	4.03	1.69	10.19	12.12
	eclipsed	-3.16308	60.43	8.19	15.84	2.43	11.95	14.64
d_{yz}	trans	-2.9247	66.54	14.48	1.96	11.85	4.19	16.04
	cis	-3.36635	68.80	13.26	4.61	3.51	8.47	12.44
	eclipsed	-2.92552	68.74	10.76	6.94	6.01	6.34	12.89
$d_{x^2-y^2}$	trans	-1.6629	34.07	0.01	11.30	14.05	38.31	52.35
	cis	-1.21092	50.84	0.25	16.50	8.92	18.00	30.27
	eclipsed	-1.34507	39.02	2.40	7.36	14.42	29.70	48.95
d_{z^2}	trans	0.66614	22.82	1.85	3.03	52.72	13.40	66.13
	cis	0.46613	28.35	4.35	2.87	7.82	33.20	44.24
	eclipsed	-0.00463	22.81	4.05	3.68	13.99	46.80	64.12

Table 4.4: Bond distances in optimized geometries; experimental values are in parenthesis; * indicates disorder						
Isomer	**Mo=O**	**Mo-N (trans Ot)**	**Mo-N (trans Cl)**	**Mo-Cl (trans N)**	**Mo-Cl (trans O/S)**	**Mo-OPh/ Mo-S(CH)**
cis-(LO)$Mo^{V}OCl_2$	1.70	2.33	2.21	2.37	2.42	1.96
trans-(LO)$Mo^{V}OCl_2$	1.72 (1.66)	2.26 (2.16)	2.26 (2.21)	2.39 (2.35)	2.39 (2.38)	1.99
cis-L1O $Mo^{V}OCl_2$	1.71	2.38	2.19	2.35	2.39	1.95 (1.96)
trans- L1O $Mo^{V}OCl_2$	1.72 (*)	2.22 (*)	2.22 (*)	2.36 (*)	2.36	1.99 (1.96)
cis-(L3S) $Mo^{V}OCl_2$	1.7 (*)	2.42 (2.36)	2.22 (2.24)	2.37 (*)	2.43 (2.38)	2.43 (2.36)
trans-(L3S) $Mo^{V}OCl_2$	1.73	2.25	2.25	2.37	2.37	2.53

Electronic Structure, Stability and Mechanistic Calculations in cis and trans-(LO)$MoOCl_2$ and cis and trans-(L3S)$MoOCl_2$

Because the X-ray crystal structures are not available for *cis*-(LO)$MoOCl_2$ or *trans*-(L3S)$MoOCl_2$, we have used a computational approach to understand the influence of the trans effect on the geometry and stability of these complexes. The most important bond distances in the optimized geometries of all of the six possible structures (i.e., *cis* and *trans*-(LO)$MoOCl_2$, *cis* and *trans*-(L1O)$MoOCl_2$ and (L3S)$MoOCl_2$) are presented in **Table 4.4**.

A comparison of Prof. Carrano's X-ray determined structures with the optimized geometries shows them to be in good agreement. When the trans effects in both isomers were compared as a function of the heteroatom (i.e., sulfur in (L3S)$MoOCl_2$ and oxygen in (L1O)$MoOCl_2$ or (LO)$MoOCl_2$), the heteroatom in (L3S)$MoOCl_2$ experiences a 5-fold larger bond elongation than that in either (L1O)$MoOCl_2$ or (LO)$MoOCl_2$. More explicitly, the Mo-S bond in the (L3S)$MoOCl_2$ complex has been calculated to be elongated by nearly 0.1 Å on going from the cis to the trans isomer, while the analogous Mo-O(Ph) bond changes only by 0.02 Å. Experimentally, the X-ray structure of *trans*-(LO)$MoOCl_2$ demonstrates that the difference between Mo-O(Ph) bonds cis or trans to an oxo group is even less (essentially zero). Similarly, the Mo-Cl bond distances, in the cis and trans isomers of (L3S)$MoOCl_2$, differ by 0.06 Å, while that difference is only 0.03 Å for the two isomers of (L1O)$MoOCl_2$ and (LO)$MoOCl_2$. On the other hand, the Mo=O distances for all six complexes remain essentially invariant. The calculated geometries of the cis and trans isomers of (L3S)$MoOCl_2$, (L1O)$MoOCl_2$ and (LO)$MoOCl_2$ complexes are in good agreement with crystallography. Accordingly, *cis*-

(L3S)$MoOCl_2$ is calculated (using the unrestricted DFT approach) to be 36.4 kJ/mol more stable than the trans isomer, while *trans*-(LO)$MoOCl_2$ was calculated to be 4.7 kJ/mol more stable than the cis isomer and *trans*-(LO)$MoOCl_2$ was calculated to be 8.4 kJ/mol more stable than the cis isomer. **Table 4.5a** and **4.5b** list the atomic orbital contribution analysis for selected molecular orbitals in the (L3S)$MoOCl_2$, and (LO)$MoOCl_2$ complexes. In general the semioccupied orbital has a predominant molybdenum $4d_{xy}$ character and as such is in good agreement with both ligand-field theory and experimental data. In addition, this orbital always experiences antibonding interactions with the in-plane π-orbitals of the equatorial chlorine atoms. More importantly, the difference in the reduction potential between the cis and trans isomers of (LO)$MoOCl_2$ (as experimental data on both isomers of (L3S)$MoOCl_2$ are not available) are in qualitative agreement with the energy difference between their calculated, α-set, LUMO orbitals. Indeed, the energy difference between these orbitals, for the cis and trans isomers of (LO)$MoOCl_2$, was calculated to be 193 mV, in good agreement with the experimentally observed 207 mV difference. While the calculated 200 mV difference in between the two isomers of (L1O)$MoOCl_2$ are in good agreement with the experimentally determined 216 mV. Similarly, the calculated difference in the reduction potential of the cis and trans isomers of (L3S)$MoOCl_2$ is found to be 66 mV, with the cis isomer being more easily reduced. It should be noted that accurate predictions of the redox potential require a rigorous treatment of the complete redox cycle and the inclusion of solvation effects[55]. Due to the spin-polarization effect, we have limited the preceding discussion to the spin-unrestricted calculations; however, the electronic structures calculated by the restricted open formalism are discussed in the following text.

Table 4.5a: Composition of the α-spin (LO)$MoOCl_2$ molybdenum d manifold.								
Orbital	Geometry	E, eV	% Mo	% O_t	% Cl	% OPh	% N	% LO
d_{xy}	trans	-3.161	81.4	0.0	13.4	0.4	1.1	5.2
	cis	-3.013	81.0	0.1	9.3	4.6	0.4	9.6
d_{xz}	trans	-2.533	71.2	13.0	2.8	2.0	1.1	13.1
	cis	-2.771	69.8	14.2	5.0	0.1	2.2	11.0
d_{yz}	trans	-2.202	69.7	13.1	2.8	5.1	0.6	14.3
	cis	-2.446	71.1	12.1	5.8	3.5	0.5	11.1
$d_{x^2-y^2}$	trans	-1.171	56.4	0.5	17.8	0.0	11.8	25.2
	cis	-.892	48.8	0.3	13.5	4.6	7.5	37.4
dz^2	trans	0.651	30.1	4.0	5.2	1.4	2.6	60.7
	cis	0.418	40.3	6.8	5.8	3.3	7.1	47.1

The calculated LUMO is predominantly molybdenum $4d_{xz}$ in character, and the predicted ordering of the metal orbitals is consistent with ligand field theory for tetragonally distorted octahedral geometry. Accordingly, the next metal-based orbital is the $4d_{yz}$. Interestingly, in all the cases, the molybdenum $4d_{x^2-y^2}$ orbital is delocalized between two molecular orbitals ($d_{x^2-y^2}$ + L and L + $d_{x^2-y^2}$) with the first orbital having a larger metal contribution except in *cis*-(LO)$MoOCl_2$, where the $d_{x^2-y^2}$ + L orbital is lower in energy than the L + $d_{x^2-y^2}$. Last, the $4d_{z^2}$ orbital has been found to be the highest energy orbital within the d-manifold.

Table 4.5b: Composition of the α-spin (L3S)$MoOCl_2$ complexes molybdenum d manifold.								
Orbital	Geometry	E, eV	% Mo	% O_t	% Cl	% SCH	% N	% L3S
d_{xy}	trans	-3.172	82.4	0.0	13.0	0.6	1.0	4.6
	cis	-3.187	81.7	0.0	11.8	2.7	0.5	6.5
d_{xz}	trans	-2.646	71.4	12.6	2.9	4.9	1.5	13.1
	cis	-2.700	69.9	13.7	0.1	5.0	2.5	11.4
d_{yz}	trans	-2.520	65.8	12.6	5.9	7.5	0.8	15.7
	cis	-2.433	68.0	12.5	5.4	6.0	0.4	14.1
$d_{x^2-y^2}$	trans	-1.123	51.0	0.3	16.9	0.0	12.3	31.7
	cis	-1.032	48.8	0.3	13.8	11.7	6.3	37.1
dz^2	trans	0.311	39.9	5.8	4.4	12.0	4.7	49.9
	cis	0.201	52.8	6.8	5.8	3.9	7.9	34.6

Taken together, all of the predominantly molybdenum d-orbitals were found to give the following order of increasing energy: $4d_{xy} < 4d_{xz} \sim 4d_{yz} < 4d_{x^2-y^2} < 4d_{z^2}$. Another interesting feature revealed by the calculations is that the highest doubly occupied orbital, for all four complexes, had almost purely heteroscorpionate π-orbital character with significant contributions arising from the heteroscorpionate sulfur or oxygen atom. In contrast, the lower energy orbitals are found to be a mixture of the heteroscorpionate ligand and chlorine atom orbitals. Interestingly, the ligand π-acceptor orbitals were found between the molybdenum $4d_{yz}$ - $4d_{x^2-y^2}$ and $4d_{x^2-y^2}$ - $4d_{z^2}$ orbitals suggesting that low-lying scorpionate π-acceptor orbitals may play a role in defining the electronic structure of these complexes.

EPR Spectroscopy:

The X-band EPR spectra of the *cis*- and *trans*-(L1O)$MoOCl_2$ complexes are shown in **Figures 4.9** respectively while **Table 4.7** provides the simulated g and A tensors for both the isomers. **Table 4.8** provides both the experimentally derived and theoretically derived ligand field energies for the dπ orbitals and A-tensors for the *cis*- and *trans*- (L1O)$MoOCl_2$ complexes. The dotted lines on the spectra represent the computer simulations using **Equation 4.1**. The spectra show the nuclear hyperfine features from ^{95}Mo and ^{97}Mo isotopes (combined percent natural abundance of 24.8) with nuclear spin (I) 5/2. Although the observed g and A values are in agreement with the previously reported values for molybdenum (V) containing enzymes and model complexes,[56] the g and A tensors for *cis*-(L1O)$MoOCl_2$ are found to be misaligned by 20º and 37º in the xy (α_{xy}) and xz (β_{xz}) plane, respectively. On the other hand, a misalignment by an angle of 35º was only observed in the xy plane (β_{xy}) for *trans*-(L1O)$MoOCl_2$. Indeed, a similar misalignment of the g and A tensor for other low symmetry molybdenum complexes has been reported previously.[57,58,59] Interestingly, the largest component of A (A_z) was found to be associated with the largest component of g (g_z) in *cis*-(L1O)$MoOCl_2$, while the largest A value (A_z) corresponds to the lowest value in g (g_z) for *trans*-(L1O)$MoOCl_2$.

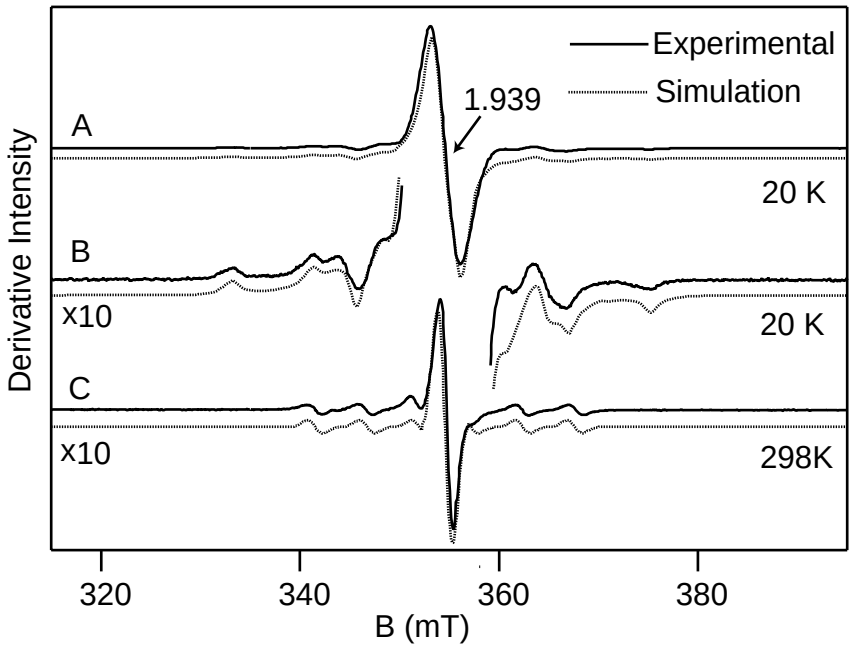

Figure 4.9. EPR spectra in *cis*-[(L1O)$MoOCl_2$] A I=1/2 ; B I=5/2 and C room temperature spectrum

Table 4.7: EPR parameters for Oxo Molybdenum (V) complexes.

	g				
Complex	**X**	**y**	**z**	**av**	
cis-L1OMoOCl_2	1.9291	1.9411	1.9468	1.9390	
trans-L1OMoOCl_2	1.9652	1.9566	1.9462	1.956	
	A (^{95}Mo, ^{97}Mo)				
Complex	**x**	**y**	**z**	**av**	**(α_{xy}, β_{xz})**
cis-L1OMoOCl_2	104.97	95.8	225.9	142	20, 37
trans-L1OMoOCl_2	95.31	104.16	225.47	141.6	0, 35

Table 4.8: Comparison of experimental and calculated parameters from EPR experiments and calculations, unless otherwise noted, numbers are from reference 60

	cis-(L1O)$MoOCl_2$		*trans*-(L1O)$MoOCl_2$	
	Experiment	Calculated	Experiment	Calculated
ΔE_{x2-y2} (cm^{-1})	16,902	39,835 (37)	23,118	40,105 (37)
ΔE_{xz} (cm^{-1})	10,981	20,265 (37)	17,966	28,954 (37)
ΔE_{yz} (cm^{-1})	11,818	21,723 (37)	14,573	29,926 (37)
A_x (MHz)	105	115.41	95.31	104.47
A_y (MHz)	95.8	112.83	104.16	109.68
A_z (MHz)	225.9	333.5	225.47	308

The room temperature spectra of the two samples, shown in **Figure 4.9,** were recorded immediately after thawing the samples. Spectra recorded after 40 minutes of incubation at room temperature showed an approximate 40% conversion of *cis*-(L1O)$MoOCl_2$ to *trans*-(L1O)$MoOCl_2$, which is consistent with the rates observed in the optical spectra.

Theoretical EPR Calculations:

The experimental g- and A-values and calculated g- and A-values (from the DFT approach which implemented basis sets 1 and 2) for the *cis*- and the *trans*-(L1O)$MoOCl_2$ isomers are presented in **Table 4.9**, along with experimentally determined values for the enzyme. Furthermore, the calculated g-values for the average x-ray determined geometry's of the *cis*- and the *trans*-(L1O)$MoOCl_2$ complexes follow the experimentally observed trends for the trans-isomer, $g_1 > g_2 > g_3$, while the agreement for *cis*-(L1O)$MoOCl_2$, $g_1 < g_2 \approx g_3$, was found to be poor. On the other hand, the trends in the calculated g-values using the optimized geometries for the cis- and the trans- (L1O)

isomers are in a good agreement with experimental observations. Interestingly, small deviations from C_s symmetry to C_1 symmetry, in the case of *trans*-(L1O)$MoOCl_2$, lead to an appreciable change in the calculated g-values with the best experimental agreement resulting from the C_1 symmetry calculations (**Table 4.9**).

Although both basis sets express good internal consistency, basis set 1 provides a slightly closer quantitative agreement with experimental data for the (L1O)$MoOCl_2$ complexes. Thus, the computationally expensive relativistic calculations were conducted using basis set 1 for the (L1O)$MoOCl_2$ complexes. However, the incorporation of the relativistic effects into the core Hamiltonian for (L1O)$MoOCl_2$ did not significantly change either the qualitative or quantitative agreement with the experimental data (i.e., the g- and A_{aniso} values). However, relativistic effects allowed the A_{iso} (Fermi contact term) values to be expressed in a reasonable range. Interestingly, the A-values that were calculated using the DFT approach were found to be much less sensitive than the g-values with respect to the starting geometry. Correspondingly, a good agreement between the calculated and experimental anisotropic contributions to the A-tensor values have been observed for both the x-ray determined and DFT optimized geometries for *cis*- and *trans*-(L1O)$MoOCl_2$. In contrast to the g-values, slightly better agreement between the experimental and calculated A-tensor values for (L1O)$MoOCl_2$ was observed when basis set 2 was employed.

Table 4.9: Comparison of EPR parameters for Synthetic Complexes and DMSOR Enzyme Preparations							
Compound	**Method**	**g_1**	**g_2**	**g_3**	**g_{av}**	**Anisotropy**	**Rhombicity**
cis-(L1O)$MoOCl_2$							
	exp	1.929	1.941	1.947	1.939	0.0177	0.322
	opt-DZVP-Resc	1.891	1.899	1.901	1.897	0.0104	0.181
	Ligand Field 1	1.912	1.952	1.988	1.951	0.0763	0.465
	Ligand Field 2	1.905	1.918	1.944	1.922	0.0389	0.686
trans-(L1O)$MoOCl_2$							
	exp	1.946	1.957	1.965	1.956	0.0190	0.453
	C_s opt-DZVP-Resc	1.925	1.927	1.944	1.932	0.0191	0.885
	C_1 opt-DZVP-Resc	1.927	1.931	1.938	1.932	0.0111	0.698
	C_s Ligand Field 1	1.955	1.972	2.005	1.977	0.0500	0.642
	Ligand Field 2	1.962	1.969	1.974	1.968	0.0119	0.487
cis-$MoOCl_3$(bpy)	Experimental [61]	1.938	1.953	1.968	1.968		
trans- $MoOCl_3$(bpy)	Experimental [58]	1.931	1.944	1.971	1.944		
DMSOR wild type 1	Experimental [9a]	1.965	1.981	1.992	1.979	0.0279	0.397
DMSOR wild type 2	Experimental [9a]	1.965	1.982	1.992	1.979	0.0266	0.379
DMSOR high g unsplit	Experimental [58]	1.961	1.983	1.991	1.978	0.0238	0.160
DMSOR high g split	Experimental [58]	1.967	1.982	1.992	1.980	0.0249	0.420
DMSOR DMS treated	Experimental [62]	1.963	1.982	1.986	1.977	0.0233	0.175
DMSOR $BV^{\bullet}$ treated	Experimental [59]	1.967	1.981	1.992	1.979	0.0247	0.425
DMSOR	Experimental [9b]	1.962	1.984	1.991	1.979	0.0288	0.239
DMSOR low g type 1	Experimental [63]	1.956	1.969	1.970	1.964	0.0142	0.169
DMSOR low g type 2	Experimental [60]	1.936	1.954	1.976	1.955	0.0400	0.548
DMSOR high-g unsplit type 1	Experimental [60]	1.961	1.983	1.991	1.978	0.0295	0.271
DMSOR high-g unsplit type 2	Experimental [60]	1.9627	1.9826	1.9865	1.977	0.0238	0.164
DMSOR borohydride reduced	Experimental [60]	1.9625	1.9658	1.9794	1.969	0.0169	0.800
DMSOR high-g Split	Experimental [60]	1.961	1.977	1.988	1.975	0.0270	0.410

However, in all (L1O)$MoOCl_2$ calculations, the contact Fermi isotropic contribution was underestimated by approximately a factor of two. On the other hand, excellent agreement between the calculated and experimental isotropic contact shifts in (L1O)$MoOCl_2$ could be achieved through the incorporation of the relativistic effects. Finally, the calculated Euler angles α_{xy}, β_{xz} for the *cis*-(L1O)$MoOCl_2$ complex were found to be less axial than those found in the *trans*-(L1O)$MoOCl_2$ isomer. In addition, the calculated Euler angles α_{xy}, β_{xz} for the *cis*-(L1O)$MoOCl_2$ were found to be in close agreement with the experimental data while the calculated Euler angle β_{xz} for the trans-(L1O)$MoOCl_2$ isomer was underestimated when restricted to C_s symmetry. Moreover, significant improvement in the *trans*-(L1O)$Mo^{V}OCl_2$ Euler angle β_{xz} could be achieved, without compromising the agreement in the Euler angle α_{xy}, by reducing the starting symmetry to C_1.

Discussion

Electronic Structures of the (L1O)$MoOCl_2$ Complexes.

In general, electronic structure calculations of transition-metal complexes are carried out with simplified ligand architectures.[49,64,65,66] Although simplified ligand architectures are computationally less expensive, they were not able to profile our system accurately. In fact, when these approximations were applied to the cis and trans isomers, the cis isomer was found to be more stable than the trans. Therefore, we conducted all electronic structure calculations with near-complete ligand architecture, with only the distal methyl groups excluded. In addition, a large basis set for the molybdenum atom was employed for all calculations. Although this strategy increased the computational

requirements, it revealed a number of differences in the electronic structures compared to those obtained by calculations conducted on simplified ligand architectures.[67] As expected, the molybdenum metal d-fold splitting follows the order $d_{xy} < d_{xz} \sim d_{yz} < d_{x^2-y^2} < d_{z^2}$, with d_{z^2} being the most destabilized orbital. The contribution of the $(L1O)^-$ ligand to the destabilization of the dz^2 orbital is revealed from the Walsh-like diagram for the cis, eclipsed , and trans geometries **(Figure 4.8a).** A higher destabilization of the dz^2 orbital is observed for the trans isomer and is due to the negative charge of the phenolic oxygen atom. As discussed earlier, the deviation of the molybdenum atom from the *xy* plane reduces the L^{σ} Mo overlap and thus stabilizes this orbital with respect to the dz^2 orbital. The composition of the $d_{x^2-y^2}$ orbital is clearly indicative of significant mixing between the metal-based orbitals and the orbitals from the atoms of the $(L1O)^-$ ligand. A similar situation has recently been reported for a series of molybdenum complexes with tetrathiophenolates.[64a,65c] In agreement with the strength of pyrazole π orbitals,[68] several low-lying pyrazole orbitals could be located within the metal manifolds by DFT calculations **(Figure 4.8a** and **Figure 4.8b)**. Similar situations have been described previously.[69] This observation suggests that, for electronic structure calculations, it is important to use geometries that closely resemble the actual architecture instead of simplified or truncated versions. DFT calculations on simplified models with identical basis sets, where pyrazole and phenolate rings are represented by ammonia and methoxide groups, respectively, show poor agreement with the experimental data. As mentioned earlier, these calculations show the cis isomer to be more stable than the trans. Bonding of the terminal oxygen to molybdenum has been intensely investigated.[64b,65c,48,70] The molybdenum-to-oxygen terminal bonds consist of a σ

interaction (between the O p_z orbital and the Mo d_z^2 orbital) and two π interactions (between the O p_x and p_y orbitals and the Mo d_π orbitals). A similar orbital picture can be used to describe the bonding between the molybdenum atom and the axial (axial to the terminal oxo group) donor atom. Stronger π and σ interactions with the axial donor strongly destabilize the d_z^2 and the d_π orbitals of molybdenum. In the trans isomer, the axial oxygen from the $(L1O)^-$ ligand, being a stronger σ and π donor than nitrogen in the cis isomer, destabilizes both the d_z^2 and the d_π orbitals by 0.2 and 0.5 eV, respectively **(Figure 4.8a)**. As a result, the Mo=O bond is weakened in the trans isomer. This situation is manifested in the Mo=O stretching frequencies in the two isomers: in the cis isomer, the Mo=O bond vibrates 14 cm^{-1} higher in energy than does the trans isomer. In the eclipsed geometry, on the other hand, the d_z^2 orbital is destabilized only by the terminal oxo ligand; this destabilization enhances the energy difference between the d_x^2-$_y^2$ and dz^2 orbitals to more than 1 eV **(Figure 4.8a).** It is instructive to point out that the redox orbital in oxo- Mo(V) complexes is primarily composed of the molybdenum d_{xy} orbital, with large contributions from the equatorial donor atoms.[64a,71,72] The antibonding interaction with equatorial chlorine atoms contributes nearly 30% to the HOMO of the trans compound; however, this contribution is smaller in the cis and the eclipsed geometries (~11% for cis and ~14% for eclipsed isomers, respectively). For both the cis and eclipsed geometries, the contribution from the L1O- ligand is increased. In the cis isomer, the antibonding interaction due to the phenolic group of the L1O- ligand is ~36%. Such effective mixing between the d_{xy} and ligand π orbitals has been noted for the oxo-Mo(V) complexes coordinated by thiolate donors.[64a,66] The net result of this interaction is the overall destabilization of the half-filled HOMO in the cis isomer by

~0.6 eV relative to the trans isomer. This destabilization is consistent with the observed position of the reductive and oxidative couples for the cis isomer. Indeed, experimentally, a difference of ~100 mV was observed between oxidative couples of the cis and trans isomers, while a difference of 216 mV was observed for the reductive couples. In contrast to the equatorial-donor-atom contribution to the HOMO, the contribution from the axial donor (axial to the terminal oxo group) contributes negligibly to this orbital. Thus, from an electronic point of view, the six-coordinate complexes with heteroscorpionate ligands behave like square-pyramidal pentacoordinate complexes (e.g., tetrathiolate complexes of molybdenum, where the metal center is coordinated by four equatorial thiolato sulfur atoms). The same description also holds for the more popular hydrotris(3,5-dimethylpyrazolyl)borate ligand (Tp^{Me2}). Therefore, it is evident that, both experimentally and computationally, the trans isomer is more stable than the cis isomer. The increased stability of the trans isomer may be accounted for by two distinct arguments involving electronic and steric components. First, the electronic structural calculations demonstrate that the half-filled molecular orbitals of the cis and trans isomers differ significantly in both their compositions and energetic properties. The cis isomer possesses a relatively strong antibonding interaction between the molybdenum d_{xy} orbital and the π orbitals of the phenolato oxygen atom; however, such an interaction is not present in the trans isomer. This interaction raises the energy of the HOMO in the cis isomer. In addition to the electronic factor discussed above, there is a steric component that accounts for the higher stability of the trans isomer. In the trans isomer, a strong trans influence of the terminal oxo group elongates the molybdenum- phenolic oxygen bond. As a consequence of this elongation, the bulky *t*-Bu group is positioned farther from the

methyl groups of the pyrazol rings. This stereochemical arrangement in the trans isomer makes the molybdenum center less crowded and thus more stable. In an attempt to fully clarify the importance of this steric factor, the stability of the cis and trans isomers was calculated at the semi-empirical (PM3) level with and without the bulky alkyl groups **(Figure 4.10)**. By computation, it was determined that steric considerations were accountable for only about 20% of the relative stability of the trans isomer over the cis isomer and as such indicate that electronic factors play the dominant role in controlling the stability.

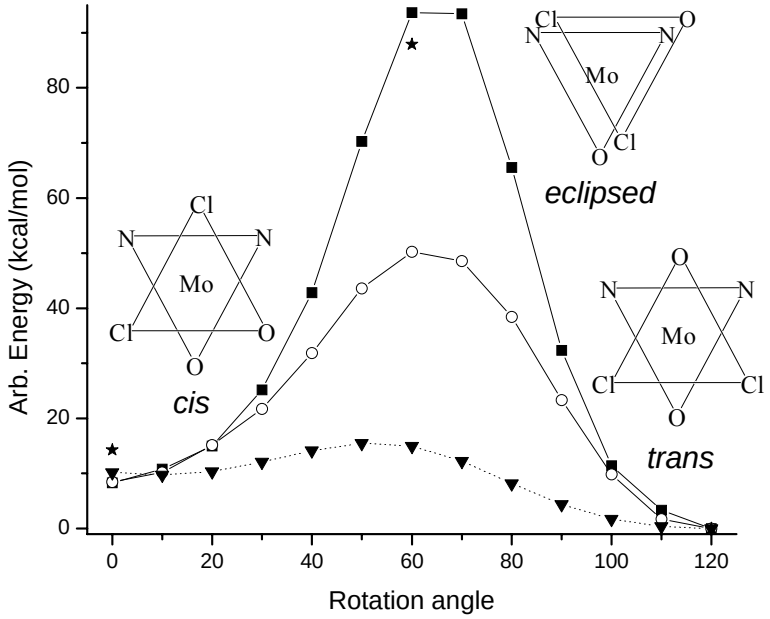

Figure 4.10. Calculated energy profile for the twist mechanism. The top trace represents the calculation with no optimization of the methyl group position. The middle trace represents the energy profile when the methyl groups are placed at energetically favorable positions. The bottom trace represents the energy profile without the t-Bu and methyl groups. The asterisks represent energy calculated by the B3P86 DFT method, while other calculations were done at the semi-emperical (PM3) level.

In further investigating the electronic effects it was found that by simply changing the donor atom in an otherwise isoelectronic, isosteric, and isostructural L=(N_2X) tripodal ligand system, the relative stability of the geometric isomers of [(L)$MoOCl_2$] complexes changes. In the previously mentioned case, (where X =$O_{phenolate}$), the trans isomer is the more stable than the cis isomer. On the other hand, when X= $S_{thiolate}$ the cis isomer enjoys greater stability over the trans isomer. One obvious question is concerned with the origin of this effect. The structural trans effect is well known and widely evoked in oxo-molybdenum chemistry. Bond lengths between Mo and atoms trans to the very tightly bound oxo group are usually extensively elongated. For example, the Mo-N_{trans} distances (trans to the oxo group) in [(L3S)$MoO(SPh)_2$], [(L3S)MoO(bdt)], [(Tp)$MoO(SPh)_2$], and [(Tp)MoO(bdt)] are 0.2-0.4 Å longer than the corresponding Mo-Ncis (cis to the oxo group). Similarly, the calculated Mo-S_{trans} (trans to the oxo group) distance in *trans*-[(L3S)$MoOCl_2$] is 0.1 Å longer that the Mo-S_{cis} (cis to the oxo group) distance in *cis*-[(L3S)$MoOCl_2$]. On the other hand, the expected trans elongation is calculated to be small in *trans*-[(LO)$MoOCl_2$], and crystallographically. Interestingly, the latter is a rare example of an oxo-molybdenum complex containing both cis and trans phenolate groups, thus providing an internal reference for evaluating the trans effect induced by the terminal oxo-group. In the case of [(L3S)$MoOCl_2$], the calculations suggest a difference in the α-LUMO, the redox orbital, of the cis to the trans isomer of ~66 mV. Although only the cis isomer has been isolated for [(L3S)$MoOCl_2$], it is reasonable to suggest the corresponding trans isomer would be more difficult to reduce, a behavior experimentally verified for [(L1O)$MoOCl_2$] where the cis isomer is ~213 mV more difficult to reduce than the trans isomer. The reasons for this assumption are 2-fold. First, in all cases, the

redox orbital (d_{xy} orbital) has a significantly greater heteroatom character in the cis isomer relative to the trans, while in the trans isomer the redox orbital has a greater chlorine atom character. Second, the energy difference between the d_{xy} orbitals of the cis and trans isomers of [(L3S)$MoOCl_2$] are smaller than those observed in the [(LO)-$MoOCl_2$] or [(L1O)$MoOCl_2$] complexes.

Theoretical Calculation of EPR parameters.

It is clear that the calculated g-values for the cis-isomer, using the X-ray geometry, are not in good agreement with the experimental data. However, the observed disagreement between the experimental and calculated values may possibly originate from the use of average geometry determined by X-ray crystallography for both the cis- and the trans-isomers. Indeed, the optimized geometries suggest the presence of the small trans-effect for the phenolic oxygen in the cis- and trans- isomers (~0.03 Å); while this effect is more prominent for the pyrazole nitrogen (~0.19 Å). Thus using the optimized geometry for the cis-isomer clearly improved the results (**Table 4.7 and 4.8**). In addition, the small rhombicity observed in the cis-isomer was also reproducible when the non-relativistic DFT approach was used with basis set 1 and 2, while less satisfactory agreement was obtained when compared to the relativistic calculations. In the case of the trans-isomer, the calculated g-values for the optimized C_s and C_1 geometries agree well with the experimental data, however, the rhombicity was best reproduced when the C_1 geometry and basis set 1 was used. Furthermore, the trends in the average g-values were also reproduced through the DFT calculations, to the extent that the average g-values for the cis-isomer were found to be smaller than in the trans-complex. When a basis set with

a very flexible valence and core region was employed, such as basis set 1 and 2, good agreement between the calculated and experimental anisotropic contributions to the A-tensor values were achieved (**Table 4.8**). Although slightly better agreement between the experimental and calculated anisotropic values were obtained for the cis-isomer relative to the trans-complex. This trend is the same the calculated Euler angles α_{xy}, β_{xz}, where better agreement has been observed in the cis-isomer. As previously mentioned, reducing the starting geometry to C_1 significantly improves this β_{xz} value for *trans*-(L1O)$MoOCl_2$ without an appreciable change in the Euler angle α_{xy}.

Mechanism of Isomerization.

In general, the mechanisms of geometric isomerization in coordination complexes have been studied in detail; however, such studies on oxomolybdenum complexes are very rare.[73] Even rarer is geometric isomerization in oxo-molybdenum complexes where three sites are occupied by a facially coordinating ligand, and to our knowledge the mechanisms of such isomerization reactions have not been reported in detail. In general, there are two major processes by which isomerization reactions may proceed: the twist mechanism and the dissociative mechanism. In the case of the twist mechanism, the geometric rearrangement originates through a rotation about a pseudo-three-fold axis at the middle of a trigonal face (**Figure 4.10**). In contrast, the dissociative mechanism (**Figure 4.11**) proceeds via geometric rearrangements through breaking of metal-ligand bonds, followed by reconstitution at a stereochemically different position relative to the first. With these possible mechanisms, two distinct types of dissociative interactions may be immediately ruled as unlikely possibilities.

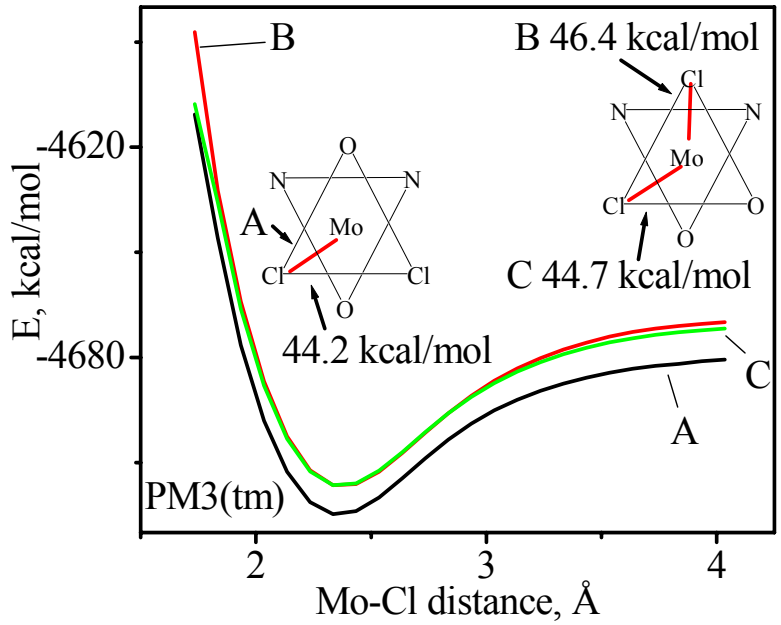

Figure 4.11. Calculated Bond dissociation in *trans*-(L1O)MoO^{V}Cl$_2$

First, it is unlikely that a metal-ligand bond from the tridentate ligand will be broken because of a high entropic penalty. Second, it is improbable that the terminal oxo bond (a metal-ligand multiple bond) will dissociate in dry organic solvents. Thus, the only probable dissociative pathway, if this mechanism is operable, must involve the dissociation of a metal-halide bond. In addition, variable-temperature kinetic measurements demonstrate a negative entropy of activation, which is suggestive of a more ordered transition state relative to that of the cis isomer. The negative entropy provides evidence that the bond dissociation pathway may not be a likely mechanism. Unfortunately, the magnitude of the entropy of activation is too small to definitely assign as a twist mechanism. To understand the relative ease of the two mechanistic possibilities, the energy associated with the two processes has been computed at the PM3

level. The energy profiles of the two processes are shown in Figures 9 and 10. For the twist mechanism, the OCl_2 face, consisting of the axial terminal-oxo group and the two equatorial chlorine atoms of the octahedron, was rotated from 0 to 120° with a 10° interval along the pseudo-three-fold axis. As expected, the 60° rotation provides an eclipsed conformation with the highest energy: 356.8 kJ/mol (307.9 kJ/mol from DFT calculations). To determine the most favorable orientation of the proximal methyl groups, they were rotated individually and the total energy of the molecule was calculated for each conformer. The results are summarized in **Figure 4.8a** and **Figure 4.8b.** The calculations suggest that the orientation of the methyl groups of the pyrazol ring can significantly alter the energy of the process. When the most favorable orientation of the methyl groups is incorporated into the calculation, the energy of activation is reduced to 174.6 kJ/mol. Interestingly, the difference in energy between the two isomers calculated both at the semiempirical and DFT levels is in excellent agreement with that observed from the electrochemical measurements. The influence of the steric interaction between the bulky *tert*-butyl and methyl groups of the (L1O)H ligand was assessed by calculating the energies of different conformers along the reaction pathway. In these calculations, a truncated model system was used where all bulky groups were omitted**.** Using this methodology, an activation barrier of 22.2 kJ/mol was estimated, indicating that the steric interaction is the main contributor to the barrier for the twist mechanism. Similarly, a possible dissociative mechanism was also probed by calculating the bond dissociation energies for the Mo-Cl bond at the semiempirical PM3 level (**Figure 11**).[74] Although the calculated energies are only estimation, they are slightly higher than those found for the twist mechanism. As in the usual case, the calculations described above were carried out

purely in the gas phase and as such do not account for the solvent effects. One direct consequence of this approximation is that the calculated energy barriers, although comparable to other calculated values, are in poor agreement with experimentally determined energy barriers. Thus, in the absence of other supporting evidence, these calculations cannot be used to determine accurately the relative fitness of either mechanism because of poor resolution of the calculated energies. To probe the possibility of a bond dissociation mechanism, the isomerization reaction has been further investigated in the presence of excess tetraalkylammonium salts. We hypothesized that if the reaction involved the dissociation of the metal-halide bond the addition of large excesses of halides during the cis-to-trans conversion would result in the formation of mixed-halide trans isomers that could be easily detected by mass spectrometry **(Figure 4.7** and **Chart 4.1)**. As has been previously mentioned, only the $[(L1O)Mo^{V}OCl_2]X$ type mixed halides were observed in solution when the isomerization reaction was carried out in the presence of excess alkylammonium halides. The significance of this finding is that if the reaction were to proceed via a dissociative mechanism the excess halide should induce the formation of mixed-halide species (e.g., $[(L1O)Mo^{V}OX_2]Cl^-$, $[(L1O)Mo^{V}OXCl]X^-$). It should be noted that mass spectrometry cannot differentiate between linkage isomers (e.g., $[(L1O)MoOCl_2]Br$ and [(L1O)MoOClBr]Cl). Indeed, a peak cluster resulting from [(L1O)MoOClBr]Cl would indicate a breaking of the Mo-Cl bond. If this were the case, one would expect to observe the formation of peaks attributable to the formation of $[(L1O)MoO_2Br]Br$ or $[(L1O)MoOClBr]^-$ Br; however, no such peak was detected. Similar results were also obtained in experiments with excess nBuNI. We have already mentioned that both *cis*- and *trans*-$(L1O)MoOCl_2$ are oxidized

under mass spectrometric conditions to generate the dioxo-molybdenum species $[(L1O)Mo^{VI}O_2]^-$ Cl. Oxidation under mass spectrometric conditions is not uncommon and has been noted earlier.[75] Furthermore, in all cases and under identical conditions, the intensity of the peak cluster due to $[(L1O)Mo^{VI}O_2Cl]X^-$ (X is a halogen) is higher than that of due to $[(L1O)Mo^{V}OCl_2]X^-$ for the cis isomer compared to that for the trans isomer. This observation is in agreement with the electrochemical data. We are aware that one cannot prove a mechanism; rather, one may only disprove alternative possibilities. In this case, the preponderance of the evidence (i.e., negative entropy, the absence of halide incorporation into the coordination sphere, and quantum chemical calculations) is inconsistent with a dissociative mechanism. Thus, we believe that a twist mechanism is operative in the geometric isomerism.

Assuming that the energy of the *cis*-$(L1O)MoOCl_2$ is invariant, one would expect that less polar transition state structure be more stabilized in non-polar solvents and lead to faster rates while slower rates of reaction would be expected in polar solvents due to a lesser stabilization of the transition state. Thermodynamically, an opposite situation would be expected in that the formation of the more polar *trans*-$(L1O)MoOCl_2$ would be favored in polar solvents and provide a larger driving force than in non-polar solvents. In either case, the observed trend in the reaction rate cannot be explained adequately by a simple polarity argument. In general, many of the chemical and physical parameters that are defined for each solvent are applicable over only a narrower temperature range than that used in this study. Furthermore, the $\Delta S^{\ddagger}$ for *cis*-$(L1O)MoOCl_2$ was found to be inversely related to the solvent dielectric constant, such that higher dielectric constants provide for positive $\Delta S^{\ddagger}$ while the lower dielectric constants provide for negative $\Delta S^{\ddagger}$.

These results suggest a role of solvent assistance in the above defined twist mechanism, based not only upon the solvent dielectric but also upon the charge of the solvent donor atom. In the case of polar solvents, the transition state is clearly more ordered, and it is more disordered in non-polar solvents, but it is not possible to partition the solvent reorganization from the complex. It has been amply demonstrated that in heteroscorpionate as well as with the more symmetrical hydrotris(pyrazolyl) borate complexes, the Mo-N(pyrazole) bond trans to the Mo=O unit is significantly elongated compared to the equatorial Mo-N(pyrazole) bond. Although the crystal structures reflect the static stable picture, it is possible that the *trans*-Mo-N bond is a likely candidate for dissociation. Thus the most likely mechanism or the isomerization in non-polar solvents involves either a dissociation followed by a twist or a dissociation that is concurrent with a twist.

Summary

Implication to the Function of DMSO and Nitrate Reductase.

The dependence of the reduction potential on geometry is an important observation, demonstrating that the position of an oxygen or sulfur donor relative to the terminal oxo functions to modulate the reduction potential of the metal center**.** With respect to the mechanism of the molybdenum reductases, this situation leads to the provocative suggestion that the position of the serinato oxygen, or cystenato sulfur, relative to the terminal oxo may play a critical role in gating the electron-transfer process in the regeneration step. In fact, substrate-bound forms of DMSO reductase exhibit different O_t-Mo-O_{ser} angles when compared to the structure with unbound substrate. For

example, the O_t- Mo-O_{ser} angle in the DMSO-bound form of the *R. capsulatus* enzyme is 80°, while a much smaller angle is observed for the cacodoic acid-bound form of the *R. sphaeroides* enzyme. Our data suggests that the lower the angle, the easier it is to oxidize Mo(V), while the concomitant reduction becomes more difficult. This geometric flexibility ensures that electron transfer is gated as a function of active-site conformation. We call this proposal the serine-gated electron transfer hypothesis, or SGET. The mechanistic investigations reported here suggest that no bond-breaking is necessary for accomplishing such a geometric transformation. A similar kind of geometric alteration with a very low energy barrier has been proposed for the function of xanthine oxidase.[76] However, an alternate pathway involving the dissociation of one of the dithiolene S-donors may provide a driving force for a twist-type isomerization mechnanism. Indeed, it has been suggested that the dithiolene ligand may dissociate from the metal center as provided in the crystal structure of DMSOR from *Rhodobacter capsulatus.* Furthermore this dissociation was also proposed to account for the low and high g-forms of the isolated enzyme. Here we provide an alternative view for the existence of the high and low g forms of the enzyme, based upon geometric isomerism at the metal center. Furthermore we provide insight into the possible origin of the dissociated dithiolene as resulting from changes in the local dielectric through crystallization and purification procedures. Regardless, the data suggests that there may be significant entropic contributions to the reorganization of the proteins active site as a function of the local dielectric constant. This suggests that global changes in the protein matrix may introduce significant constriction or expansion of the enzyme active site volume, and influence the

movement for a coordinated serine or cysteine ligand during catalysis. Such a change then can influence the mechanism of the reaction or at the least the rate of the reaction.

In addition, the model investigation provides an electronic argument of the preferred geometry for the amino acid based donors in DMSO reductase and nitrate reductase, which is supported by the previously mentioned differences in the O-Mo-(O_{ser}/S_{cys}) bond angles in published crystal structures. Finally, when a mismatched coordination is created, via site-directed mutagenesis, the proteins are found to be either less active or inactive as compared to the wild type enzymes. Thus, when cysteine-207 (coordinated to molybdenum) in human sulfite oxidase is mutated to a serine, the enzyme loses its activity, and the extended X-ray absorption fine structure (EXAFS) reveals a trioxo-Mo center at the fully oxidized state[77,78]. In a similar type of experiment, when serine 147 (that coordinates to molybdenum) is mutated to a cysteine in DMSOR, the resultant enzyme is again 61-99% less reactive than the wild-type enzyme.[79] In light of the previously described SGET model, it is provocative to suggest that, in the mutated proteins, a mismatched geometry is produced upon coordination of amino acids with different donor groups. More explicitly, the fold of the protein may impart constraints upon the local flexibility at the active site to accommodate relatively small movements of coordinated amino acid donor ligands about that donor ligands preferred location in the coordination sphere. Thus in the mutant proteins, a more "trans-loving" ligand such as a serinato oxygen would be destabilized through O_{π}-d_{π} interactions arising from its exchange with the "cis-loving" cystenato sulfur and result in an inactive protein.

References

[1] Pilato, R.S.; Stiefel, E. I. In *Inorganic Catalysis*, 2nd ed.; Reedjik, J., Bouwman, E., Eds.; Marcel Dekker: New York, **1999**; pp 81-152.

[2] Enemark, J.H.; Young, C.G. *Adv. Inorg. Chem.* **1993**, 40, 1.

[3] Romao, M.J.; Knablein, J.; Huber, R.; Moura, J.J. *Prog. Biophys. Mol. Biol.* **1997**, 68, 121.

[4] Hatton, A.D.; Malin, G.; Turner, S.M.; Liss, P.S.; In *Proceedings of the International Symposium on DMSP and Related Sulfonium Compounds*, Eds: Kiene, R.P., Mobile Ala. **1996**, pp 405-412.

[5] **a)** Cobb, N.; ConradsT.; Hille, R. *J. Biol. Chem.* **2005**, 280, 11007-11017. **b)** Li, H-K.; Temple, C.; Rajagopalan, K. V.; Schindelin, H. *J. Am. Chem. Soc.,* **2000**, 122, 7673-7680. **c)** Raitsimring, A.M.; Astashkin, A.V.; Feng, C.; Enemark, J.H.; Nelson, K.J; Rajagopalan, K.V. *J. Biol. Inorg. Chem.* **2003**, 8, 95-104.

[6] **a)** Ridge, J.P.; Aguey-Zinsou, K-F., Bernhardt, P.V.; Hanson, G.R.; McEwan, A.G. *FEBS Letts.* **2004**, 563, 197-202. **b)** Ridge, J.P.; Aguey-Zinsou; Bernhardt, P.V.; Brereton, I.M.; Hanson, G.R.; McEwan, A.G. *Biochemistry* **2002**, 41, 15762-15769. **c)** McAlpine, A.S.: McEwan, A.G.; Bailey, S. *J. Mol. Biol.* **1998**, 275, 613-623.

[7] Sambasivarao, D.; Dawson, H.A.; Zhang, G.;Shaw, G.; Hu, J.; Weiner, J.H. *J. Biol. Chem.* **2001**, 276, 20167-20174.

[8] Baugh, P.E.; Garner, C.D.; Charnock, J.M.; Collison, D.; Davies, E.S.; McAlpine, A.S.; Bailey, S.; Hanson, G.R.; Lane, I.; McEwain, A.G. *J. Biol. Inorg. Chem.* **1997**, 2, 634.

[9] **a)** George, G.N.; Hilton, J.; Temple, C.; Prince, R.C.; Rajagopalan, K.V.; *J. Am. Chem. Soc.* **1999,** 121, 1256. **b)** George, G.N.; Hilton, J.; Rajagopalan, K.V. *J. Am. Chem. Soc.* **1996**, 118, 1113.

[10] **a)** Garton, S.D.; Hilton, J.; Oku, H.; Crouse, B.R.; Rajagopalan, K.V.; Johnson, M.K. *J. Am. Chem. Soc.* **1997**, 119,12906. **b)** Johnson, M.K.; Garton, S.D.; Oku, H. *J. Biol. Inorg. Chem.* **1997**, 2, 797.

[11] Bell, A.F.; He, X.; Ridge, J.P.;Hanson, G.R.; McEwan, A.G.; Tonge, P.J. *Biochemistry*, **2001**, 40, 440.

[12] **a)** Gruber, S.; Kilpatrick, L.; Bastian, N.R.; Rajagopalan, K.V.; Spiro, T.G. *J. Am. Chem. Soc.* **1990**, 112 8179. **b)** Kilpatrick, L. Rajagopalan, K.V.; Hilton, J.; Bastian, N.R.; Stiefel, E.I.; Pilato, R.S.; Spiro, T.G. *Biochemistry,* **1995**, 34, 3032.

[13] **a)** Benson, N.; Farrar, J.A.; McEwan, A.G.; Thompson, A.J. *FEBS Lett.* **1992**, 307, 169-72. **b)** Finnegan, M.G.; Hilton, J.; Rajagopalan, K.V.; Johnson, M.K. *Inorg. Chem.* **1993**, 32, 2616.

[14] **a)** Stewart, L. J.; Bailey, S.; Bennett, B.; Charnock, J.M.; Garner, C.D.; McAlpine, A.S. *J. Mol. Biol.* **2000**, 299, 593. **b)** Bennett, B.; Benson, N.; McEwan, A.G.; Bray, R.C. *Eur. J. Biochem.* **1994**, 225,321.

[15] **a)** Schindelin, H.; Kisker, C.; Hilton, J.; Rajagopalan, K.V.; Rees, D.C. *Science* **1996**, 272, 1615. **b)** McApline, A.S.; McEwan, A.G.; Shaw, A.L.; Bailey, S.J. *Biol. Inorg. Chem.* **1997**, 2, 690. Schindelin, F.; Loewe, J.; Huber, R.; Schindelin, H.; KIsker, C.; Knaeblein, J. *J. Mol. Biol.* **1996**, 263, 53. **c)** Knablein, J.; Dobbek, H.; Ehlert, S.; Schneider, F. *J. Biol. Chem.* **1997**, 378, 293. **d)** Sato, K.; Saski, H.; Okubo, A.; Tanokura, M.; Yamazaki, S. *S. Proc. Jpn. Acad. Ser. B.* **1997**, 73B, 30.

[16] Boyington, J.C.;Gladyshev, V.N.;Khanguklov, S.V.;Stadtman, T.C.; Sun, P.D. *Science* **1997**, 275, 1305-1308.

[17] **a)** Bray, R.C.; Adams, B.; Smith, A.T.; Bennett, B.; Bailey, S. *Biochemistry* **2000**, 39, 11258. **b)** Adams, B.; Smith, A.T.; Bailey, S.; McEwan, A.G.; Bray, R.C. *Biochemistry,* **1999**, 38, 8501.

[18] Arzoumanian, H.; Corao, C.; Krentzien, H.; Lopez, R.; Teruel, H. J.; *Chem. Soc., Chem Commun.* **1992**, 856.

[19] Sung, K-M.; Holm, R.H.; *J. Am. Chem. Soc.* **2001**, 123, 1931. **b)** Lim, B.S.; Holm, R.H. *J. Am. Chem. Soc.* **2001**, 123, 1920. **c)** Lim, B.S.; Sung, K-M.; Holm, R.H. *J. Am. Chem. Soc.* **2000**, 122, 7410. **d)** Lim, B. S.; Donahue, J. P.; Holm, R. H. *Inorg. Chem.* **2000**, 39, 263. **e)** Donahue, J.P.; Goldsmith, C.R.; Nadiminti, U.; Holm, R.H. *J. Am. Chem. Soc.* **1998**, 120, 12869. **f)** Donahue, J.P.; Lorber, C.; Nordlander, E.; Holm, R.H. *J. Am. Chem. Soc.* **1998**, 120, 3259. .

[20] Davie, S.R.; Rubie, N.D.; Hammes, B.S.; Carrano, C.J.; Kirk, M.L.; Basu, P. *Inorg. Chem.* **2001**, 40, 2632.

[21] Kirk, M.L. *ACS Symposium Series,* **2003**, 858, 340-357. **b)** Enemark, J.H.; Astashkin, A.V.; Raitsimring, A.M. *ACS Symposium Series,* **2003**, 858, 179-192. **c)** G.N. George, *JBIC, J. Biol. Inorg. Chem.* **1997**, 2, 790-796.

[22] Lee, K.K.; Fitch, A. A.; Lecomte, J.T.J.; Garcia-Moreno, B. E. *Biochemistry* **2002**, 41, 5656.

[23] Fitch, C. A.; Karp, D. A.; Lee, K. K.; Stites, W. E.; Lattman, E. E.; Garcia-Moreno, B. E. *Biophys. J.* **2002,** 82, 3289.

[24] Dwyer, J.J.; Apostolos, G. G.; Karp, D. A.; Lattman, E. E.; Spencer, D. S.; Stites, W. E.; Garcia-Moreno, B. E. *Biophys. J.* **2000**, 79, 1610.

[25] Kisker, C; Schindelin, H; Pacheco, A; Wehbi, W. A.; Garrett, R. M.; Rajagopalan, K.V.; Enemark, J.H.; Rees, D.C. *Cell*, **1997**, 91, 973

[26] Garrett, R.M.; Rajagopalan, K.V. *J. Biol Chem.* **1996**, 271, 7387-7391.

[27] **a)** Musgrave, K.B.; Lim, B.S.; Sung, K-M.; Holm, R.H.; Hedman, B.; Hodgson, K. O. *Inorg. Chem.* **2000**, 39, 5238-5247. **b)** Xiao, Z.; Young, C.G.; Enemark, J.H.; Wedd, A.G. *J. Am. Chem. Soc* .**1992**, 114, 9194-9195. **c)** Laughlin, L.J.; Young, C.Y. *Inorg. Chem.* **1996**, 35, 1050-1058.

[28] **a)** Das, S. K.; Choudhury, P.K.; Biswas, D.; Sarker, S. *J. Am. Chem Soc.* **1994**, 116, 9061-9070. **b)** Oku, H.; Ueyama, N.; Kndo, M.; Nakamura, A. *Inorg. Chem.* **1994**, 33, 209-216. **c)** Ueyama, N.; Okamura, T.; Nakamura, A. *J. Am. Chem. Soc.* **1992**, 114, 8129-8137.

[29] **a)** Smith, P.D.; Millar, A.J.; Young, C.G.; Ghosh, A.; Basu, P. *J. Am. Chem. Soc.* **2000**, 122, 9298-9299. **b)** Mondal, S.; Basu, P. *Inorg. Chem* **2001**, 40, 192-193. **c)** Nemykin, V.N.; Davie, S.R.; Mondal, S; Rubie, N.; Somogyi, A.; Kirk, M.L.; Basu, P. *J. Am. Chem. Soc.* **2002**, 124, 756-757.

[30] **a)** Inscore, F. E.; McNaughton, R.; Westcott, B.L.; Helton, M. E.; Jones, R.; Dhawan, I.K.; Enemark, J. H.; Kirk, M.L. *Inorg. Chem.* **1999**, 38, 1401-1410. **b)** McNaughton, R.L.; Helton, M. E.; Rubie, N.D.; Kirk, M.L. *Inorg. Chem* .**2000**, 39, 4386-4387.

[31] **a)** Cleland, W.E.; Barnhart, K. M.; Yamanouchi, K.; Collison, D.; Mabbs, F.E.; Ortega, R.B.; Enemark, J.H. *Inorg. Chem.* **1987**, 26, 1017-1025. b) Roberts, S.A.; Young, C.G.; Kipke, C. A.; Cleland, W.E.; Yamanouchi, K.; Carducci, M.D.; Enemark, J.H. *Inorg.*

Chem. **1990**, 29, 3650. c) Dhawan, I.K.; Pacheco, A.; Enemark, J.H. *J. Am. Chem. Soc.* **1994**, 116, 7911.

[32] Carrano, C.J.; Balwant, C.S.; Hammes, B.S.; Kail, B.W.; Nemykin, V.N.; Basu, P. *Inorg. Chem.* **2003**, 42, 5999-6007.

[33] Sarpone, N; Bickley, D.G. *Prog. Inorg. Chem.*, **1972**, 17, 391.

[34] Mondal, J.U.; Zamora, J.G.; Kinon, M.D.; Schultz, F.A. *Inorg. Chim. Acta.* **2000**, 309.

[35] Hammes, B.S.; Carrano, C.J. *Inorg. Chem.* **1999**, 38, 3562.

[36] Kail, B.W.; Nemykin, V.N.; Davie, S.R.; Carrano, C.J.; Hammes, B.; Basu, P. *Inorg. Chem.* **2002**, 41, 1281-1291.

[37] Kail, B.W.; Basu, P. **2006***, JCS, Dalton Trans.* (11) 1419.

[38] Basis sets were obtained from the Extensible Computational Chemistry Environment Basis Set Database, version 4/22/01, as developed and distributed by the Molecular Science Computing Facility, Environmental and Molecular Sciences Laboratory, which is part of the Pacific Northwest Laboratory, P.O. Box 999, Richland, WA 99352, and funded by the U.S. Department of Energy. The Pacific Northwest Laboratory is a multiprogram laboratory operated by Battelle Memorial Institute for the U.S. Department of Energy under contract DE-AC06- 76RLO 1830. Contact David Feller or Karen Schuchardt for further information

[39] **a**) McLean, A. D.; Chandler, G. S. *J. Chem. Phys.* **1980**, *72*, 5639. **b)** Krishnan, R.; Binkley, J. S.; Seeger, R.; Pople, J. A. *J. Chem. Phys.* **1980**, *72*, 650

[40] Frisch, M. J.; Trucks, G. W.; Schlegel, H. B.; Scuseria, G. E.; Robb, M. A.; Cheeseman, J. R.; Zakrzewski, V. G.; Montgomery, J. A., Jr.; Stratmann, R. E.; Burant, J. C.; Dapprich, S.; Millam, J. M.; Daniels, A. D.; Kudin, K. N.; Strain, M.

C.; Farkas, O.; Tomasi, J.; Barone, V.; Cossi, M.; Cammi, R.; Mennucci, B.; Pomelli, C.; Adamo, C.; Clifford, S.; Ochterski, J.; Petersson, G. A.; Ayala, P. Y.; Cui, Q.; Morokuma, K.; Malick, D. K.; Rabuck, A. D.; Raghavachari, K.; Foresman, J. B.; Cioslowski, J.; Ortiz, J. V.; Stefanov, B. B.; Liu, G.; Liashenko, A.; Piskorz, P.; Komaromi, I.; Gomperts, R.; Martin, R. L.; Fox, D. J.; Keith, T.; Al-Laham, M. A.; Peng, C. Y.; Nanayakkara, A.; Gonzalez, C.; Challacombe, M.; Gill, P. M. W.; Johnson, B. G.; Chen, W.; Wong, M. W.; Andres, J. L.; Head-Gordon, M.; Replogle, E. S.; Pople, J. A. *Gaussian 98*; Gaussian, Inc.: Pittsburgh, PA, **1998**

[41] Nemykin, V.N.; Basu, P. *VMOdes: Virtual Molecular Orbital description program for Gaussian, GAMESS, and hyperchem, revision B 6.2.*

[42] Nemykin, V.N.; Kobayashi, N.;Chernii, V.Y.;Belsky, V.K. *Eur. J. Inorg. Chem.* **2001**, 733.

[43] Grodzicki, M.; Flint, H.; Winkler, H.; Walker, F.A.; Trautwein, A. X. J. *J. Phys. Chem. A.* **1997**, 101, 4202.

[44] Stewart, J.I.P. *Comput.-Aided Mol. Des.* **1990**, 4, 1.

[45] *Hyperchem Pro*, version 6.03; Hypercube, Inc.: Gainsville, FL, 2001.

[46] Becke, A.D. *J. Chem. Phys.* **1993**, 98, 5648.

[47] Perdew, J.P. *Phys. Rev. B: Condens. Matter* **1986**, 33, 8822.

[48] Lee, C.; Yang, W.; Parr, R.G. *Phys. Rev. B: Condens. Matter* **1988**, 37, 785.

[49] Thompson, L.M.; Hall, M.B. *J. Am. Chem.Soc.* **2001**, 123, 3995.

[50] **a)** Neumann, R.; Nobes, R.H.; Handy, N.C. *Mol. Phys.* **1996**, 87,1. **b)** Wilberg, K.B.; Stratmann, R.E.; Frisch, M.J. *Chem. Phys. Lett.* **1988**, 297, 60.

[51] offered by Professor Carl Carrano through collaborative arrangements

[52] Rubie, N.; Davie, S.R.; Kail, B.W.; Hammes, B.S,; Carrano, C.J.; Basu, P.; Kirk, M.L. Manuscript in preparation.

[53] CV Results for the *cis*-[(L3S)$MoOCl_2$] complex were obtained through collaborative arrangement with Professor Carl Carrano.

[54] Handbook of Chemistry and Physics 1994

[55] Mouesca, J-M,; Chen, J. L.; Noodleman, L.; Brashford, D.; Case, D. A. *J. Am. Chem. Soc.* **1994**, 116, 11898-11914.

[56] Wilson, G. L.; Greenwood, R. J.; Pilbrow, J. R.; Spence, J. T.; Wedd, A. G. *J. Am. Chem. Soc.* **1991**, 113, 6803-6812.

[57] Nipales, N. S.; Westmoreland, T. D. *Inorg. Chem.* **1997**, 36, 756-757

[58] George, G. N.; Bray, R. C. *Biochemistry*, **1988**, 27, 3603-3609.

[59] Scullane M. I.; Taylor, R. D.; Minelli, M.; Spence, J. T.; Yamanouchi, K.; Enemark, J. H.; Chasteen, N. D. *Inorg. Chem.* **1979**, 18, 3213-3219.

[60] Nemykin,V.N., Kail,B.W., Upadhyay, A.., Hendrich,M.P. and Basu,P. Manuscript in preparation.

[61] Scullane M. I.; Taylor, R. D.; Minelli, M.; Spence, J. T.; Yamanouchi, K.; Enemark, J. H.; Chasteen, N. D. *Inorg. Chem.* **1979**, 18, 3213-3219.

[62] Bray, R. C.; Adams, B.; Smith, A. T.; Richards, R. L.; Lowe, D. J.; Bailey, S. *Biochemistry* **2001**, *40*, 9810-9820.

[63] Carducci, M. D.; Brown, C.; Solomon, E. I.; Enemark, J. H. *J. Am. Chem. Soc.* **1994**, *116*, 11856-68

[64] a) McMaster, J; Carducci, M. D.; Yang, Y.S.; Solomon, E. I.; Enemark, J.H. *Inorg. Chem.* **2001**, 40, 687. b) Izumi, Y.; Glaser, T.; Rose, K.; McMaster, J.; Basu, P.;

Enemark, J. H.; Hedman, B.; Hodson, K.O.; Solomon, E. I. *J. Am. Chem. Soc.* **1999**, 121, 10035.

[65] a) Webster, C.E.; Hall, M.B. *J. Am Chem Soc.* **2001**, 123, 5820. b) Pietsch, M.A.; Hall, M.B. *Inorg. Chem* **2001,** 35, 1273. c) McNaughton, R.; Tipton, A.A.; Rubie, N.D.; Conry, R.; Kirk, M.L. *Inorg. Chem.* **2000**, 39, 5697.

[66] a) Bray, M.R.; Deeth, R.J. *Inorg. Chem.* **1999**, 35, 5720, b) Ilich, P.; Hille, R. *J. Phys. Chem B* **1999**, 103, 5406. c) Voityuk, A.A.; Albert, K.; Romão, M.J.; Huber, R.; Rösch, N. *Inorg. Chem.* **1998**, 37, 176.

[67] Nemykin, V.N.; Basu, P. *Manuscript in preparation.*

[68] Nemykin, V.N.; Polishin, E.V.; Kobayashi, N. *Mendeleev Commun.* **2000**, 54. b) Nemykin, V.N.; Polishina, A. E.; Chernii, V.Y.; Polishin, E. V.; Kobayashi, N. *J. Chem. Soc. Dalton Trans* **2000**, 1019.

[69] a) Detrich, J.L; Konecnỳ, R.; Vetter, W.M.; Doren, D.; Reingold, A.L.; Theopold, K.H. *J. Am. Chem. Soc.* **1996**, 118, 1703. b) Gunnoe, T. B.; Meiere, S. H. ; Sabat, M.; Harman, W. D. *Inorg. Chem.* **2000.** 39, 6127. c) Zaric, S. Hall, M.B., *J. Phys. Chem. B.* **1998,** 102, 1963.

[70] a) Miskowski, V.M.; Gray, H.B.; Hopkins, M.D. *Adv. Transition Met. Coord. Chem.* **1996**, 1, 159. b) Mayer, J.M. *Comments Inorg. Chem.* **1988**, 8, 125. c) Solomon, E.I.; Enemark, J.H. *J. Am. Chem. Soc* **1994**, 116, 11856. d) Sabel, D.M.; Gewirth, A.A. *Inorg. Chem.* **1994**, 33, 148. e) Neuhaus, A.; Veldkamp, A.; Frenking, G. *Inorg. Chem.* **1994**, 33, 5278. f) Deeth, R.J. *J. Chem. Soc., Dalton Trans.* **1991,** 1895.

[71] Helton, M. E.; Kirk, M.L. *Inorg. Chem.* **1999**, 38, 4384. Inscore, F.E.; McNaughton, R.; Wescott, B.L.; Helton, M.E.; Jones, R.; Dhawan, I.K.; Enemark, J.H.; Kirk, M.L. *Inorg. Chem.* **1999**, 38, 1401.

[72] Mondal, S.; Basu, P. *Inorg. Chem.* **2001**, 40**,** 192.

[73] a) Argyropoulos, D.; Mitsopoulou, C.-A.; Katakis, D. *Inorg. Chem.* **1996**, 35, 5549. b) Mondal, J.U.; Zamora, J.G.; Kinon, M.D.; Schultz, F.A. *Inorg. Chem.* **1997**, 36, 637. c) Duhme, A.-K. *J.Chem. Soc., Dalton Trans.* **1997,** 773.

[74] Foresman, J.B.; Frisch, A. *Exploring Chemistry with Electronic Structure Methods;* Gaussian, Inc: Pittsburgh, PA, **1996**.

[75] Falaras, P.; Mitsopoulou, C.-A.; Argyropolous, D.; Lyris, E.; Psaroudakis, N.; Vrachnou, E.; Katakis, D. *Inorg. Chem.* **1995**, 34, 4536.

[76] Jones, R. M.; Inscore, F. E.; Hille, R.; Kirk, M. L. *Inorg. Chem*. **1999**, 38, 4963.

[77] George, G. N.; Gerrett, R. M.; Prince, R. C.; Rajagopalan, K. V. J. *Am. Chem. Soc.* **1996**, 118, 8588-8592.

[78] Gerrett, R. M.; Rajagopalan, K. V. *J. Biol. Chem*. **1996**, 271, 7387-7391

[79] Hilton, J. C.; Temple, C. A.; Rajagopalan, K. V. *J. Biol. Chem*. **1999**, 274, 8428-8436.

Conclusions:

It has been established that there are three main physico-chemical parameters that contribute to the reactivity of phosphorous (III) compounds, two of which are electronic and the third is of steric origin. It is commonly accepted that chemical reactivity involves a σ-basicity component, a π-acidity component and a steric/size component. However, there has been little investigation into the reactivity of the analogue oxo-phosphorous (V) compounds. These compounds are typically generated during oxygen atom transfer reactions (OAT) when the parent phosphorous (III) compounds act as nucleophiles toward oxygen.

Mechanistically, the understanding of oxygen atom transfer has progressed dramatically over the years. This rich history shows a progression in understanding from a single transition state that involved concomitant transfer of two electrons with the labile oxygen atom to one of formal electron transfer followed by complete separation of the donor and acceptor pair. Thus, this new perspective on the mechanism of oxygen atom transfer challenges the definition of the complete and incomplete formalism of the reaction by blurring the limits of "completeness". More specifically, the data presented in **Chapter 2**, along with the analysis in **Chapter 3**, shows that there are two steps in the atom transfer process: The first nucleophilic attack step involves formal oxidation/reduction while the second solvation step results in complete separation of the donor/acceptor pair. Furthermore in **Chapter 1** and **Chapter 3**, we show that both biological and model complex reactivity appear to depend upon both the steric and electronic parameters associated with the substrate and metal complex. More explicitly, in **Chapter 2**, we have shown that the rate of OAT intermediate formation, and ultimate

phosphine oxide production, are strongly influenced by the basicity of the phosphine as well as the size of the phosphine. For example a small basic phosphine like PMe_3, shows relatively rapid intermediate formation, but comparatively slow intermediate solvation as determined by the k_2/k_1 ratio of ~0.25. On the other hand a larger, more acidic substrate, like $PEtPh_2$, shows reactivity that is directly opposite to that of PMe_3 with a k_2/k_1 ratio of 103.5 when $Tp^{iPr}MoO_2OPh$ is considered. When the data on SO reactivity from **Chapter 1** is considered, this same trend is shown through the k_{cat}/K_m ratios with sulfite and DMS which are 2.82 and 0.01 respectively. Here the individual K_m values, 28 μM for sulfite and 6300 μM for dimethyl sulfite, suggest that the nucleophilic attack step for sulfite is more favorable than that of dimethyl sulfite. However, the release rates of the oxidized substrates are nearly identical with k_{cat} values of 79 s^{-1} and 89 s^{-1} respectively.

In **Chapter 3** we have explored the current concepts associated with reactivity, the origin of reaction parameters and the general applicability of phosphorous (III) parameters toward reactions that evolve phosphorous (V) products. More explicitly, we have explored the application of linear free energy relationships that center upon these parameters to the oxygen atom transfer process. We have shown that these parameters are indeed a valid model to the OAT reactions, presented in **Chapter 1** and **Chapter 2**, provided that intermediate complexes are not observable during the reaction. More concretely, we have found that the parameters fail when the individual reaction steps (formation and solvation rates) are scrutinized independently. In contrast we have also shown that when either the k_1/k_2 or k_2/k_1 ratios of the intermediates are considered as a single rate constant, the parameters are valid. This poses a provocative question as to whether the observed reactivity in other model complexes follows a mechanistic pathway

that is similar to the one we have described in **Chapter 2**. Support for this argument is detailed in **Chapter 3**.

We have also shown that metal-based ligands have a profound influence on the rate of the OAT reaction. For example, the data tabulated in **Chapter 1** clearly suggests that S_4 donors result in complexes that are ~7 times more reactive than complexes with ONS donors. This concept is not unique to our study having been previously addressed by Holm. However, when the data tabulated in **Chapter 1** and the experiments performed in this laboratory (**Chapter 2**) are scrutinized together, a clearer view of this concept becomes evident. Thus, the data suggests that the increase in reactivity that is achieved with S_4 donors relative to ONS donors originates in the nucleophilic attack step of the reaction and is less important in phosphine oxide release. The support for this argument is evident when the k_1, and k_2 rate constants are compared between $Tp^{iPr}MoO_2OPh$, $Tp^{Me2}MoO_2OPh$ and $Tp^{Me2}MoO_2SPh$ complexes. First it is clearly evident that the $Tp^{Me2}MoO_2SPh$ analog is ~ 7 times more reactive towards nucleophilic attack (k_1) than the related $Tp^{Me2}MoO_2OPh$ complex and ~ 1.5 times more reactive than the $Tp^{iPr}MoO_2OPh$ complex when PMe_3 is considered. In addition, the $Tp^{Me2}MoO_2SPh$ analog is 20 times more reactive than the $Tp^{Me2}MoO_2OPh$ complex and ~ 6 times more reactive than the $Tp^{iPr}MoO_2OPh$ complex when $PEtPh_2$ is considered. However, when the solvation reactions (k_2) are compared the rates are nearly identical for $Tp^{iPr}MoO_2OPh$ and $Tp^{Me2}MoO_2SPh$ when either PMe_3 or $PEtPh_2$ are considered.

Mechanistically, OAT reactions involve a first nucleophilic step which follows a second-order rate with an associative transition state in all cases. The reaction follows a dissociative interchange (I_d) or associative interchange (I_a) type mechanism, as it shows

substrate and metal complex dependence. The second step of the reaction, i.e., the exchange of the coordinated phosphine oxide with acetonitrile, follows a second-order process, provided the concentration of coordinating solvent is not saturating.

Lastly, the regeneration of a catalytically active enzyme, after formal OAT has occurred, is believed to involve two, one electron/ one proton transfer steps that result in a formal Mo(V) intermediate. In **Chapter 4** we show the synthesis, and fully characterization a series of monooxo-Mo(V) complexes, that were developed in attempt to model the transient Mo(V) state of the enzyme. Furthermore we show that these complexes can be isolated as two discrete isomers with respect to the position of a heteroatom donor relative to the oxo-group and have detailed the kinetics of isomerization and electronic structure of these complexes. Based upon our findings we have postulated a serine gated electron transfer hypothesis (SGET) to provide a possible explanation for the role of isomerism in the regeneration step of a catalytically active protein.